Universitat Autònoma de Barcelona

Multimodal Imaging PLGA Nanocapsules as Protein Carrier for Potential Neurorepair in Ischemic Brain

Yajie Zhang

Universitat Autònoma de Barcelona

Multimodal Imaging PLGA Nanocapsules as Protein Carrier for Potential Neurorepair in Ischemic Brain

Yajie Zhang
张亚杰

DOCTORAL THESIS

Doctoral Studies in Materials Science

Supervised by Dr. Anna Roig Serra and Dr. Anna Rosell Novel
Tutor Dr. Rosa María Sebastián Pérez

Departament de Química, Facultat de Ciències
Universitat Autònoma de Barcelona

2020

Dra. Anna Roig Serra, Professora d'Investigació del CSIC, la **Dra. Anna Rosell Novel** Investigadora Senior del VHIR, i el **Dra. Rosa María Sebastián Pérez,** Professora agregada, UAB

CERTIFIQUEN:

Que Yajie Zhang, amb un Màster en Química Aplicada per la "Ocean University of China", Xina, ha dut a terme aquesta thesis doctoral sota la seva direcció i que porta per títol "PLGA Nanocapsules with Multimodal Imaging Abilities as Drug Carrier for Potential Neurorepair in Ischemic Brain", la qual queda recollida en aquesta memòria per optar al grau de Doctor en Ciència en el Programa de Ciència de Materials.

I perquè així consti, signen el present certificat

Firmado por ROIG SERRA ANNA - DNI 39855642T el día 06/07/2020 con un certificado emitido por AC Administración Pública

Dr. Anna Roig Serra

Directora de la Tesi

Dr. Anna Rosell Novel

Directora de la Tesi

ROSA MARIA SEBASTIAN PEREZ - DNI 46646015Z

Firmado digitalmente por ROSA MARIA SEBASTIAN PEREZ - DNI 46646015Z
Fecha: 2020.07.06 11:29:54 +02'00'

Dr. Rosa María Sebastián Pérez

Tutora de la Tesi

Bellaterra, 3 de juliol 2020

知足常乐

A contented mind is a perpetual feast.

Acknowledgments

I arrived in Barcelona for the first time four years ago and I did not know how interesting the experience would turn out to be, for many reasons. Indeed, I was not aware of what was expecting me during my PhD work on Nanomedicine. Before I had heard about Nanomedicine during the Master's Degree in China and I was soon fascinated by the subject. During these years I have become not only fascinated but also passionate! Definitely, this period has been very important for my professional and personal growth: it has changed my way to face problems and to explore the "unknown". I am very grateful to my supervisors Anna Roig and Anna Rosell for accepting me as PhD candidate. They always encouraged me to do my best. It was very interesting to work side by side: they engaged me in a fruitful and constant dialogue, very useful for the progress of the thesis, offering both the materials science and the medical point of view.

My sincere gratitude also goes to:

Miguel García Gabilondo and Alba Grayston, thank you for the execution of *in vitro* and *in vivo* evaluation of NCs.

Jordi Llop and Xabier Rios, thank you for the support in radiolabeling and PET *in vivo* experimentation.

Technicians from ICMAB, UAB and VHIR, thank you for the support to do the sample characterization.

People of the "N&N group", I really enjoyed the time spent with you inside and outside the lab.

Sportsmen in the basketball team and skiing team, thank you for your company in the spare time, I kept healthy for work.

The China Scholarship Council, thanks for the four years' financial support for my livelihood here.

My family members.

My wife.

Foreword and aim of the thesis

Theranostics is a promising field that combines therapeutics and diagnostics into a single multifunctional formulation. This field is driven by the advancements in nanoparticulated systems capable of providing the necessary functionalities. By utilizing these powerful nanomedicines, the possibility to combine non-invasive disease detection methods with individualized treatments is becoming a reality in personalized medicine. Besides, the advancements in nanomedicine for theranostics have configured the development of image-guided drug delivery, a promising methodology to improve the efficiency of pharmaceuticals by visualizing non-invasively their delivery, effects on specific molecular and cellular targets, and the corresponding therapeutic effects.

The MAGBBRIS (new MAGnetic Biomaterials for Brain Repair and Imaging after Stroke) project, which this thesis is involved with, is devoted to engineering novel magnetic nano-biomaterials to address neurorepair by enhancing angiogenesis in the context of a ischemic stroke. MAGBBRIS aims to demonstrate that growth factors, secreted by endothelial progenitor cells (EPCs), with proved potential to induce angiogenesis, can be encapsulated in magnetic poly(D,L-lactic-co-glycolic acid) (PLGA)-based nanocapsules (NCs) and be delivered to mice brain and retained by an external magnetic field, to finally achieve controlled release and induce vascular remodeling and neurogenic tissue regeneration after stroke.

The work shown in this thesis has been realized at the Nanoparticles and Nanocomposites group, ICMAB-CSIC, in close collaboration with the Neurovascular Research Group at the Vall d'Hebron Research Institute, supervised by Dr. Anna Roig and Dr. Anna Rosell respectively. Previous to the start of this thesis, the group had already initiated a study for non-invasive angiogenic treatment after a brain ischemic event using nanomedicine. Fabrication of biodegradable and biocompatible PLGA NCs loading superparamagnetic iron oxide nanoparticles (SPIONs) and pro-angiogenic human vascular endothelial growth factor (hVEGF) had been evaluated in terms of magnetic resonance imaging (MRI) tracking performance of the nanocarrier and bioactivity for angiogenesis *in vitro* of the released protein. Based on these previous studies, **this thesis aims to expand and improve the drug delivery system for theranostics by**

EPCs-secretome encapsulation into magnetic PLGA NCs and labeled them with versatile imaging reporters allowing magnetic retention and *in vitro*/*in vivo* product tracking for potential non-invasive neurorepair after stroke.

The main specific objectives of the thesis are the following:

1- To optimize the PLGA NC formulation for magnetic targeted delivery, stealthiness and controlled encapsulation and release of therapeutic proteins.

2- To functionalize the PLGA NC formulation with versatile imaging reporters (MRI, fluorescence, positron emission tomography (PET)) for monitoring.

3- To understand the approaches by which the formulated PLGA NCs could improve brain accumulation and increase EPCs secretome loading.

The thesis is organized in 6 chapters.

– **Chapter 1** introduces the state-of-the-art regarding the use of PLGA-based nanoparticles in nanomedicine. It summarizes the loading of various therapeutic agents and the functionalization of PLGA nanocarriers for theronostics. Finally, the MAGBBRIS project is briefly introduced to illustrate the motivation of the thesis work towards the development of PLGA-based nanomedicines for neurorepair after a stroke.

– **Chapter 2** describes the optimization and evaluation of the proposed PLGA NC formulation with potential for clinical translation. Regarding the physicochemical properties of the nanocarrier, it illustrates improvements of the intrinsic capacities of magnetic guidance and MRI and a PEGylation strategy is presented. Moreover, the biosafety, shelf-life and basic quality control of the NC formulation are discussed.

– **Chapter 3** reports on the functionalization of the PLGA NC formulation for multichannel fluorescence imaging demand. It describes several chemical synthetic routes to covalently label the PLGA with biocompatible small molecule fluorophores at different emitting wavelengths (blue, green, red and near-infrared (NIR)). It shows that the size, shape and main compositional traits of the fabricated nanocarrier are not affected by the inclusion or removal of the imaging probes. Finally, the *in vitro*/*in vivo* fluorescence imaging performances of the functionalized nanoformulations are evaluated and the biodistribution of the

intravenous (*i.v.*) administered NCs is investigated.

- **Chapter 4** reports on the functionalization of the PLGA NC formulation with a radiolabel for PET imaging modality. It starts with the synthetic routes to obtain chelator deferoxamine (DFO) conjugated PLGA NCs and the radiolabeling with ^{89}Zr. Then the influences of PEGylation and external magnetic field on the biodistribution of the *i.v.* administered NCs is preliminarily investigated using PET imaging.
- **Chapter 5** explores improved administration protocols to guarantee better brain delivery according to the collected data of the previous chapters. The protein loading and release kinetics are also investigated and efforts are made to increase the therapeutic secretome loading to potentially increase the therapeutic effect.
- **Chapter 6** reports on general conclusions from the work of the thesis and suggests directions for future work.

Attributions

I would like to thank the people who contributed to this thesis.

Anna Rosell, **Alba Grayston** and **Miguel García Gabilondo** (VHIR) for cytoxicity/proliferation studies in human endothelial cells, EPCs-secretome production and its superconcentration, protein determinations and for the *in vivo/ex vivo* MRI and fluorescent imaging studies.

Jordi Llop, **Irene V. J. Feiner** and **Xabier Rios** (CICbiomaGUNE) for radiolabeling PLGA-DFO NCs with ^{89}Zr and for the PET *in vivo* investigations.

Irene Anton Sales (ICMAB) who helped me in the optimization of the protocol for NC fabrication.

Pedro Ramos-Cabrer (CICBiomagune) and **Ignasi Barba** (VHIR) for the pre-clinical *in vivo* MRI.

Jose Amable Bernabé (ICMAB) trained me for the DLS, Nanosight and Turbiscan.

Neus Romà and **Marta Riba** (ICMAB) trained me for the microwave reactor and the spectrophotometer.

Anna Esther Carrillo (ICMAB) for the SEM measurements.

Bernat Bozzo (ICMAB) for the SQUID measurements.

Judit Oró (ICMAB) for the TEM measurements.

Roberta Ceravola (ICMAB) for the TGA measurements.

Fabien Gosselet and **Rodrigo Azevedo** (University of Artois) for MTT with CD34+ cells.

Peter Kopcansky (Institute of Experimental Physics, Slovakia) for the supply of several magnets prototypes.

Fran Cortés and **Olga Garreta Guerra** (SCAC, UAB) trained me for culturing cells.

Silvia Lope Pedrafita (Servei RMN, UAB) ran the MRI measurements for the NC samples *in vitro*.

List of symbols, abbreviations and acronyms

ATR-FTIR	attenuated total reflectance-Fourier transform infrared
BBB	blood–brain barrier
BPLP	biodegradable photoluminescent polyester
BSA	bovine serum albumin
CT	computed tomography
CUR	curcumin
Cy	cyanine
DCC	N,N'-dicyclohexylcarbodiimide
DCM	dichloromethane
DFO	deferoxamine
DOX	doxorubicin
DTX	docetaxel
DLS	dynamic light scattering
EBM	endothelial basal medium
EGM	endothelial growth medium
EPCs	endothelial progenitor cells
EPR	enhanced permeability and retention
i.a.	intra-arterial
i.v.	intravenous
MAGBBRIS	new MAGnetic Biomaterials for Brain Repair and Imaging after Stroke
MRI	magnetic resonance imaging
Mr	remnant magnetization
Ms	saturation magnetization
NHS	N-hydroxysuccinimide
NCs	nanocapsules
NIRF	near-infrared fluorescence imaging
NPs	nanoparticles
NSCs	neural stem cells

OA	oleic acid
PdI	polydispersity index
PDOX	poly(p-dioxanone)
PET	positron emission tomography
PEG	polyethylene glycol
PGA	poly(glycolic acid)
PLA	poly(lactic acid)
PLGA	poly(D,L-lactic-co-glycolic acid)
PTX	paclitaxel
ROIs	regions of interest
SEM	scanning electron microscope
SPECT	single-photon emission computed tomography
SPIONs	superparamagnetic iron oxide nanoparticles
SQUID	superconductive quantum interference device
TEM	transmission electron microscope
TGA	thermogravimetric analysis
TRE	total radiant efficiency

Table of Contents

1
Introduction

1.1 Cargo types and therapeutic purposes of PLGA-based nanoparticles used as drug delivery systems

Polymers are used extensively in the contemporary biomedical arena because of their biocompatibility, biodegradability, and functionality.[1] Biodegradable synthetic polymers (BDSPs) such as poly(*p*-dioxanone) (PDOX), poly(lactic acid) (PLA), poly(glycolic acid) (PGA), and their copolymers such as PLGA have been widely exploited in biomedicine.[2-4] Among the BDSPs, PLGA is one of the most popular since it undergoes complete biodegradation in physiological medium *via* hydrolytic breakdown of the ester bonds, resulting in the formation of the original monomers lactic and glycolic acids that are rapidly metabolized.[5] PLGA has been approved by the Food and Drug Administration of the United States (USFDA) and the European Medicine Agency (EMA) for application in a variety of drug delivery systems.[6-8]

Polymeric nanoparticles (NPs) have received increased attention in nanomedicine for drug delivery.[9] They are characterized by being able to incorporate tunable functionalities and high capacity to load various therapeutic agents. Polymeric NPs have become optimal carriers to improve the efficacy of the loaded cargos in terms of increasing their bioavailability, solubility in physiological environment and retention time in the target organ or tissue while overcoming limitations such as low absorption, short biological half-life, low specificity and undesired side effects of using non-encapsulated therapeutic agents. PLGA-based NPs would fulfill the requirements including high biocompatibility and biodegradability, low toxicity, appropriate elimination and ease of processing.[10] During the last decades, many efforts have been devoted to rendering PLGA-based NPs suitable for drug delivery applications.[11, 12] Various types of therapeutic agents (e.g., chemotherapy, antibiotics, antiseptic, anti-inflammatory and antioxidant drugs, proteins) have been incorporated into PLGA-based

NPs depending on the therapeutic purposes.[13] Some areas of PLGA nanoformulations in nanomedicine are illustrated in the following sections where the progress of the formulations for pro-angiogenesis therapies, related to the thesis work, is also introduced.

1.1.1 Illustration of various therapeutic nanoformulations

1.1.1.1 PLGA-based NPs for antimicrobial therapy

PLGA-based NPs have been used as carriers for the delivery of various antibiotics to treat bacterial infections such as; ciprofloxacin-loaded PLGA NPs[14, 15] or azithromycin-loaded TPGS−PLGA hybrid NPs[16] against cystic fibrosis *Pseudomonas aeruginosa* lung infections, rifampicin-loaded PLGA NPs[17] against *Francisella* infections, enrofloxacin-loaded PLGA NPs[18] against Gram-negative bacterial infections and trimethoprim-loaded PLGA NPs[19] for instillative treatment of urinary tract infections. These nanoformulations have been proved to offer several advantages over the conventional application of non-encapsulated active pharmaceuticals. Firstly, incorporation of drugs into PLGA matrix reduces the innate cell toxicity of the antibiotics by minimizing the reactive oxygen species (ROS) formation within the host cells, while at the same time retains their antimicrobial efficacy.[18] Moreover, nanoformulations increase the bioavailability of drugs at the site of action and thus the possibility to reduce drug dosage and hence their side effects.[14] Finally, the controlled release of the antibiotic from PLGA NPs is expected to serve for high and sustained local drug concentration.

To meet the challenges of multidrug resistance of bacterial strains[20] as well as the narrow active spectrum of antibiotics on those bacteria[21], various antimicrobial metal-based nanostructures (MNSs have been developed, which can reduce the dosage of antibacterial agents, decrease side effects, overcome bacterial resistance, and reduce costs for patients)[22-26]. Incorporation of antiseptic MNSs into PLGA matrices considerably alters the physicochemical and biological characteristics of these nanometals with improved biocompatibility and decreased toxicity. For example, ZnO/PLGA NPs have significantly lower cytotoxicity compared with ZnO NPs alone and the nanocomposites are nontoxic against host cells but demonstrate antimicrobial activity against bacterial strains.[27] Another example is the encapsulation of Ag NPs into PLGA particles. The resulting composite possesses antimicrobia

activities and is more biocompatible than Ag NPs alone.[28]

1.1.1.2 PLGA-based NPs for cancer treatment

PLGA-based NPs have been deeply investigated for cancer treatment. Regarding chemotherapy, various chemotherapeutic drugs have been loaded into PLGA-based NPs, for instance, doxorubicin (DOX)-loaded PLGA NPs against glioblastoma[29] or colon carcinoma[30], docetaxel (DTX)-loaded PLGA NPs against lung[31, 32] or breast cancer[33, 34], 5-fluorouracil (5-FU)-loaded PLGA NPs against malignancies[35], sorafenib-loaded PLGA NPs against liver fibrosis[36], and curcumin (CUR)-loaded PLGA NPs against colon cancer[37]. Such nanoformulations can extend the drugs' circulation time, sustain drug release and also inhibit the development of drug resistance as well as increase drug accumulation in tumors.[38] Moreover, various pairs of drugs with varying hydrophobicity and pharmacokinetic profiles could be co-encapsulated into the PLGA NPs to provide synergy of a combination treatment. Among the many combinations co-loaded in one particle are paclitaxel (PTX)-cisplatin[39], PTX-Erlotinib[40], DOX-CUR[41], PTX-Verapamil[42], and PTX-epigallocatechin gallate (EGCG)[43], which significantly improvement of their therapeutic efficiency. Next to the synergistic effect of different chemotherapeutic drugs, an additional beneficial therapeutic outcome can be achieved *via* combination treatment with radiotherapy considering that drugs like DOX, DTX and PTX are also prominent radiosensitizers.[38] In this context, Werner et al. encapsulated DTX in PLGA NPs with a lecithin-PEG folate surface modification to optimize radiotherapy. Results revealed that radiation 12 h post-NPs administration had a maximum effect on tumor growth inhibition [44].

Local hyperthermia is also used to damage and kill tumor cells by increasing their temperature to about 42–46°C. Magnetic NPs under the effect of an alternating magnetic field can induce local temperature increase and hyperthermia when injected into the tumors.[45] PLGA NPs have been used to co-encapsulate magnetic iron oxide NPs and chemo-therapeutics and apply hyperthermia in combination with chemotherapy for cancer treatment.[46-48] Aside of magnetic hyperthermia, photothermal therapy offers another approach through light irradiation to induce local hyperthermia, in which a photothermal agent, usually a light-absorbing nanomaterial, absorbs photon energy and dissipates it in form of heat, this heat results in the disruption of cellular membranes and induces apoptosis

and/or necrosis.[49] Many photothermal agents have been studied, for instance, carbon and gold nanomaterials or NIR-absorbing molecules such as indocyanine green (ICG), polydopamine (PDA) and polypyrrole (PPy). And they have been co-loaded with chemo-therapeutics on PLGA-based NPs for a combination therapy, for instance, Au-DTX[50], PDA-DTX[51] or PPy-DTX[52]. In general, promising therapeutic efficacy could exclusively be achieved *via* combination treatments, neither the sole delivery of chemotherapy nor the local hyperthermia could outperform the proposed and presented combination treatments. This can be due to synergistic effects and/or due to an increased drug accumulation following the hyperthermia-related enhanced permeability and retention (EPR) effect.[52, 53]

Recently, gene therapies such as gene delivery, gene silencing or gene editing, and immunotherapies such as cancer vaccines, cytokine therapy, checkpoint-blockade therapy, adoptive T-cell transfer, or chimeric antigen receptor T (CAR-T) cell therapy, are emerging approaches in the anticancer field. The major obstacle in these biotherapies is the protection and targeted delivery of the sensitive cargos (e.g., nucleic acids, nuclease, antigens, adjuvants, etc.), formulations of PLGA-based NPs with versatile modifications are being investigated as drug delivery systems to address this obstacle. [54-57]

1.1.1.3 PLGA-based NPs for tissue regeneration

Tissue regeneration promotes self-repair of damaged tissues *via* the use of cells that possess proliferation and differentiation capability, and aims to restore, maintain or improve the function of damaged tissues.[58] Scaffolds are widely used in regenerative medicine creating an artificial environment to support the cells used for regenerating damaged tissues, and the growth factors that stimulate the cells to differentiate.[59] The tissue engineering applications of PLGA-based scaffolds, for instance, metallic nanostructures (MNSs)/PLGA nanocomposites[60], are mostly focused on bone regeneration.

In terms of injectable PLGA NPs used for regenerative medicine, studies are mainly focused on exploring PLGA microspheres as cell delivery devices due to their ability to deploy cells growth while releasing them at damaged or degenerated tissues.[7] These microspheres offer a favorable surface area substrate for cellular

adhesion and proliferation, and also a biodegradable cell carrier. For example, PLGA-based microspheres used to carry and deliver chondrocytes or their stem cells for the initiation of cartilaginous tissue regeneration[61-63], or as smooth muscle-like cells vehicles to be applied in the therapy of muscle degeneration diseases to restore lost smooth muscle function and promote the regeneration of the damaged tissues[64, 65].

Regarding PLGA NPs for tissue regeneration, they are often used as carriers for hormones or proteins with physiological functions[66]. In addition to all the advantages associated to PLGA microparticles, the NPs present advantages related with their nanoscale size. For example, estradiol (E2) is encapsulated into PLGA NPs for osteoporosis treatment to improve bone mineral density in postmenopausal women.[67] This nanoformulation is highly useful for the recovering of bone mineral density as well as reducing the administration intervals with the transdermal administration route.

1.1.2 Overview of PLGA-based formulations for pro-angiogenesis therapy and related neurorepair

New blood vessel formation is a critical requirement for treating vascular and ischemia related diseases, the involved angiogenesis and vasculogenesis represent crucial processes for the functional regeneration of complex tissues. Growth factors represent a group of functional proteins that stimulate cell growth, proliferation and differentiation and are crucial in the regulation of multiple cellular processes.[12] Several proangiogenic growth factors, for instance, platelet-derived growth factor (PDGF-BB), fibroblast growth factor (FGF-2) and vascular endothelial growth factor (VEGF) have been successfully encapsulated into PLGA-based NPs for pro-angiogenesis therapies.[68-70] Chereddy et al. demonstrated that VEGF-loaded PLGA NPs accelerate neovascularization and promote wound healing, enhancement of migration and proliferation of keratinocytes and upregulation of expression of VEGFR2 at mRNA level are revealed (**Figure 1-1**).[71] Xiong et al. also showed a successful action of VEGF-loaded PLGA NPs in the promotion of blood vessels and smooth muscle fibers regeneration in the bladder of a swine model, the NPs could release VEGF for at least 3 months.[72]

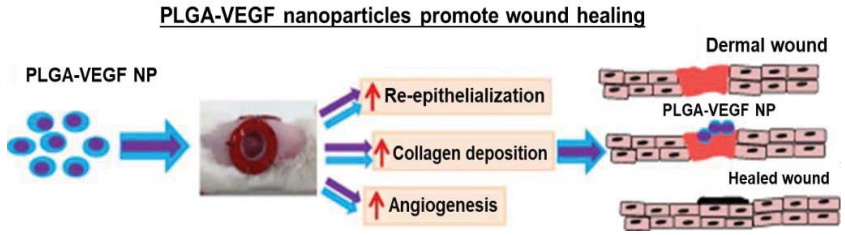

Figure 1-1. The wound healing effects of PLGA-VEGF NPs were evaluated in splinted mouse full-thickness excisional model. The silicone splints avoid the contraction of wound and thereby the wound healing is majorly conducted by re-epithelialization similar to that of humans. PLGA-VEGF NPs induce higher re-epithelialization, granulation tissue formation and angiogenesis, thus promote wound healing. This figure is obtained from *Nanomedicine: Nanotechnology, Biology and Medicine (2015)* by K.K. Chereddy et al.[71]

Regarding pro-angiogenesis therapy for neurotissue remodeling after an ischemic stroke episode, which is related to the study in this thesis, PLGA-based microspheres have been used to support human neural stem cells (hNSCs), and simultaneously release VEGF. After injection of the microspheres in the rat brain directly to the lesion site, VEGF provides the recruitment of endothelial cells (ECs) from the host tissue, hence initiating the neovascularization in the lesion cavity, which is associated with the integration and differentiation of the NSCs (**Figure 1-2**).[73] However, this strategy for ischemic stroke treatment may have potential side effects. On the one hand, the VEGF induced hypervascularization that may be detrimental leading to hNSCs preferentially differentiate into astrocytes, despite that the neuronal differentiation of hNSCs is always challenging. Moreover, even VEGF is known to induce angiogenesis, it also creates a more permeable blood-brain-barrier (BBB)[74]. Its continued presence and release might lead to overexpansion of individual unorganized ECs, whilst also permitting the invasion of inflammatory cells through a compromised BBB[73].

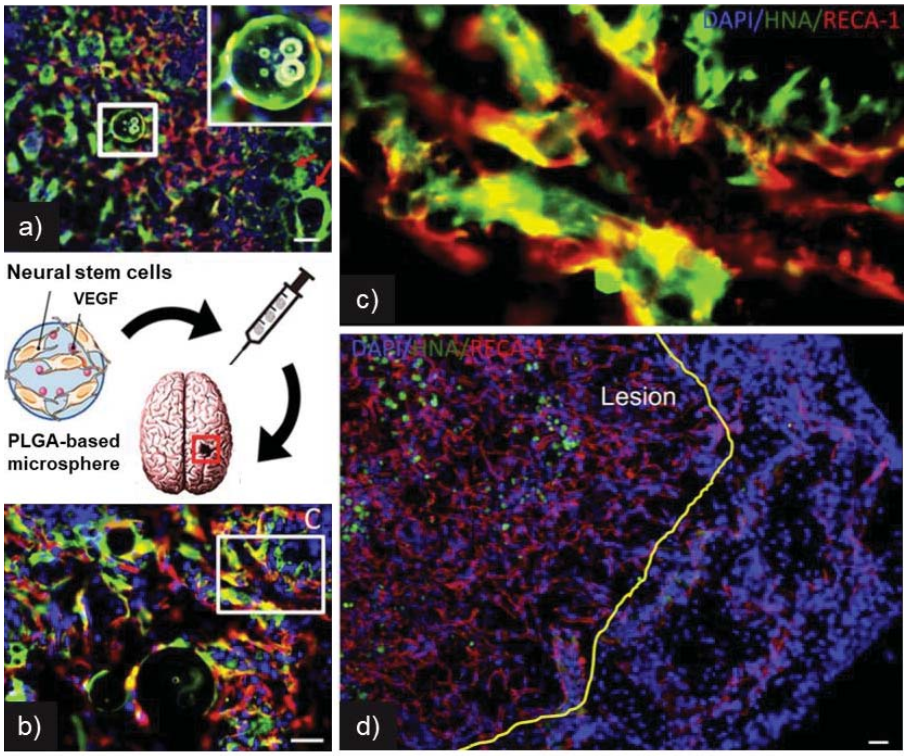

Figure 1-2. Neurotissue regeneration after a stroke episode based on local injectable VEGF-releasing PLGA microspheres (50–100 μm) with NSCs attached. a) Vascularization of the lesion cavity is a gradual process with cells migrating in and gradually covering the lesion space. Therefore, some areas contain human NSCs (HNA in green) attached to particles (red arrows), but no endothelial cells (Reca-1 in red). Some particles are still clearly visible as a whole particle (boxed insert) with cells attached; b, c) in some instances, it is evident that a primitive neurovascular environment is emerging where human NSCs support the formation of tubules formed by endothelial cells. However, these are non-functional elements as these remained incomplete; d) the density of endothelial cells and newly forming blood vessels is much denser than found in normal tissue. It is unclear here if this is part of an attempt to establish a vascular network that for instance, will eventually prune some unnecessary branches or if this could remain as a hyper-vascularized tissue (Scale bar = 50 μm). This figure is obtained from *Biomaterials (2012)* by E. Bible et al.[73]

Accumulating evidence indicates that bone marrow-derived EPCs equipped with an inherent capacity to repair endothelial damage and differentiate into mature endothelial cells contribute towards a favorable neurovascular remodeling environment that supports neuronal regeneration and unctional recovery in the delayed phases of stroke (**Figure 1-3**).[75, 76] Many EPCs-based cell therapies have been investigated in pre-clinical models of stroke.[77-79] Despite the

high potential of EPCs for stroke therapy, an outstanding hurdle for its application is the lack of efficient administration systems, resulting in a low number of cells reach the desired area together with undesirable side effects.[80]

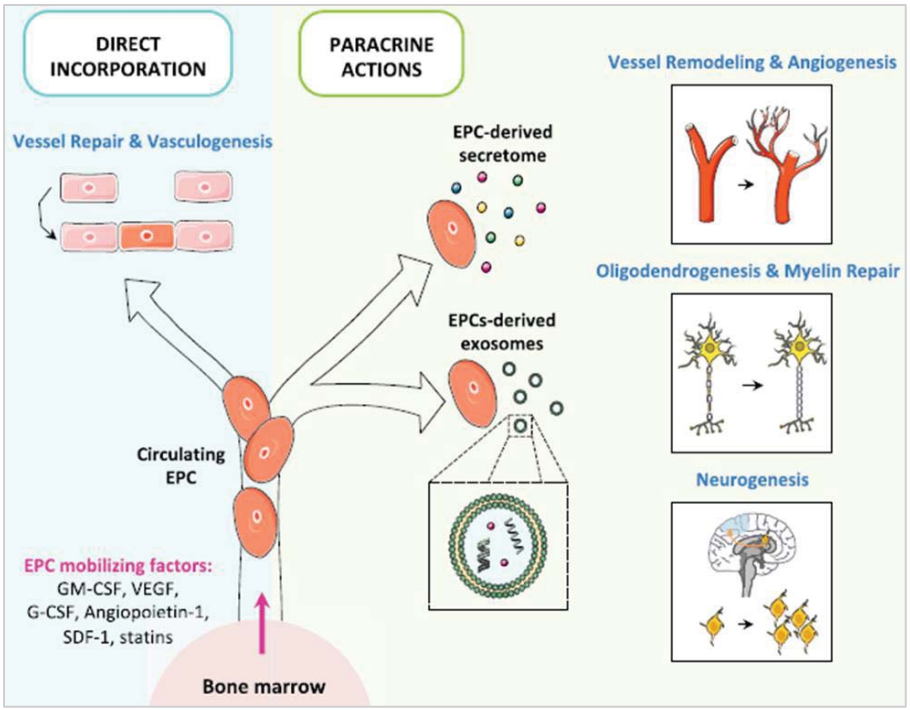

Figure 1-3. Scheme of the main EPC functions related to neovascularization and contribution to mechanisms of neurorepair after stroke. Direct actions include the incorporation to damaged vessels or vessel remodeling by vasculogenesis whereas indirect contributions on vessel remodeling, remyelination, oligodendrogenesis, or neurogenesis are mediated by secreted molecules, including exosomes (G-CSF, granulocyte colony stimulating factor; GM-CSF, granulocyte macrophage-colony stimulating factor; SDF-1, stromal-derived factor-1). This scheme is obtained from *American Journal of Physiology-Cell Physiology (2018)* by G. Esquiva et al.[76]

Previous study from the Neurovascular Group at VHIR demonstrated that not only EPCs but also their secreted growth factors (secretome) can promote vascular plasticity after ischemic stroke.[81] Also others have noted the importance of a multifactorial stimulation of angiogenesis for mature blood vessel formation with a functional BBB.[82, 83] Therefore EPCs-secretome is emerging as a promising cell-free therapeutic product that could be administrated safely in large amounts for revascularizing and remodeling purposes[84, 85] Taking into account that the pharmaceutical market using therapeutic

proteins is incredibly increasing[86] and PLGA NPs are already used as protein carriers for protective, efficient and sustained delivery[87-89]. Those previous results encouraged us to direct this thesis work towards the development of PLGA-based NPs to deliver EPCs-secretome, proposing its therapeutic pro-angiogenesis actions in the ischemic brain.

1.2 Customizing the PLGA-based nano delivery systems for theranostics

Theranostics combines therapeutics and diagnostics into single multifunctional formulations. Advancements in nanoparticle systems have provided the necessary functionalities for their theronostic applications.[90] Typical theranostic NPs include three components: 1) diagnostic imaging probe, 2) targeting ligand, and 3) therapeutic. As illustrated in **Figure 1-4**, various desired elements categorized into the three categories are incorporated into the PLGA nanoparticle, converting this nanoplatform into a theranostic delivery system. Diagnostic imaging probes can aid to either monitor the interactions and fate of NPs with biological entities *in vitro*/*in vivo*, or visualize the exact nature, phenotype, and stage of the disease to guide treatment. Targeted delivery achieved either through the active targeting ligands or passively is also an advantageous property for imaging outcomes because it reduces unwanted interruption in signaling and improves selectivity and sensitivity. Therefore, a customized theranostic PLGA-based NPs can guided in the study of the treatment, the efficacy of the dosage delivered, or to predict the response to treatment. It can help to maximize drug efficacy and reduce the guesswork associated with the development of disease treatments. What follows are examples of imaging and targeted delivery functionalization of the PLGA nanocarriers. Integrating different components in a PLGA-based theranostic system is introduced.

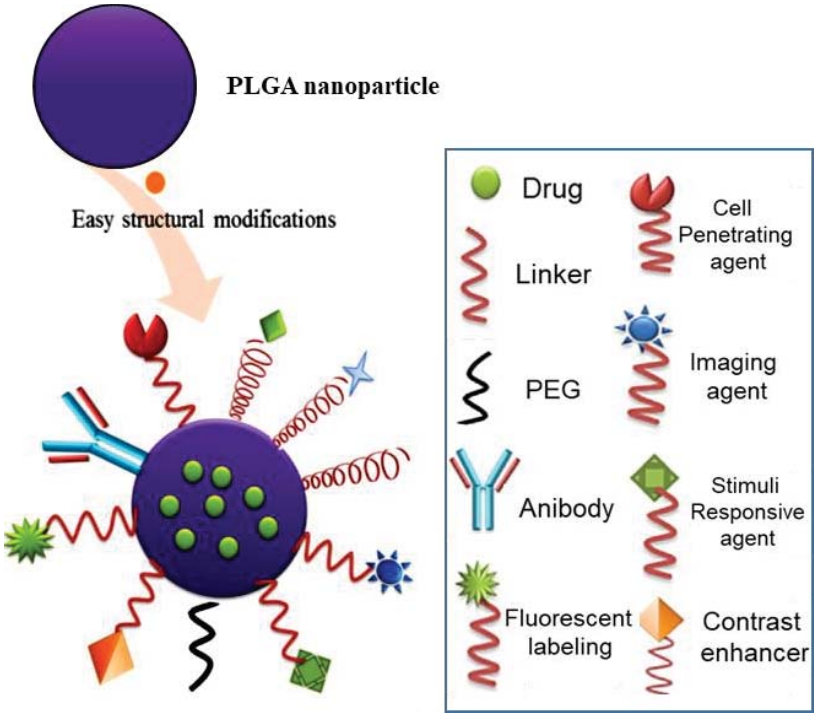

Figure 1-4. Schematic illustration of the modification of PLGA-based nano delivery system. This scheme is obtained from *Colloids and Surfaces B: Biointerfaces (2017)* by M. Mir et al.[10]

1.2.1 Imaging functionalization of the PLGA nanocarrier

Optical imaging utilizes photons emitted from bioluminescent or fluorescent probes for the detection. It is considered to be an attractive option for *in-vitro* and pre-clinical imaging due to its lack of non-ionizing radiation, the ability to image the spectrum from visible to NIR in real-time and that it is inexpensive.[91] Various probes used for this imaging, including organic dyes[92-95], synthetic fluorophores[96, 97], quantum dots[98, 99] and lanthanide upconversion nanomaterials[100, 101], can be integrated into the PLGA nanocarriers during the particle synthesis. For the theranostic applications, the imaging domain is used to follow the tissue or cellular uptake, *in vivo* biodistribution and accumulation in specific body areas following the local or systemic administration of the NPs. Conventional approaches to physically blend imaging probes within the carrier always encounter the leakage of fluorescent labels from the PLGA matrix that makes it difficult to differentiate the signal of the entrapped marker associated with NPs and the free leaking fluorescent material and this can sometimes lead to incomplete conclusions or

misinterpretations on the carrier's biodistribution[99, 102]. For example, loading two different molecules as probes into the same carrier led to opposite conclusions regarding the kinetics of brain-specific delivery.[102] Therefore, a stable fluorescent label is of crucial importance for the sensitivity of quantitative and qualitative detection as well as the contrast of fluorescent microscopical imaging. Thus, covalent conjugation of the fluorescent probes offers a promising tool to obtain more time-stable fluorescent NPs. Due to that native PLGA does not include easily accessible "chemical handles" for fluorescent labeling, some strategies were developed to modify the PLGA through the carboxylic end. The most used reaction is the carbodiimide one (**Figure 1-5**), which conjugates the carboxylic end group of PLGA with the amine end group of the ligands by forming an amide group[98, 103]. Besides, the amide bridge can be used to introduce other reactive groups to the end of PLGA molecule, thus any desired ligands can be further bound, which enables the functionalization of PLGA tailor-made.

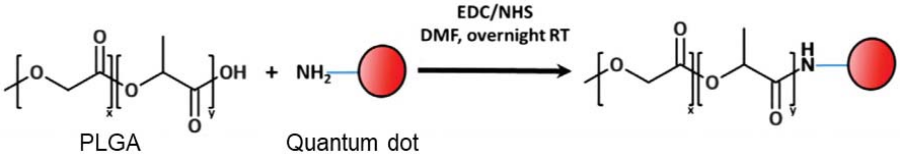

Figure 1-5. Schematic illustration of the process of labeling PLGA (-COOH) with quantum dot (QD-NH_2) through carbodiimide chemistry. This scheme is obtained from *Journal of Control Release (2017)* by D.X. Medina et al. [98]

MRI is a prevalent diagnostic imaging technique that is used primarily for acquiring high-resolution anatomical images in the body thanks to its excellent spatial resolution.[90, 104] The physical principles of MRI rely on the differing relaxation time of water protons under external magnetic fields resulting from the heterogeneous distribution and environment of water protons in the organism. The differences in relaxation times can be either longitudinal (T1) or transverse (T2) and are used to generate image contrast. Usually, the contrast has to be amplified to better image a local site, thus different types of contrast-enhancing agents (T1 or T2) are developed for an increased MRI signal intensity. In general, the contrast agents can be categorized into gadolinium-based or manganese-based paramagnetic T1 contrast agents[101, 105, 106] and iron oxide or iron platinum superparamagnetic T2 contrast agents[107-109]. Some contrast agents are extensively applied preclinically for diagnostics while others are routinely applied in clinics for instance,

Gd-DTPA (gadolinium (III) diethylene triamine pentaacetate) from Magnevist and Ferristene (micron size iron oxide particles) from Abdoscan [110]. Among them, the superparamagnetic iron oxide nanoparticles (SPIONs) have been combined with PLGA NPs for the advantages of simultaneous T2-weighted MRI and magnetic targeting drug delivery[30, 48, 97, 107, 108, 111, 112]. Moreover, the obtained magnetic nanocarrier can be used to generate localized magnetic hyperthermia by alternating magnetic fields, which can be exploited for cancer therapy or/and thermally activated drug release.[48, 107]

Radionuclide imaging techniques such as PET and single-photon emission computed tomography (SPECT) detect the gamma rays generated by radionuclides. These techniques enable the quantification of the concentration of a nanoformulation once the nanoformulation is labeled with a radioisotope. Once administered, it can be monitored and quantified over time with high sensitivity. More importantly, both PET and SPECT are fully translational which enable the evaluation of pharmacokinetics both in the preclinical and clinical fields. Thus, radiolabeling is a key step to apply nuclear imaging techniques in nanomedicine. Early radiolabeling of PLGA-based NPs involved direct entrapment of radioligands into the NPs, some examples are the encapsulating hydrophilic macrocyclic copper complex into hollow PLGA nanocapsules for PET[113], and entrapping ^{111}In-doped iron oxide NPs into solid PLGA matrix for SPECT[114]. In general, theranostic nanoformulations are usually designed and fabricated first, with anchor points reserved for the radioligands, which allows full characterization of the nanoformulations and incorporation of the radioligands at the very last stage. Then, the anchoring of radioligands usually takes place under mild chemical conditions without altering the main properties of the pre-designed nanoformulations. For example, anchor points provided by avidin on the PLGA NP surface allow the rapid and nearly irreversible linkage of biotinylated ^{18}F radioligands through avidin−biotin interaction[115], and anchor points provided by chelator NODA (2,2'-(7-(4-((2-aminoethyl) amino)-1-carboxy-4-oxobutyl)-1,4,7-triazonane-1,4-diyl)diacetic acid) on the PLGA NP surface permitting the chelating of ^{68}Ga[116].

In addition to the imaging modalities introduced above, other modalities such as photoacoustic imaging, X-ray imaging have been also reported by integrating the corresponding imaging probes into the PLGA nanocarrier[50, 117]. In general, the imaging

functionalization of PLGA-based NPs is customizable and, various imaging moieties can be incorporated depending on the desired application. The possibility for simultaneous incorporation of several probes has turned PLGA nanocarriers into a platform with multimodalities to meet the need for hybrid imaging methodologies, able to overcome the shortcomings of a single modality and acquire complementary information regarding monitoring, diagnosis, and treatment[118]. For instance, MRI offers a high spatial resolution and has many advantages over other imaging techniques such as X-ray and computed tomography, including the fact that it is non-invasive and uses non-ionizing radiation to acquire the images. However, MRI is expensive, and it cannot be used in patients with metallic medical devices implanted, in our case the magnet. NIRF provides a fast and convenient way to monitor whole-body NCs in real-time but has the disadvantages of poor tissue penetration and susceptibility to noise due to scattering. PET is sensitive with low noise and produces three-dimensional images, while the disadvantages include spatial resolution limitations, cost of the equipment, imaging only one radionuclide at a time, and radiation concerns. Some combinations, for example, MRI-X-ray imaging-fluorescence imaging[108], photoacoustic-fluorescent imaging[117] or ^{19}F MRI-fluorescence imaging[119] are reported to be used for the functionalized PLGA-based nanocarrier.

1.2.2 Targeted delivery functionalization of the PLGA nanocarrier

Targeted drug delivery aims to accumulate the therapeutic agent at the site of interest to increase therapeutic efficacy, lower drug dose and side effects. Passive targeting, *via* the EPR effect, has been widely utilized in nanomedicine for tumor targeting. This effect, due to the abnormal architectures and impaired functional regulation of tumor blood vessels, is the hallmark of solid tumor vasculature and related to the selective transport of NPs into the tumor.[120] For example, the formulation of curcumin-loaded PEGylated PLGA nanocapsules was developed to treat colon cancer and showed good tumor accumulation and prolonged blood circulation profile facilitating EPR effect.[37] Other nanoparticle formulations have been clinically approved and administered for the passive targeting to the site of interest *via* this EPR effect.[121] However, passive targeting *via* EPR effect is limited to certain types of tumors and the EPR effect varies among patients, tumors, tumor types and even changes over

time[122], also it is not a suitable alternative for targeting in other diseases, for instance, in regenerative medicine.

An alternative strategy is to use active targeting strategies achieved through the attachment of specific ligands to the PLGA nanocarrier surface. This strategy facilitates selective or preferential interaction of the nanocarrier with specific receptors or transporters of a cell type by molecular recognition and thus increases the specificity of NPs for the target site. The interaction between the nanocarrier and the objective cell can be done *via* ligand-receptor interaction, antigen–antibody interaction or aptamer-mediated targeting.[123] Examples of active targeting of PLGA-based nano delivery systems are presented in **Table 1-1**.

Table 1-1. Active targeting of PLGA NPs concerning the ligand–receptor interaction, antigen–antibody interaction, and the targeting through aptamers.

	Targeting moiety	Drug	Therapy
Ligand–receptor interaction	Lectin	Paclitaxel	Colon cancer[124]
	Sialic acid	Loperamide	Brain delivery[125]
	Transferrin	Aromatase inhibitor	Breast cancer[126]
	T7 peptide	Carmustine	Glioma[127]
	Mannan	Nondefined	Bone marrow diseases[128]
Aptamer-mediated targeting	A10 20-fluoropyrimidine RNA	Docetaxel	Prostate cancer[129]
	Antinucleolin AS1411 aptamer	Doxorubicin	Glioma[130]
	CD133 aptamers A15 and EGFR aptamers CL4	Salinomycin	Hepatocellular carcinoma[131]
Antigen–antibody interaction	Fab fragments from a humanized anti-HER2 monoclonal antibody (rhuMAbHER2)	Pseudomonas exotoxin	Breast cancer[132]
	Human/ mouse chimeric anti-GD2 antibody ch14.18/ CHO	Letrozole	Glioblastoma[133]

Another (active) targeting strategy for drug delivery is magnetic guidance of the NPs to the target site. In this approach, PLGA-based NPs are combined with magnetic nanoparticles (MNPs), which can be accumulated at the target site by applying an external magnetic field. As already elaborated in the last section, the incorporation of SPIONs into the PLGA-based nano delivery system could allow a simultaneous magnetic targeting and MRI, as well as the potential for magnetic hyperthermia. Compared to the utilization of specific

ligands, which may suffer from not enough amount of functionalized NPs and not enough affinity and specificity to target molecules[134], the use of MNPs and external magnetic field may lower the complexity of the nanocarrier. On the other hand, to improve the targeting performance, magnetic targeting could also be combined with other active targeting approaches. Cui et al.[108] reported that the combination of active transferrin receptor binding peptide T7 and magnetic targeting increased the NPs accumulation and cellular uptake. More than 10-fold higher tumor accumulation and improved crossing of the blood–brain barrier by 5-fold was achieved in an orthotopic glioma model compared with non-targeted NPs (**Figure 1-6**). Also, the incorporation of SPIONs can also be utilized for the emerging magnetic particle imaging (MPI), which might not only be used as a non-invasive imaging modality, but also promote magnetic targeting and guide the magnetic PLGA NPs to the target tissue. Additionally, MPI can be combined with magnetic hyperthermia yielding an image-guided theranostic tool.[135]

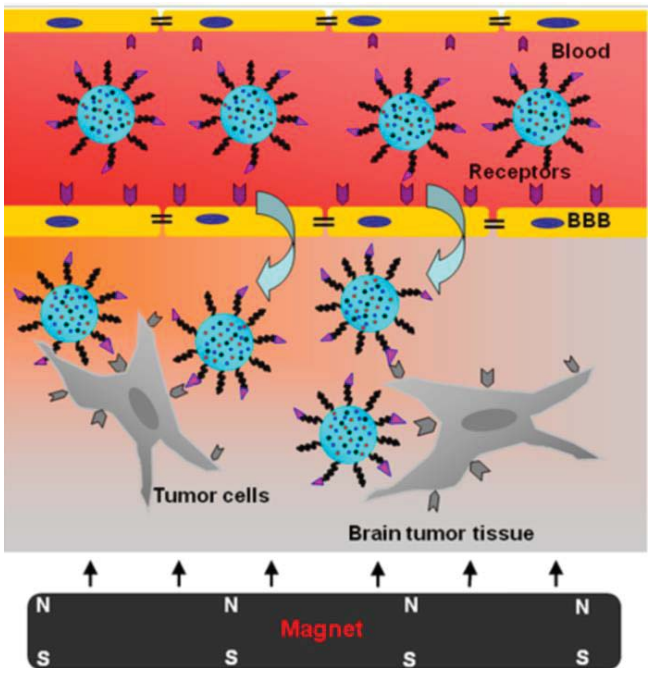

Figure 1-6. Schematic illustration of BBB-penetrating and tumor-targeting delivery *via* the peptide T7-mediated and magnetic-guided, dual-targeting MNP/T7-PLGA NPs. This scheme is obtained from *ACS Applied Materials & Interfaces (2016)* by Y. Cui et al. [108]

1.3 Background of the thesis work: the MAGBBRIS project

According to the World Health Organization data, 15 million people worldwide experience a stroke each year; of these, 5 million are permanently disabled, and five do not survive the disease. Ischemic stroke is the most common type usually caused by a blood vessel obstruction due to thrombus or embolism, which can produce severe and permanent brain tissue damage. Today, the only approved treatment is the acute thrombolytic therapy (pharmacological or mechanical), which has to be administrated at very early from the onset of clinical symptoms, and less than 10% of patients receive treatment due to strict selection criteria. In contrast, neuro-repair treatments could offer the opportunity to include most stroke patients by extending the therapeutic time window. Regenerative medicine has proposed therapeutic strategies based on the potentiation of angiogenesis, which linked to different remodeling processes (neurogenesis, osteogenesis, among others) during tissue repair. In the context of neurorepair after a stroke, the potentiation of angiogenesis can play a significant role.

The MAGBBRIS (MAGnetic Biomaterials for Brain Repair and Imaging after Stroke) project, funded in the EuroNanoMed III joint transnational call (2017) for "European innovative research & and technological development projects in nanomedicine", is devoted to engineering novel magnetic nano-biomaterials to address tissue repair guided by angiogenesis in the context of an ischemic event. As illustrated in **Figure 1-7**, MAGBBRIS will demonstrate that the secretome, a collection of growth factors secreted by EPCs, with proved potential to induce angiogenesis and neurorepair, can be encapsulated in magnetic PLGA-based nanocapsules and be successfully and safely delivered to mice brain and retained by an external magnetic field, to finally achieve controlled release and induce vascular remodeling and neurogenic tissue regeneration after stroke. This nanomedicine approach will provide an advanced therapy that could be translated to a clinical-stage as noninvasive, safe and available to most stroke patients.

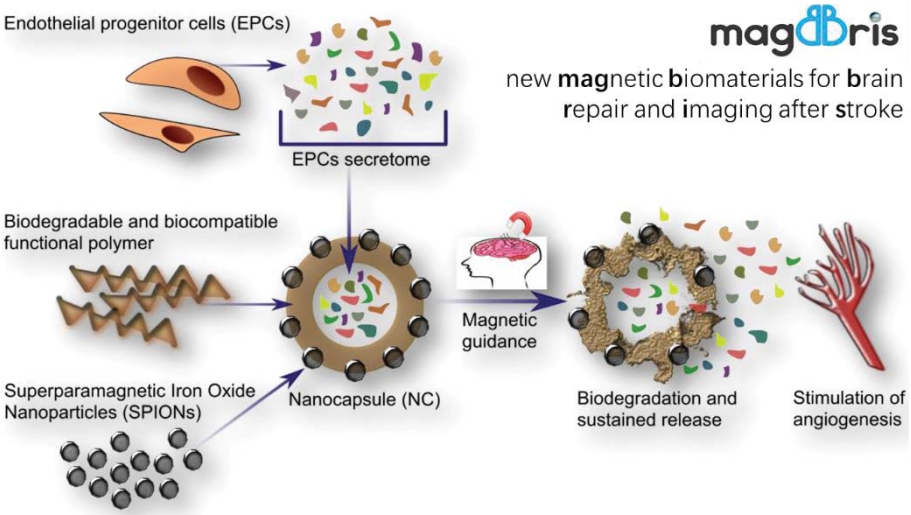

Figure 1-7. Schematic illustration of the nanomedicine approach for brain repair.

The consortium is highly multidisciplinary, made up of materials science, biomedical and clinical research, and industrial partnership, includes 6 partners from 5 member states (VHIR, ICMAB-CSIC Spain, Univ Artois, France, Ospedale San Raffaele, Italy, Pure Biologics Ltd, Poland and the Institute of Experimental Physics, Slovakia).

1.4 Chapter references

[1] M.M. Zagho, E.A. Hussein, A.A. Elzatahry, Recent overviews in functional polymer composites for biomedical applications, *Polymers* 10(7) (2018) 739.

[2] J.Y. Lee, S.E. Kim, Y.-P. Yun, S.-W. Choi, D.I. Jeon, H.-J. Kim, K. Park, H.-R. Song, Osteogenesis and new bone formation of alendronate-immobilized porous PLGA microspheres in a rat calvarial defect model, *Journal of Industrial and Engineering Chemistry* 52 (2017) 277-286.

[3] R. Kamalakannan, G. Mani, P. Muthusamy, A.A. Susaimanickam, K. Kim, Caffeine-loaded gold nanoparticles conjugated with PLA-PEG-PLA copolymer for in vitro cytotoxicity and anti-inflammatory activity, *Journal of Industrial and Engineering Chemistry* 51 (2017) 113-121.

[4] Y.-B. Shim, H.-H. Jung, J.W. Jang, H.S. Yang, H. Bae, J.-C. Park, B. Choi, S.-H. Lee, Fabrication of hollow porous PLGA microspheres using sucrose for controlled dual delivery of dexamethasone and BMP2, *Journal of Industrial and Engineering Chemistry* 37 (2016) 101-106.

[5] M. Muthu, Nanoparticles based on PLGA and its co-polymer: An overview, *Asian Journal of Pharmaceutics* 3(4) (2014).

[6] S. Mohanty, S. Panda, D. Purohit, S.C. Si, A Comprehensive Review on PLGA-based Nanoparticles used for Rheumatoid Arthritis, *Research Journal of Pharmacy and Technology* 12(3) (2019) 1481-1488.

[7] C. Martins, F. Sousa, F. Araujo, B. Sarmento, Functionalizing PLGA and PLGA derivatives for drug delivery and tissue regeneration applications, *Advanced Healthcare Materials* 7(1) (2018) 1701035.

[8] P. Gentile, V. Chiono, I. Carmagnola, P.V. Hatton, An overview of poly (lactic-co-glycolic) acid (PLGA)-based biomaterials for bone tissue engineering, *International Journal of Molecular Sciences* 15(3) (2014) 3640-3659.

[9] G. Singh, A. Faruk, P.M.S. Bedi, Technology Overview and Current Biomedical Application of Polymeric Nanoparticles, *Journal of Drug Delivery and Therapeutics* 8(6) (2018) 285-295.

[10] M. Mir, N. Ahmed, A. ur Rehman, Recent applications of PLGA based nanostructures in drug delivery*, Colloids and Surfaces B: Biointerfaces* 159 (2017) 217-231.

[11] S. Sharma, A. Parmar, S. Kori, R. Sandhir, PLGA-based nanoparticles: a new paradigm in biomedical applications, *TrAC Trends in Analytical Chemistry* 80 (2016) 30-40.

[12] D. Ding, Q. Zhu, Recent advances of PLGA micro/nanoparticles for the delivery of biomacromolecular therapeutics, *Materials Science and Engineering: C* 92 (2018) 1041-1060.

[13] F. Danhier, E. Ansorena, J.M. Silva, R. Coco, A. Le Breton, V. Préat, PLGA-based nanoparticles: an overview of biomedical applications, *Journal of Controlled Release* 161(2) (2012) 505-522.

[14] N.G. Türeli, A. Torge, J. Juntke, B.C. Schwarz, N. Schneider-Daum, A.E. Türeli, C.-M. Lehr, M. Schneider, Ciprofloxacin-loaded PLGA nanoparticles against cystic fibrosis P. aeruginosa lung infections, *European Journal of Pharmaceutics and Biopharmaceutics* 117 (2017) 363-371.

[15] N. Thomas, C. Thorn, K. Richter, B. Thierry, C. Prestidge, Efficacy of poly-lactic-co-glycolic acid micro-and nanoparticles of ciprofloxacin against bacterial biofilms, *Journal of Pharmaceutical Sciences* 105(10) (2016) 3115-3122.

[16] F. Wan, S.S.-R. Bohr, S.N. Kłodzińska, H. Jumaa, Z. Huang, T. Nylander, M.B. Thygesen, K.K. Sørensen, K.J. Jensen, C. Sternberg, Ultra-small TPGS-PLGA Hybrid Nanoparticles for Site-specific Delivery of Antibiotics into Pseudomonas Aeruginosa Biofilms in Lungs, *ACS Applied Materials & Interfaces* (2019).

[17] L.S. Ulanova, M. Pinheiro, C. Vibe, C. Nunes, D. Misaghian, S. Wilson, K. Zhu, F. Fenaroli, H.C. Winther-Larsen, S. Reis, Treatment of Francisella infections via PLGA-and lipid-based nanoparticle delivery of antibiotics in a zebrafish model, *Diseases of Aquatic Organisms* 125(1) (2017) 19-29.

[18] S. Paudel, C. Cerbu, C.E. Astete, S.M. Louie, C. Sabliov, D.F. Rodrigues, Enrofloxacin-Impregnated PLGA Nanocarriers for Efficient Therapeutics and Diminished Generation of Reactive Oxygen Species, *ACS Applied Nano Materials* 2(8) (2019) 5035-5043.

[19] B. Brauner, P. Schwarz, M. Wirth, F. Gabor, Micro vs. nano: PLGA particles loaded with trimethoprim for instillative treatment of urinary tract infections, *International Journal of Pharmaceutics* 579 (2020) 119158.

[20] K. Dheda, T. Gumbo, G. Maartens, K.E. Dooley, R. McNerney, M. Murray, J. Furin, E.A. Nardell, L. London, E. Lessem, The epidemiology, pathogenesis, transmission, diagnosis, and management of multidrug-resistant, extensively drug-resistant, and incurable tuberculosis, *The Lancet Respiratory Medicine* 5(4) (2017) 291-360.

[21] C.R. Arciola, D. Campoccia, L. Montanaro, Implant infections: adhesion, biofilm formation and immune evasion, *Nature Reviews Microbiology* 16(7) (2018) 397.

[22] S. Raja, V. Ramesh, V. Thivaharan, Green biosynthesis of silver nanoparticles using Calliandra haematocephala leaf extract, their antibacterial activity and hydrogen peroxide sensing capability, *Arabian Journal of Chemistry* 10(2) (2017) 253-261.

[23] M. Hoseinnejad, S.M. Jafari, I. Katouzian, Inorganic and metal nanoparticles and their antimicrobial activity in food packaging applications, *Critical Reviews in Microbiology* 44(2) (2018) 161-181.

[24] A. Ashour, A.I. El-Batal, M.A. Maksoud, G.S. El-Sayyad, S. Labib, E. Abdeltwab, M. El-Okr, Antimicrobial activity of metal-substituted cobalt ferrite nanoparticles synthesized by sol–gel technique, *Particuology* 40 (2018) 141-151.

[25] K. Gold, B. Slay, M. Knackstedt, A.K. Gaharwar, Antimicrobial activity of

metal and metal‐oxide based nanoparticles, *Advanced Therapeutics* 1(3) (2018) 1700033.

[26] K. Niska, E. Zielinska, M.W. Radomski, I. Inkielewicz-Stepniak, Metal nanoparticles in dermatology and cosmetology: Interactions with human skin cells, *Chemico-Biological Interactions* 295 (2018) 38-51.

[27] A. Stanković, M. Sezen, M. Milenković, S. Kaišarević, N. Andrić, M. Stevanović, PLGA/nano-ZnO composite particles for use in biomedical applications: preparation, characterization, and antimicrobial activity, *Journal of Nanomaterials* 2016 (2016).

[28] M. Stevanović, I. Bračko, M. Milenković, N. Filipović, J. Nunić, M. Filipič, D.P. Uskoković, Multifunctional PLGA particles containing poly (l-glutamic acid)-capped silver nanoparticles and ascorbic acid with simultaneous antioxidative and prolonged antimicrobial activity, *Acta Biomaterialia* 10(1) (2014) 151-162.

[29] O. Maksimenko, J. Malinovskaya, E. Shipulo, N. Osipova, V. Razzhivina, D. Arantseva, O. Yarovaya, U. Mostovaya, A. Khalansky, V. Fedoseeva, Doxorubicin-loaded PLGA nanoparticles for the chemotherapy of glioblastoma: Towards the pharmaceutical development, *International Journal of Pharmaceutics* 572 (2019) 118733.

[30] J. Mosafer, K. Abnous, M. Tafaghodi, A. Mokhtarzadeh, M. Ramezani, In vitro and in vivo evaluation of anti-nucleolin-targeted magnetic PLGA nanoparticles loaded with doxorubicin as a theranostic agent for enhanced targeted cancer imaging and therapy, *European Journal of Pharmaceutics and Biopharmaceutic*s 113 (2017) 60-74.

[31] J. Patel, J. Amrutiya, P. Bhatt, A. Javia, M. Jain, A. Misra, Targeted delivery of monoclonal antibody conjugated docetaxel loaded PLGA nanoparticles into EGFR overexpressed lung tumour cells, *Journal of Microencapsulation* 35(2) (2018) 204-217.

[32] J. Wu, C. Deng, F. Meng, J. Zhang, H. Sun, Z. Zhong, Hyaluronic acid coated PLGA nanoparticulate docetaxel effectively targets and suppresses orthotopic human lung cancer, *Journal of Controlled Release* 259 (2017) 76-82.

[33] C.J. Bowerman, J.D. Byrne, K.S. Chu, A.N. Schorzman, A.W. Keeler, C.A. Sherwood, J.L. Perry, J.C. Luft, D.B. Darr, A.M. Deal, Docetaxel-loaded PLGA nanoparticles improve efficacy in taxane-resistant triple-negative breast cancer, *Nano Letters* 17(1) (2017) 242-248.

[34] W. Tao, X. Zeng, J. Wu, X. Zhu, X. Yu, X. Zhang, J. Zhang, G. Liu, L. Mei, Polydopamine-Based Surface Modification of Novel Nanoparticle-Aptamer Bioconjugates for In Vivo Breast Cancer Targeting and Enhanced Therapeutic Effects, *Theranostics* 6(4) (2016) 470-84.

[35] M.M. El-Hammadi, Á.V. Delgado, C. Melguizo, J.C. Prados, J.L. Arias, Folic acid-decorated and PEGylated PLGA nanoparticles for improving the antitumour activity of 5-fluorouracil, *International Journal of Pharmaceutics* 516(1-2) (2017) 61-70.

[36] T.-T. Lin, D.-Y. Gao, Y.-C. Liu, Y.-C. Sung, D. Wan, J.-Y. Liu, T. Chiang,

L. Wang, Y. Chen, Development and characterization of sorafenib-loaded PLGA nanoparticles for the systemic treatment of liver fibrosis, *Journal of Controlled Release* 221 (2016) 62-70.

[37] R. Klippstein, J.T.W. Wang, R.I. El-Gogary, J. Bai, F. Mustafa, N. Rubio, S. Bansal, W.T. Al-Jamal, K.T. Al-Jamal, Passively Targeted Curcumin-Loaded PEGylated PLGA Nanocapsules for Colon Cancer Therapy *In Vivo*, *Small* 11(36) (2015) 4704-4722.

[38] S. Rezvantalab, N.I. Drude, M.K. Moraveji, N. Güvener, E.K. Koons, Y. Shi, T. Lammers, F. Kiessling, PLGA-based nanoparticles in cancer treatment, *Frontiers in Pharmacology* 9 (2018) 1260.

[39] J. Tian, Y. Min, Z. Rodgers, K.M. Au, C.T. Hagan, M. Zhang, K. Roche, F. Yang, K. Wagner, A.Z. Wang, Co-delivery of paclitaxel and cisplatin with biocompatible PLGA–PEG nanoparticles enhances chemoradiotherapy in non-small cell lung cancer models, *Journal of Materials Chemistry B* 5(30) (2017) 6049-6057.

[40] T. Khuroo, D. Verma, A. Khuroo, A. Ali, Z. Iqbal, Simultaneous delivery of paclitaxel and erlotinib from dual drug loaded PLGA nanoparticles: Formulation development, thorough optimization and in vitro release, *Journal of Molecular Liquids* 257 (2018) 52-68.

[41] R. Misra, S.K. Sahoo, Coformulation of doxorubicin and curcumin in poly (D, L-lactide-co-glycolide) nanoparticles suppresses the development of multidrug resistance in K562 cells, *Molecular Pharmaceutics* 8(3) (2011) 852-866.

[42] H. Afrooz, F. Ahmadi, F. Fallahzadeh, S.H. Mousavi-Fard, S. Alipour, Design and characterization of paclitaxel-verapamil co-encapsulated PLGA nanoparticles: Potential system for overcoming P-glycoprotein mediated MDR, *Journal of Drug Delivery Science and Technology* 41 (2017) 174-181.

[43] S. Narayanan, M. Pavithran, A. Viswanath, D. Narayanan, C.C. Mohan, K. Manzoor, D. Menon, Sequentially releasing dual-drug-loaded PLGA–casein core/shell nanomedicine: Design, synthesis, biocompatibility and pharmacokinetics, *Acta Biomaterialia* 10(5) (2014) 2112-2124.

[44] M.E. Werner, J.A. Copp, S. Karve, N.D. Cummings, R. Sukumar, C. Li, M.E. Napier, R.C. Chen, A.D. Cox, A.Z. Wang, Folate-targeted polymeric nanoparticle formulation of docetaxel is an effective molecularly targeted radiosensitizer with efficacy dependent on the timing of radiotherapy*, ACS Nano* 5(11) (2011) 8990-8998.

[45] N. Thorat, R. Bohara, H. Yadav, S. Otari, S. Pawar, S. Tofail, Multifunctional Magnetic Nanostructures for Cancer Hyperthermia Therapy, *Nanoarchitectonics for Smart Delivery and Drug Targeting* (2016) 589-612.

[46] A. Aravind, R. Nair, S. Raveendran, S. Veeranarayanan, Y. Nagaoka, T. Fukuda, T. Hasumura, H. Morimoto, Y. Yoshida, T. Maekawa, Aptamer conjugated paclitaxel and magnetic fluid loaded fluorescently tagged PLGA nanoparticles for targeted cancer therapy, *Journal of Magnetism and Magnetic Materials* 344 (2013) 116-123.

[47] R. Vivek, R. Thangam, S.R. Kumar, C. Rejeeth, S. Sivasubramanian, S. Vincent, D. Gopi, S. Kannan, HER2 targeted breast cancer therapy with switchable “Off/On” multifunctional “Smart” magnetic polymer core–shell nanocomposites, *ACS Applied Materials & Interfaces* 8(3) (2016) 2262-2279.

[48] M.R. Ruggiero, S. Geninatti Crich, E. Sieni, P. Sgarbossa, E. Cavallari, R. Stefania, F. Dughiero, S. Aime, Iron oxide/PLGA nanoparticles for magnetically controlled drug release, International *Journal of Applied Electromagnetics and Mechanics* 53(S1) (2017) S53-S60.

[49] W. Wei, X. Zhang, S. Zhang, G. Wei, Z. Su, Biocompatible and bioactive engineered nanomaterials for targeted tumor photothermal therapy: A review, *Materials Science and Engineering: C* (2019) 109891.

[50] Y. Hao, B. Zhang, C. Zheng, R. Ji, X. Ren, F. Guo, S. Sun, J. Shi, H. Zhang, Z. Zhang, The tumor-targeting core–shell structured DTX-loaded PLGA@ Au nanoparticles for chemo-photothermal therapy and X-ray imaging, *Journal of Controlled Release* 220 (2015) 545-555.

[51] Y. Peng, J. Nie, W. Cheng, G. Liu, D. Zhu, L. Zhang, C. Liang, L. Mei, L. Huang, X. Zeng, A multifunctional nanoplatform for cancer chemo-photothermal synergistic therapy and overcoming multidrug resistance, *Biomaterials Science* 6(5) (2018) 1084-1098.

[52] J. Yuan, J. Liu, Q. Song, D. Wang, W. Xie, H. Yan, J. Zhou, Y. Wei, X. Sun, L. Zhao, Photoinduced mild hyperthermia and synergistic chemotherapy by one-pot-synthesized docetaxel-loaded poly (lactic-co-glycolic acid)/polypyrrole nanocomposites, *ACS Applied Materials & Interfaces* 8(37) (2016) 24445-24454.

[53] B. Chen, B.W. Pogue, J.M. Luna, R.L. Hardman, P.J. Hoopes, T. Hasan, Tumor vascular permeabilization by vascular-targeting photosensitization: effects, mechanism, and therapeutic implications, *Clinical Cancer Research* 12(3) (2006) 917-923.

[54] K. Wang, F.M. Kievit, M. Zhang, Nanoparticles for cancer gene therapy: Recent advances, challenges, and strategies, *Pharmacological Research* 114 (2016) 56-66.

[55] Y. Liu, G. Zhao, C.-F. Xu, Y.-L. Luo, Z.-D. Lu, J. Wang, Systemic delivery of CRISPR/Cas9 with PEG-PLGA nanoparticles for chronic myeloid leukemia targeted therapy, *Biomaterials Science* 6(6) (2018) 1592-1603.

[56] X. Zhang, Q. Wang, L. Qin, H. Fu, Y. Fang, B. Han, Y. Duan, EGF-modified mPEG-PLGA-PLL nanoparticle for delivering doxorubicin combined with Bcl-2 siRNA as a potential treatment strategy for lung cancer, *Drug Delivery* 23(8) (2016) 2936-2945.

[57] W. Jiang, H. Yuan, C.K. Chan, C.A. Von Roemeling, Z. Yan, I.L. Weissman, B.Y. Kim, Lessons from immuno-oncology: a new era for cancer nanomedicine?, *Nature Reviews Drug Discovery* 16(6) (2017) 369.

[58] A.V. Do, B. Khorsand, S.M. Geary, A.K. Salem, 3D printing of scaffolds for tissue regeneration applications, *Advanced Healthcare Materials* 4(12) (2015) 1742-1762.

[59] S.K. Sarkar, B.T. Lee, Hard tissue regeneration using bone substitutes: an update on innovations in materials, *The Korean Journal of Internal Medicine* 30(3) (2015) 279.

[60] E. Nazarzadeh Zare, R. Jamaledin, P. Naserzadeh, E. Afjeh-Dana, B. Ashtari, M. Hosseinzadeh, R. Vecchione, A. Wu, F. R Tay, A. Borzacchiello, Metal-based Nanostructures/PLGA Nanocomposites: Antimicrobial Activity, Cytotoxicity and Their Biomedical Applications, *ACS Applied Materials & Interfaces* (2019).

[61] K.W. Chun, H.S. Yoo, J.J. Yoon, T.G. Park, Biodegradable PLGA microcarriers for injectable delivery of chondrocytes: effect of surface modification on cell attachment and function, *Biotechnology Progress* 20(6) (2004) 1797-1801.

[62] M. Morille, K. Toupet, C.N. Montero-Menei, C. Jorgensen, D. Noël, PLGA-based microcarriers induce mesenchymal stem cell chondrogenesis and stimulate cartilage repair in osteoarthritis, *Biomaterials* 88 (2016) 60-69.

[63] J.S. Park, H.-J. Lim, S.W. Yi, K.-H. Park, Stem cell differentiation-related protein-loaded PLGA microspheres as a novel platform micro-typed scaffold for chondrogenesis, *Biomedical Materials* 11(5) (2016) 055003.

[64] R. Ahmadi, N. Mordan, A. Forbes, R. Day, Enhanced attachment, growth and migration of smooth muscle cells on microcarriers produced using thermally induced phase separation, *Acta biomaterialia* 7(4) (2011) 1542-1549.

[65] N. Parmar, R. Ahmadi, R.M. Day, A novel method for differentiation of human mesenchymal stem cells into smooth muscle-like cells on clinically deliverable thermally induced phase separation microspheres, *Tissue Engineering Part C: Methods* 21(4) (2015) 404-412.

[66] I. Ortega-Oller, M. Padial-Molina, P. Galindo-Moreno, F. O'Valle, A.B. Jódar-Reyes, J.M. Peula-García, Bone regeneration from PLGA micro-nanoparticles, *BioMed Research International* 2015 (2015).

[67] I. Takeuchi, S. Kobayashi, Y. Hida, K. Makino, Estradiol-loaded PLGA nanoparticles for improving low bone mineral density of cancellous bone caused by osteoporosis: Application of enhanced charged nanoparticles with iontophoresis, *Colloids and Surfaces B: Biointerfaces* 155 (2017) 35-40.

[68] I. d'Angelo, M. Garcia-Fuentes, Y. Parajó, A. Welle, T. Vántus, A. Horváth, G. Bökönyi, G. Kéri, M.J. Alonso, Nanoparticles based on PLGA: poloxamer blends for the delivery of proangiogenic growth factors, *Molecular Pharmaceutics* 7(5) (2010) 1724-1733.

[69] J.S. Golub, Y.-t. Kim, C.L. Duvall, R.V. Bellamkonda, D. Gupta, A.S. Lin, D. Weiss, W. Robert Taylor, R.E. Guldberg, Sustained VEGF delivery via PLGA nanoparticles promotes vascular growth, *American Journal of Physiology-Heart and Circulatory Physiology* 298(6) (2010) H1959-H1965.

[70] E. Carenza, O. Jordan, P. Martinez-San Segundo, R. Jiřík, Z. Starčuk Jr, G. Borchard, A. Rosell, A. Roig, Encapsulation of VEGF 165 into magnetic PLGA nanocapsules for potential local delivery and bioactivity in human brain endothelial cells, *Journal of Materials Chemistry B* 3(12) (2015) 2538-2544.

[71] K.K. Chereddy, A. Lopes, S. Koussoroplis, V. Payen, C. Moia, H. Zhu, P. Sonveaux, P. Carmeliet, A. des Rieux, G. Vandermeulen, Combined effects of PLGA and vascular endothelial growth factor promote the healing of non-diabetic and diabetic wounds, *Nanomedicine: Nanotechnology, Biology and Medicine* 11(8) (2015) 1975-1984.

[72] Q. Xiong, H. Lin, X. Hua, L. Liu, P. Sun, Z. Zhao, X. Shen, D. Cui, M. Xu, F. Chen, A nanomedicine approach to effectively inhibit contracture during bladder acellular matrix allograft-induced bladder regeneration by sustained delivery of vascular endothelial growth factor, *Tissue Engineering Part A* 21(1-2) (2015) 45-52.

[73] E. Bible, O. Qutachi, D.Y. Chau, M.R. Alexander, K.M. Shakesheff, M. Modo, Neo-vascularization of the stroke cavity by implantation of human neural stem cells on VEGF-releasing PLGA microparticles, *Biomaterials* 33(30) (2012) 7435-7446.

[74] B. Engelhardt, Development of the blood-brain barrier, *Cell and tissue research* 314(1) (2003) 119-129.

[75] M. Navarro-Sobrino, A. Rosell, M. Hernandez-Guillamon, A. Penalba, M. Ribó, J. Alvarez-Sabín, J. Montaner, Mobilization, endothelial differentiation and functional capacity of endothelial progenitor cells after ischemic stroke, *Microvascular Research* 80(3) (2010) 317-323.

[76] G. Esquiva, A. Grayston, A. Rosell, Revascularization and endothelial progenitor cells in stroke, *American Journal of Physiology-Cell Physiology* 315(5) (2018) C664-C674.

[77] U. Bayraktutan, Endothelial progenitor cells: Potential novel therapeutics for ischaemic stroke, *Pharmacological Research* (2019).

[78] J. Fang, Y. Guo, S. Tan, Z. Li, H. Xie, P. Chen, K. Wang, Z. He, P. He, Y. Ke, Autologous Endothelial Progenitor Cells Transplantation for Acute Ischemic Stroke: A 4 - Year Follow - Up Study, *Stem Cells Translational Medicine* 8(1) (2019) 14-21.

[79] S. Takizawa, E. Nagata, T. Nakayama, H. Masuda, T. Asahara, Recent progress in endothelial progenitor cell culture systems: potential for stroke therapy, *Neurologia Medico-Chirurgica* (2016) ra. 2016-0027.

[80] T.C. Saat, S. van den Engel, W. Bijman-Lachger, S.S. Korevaar, M.J. Hoogduijn, J.N. IJzermans, R.W. de Bruin, Fate and effect of intravenously infused mesenchymal stem cells in a mouse model of hepatic ischemia reperfusion injury and resection, *Stem Cells International* (2016).

[81] A. Rosell, A. Morancho, M. Navarro-Sobrino, E. Martínez-Saez, M. Hernández-Guillamon, S. Lope-Piedrafita, V. Barceló, F. Borrás, A. Penalba, L. García-Bonilla, Factors secreted by endothelial progenitor cells enhance neurorepair responses after cerebral ischemia in mice, *PloS One* 8(9) (2013) e73244.

[82] Y. Brudno, A.B. Ennett-Shepard, R.R. Chen, M. Aizenberg, D.J. Mooney, Enhancing microvascular formation and vessel maturation through temporal control over multiple pro-angiogenic and pro-maturation factors, *Biomaterials*

34(36) (2013) 9201-9209.

[83] J. Saif, T.M. Schwarz, D.Y. Chau, J. Henstock, P. Sami, S.F. Leicht, P.C. Hermann, S. Alcala, F. Mulero, K.M. Shakesheff, Combination of injectable multiple growth factor–releasing scaffolds and cell therapy as an advanced modality to enhance tissue neovascularization, *Arteriosclerosis, Thrombosis, and Vascular Biology* 30(10) (2010) 1897-1904.

[84] S. Di Santo, Z. Yang, M.W. von Ballmoos, J. Voelzmann, N. Diehm, I. Baumgartner, C. Kalka, Novel cell-free strategy for therapeutic angiogenesis: in vitro generated conditioned medium can replace progenitor cell transplantation, *PloS One* 4(5) (2009) e5643.

[85] Z. Yang, S. Di Santo, C. Kalka, Current developments in the use of stem cell for therapeutic neovascularisation: is the future therapy" cell-free"?, *Swiss Medical Weekly* 140 (2010) w13130.

[86] D.J. Craik, D.P. Fairlie, S. Liras, D. Price, The future of peptide‐based drugs, *Chemical Biology & Drug Design* 81(1) (2013) 136-147.

[87] F. Sousa, A. Cruz, P. Fonte, I.M. Pinto, M.T. Neves-Petersen, B. Sarmento, A new paradigm for antiangiogenic therapy through controlled release of bevacizumab from PLGA nanoparticles, *Scientific Reports* 7(1) (2017) 1-13.

[88] P. Fonte, F. Andrade, C. Azevedo, J. Pinto, V. Seabra, M. van de Weert, S. Reis, B. Sarmento, Effect of the freezing step in the stability and bioactivity of protein-loaded PLGA nanoparticles upon lyophilization, *Pharmaceutical Research* 33(11) (2016) 2777-2793.

[89] M. Allahyari, E. Mohit, Peptide/protein vaccine delivery system based on PLGA particles, *Human vaccines & immunotherapeutics* 12(3) (2016) 806-828.

[90] J.T. Cole, N.B. Holland, Multifunctional nanoparticles for use in theranostic applications, *Drug Delivery and Translational Research* 5(3) (2015) 295-309.

[91] S.M. Janib, A.S. Moses, J.A. MacKay, Imaging and drug delivery using theranostic nanoparticles, *Advanced Drug Delivery Reviews* 62(11) (2010) 1052-1063.

[92] E. Swider, S. Maharjan, K. Houkes, N.K. van Riessen, C. Figdor, M. Srinivas, O. Tagit, Förster Resonance Energy Transfer-Based Stability Assessment of PLGA Nanoparticles in Vitro and in Vivo, *ACS Applied Bio Materials* (2019).

[93] P. Kumar, T. Van Treuren, A. Ranjan, P. Chaudhary, J.K. Vishwanatha, In vivo imaging and biodistribution of near infrared dye loaded brain-metastatic-breast-cancer-cell-membrane coated polymeric nanoparticles, *Nanotechnology* (2019).

[94] J.K. Park, T. Utsumi, Y.E. Seo, Y. Deng, A. Satoh, W.M. Saltzman, Y. Iwakiri, Cellular distribution of injected PLGA-nanoparticles in the liver, *Nanomedicine* 12(5) (2016) 1365-74.

[95] M.A. Al-Natour, M.D. Yousif, R. Cavanagh, A. Abouselo, E.A. Apebende, A. Ghaemmaghami, D.-H. Kim, J.W. Aylott, V. Taresco, V.M. Chauhan, Facile

Dye-Initiated Polymerization of Lactide–Glycolide Generates Highly Fluorescent Poly (lactic-co-glycolic Acid) for Enhanced Characterization of Cellular Delivery, *ACS Macro Letters* 9(3) (2020) 431-437.

[96] J. Hu, J. Guo, Z. Xie, D. Shan, E. Gerhard, G. Qian, J. Yang, Fluorescence imaging enabled poly (lactide-co-glycolide), *Acta Biomaterialia* 29 (2016) 307-319.

[97] J.T.-W. Wang, U. Martino, R. Khan, M. Bazzar, P. Southern, D. Tuncel, K.T. Al-Jamal, Engineering red-emitting multi-functional nanocapsules for magnetic tumour targeting and imaging, *Biomaterials Science* 8(9) (2020) 2590-2599.

[98] D.X. Medina, K.T. Householder, R. Ceton, T. Kovalik, J.M. Heffernan, R.V. Shankar, R.P. Bowser, R.J. Wechsler-Reya, R.W. Sirianni, Optical barcoding of PLGA for multispectral analysis of nanoparticle fate in vivo, *Journal of Control Release* 253 (2017) 172-182.

[99] M.M. Abdel-Mottaleb, A. Beduneau, Y. Pellequer, A. Lamprecht, Stability of fluorescent labels in PLGA polymeric nanoparticles: quantum dots versus organic dyes, *International Journal of Pharmaceutics* 494(1) (2015) 471-478.

[100] M.V. DaCosta, S. Doughan, Y. Han, U.J. Krull, Lanthanide upconversion nanoparticles and applications in bioassays and bioimaging: A review, *Analytica Chimica Acta* 832 (2014) 1-33.

[101] D. Ni, J. Zhang, W. Bu, H. Xing, F. Han, Q. Xiao, Z. Yao, F. Chen, Q. He, J. Liu, Dual-targeting upconversion nanoprobes across the blood–brain barrier for magnetic resonance/fluorescence imaging of intracranial glioblastoma, *ACS Nano* 8(2) (2014) 1231-1242.

[102] R.L. Cook, K.T. Householder, E.P. Chung, A.V. Prakapenka, D.M. DiPerna, R.W. Sirianni, A critical evaluation of drug delivery from ligand modified nanoparticles: Confounding small molecule distribution and efficacy in the central nervous system, *Journal of Controlled Release* 220 (2015) 89-97.

[103] P.M. Valencia, E.M. Pridgen, M. Rhee, R. Langer, O.C. Farokhzad, R. Karnik, Microfluidic platform for combinatorial synthesis and optimization of targeted nanoparticles for cancer therapy, *ACS Nano* 7(12) (2013) 10671-10680.

[104] G. Rigaux, V. Roullin, C. Cadiou, C. Portefaix, L. Van Gulick, G. Bœuf, M. Andry, C. Hoeffel, L. Vander Elst, S. Laurent, A new magnetic resonance imaging contrast agent loaded into poly (lacide-co-glycolide) nanoparticles for long-term detection of tumors, *Nanotechnology* 25(44) (2014) 445103.

[105] J. Xi, L. Da, C. Yang, R. Chen, L. Gao, L. Fan, J. Han, Mn2+-coordinated PDA@ DOX/PLGA nanoparticles as a smart theranostic agent for synergistic chemo-photothermal tumor therapy*, International Journal of Nanomedicine* 12 (2017) 3331.

[106] V. Catanzaro, G. Digilio, F. Capuana, S. Padovan, J.C. Cutrin, F. Carniato, S. Porta, C. Grange, N. Filipović, M. Stevanović, Gadolinium-labelled cell scaffolds to follow-up cell transplantation by magnetic resonance imaging, *Journal of Functional Biomaterials* 10(3) (2019) 28.

[107] B. Sivakumar, R.G. Aswathy, R. Romero-Aburto, T. Mitcham, K.A. Mitchel, Y. Nagaoka, R.R. Bouchard, P.M. Ajayan, T. Maekawa, D.N. Sakthikumar, Highly versatile SPION encapsulated PLGA nanoparticles as photothermal ablators of cancer cells and as multimodal imaging agents, *Biomaterials Science* 5(3) (2017) 432-443.

[108] Y. Cui, M. Zhang, F. Zeng, H. Jin, Q. Xu, Y. Huang, Dual-targeting magnetic PLGA nanoparticles for codelivery of paclitaxel and curcumin for brain tumor therapy, *ACS Applied Materials & Interfaces* 8(47) (2016) 32159-32169.

[109] M.-H. Chan, M.-R. Hsieh, R.-S. Liu, D.-H. Wei, M. Hsiao, Magnetically Guided Theranostics: Optimizing Magnetic Resonance Imaging with Sandwich-Like Kaolinite-Based Iron/Platinum Nanoparticles for Magnetic Fluid Hyperthermia and Chemotherapy, *Chemistry of Materials* (2019).

[110] Y.-D. Xiao, R. Paudel, J. Liu, C. Ma, Z.-S. Zhang, S.-K. Zhou, MRI contrast agents: Classification and application, *International Journal of Molecular Medicine* 38(5) (2016) 1319-1326.

[111] K. Li, D. Ding, D. Huo, K.Y. Pu, N.N.P. Thao, Y. Hu, Z. Li, B. Liu, Conjugated polymer based nanoparticles as dual‐modal probes for targeted in vivo fluorescence and magnetic resonance imaging, *Advanced Functional Materials* 22(15) (2012) 3107-3115.

[112] A. Shakeri-Zadeh, S. Khoee, M.-B. Shiran, A.M. Sharifi, S. Khoei, Synergistic effects of magnetic drug targeting using a newly developed nanocapsule and tumor irradiation by ultrasound on CT26 tumors in BALB/c mice, *Journal of Materials Chemistry B* 3(9) (2015) 1879-1887.

[113] T. Courant, V. Roullin, C. Cadiou, F. Delavoie, M. Molinari, M. Andry, F. Chuburu, Development and physicochemical characterization of copper complexes-loaded PLGA nanoparticles, *International Journal of Pharmaceutics* 379(2) (2009) 226-234.

[114] J. Llop, P. Jiang, M. Marradi, V. Gomez-Vallejo, M. Echeverria, S. Yu, M. Puigivila, Z. Baz, B. Szczupak, C. Perez-Campana, Visualisation of dual radiolabelled poly (lactide-co-glycolide) nanoparticle degradation in vivo using energy-discriminant SPECT, *Journal of Materials Chemistry B* 3(30) (2015) 6293-6300.

[115] R.W. Sirianni, M.-Q. Zheng, T.R. Patel, T. Shafbauer, J. Zhou, W.M. Saltzman, R.E. Carson, Y. Huang, Radiolabeling of poly (lactic-co-glycolic acid)(PLGA) nanoparticles with biotinylated F-18 prosthetic groups and imaging of their delivery to the brain with positron emission tomography, *Bioconjugate Chemistry* 25(12) (2014) 2157-2165.

[116] E. Locatelli, L. Gil, L.L. Israel, L. Passoni, M. Naddaka, A. Pucci, T. Reese, V. Gomez-Vallejo, P. Milani, M. Matteoli, Biocompatible nanocomposite for PET/MRI hybrid imaging, *International Journal of Nanomedicine* 7 (2012) 6021.

[117] Y. Wang, E.M. Strohm, Y. Sun, Z. Wang, Y. Zheng, Z. Wang, M.C. Kolios, Biodegradable polymeric nanoparticles containing gold nanoparticles and

Paclitaxel for cancer imaging and drug delivery using photoacoustic methods, *Biomedical Optics Express* 7(10) (2016) 4125-4138.

[118] M. Wu, J. Shu, Multimodal molecular imaging: current status and future directions, *Contrast Media & Molecular Imaging* (2018).

[119] M. Srinivas, L.J. Cruz, F. Bonetto, A. Heerschap, C.G. Figdor, I.J.M. De Vries, Customizable, multi-functional fluorocarbon nanoparticles for quantitative in vivo imaging using 19F MRI and optical imaging, *Biomaterials* 31(27) (2010) 7070-7077.

[120] H. Maeda, K. Greish, J. Fang, The EPR effect and polymeric drugs: a paradigm shift for cancer chemotherapy in the 21st century, *Polymer Therapeutics II*, Springer2006, pp. 103-121.

[121] N. Kamaly, Z. Xiao, P.M. Valencia, A.F. Radovic-Moreno, O.C. Farokhzad, Targeted polymeric therapeutic nanoparticles: design, development and clinical translation, *Chemical Society Reviews* 41(7) (2012) 2971-3010.

[122] J. Shi, P.W. Kantoff, R. Wooster, O.C. Farokhzad, Cancer nanomedicine: progress, challenges and opportunities, *Nature Reviews Cancer* 17(1) (2017) 20.

[123] R. Bazak, M. Houri, S. El Achy, S. Kamel, T. Refaat, Cancer active targeting by nanoparticles: a comprehensive review of literature, *Journal of Cancer Research and Clinical Oncology* 141(5) (2015) 769-784.

[124] C. Wang, P.C. Ho, L.Y. Lim, Wheat germ agglutinin-conjugated PLGA nanoparticles for enhanced intracellular delivery of paclitaxel to colon cancer cells, *International Journal of Pharmaceutics* 400(1-2) (2010) 201-210.

[125] G. Tosi, A.V. Vergoni, B. Ruozi, L. Bondioli, L. Badiali, F. Rivasi, L. Costantino, F. Forni, M.A. Vandelli, Sialic acid and glycopeptides conjugated PLGA nanoparticles for central nervous system targeting: in vivo pharmacological evidence and biodistribution, *Journal of Controlled Release* 145(1) (2010) 49-57.

[126] Y. Zheng, B. Yu, W. Weecharangsan, L. Piao, M. Darby, Y. Mao, R. Koynova, X. Yang, H. Li, S. Xu, Transferrin-conjugated lipid-coated PLGA nanoparticles for targeted delivery of aromatase inhibitor 7α-APTADD to breast cancer cells, *International Journal of Pharmaceutics* 390(2) (2010) 234-241.

[127] Y. Bi, L. Liu, Y. Lu, T. Sun, C. Shen, X. Chen, Q. Chen, S. An, X. He, C. Ruan, T7 peptide-functionalized PEG-PLGA micelles loaded with carmustine for targeting therapy of glioma, *ACS Applied Materials & Interfaces* 8(41) (2016) 27465-27473.

[128] Z. Ghotbi, A. Haddadi, S. Hamdy, R.W. Hung, J. Samuel, A. Lavasanifar, Active targeting of dendritic cells with mannan-decorated PLGA nanoparticles, *Journal of Drug Targeting* 19(4) (2011) 281-292.

[129] O.C. Farokhzad, J. Cheng, B.A. Teply, I. Sherifi, S. Jon, P.W. Kantoff, J.P. Richie, R. Langer, Targeted nanoparticle-aptamer bioconjugates for cancer chemotherapy in vivo, *Proceedings of the National Academy of Sciences* 103(16) (2006) 6315-6320.

[130] J. Mosafer, M. Teymouri, K. Abnous, M. Tafaghodi, M. Ramezani, Study and evaluation of nucleolin-targeted delivery of magnetic PLGA-PEG nanospheres loaded with doxorubicin to C6 glioma cells compared with low nucleolin-expressing L929 cells, *Materials Science and Engineering: C* 72 (2017) 123-133.

[131] J. Jiang, H. Chen, C. Yu, Y. Zhang, M. Chen, S. Tian, C. Sun, The promotion of salinomycin delivery to hepatocellular carcinoma cells through EGFR and CD133 aptamers conjugation by PLGA nanoparticles, *Nanomedicine* 10(12) (2015) 1863-1879.

[132] J. Gao, G. Kou, H. Wang, H. Chen, B. Li, Y. Lu, D. Zhang, S. Wang, S. Hou, W. Qian, PE38KDEL-loaded anti-HER2 nanoparticles inhibit breast tumor progression with reduced toxicity and immunogenicity, *Breast Cancer Research and Treatment* 115(1) (2009) 29-41.

[133] A. Tivnan, T. Heilinger, J.M. Ramsey, G. O'Connor, J.L. Pokorny, J.N. Sarkaria, B.W. Stringer, B.W. Day, A.W. Boyd, E.L. Kim, Anti-GD2-ch14. 18/CHO coated nanoparticles mediate glioblastoma (GBM)-specific delivery of the aromatase inhibitor, Letrozole, reducing proliferation, migration and chemoresistance in patient-derived GBM tumor cells, *Oncotarget* 8(10) (2017) 16605.

[134] H. Sah, L.A. Thoma, H.R. Desu, E. Sah, G.C. Wood, Concepts and practices used to develop functional PLGA-based nanoparticulate systems, *International Journal of Nanomedicine* 8 (2013) 747.

[135] L.M. Bauer, S.F. Situ, M.A. Griswold, A.C.S. Samia, High-performance iron oxide nanoparticles for magnetic particle imaging–guided hyperthermia (hMPI), *Nanoscale* 8(24) (2016) 12162-12169.

2

PLGA NC formulation for potential clinical translation with intrinsic properties of magnetic guidance and MRI

In this chapter, we aim at determining an optimal and simple formulation for a magnetic PLGA nanocarrier to encapsulate proteins with potentical clinical translation. When translated to the clinical setting the external magnetic field will be the driving force to guide and retain the secretome loaded NCs to the vasculature of the ischemic area, and the secretome will be released by the degradation *via* hydrolyzation of the polymer shell. Since the magnetic guidance of the NCs is achieved by the incorporated SPIONs, a MRI T2 contrast agent, the NCs are also endowed with intrinsic MRI modality. A schematic illustration of the architecture of the drug carrier system is shown in **Figure 2-1**. An important criterion to successfully achieve the clinical translation of a drug delivery system is to minimize complexity. Any additional component of a theranostic carrier will have an enormous impact on the manufacturing process, production cost and complying with the medical regulations. In this sense, the simple therapeutic formulation presented in this chapter for magnetically guided delivery might be suitable as the final product. The optimization and assessment of nanocarrier itself is described.

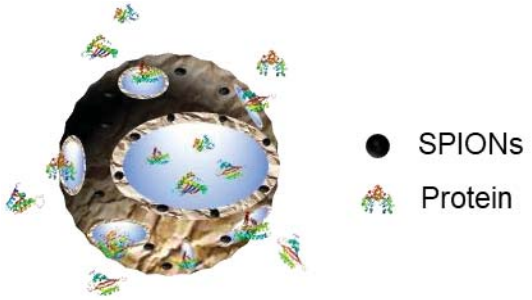

Figure 2-1. Schematic illustration of the designed magnetic PLGA NC drug delivery system.

2.1 Fabrication and optimization of the PLGA NC formulation

2.1.1 Oleic acid-coated SPIONs

As elaborated in Section 1.2, SPIONs are widely used for MRI and magnetically-guided drug delivery systems. Here, I aim to incorporate the SPIONs into the PLGA matrix of the NCs to simultaneously achieve MRI mode and brain targeting of the nanocarrier. It has been reported that regarding the SPIONs the nanoscale size-dependent magnetism and MR properties are correlated, as SPIONs size increases from 4 nm to 12 nm, the magnetization continuously increases and the T2-weighted MRI signal intensity continuously decreases[1]. SPIONs were synthesized through a microwave-assisted thermal decomposition method and different synthetic conditions were studied aiming to improve the saturation magnetization of the SPIONs for more efficient magnetic retention and larger hypotense MRI signal. As illustrated in **Figure 2-2**, several concentrations of the iron precursor $Fe(acac)_3$, reaction temperatures and times were used to synthesize the SPIONs. In all cases, an excess amount of oleic acid (OA) were added to the reaction product suspensions for the coating of OA onto the surface of SPIONs to make them oleophilic. Compared to Condition 1, Condition 2 increases the concentration of iron precursor by 10 times and doubles the reaction time, which facilitate an increase in the number of generated crystal nuclei and their growth, thus resulting in larger SPIONs together with minor fraction of smaller size NPs (**Figure 2-2** TEM images).

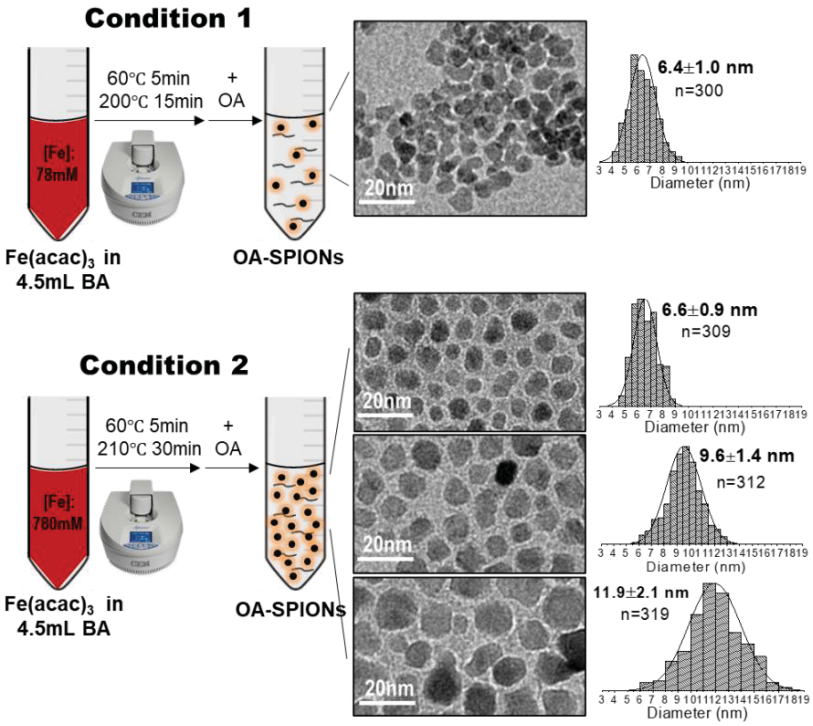

Figure 2-2. Two reaction conditions for the synthesis of SPIONs by microwave-assisted thermal decomposition. TEM analysis of the produced SPIONs shows that Condition 1 yields SPIONs with a mean size of ~6 nm, Condition 2 yields a SPIONs mixture with three size collections of ~6 nm, ~9 nm and ~12 nm respectively being the NPs of ~9 nm the most abundant fraction.

Figure 2-3 illustrates the process to separate the three size collections of SPIONs produced using Condition 2. Even though the SPIONs of ~12 nm may result in a higher magnetization, the yield was too low (11%) when compared to the SPIONs of ~9 nm (46%), so the 9 nm collection was used as the final product. The obtained powder of OA-SPIONs (9 nm) was then dispersed in dichloromethane at a concentration of 40 mg/mL, the NPs dispersion is stable and responsive to an external magnet as shown in **Figure 2-3**.

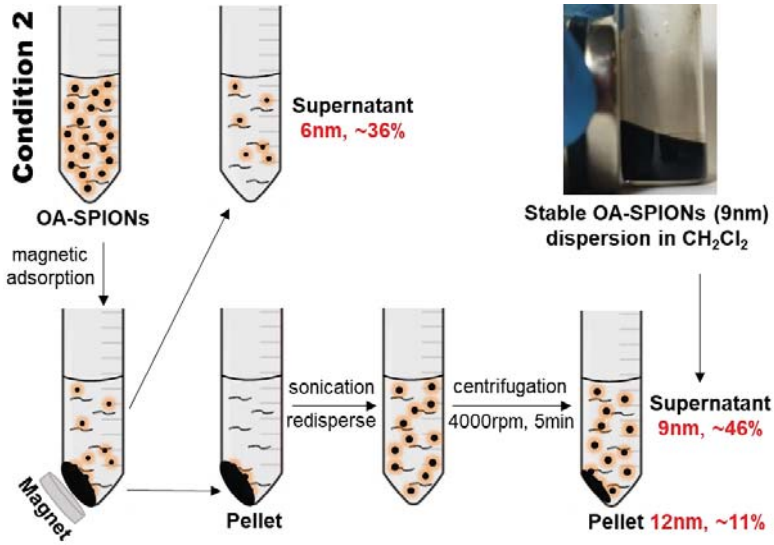

Figure 2-3. Schematic illustration of the processes to separate the three size collections of the SPIONs mixture produced by reaction of Condition 2. The yields of SPIONs of different sizes are calculated according to the Fe content of the resulted SPIONs compared to the Fe content of the initial precursor. Image on the upper right shows an stable OA-SPIONs (9 nm) dispersion in dichloromethane under the effect of a magnet.

The hydrodynamic size of OA-SPIONs_9 nm in dichloromethane is expectedly larger than that of OA-SPIONs_6 nm (Condition 1) as shown in **Figure 2-4**, from which an OA layer of 3~4 nm in thickness on the surface of SPIONs can be estimated. The OA layer can also be indirectly noticed by the homogeneous gaps between SPIONs on the TEM images (**Figure 2-2**).

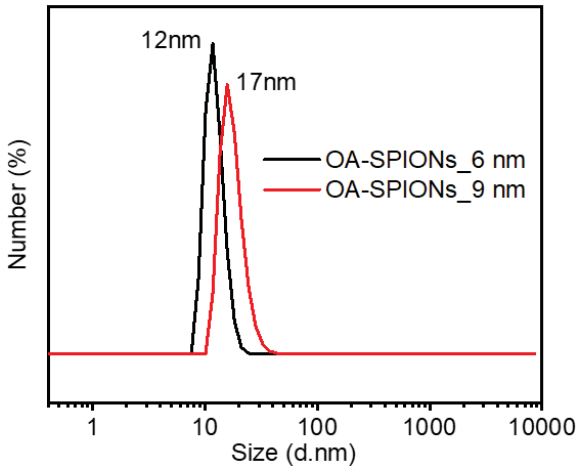

Figure 2-4. Hydrodynamic size of the OA-SPIONs in dichloromethane measured by dynamic light scattering (DLS).

To determine the OA fraction on the OA-SPIONs product, thermogravimetric analysis of the samples is done (**Figure 2-5**) and expectedly the OA fraction of OA-SPIONs_9nm (13.67 wt%) is lower than that of OA-SPIONs_6nm (17.94 wt%, Condition 1) due to a smaller surface area of larger NPs in Condition 2.

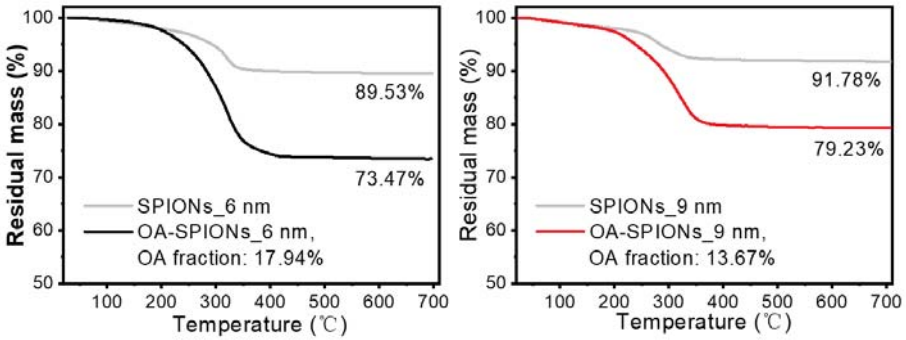

Figure 2-5. Thermogravimetric analysis (TGA) of OA coated SPIONs and pure SPIONs samples. OA fractions in the OA-SPIONs of 6 nm and 9 nm are calculated according to the thermogravimetric curves as described in Section 2.5.3.

The hysteresis loops of OA-SPIONs_6 nm (Condition 1) and OA-SPIONs_9 nm were measured by superconductive quantum interference device (SQUID) at 5 K (**Figure 2-6**), both the saturation magnetization (Ms) and remnant magnetization (Mr) of the 9 nm SPIONs are higher than those of the 6 nm SPIONs, indicating the nanoscale size-dependent magnetism.

Given the high yield, good dispersibility and enhanced magnetic properties, OA-SPIONs_9 nm were selected for the fabrication of magnetic PLGA NCs with improved magnetic retention and MRI signal.

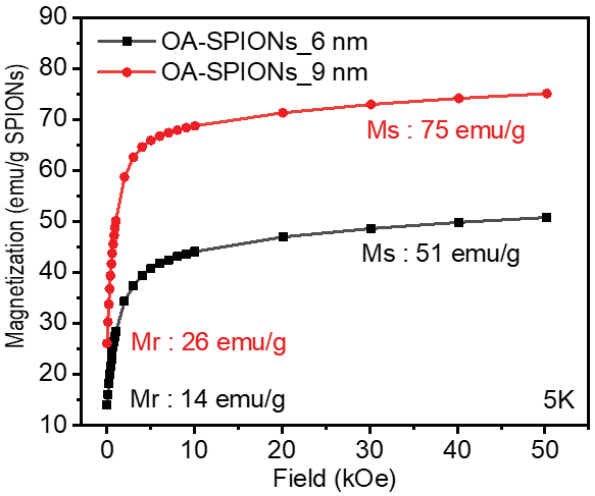

Figure 2-6. A branch of the hysteresis loop of the OA-SPIONs samples measured by SQUID at 5 K, the mass magnetization is expressed as emu/g pure SPIONs (without the organic fraction).

2.1.2 Fabrication of protein loaded magnetic NCs

After improving the magnetic characteristic of the functional moiety SPIONs, PLGA NCs were fabricated with bovine serum albumin (BSA, a model protein cargo to standardize the fabrication method) in the core and SPIONs in the shell through a double emulsion solvent evaporation method. The fabrication process is shown in **Figure 2-7**. Since both OA-SPIONs and PLGA molecules dissolve well in dichloromethane, after evaporation of the organic solvent of the mixture, SPIONs are expected to be well distributed in the PLGA film, which makes up the shell matrix of NCs. The produced NCs were washed three times with water by centrifugation and stored in powder by lyophilization which not only eliminates any trace of organic solvent but also facilitated the later manipulation and storage of the product.

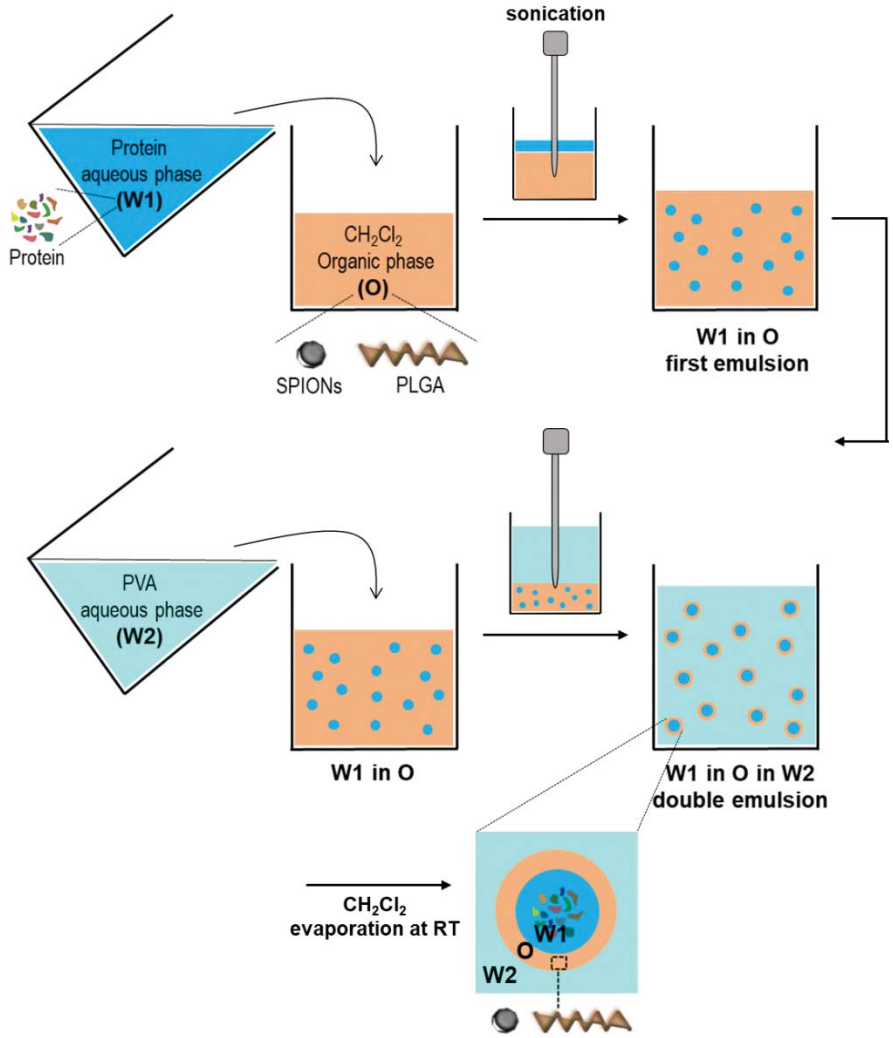

Figure 2-7. Schematic illustration of the fabrication of PLGA NCs with secretome in the core and SPIONs in the shell by double emulsion-solvent evaporation method.

The morphology and structure of the as-obtained NCs were observed by SEM and TEM as shown in **Figure 2-8**. The lyophilized NCs present homogeneous spherical morphologies. The inset dynamic light scattering (DLS) size distribution histogram of lyophilized NCs redispersed in water shows a mean hydrodynamic diameter of 276 nm of the NCs with a polydispersity index (PdI) of 0.18 reflecting good redispersibility of the NCs in water after the lyophilization process and a size which can be considered suitable for *i.v.* administration[2]. The upper inset in **Figure 2-8** shows a representative broken NC, exposing the hollow core, ideal for the

loading of protein. The TEM image in the lower inset reveals the embedding and finely homogeneous distribution of the SPIONs within the polymeric matrix. The number following the NC label indicates the batch of a given NC.

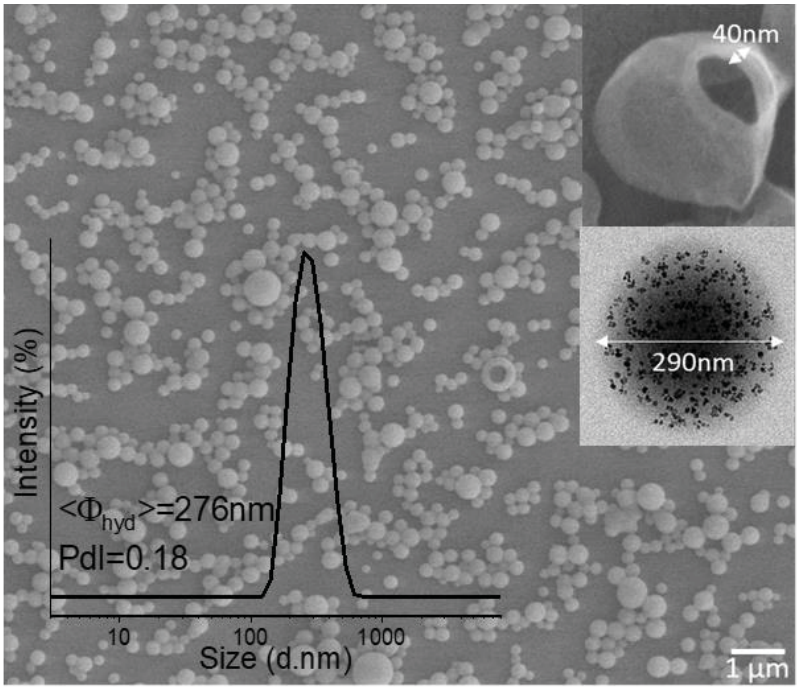

Figure 2-8. Morphological data of the representative NC.PLGA.SPIONs.BSA (NC-3 in Table 2-1). SEM image of lyophilized NCs with the upper inset showing the hollow core of the NC; lower inset TEM image shows a spherical NC with SPIONs visible as black spots, uniformly distributed in the polymer matrix; DLS curve of NCs water suspension after lyophilization with a mean diameter of 276 nm and 0.18 polydispersity.

2.1.3 Effect of SPIONs loading conditions on the morphology and magnetic retention of the NCs

The SPIONs loading ($wt\%_{SPIONs}$) in the NCs were determined by TGA and SQUID (**Figure 2-9**). The two methods yield similar results (~3.0 wt% for NC-1). After this initial analysis, SQUID characterization was the selected method to quantify the iron oxide load in the NCs since less amount of sample is needed and more importantly, the $wt\%_{SPIONs}$ and magnetization of NCs are obtained simultaneously.

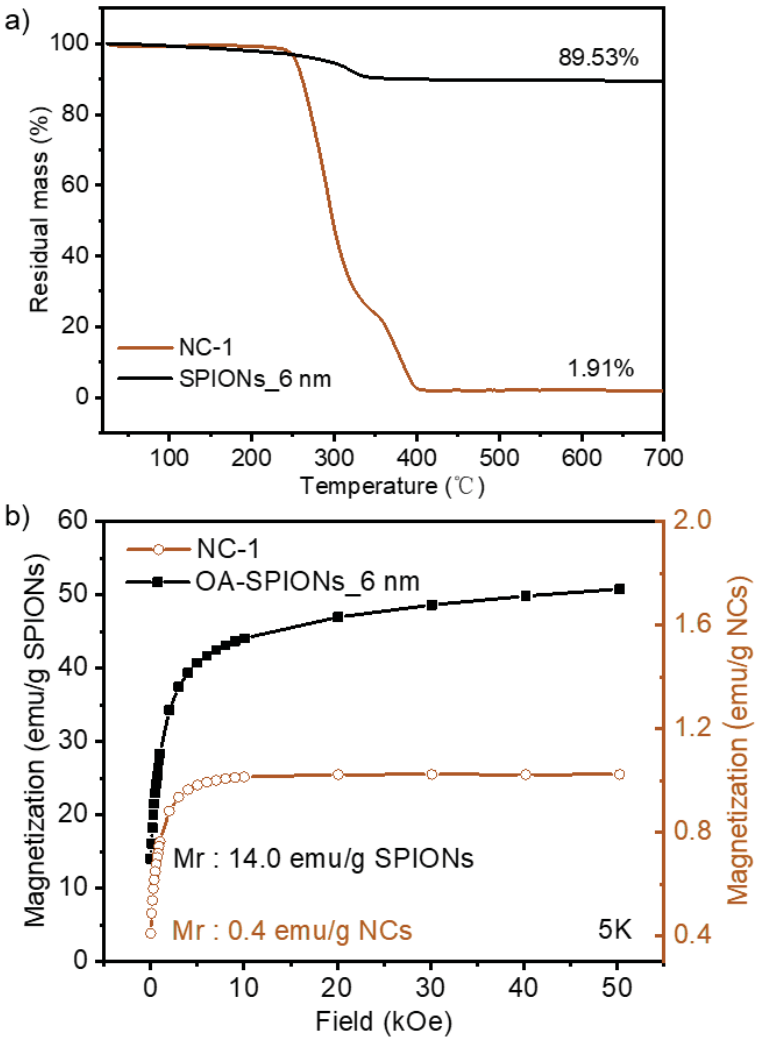

Figure 2-9. Two methods determine the wt%$_{SPIONs}$ of NCs, a) TGA of 2.8 wt%, b) SQUID of 2.9 wt%. The calculation methods are shown in Section 2.5.3 & 2.5.4 respectively.

The effects of incorporating different loadings and different sizes of SPIONs on the morphologies and magnetic response of the NCs are described below. As seen in **Table 2-1** from NC-1 to NC-3, neither increasing the SPION size nor increasing two-fold its loading affects the mean size of the NCs compared to plain PLGA NCs (NC-0), all the NCs keeping the same morphologies and also verified by SEM in **Figure 2-10**. Furthermore, the entrapment efficiencies of SPIONs (EE%$_{SPIONs}$) with different SPIONs loadings are similar, which demonstrates the NCs fabrication and SPIONs entrapment process is very reproducible. Note that for the same loading of SPIONs, the

magnetization of NC-2 is much higher than that of NC-1 given the larger size of SPIONs for NC-2.

Table 2-1. Summary of the formulations of NC.PLGA.SPIONs.BSA. Different sizes and amount of SPIONs are incorporated into the PLGA shell.

	SPIONs					Size (DLS)	
Sample type	Size (nm)	Loading (wt%)	EE%	M_R (eum/g)	M_S (eum/g)	d.nm	PdI
NC-0	—	—	—	—	—	255	0.10
NC-1	6	2.9	92%	0.4	1.0	279	0.17
NC-2	9	3.0	90%	0.8	1.9	264	0.19
NC-3	9	6.1	95%	1.6	3.9	276	0.18
OA-SPIONs[a]	6			14.0	50.8		
	9			26.1	75.1		

[a] The magnetization of OA-SPIONs is expressed as emu/g pure SPIONs.

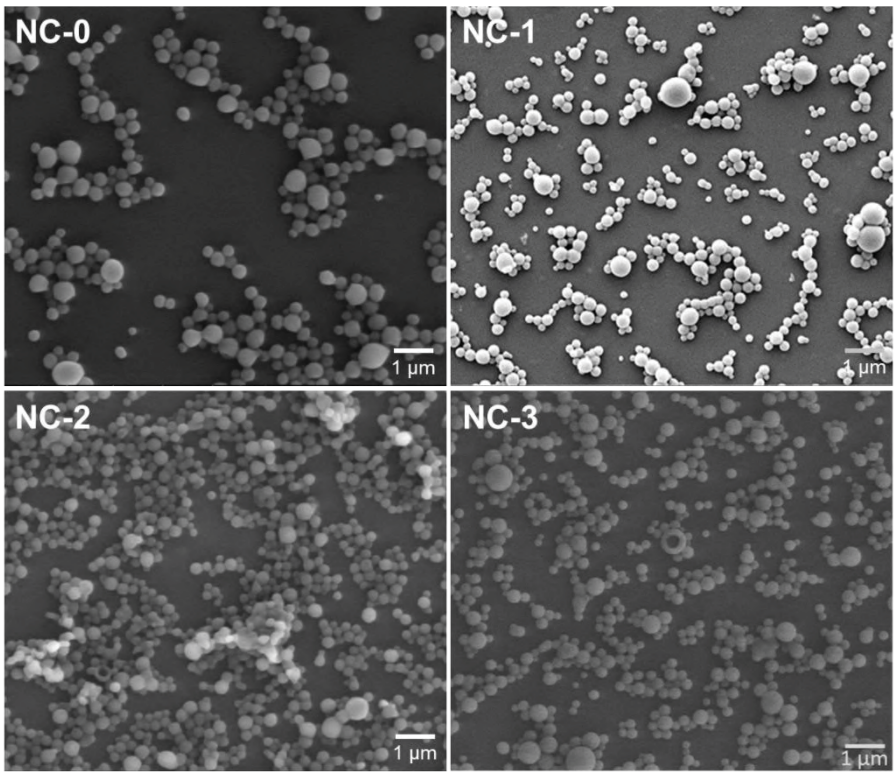

Figure 2-10. SEM images of the several types of PLGA NCs listed in Table 2-1 after lyophilization.

Therefore optimal formulation regarding SPIONs (NC-3, 9 nm SPIONs with 6 wt%) yields a Ms value of 3.9 emu/g NCs which is more than four-fold larger than the group previously reported value

(0.9 emu/g)[3]. As will be shown later, the increase of the magnetic moment of NCs resulting from using larger size SPIONs and increasing their load will positively impact on the magnetic retention, as well as the MRI signal intensity.

The magnetic hysteresis loop at room temperature of lyophilized NC-3 is displayed in **Figure 2-11** showing the superparamagnetic character of the NCs (lack of coercivity). The superparamagnetic behavior of the NCs after SPIONs encapsulation is important since, in the absence of an external magnetic field, it ensures a lack of magnetic interactions among NCs thus minimizing the risk of embolization during *i.v.* administration.

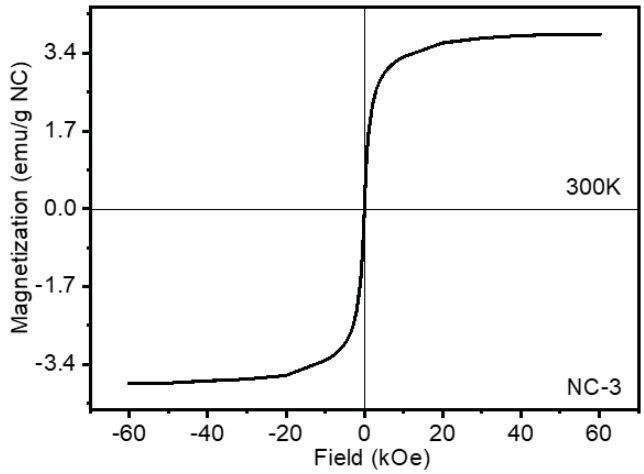

Figure 2-11. Hysteresis loop of the lyophilized NC-3 at 300 K, showing superparamagnetism at room temperature.

The magnetic retention of NCs is illustrated with the use of an external magnet. The effects of different SPIONs loadings and magnet types on the magnetic retention of NCs are studied. As seen in **Figure 2-12**, time-varying adsorptions of NCs with different SPIONs loadings (6 wt%, 3 wt%, 1 wt%) to the wall of glass tubes on the magnet side are investigated. The NCs suspension with 6 wt% of SPIONs show deeper yellow color than the others at the same concentration (2.5 mg/mL) due to the higher amount of SPIONs at time 0 h, but from 3 h the suspension becomes clearer than the others and at 7 h a much clearer round pellet of the NCs is observed under the same magnet, and at 23 h the suspension becomes totally clear while the others remain turbid.

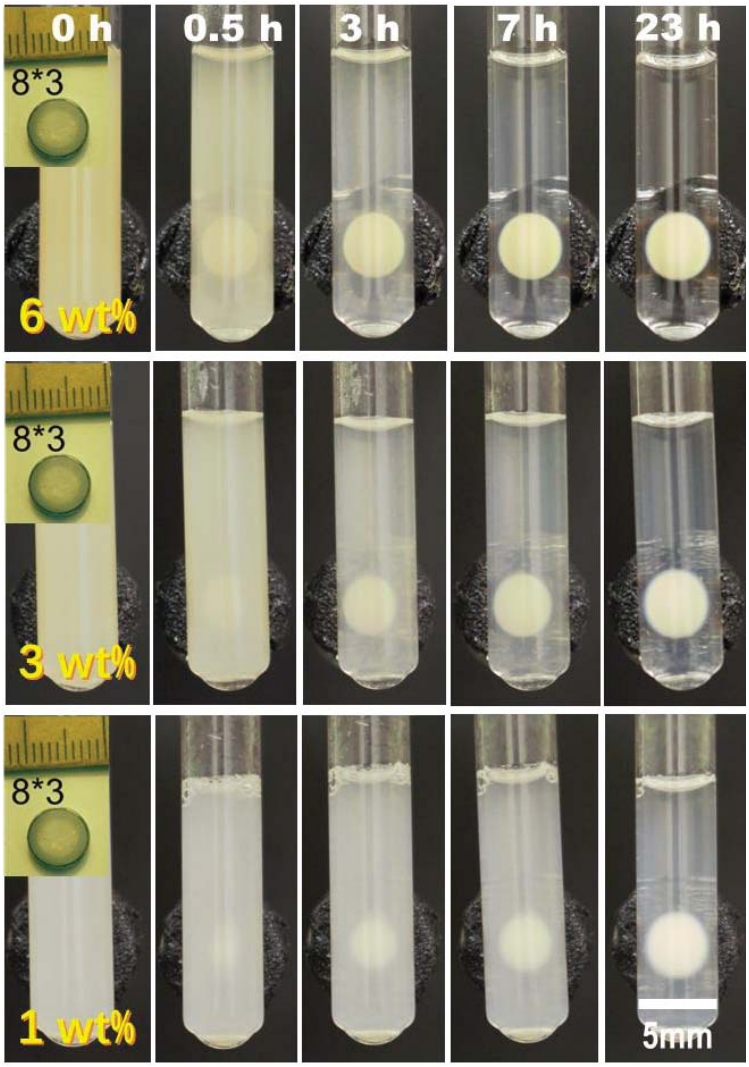

Figure 2-12. Time-varying adsorptions of NCs with different SPIONs loadings (6 wt%, 3 wt%, 1 wt%) to the wall of glass tubes on a FeNdB magnet (diameter 8 mm, thickness 3 mm, surface field ~0.4 T) side. The three water suspensions of NCs have the same concentrations of 2.5 mg/mL.

The images illustrate unmistakably that a higher SPIONs loading results in faster adsorption. Previous studies using magnetic PLGA NPs[4] or microparticles loaded with only 1 wt% iron oxide[5] could demonstrate magnetic retention in rodent brain or knees, pointing out that our protein-loaded magnetic NCs with a higher magnetic load (6 wt%, Ms ~ 4 emu/g) may still have better characteristics to address magnetic targeting.

Next, different types of magnets (produced by the MAGBBRIS

partner IEP-SAS) were used to investigate the time-varying adsorptions of NCs with same SPIONs loadings (6 wt%) aiming to use small magnet with highmagnetic field, this is of practical significance for pre-clinical *in vivo* in mice because the implantation of smaller magnets would induce less pain and discomfort to the animals. As seen in **Figure 2-13**, when the size of magnet decreases from 8x3 mm to 4x2 mm, the adsorption of NCs show no apparent difference within 7 h of the three batches with same concentrations (2.5 mg/mL) and SPIONs loadings (6 wt%), therefore the smaller magnet with similar magnetic retention would be a better option for *in vivo* experiments.

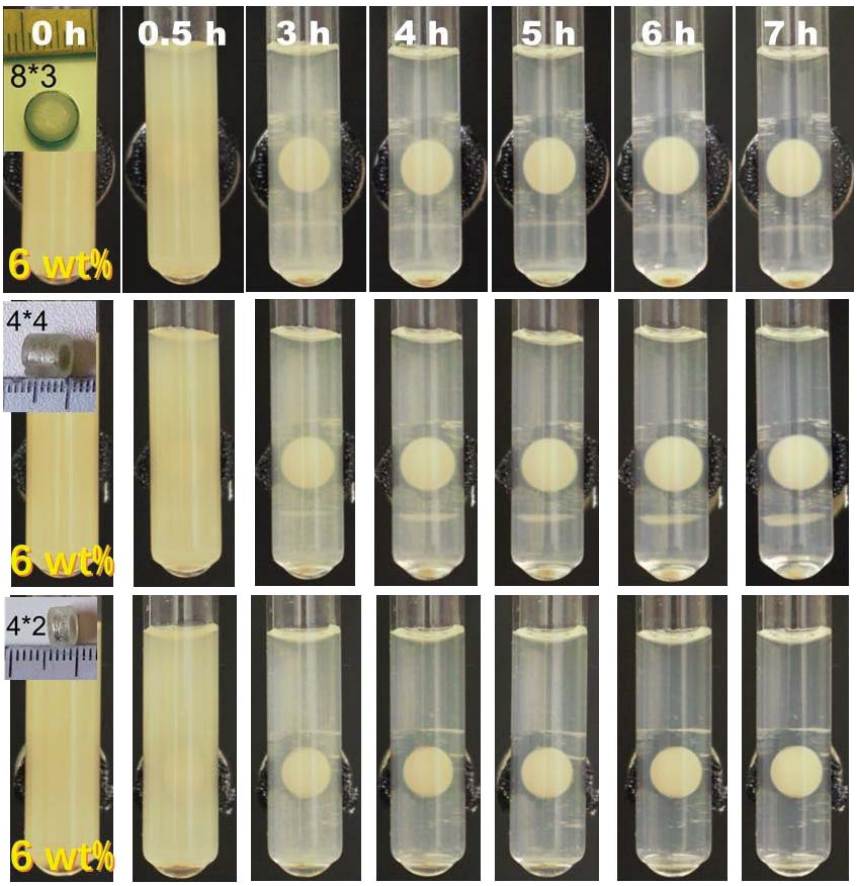

Figure 2-13. Time-dependent adsorption of NCs with the same SPIONs loadings (6 wt%) but different magnet types (diameter x thickness) to the wall of glass tubes on the magnet side. NCs concentration = 2.5 mg/mL.

2.1.4 PEGylation possibility of the established PLGA NC formulation

Making a drug delivery system more hydrophilic is a strategy to reduce nanocarrier phagocytic removal and increase its blood circulation half-life[6]. Nanocarriers that are surface-functionalized with long hydrophilic PEG chains are considered more stealth and less visible to the reticuloendothelial system thus increasing their blood circulation time and allowing successful drug delivery to a specific organ or tissue[7-9]. In this section, we provide a PEGylation option for the NC formulation which could benefit the targeted drug delivery specifically when the NCs are *i.v.* administered.

In the literature, it can be found the use of different proportions and types of PLGA and PLGA-PEG copolymer to synthesize micro- or nano- stealth particles[6, 9-12]. We have tried two types of commercial PLGA-PEG copolymers to blend with PLGA at different fractions in the organic phase during the NCs fabrication process as listed in **Table 2-2**. Type-1 is a PLGA-PEG copolymer with longer PEG molecular chain and higher PEG content than Type-2. The fabricated NCs are expected to have different PEG molecular chain lengths and density on the surface depending on the PLAG-PEG copolymer used.

Table 2-2. Two PLGA-PEG copolymers with different PEG molecular weight (Mn) are tested to fabricate PEGylated NCs at different PEG contents.

PLGA-PEG copolymer		PEGylated NCs		NCs quality
Type	Composition	PLGA-PEG added (wt%)	PEG content (wt%)	
①	(PEG Mn5000-PLGA Mn7000) PEG 42 wt%	7wt%	3wt%	Good
		12wt%	5wt%	Bad
②	(PEG Mn2000-PLGA Mn11500) PEG 15 wt%	20wt%	3wt%	Bad
		33wt%	5wt%	Bad

For Type-1 PLGA-PEG copolymer 7 wt% of it is firstly blended with PLGA to fabricate PEGylated NCs yielding a 3 wt% of PEG content with molecular chain of Mn 5000 on the surface of NCs. As shown in **Figure 2-14a** the morphology and size distribution of the NCs at 14 d after lyophilization (AL) are good. Then, a higher fraction of PLGA-PEG (12 wt%) was used to increase the content of PEG on the NCs. As shown in **Figure 2-14e** before lyophilization (BL) the size distribution of NCs is good and consistent with the SEM result from which the spherical and monodispersed NCs are observed, however many of the NCs show holes. As we know for the NCs fabrication,

after the second emulsification step the organic phase containing PLGA and PLGA-PEG forms a sandwich layer between the external water phase and the inner water phase. Higher content of hydrophilic PEG in this thin organic layer may interrupt the distinct oil-water interphase, which results in the formation of defective PLGA films after the evaporation of the organic solvent a being the origin of the holes on the NCs. Moreover, it appears that at higher PEG content the NCs spherical morphology is not well maintained after lyophilization (AL). As seen in **Figure 2-14b** the NCs not only shrink but also adhere to each other and cannot be separated after re-dispersing them in water (DLS size distribution bad), which further demonstrates that the long hydrophilic PEG chains in the NCs shell structure makes the NCs softer and fragile and the chains on the surfaces can entangle with each other and combine the particles. For NCs with a lower PEG content (3 wt%) the good morphology and size distribution is maintained even at 14 d AL (**Figure 2-14a**), but NCs still collapse after one month storage (**Figure 2-14d**). At much higher PEG content of 20 wt% the NCs cannot be formed as shown in **Figure 2-14c** which means the sandwich layer of the organic phase does not form after the double emulsion process due to the excess amount of PEG in the oil phase.

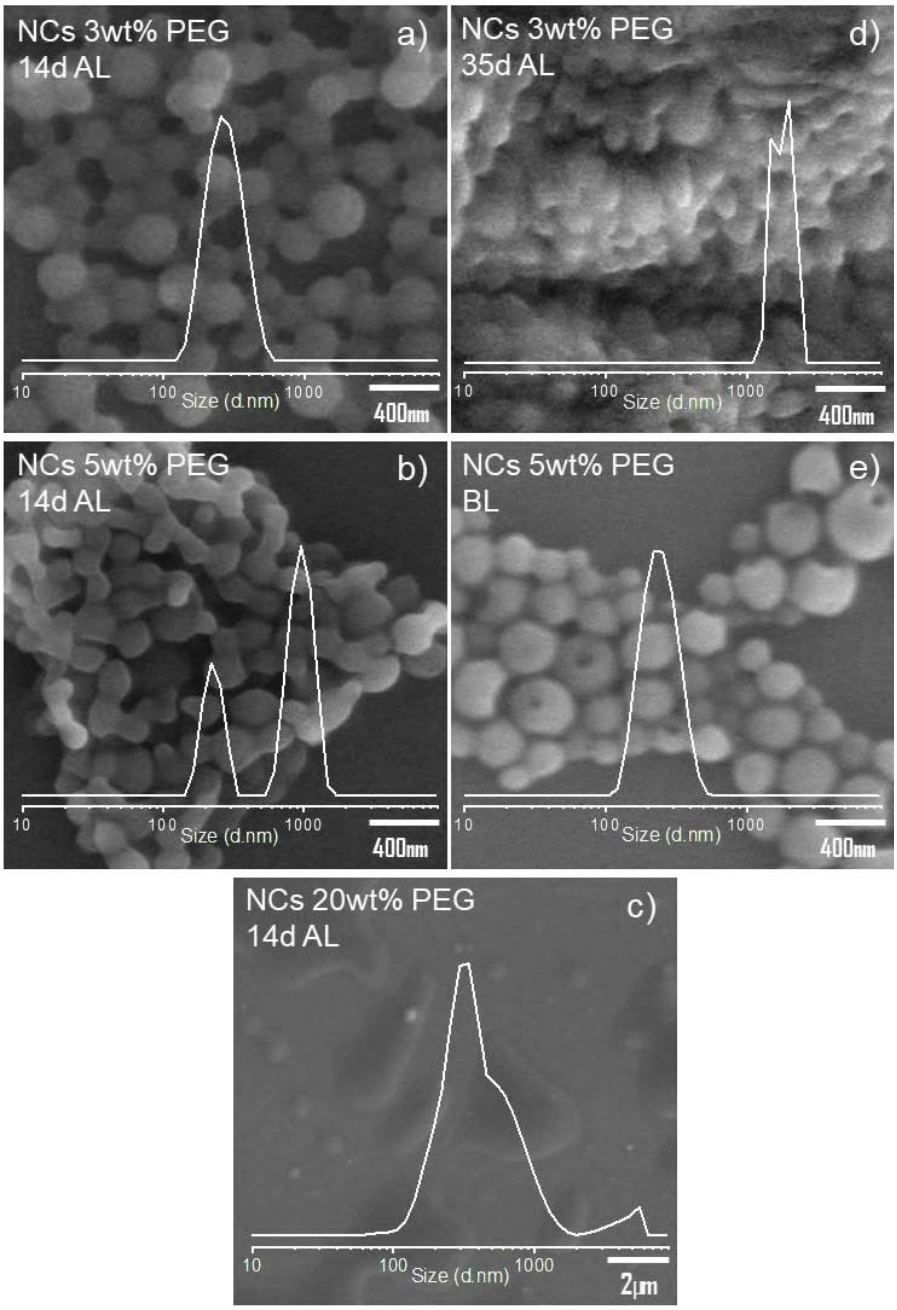

Figure 2-14. SEM morphologies and DLS size distributions (Y-axis: intensity%) of PEGylated NCs fabricated with Type-1 PLGA-PEG copolymer at PEG contents of 3 wt%, 5 wt% and 20 wt% blended in the PLGA matrix. Before and after lyophilization (BL and AL) as well as AL storage (4°C) results are shown.

For Type-2 PLGA-PEG copolymer NCs using the same mass content

of PEG (3 wt%) the quality is bad. Considering the molecular weight of PEG in this type of PLGA-PEG copolymer is smaller, the molar amount of PEG in the organic phase will be larger than using Type-1 at the same mass content, which may interrupt stronger the oil-water phase and affect the formation of PLGA NCs shell films, hindering the NCs fabrication. Thus, Type-1 PLGA-PEG copolymer was selected for the PEGylation of the NCs at a PEG content of 3 wt%. As summarized in **Table 2-3**, the selected formulation for PEGylation does not affect the SPIONs loading nor the size distribution of the NCs. And the PEGylated NCs can maintain the quality for two weeks after lyophilization as already illustrated in **Figure 2-14a**. The longer PEG chains (Mn5000) on the NCs surface may have a better stealthy effect.

Table 2-3. The selected formulations for non-PEGylated/PEGylated NCs.

NCs Type	Shell Polymers (wt%)		SPIONs Loading (wt%)	M_S (eum/g)	Size (DLS)	
	PLGA	PLGA-PEG*			d. nm	PdI
NC-3.non-PEGylated	100	/	6.1	3.9	276	0.18
NC-4.PEGylated	93	7	6.0	3.8	265	0.13

*Type-1 PLGA-PEG shown in Table 2-2 is selected for all the following NC PEGylation.

Then, I evaluated the flocculation regime of the PEGylated NCs with a Turbiscan to confirm successful surface modification with PEG. The long hydrophilic PEG chains (Mn 5000) on the surface of the NCs is expected to increase the stability of the NCs in water and decrease their sedimentation rate. Sedimentation of the NCs suspension was monitored for 24 h. **Figure 2-15a** shows that, as NCs sedimentation progresses, the backscattering signal of the bottom part of the suspension increases from an increasingly higher concentration of NCs, while the signal of the top part decreases. The sedimentation rates of non-PEGylated (NC-3) and PEGylated NCs (NC-4) are compared in **Figure 2-15b**. As expected, the bottom backscattering signal of the PEGylated NCs media increases at a slower rate than the non-PEGylated one, which demonstrates a better dispersibility of the NCs due to the surface hydrophilic PEG chains. Additionally, in **Figure 2-15a**, the backscattering signal of the middle part does not vary with time, which means that the NCs are monodisperse and flocculation or coalescence does not occur during the 24 h period.

This is consistent with the DLS size distribution results shown in **Figure 2-15c**. Both non-PEGylated and PEGylated NCs remain monodisperse in PBS for 24 h at 37 ℃, which we consider an advantage for the *i.v.* administration and *in vivo* blood circulation.

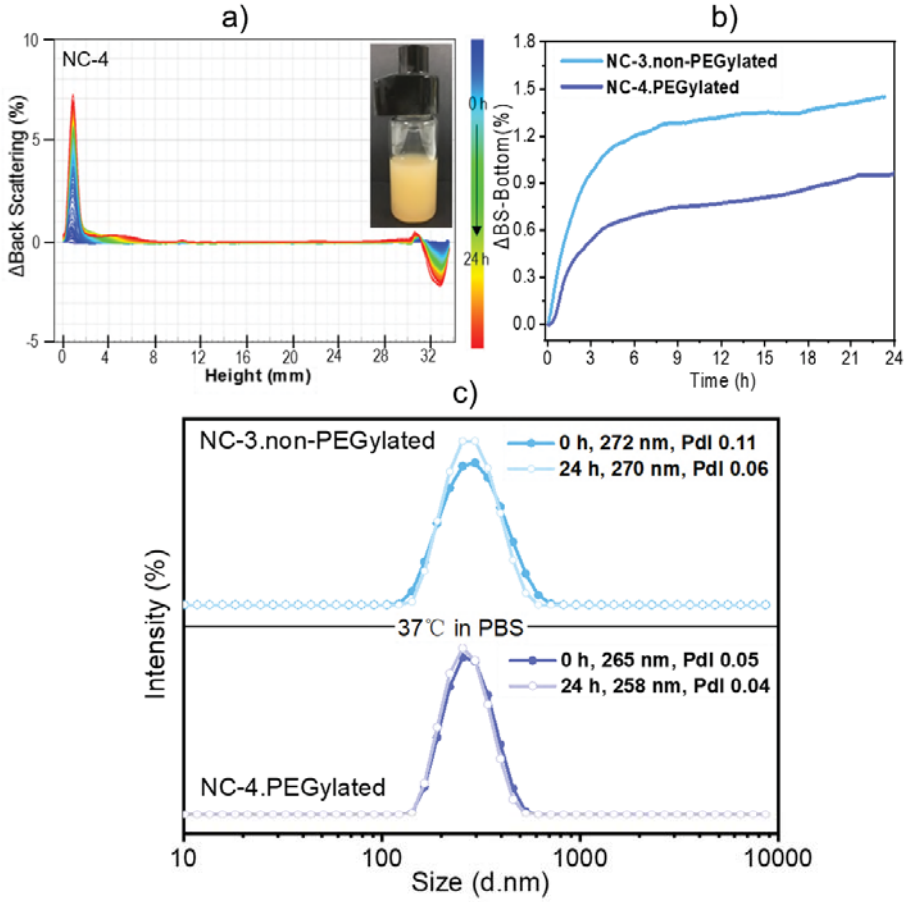

Figure 2-15. a) Backscattering intensity change of the PEGylated NCs water suspension (shown inset) at different height of the vial along 24 h measured by Turbiscan; b) Backscattering intensity change of the bottom part of the vial along 24 h for NCs water suspensions of non-PEGylated and PEGylated measured by Turbiscan; c) DLS size distribution of NCs water suspensions of non-PEGylated and PEGylated at 0 h and after 24 h incubated in PBS at 37℃.

2.2 Evaluation of Biomedical Aspects of the PLGA NC formulations

2.2.1 MRI performance

In section 2.1, I have shown that NC-3 with 6 wt% of SPIONs_9 nm has the optimal magnetization and magnetic retention characteristics.

Here phantom studies are conducted to confirm the positive impact of higher SPIONs loading on the MRI performance of NCs. Phantoms from two batches (NC-2 and NC-3) with different SPIONs loadings at a series of concentrations were prepared and spin–spin relaxation times (T2) recorded (**Table 2-4**). The T2 value decreases (1/T2 increases) as the concentration of NCs increases for both NC-2 and NC-3. For the same concentration, NC-3 shows a lower T2 value (larger 1/T2) than NC-2 due to the higher loading of SPIONs, indicating a more efficient behavior as a T2-contrast agent.

Table 2-4. MRI T2 relaxation times (expressed as 1/T2, sec^{-1}) of the NCs in agarose phantoms at increasing concentrations. NC-2 and NC-3 with different SPIONs loadings are measured respectively.

NCs water suspension		NC-3 (6wt% SPIONs_9nm)		NC-2 (3wt% SPIONs_9nm)	
Agarose (wt%)	[NCs] mg/L	[Fe] mmol/L	1/T2 (sec^{-1})	[Fe] mmol/L	1/T2 (sec^{-1})
0.63	320	0.178	69.9	0.088	33.6
0.63	160	0.089	36.3	0.044	22.7
0.63	80	0.045	25.9	0.022	16.2
0.63	40	0.022	16.9	0.011	12.5
0.63	20	0.011	12.6	0.006	11.0
0.63	10	0.006	11.1	0.003	10.0
0.63	0	0.000	8.8	0.000	8.9

The corresponding T2-weighted color-coded MRI maps clearly exhibit signal decay in a concentration-dependent manner (**Figure 2-16a**). Importantly, at the same NCs concentration NC-3 shows a higher T2 signal decay rate than NC-2 indicating that NC-3 with higher SPIONs loading will be easier to track *in vivo* by MRI. Furthermore, the transverse relaxivity (r_2) value at 7 Tesla of NC-3 (336 mM^{-1} s^{-1}) is higher, as expected, than that of NC-2 (278 mM^{-1} s^{-1}) as seen in **Figure 2-16b**, indicating that the denser packing of SPIONs in a single NC, as in NC-3, endows the NCs with a larger magnetic moment and increases its efficiency as a spin–spin relaxation agent[13]. Compared with other clinically used SPIONs systems such as Feridex (98 mM^{-1} s^{-1}) and Resovist (151 mM^{-1} s^{-1})[14], the much higher r_2 value in our final NCs formula (6 wt% SPIONs of 9 nm in diameter) is expected to be useful for *in vivo* MRI tracking of the NCs.

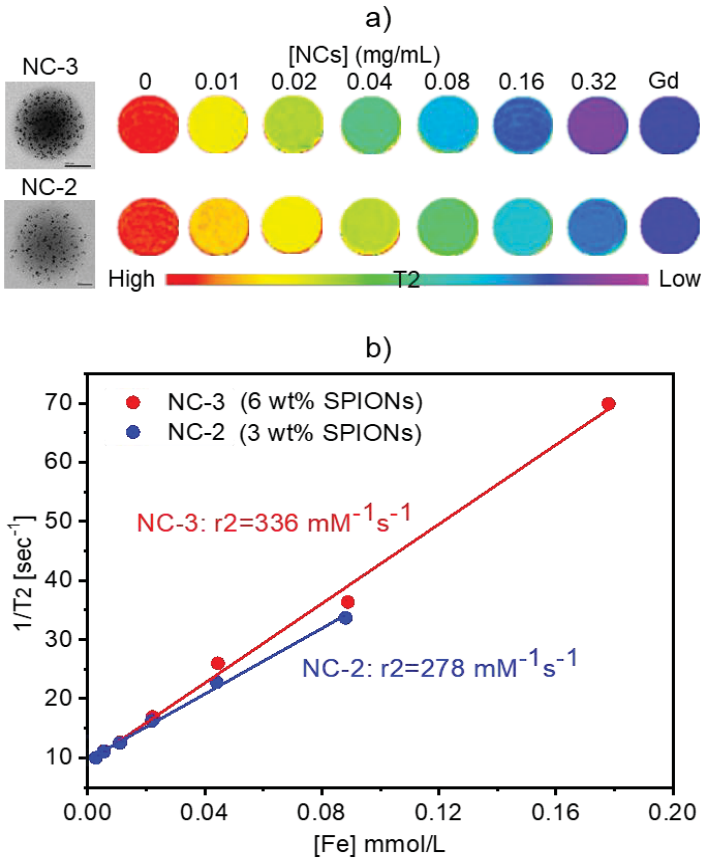

Figure 2-16. a) T2-weighted maps of a series of concentrations of NCs in agarose phantoms shown in Table 2-4, on the left are TEM images of NCs; b) evaluation of r_2 relaxivities for NC-3 and NC-2.

As the representative abdominal images showed in **Figure 2-17b**, a clearer increase of the contrast of the liver is observed in both T2WI and T2 maps after NCs administration, illustrating the fast accumulation of NCs in the liver. Quantitative ROI analysis in **Figure 2-17d** shows a 55% drop of signal intensity (SI) on T2W images and a 26% drop of T2 relaxation time in the liver, while a negligible signal drop was observed in the kidney, which further demonstrates the large accumulation of NCs in the liver. To further confirm the presence of NCs in the tissue, Prussian blue staining on liver sections confirmed the presence of ferric iron (**Figure 2-17c**) after the *in vivo* MRI, blue dots in the liver tissue after NCs administration arises from the SPIONs in the NCs.

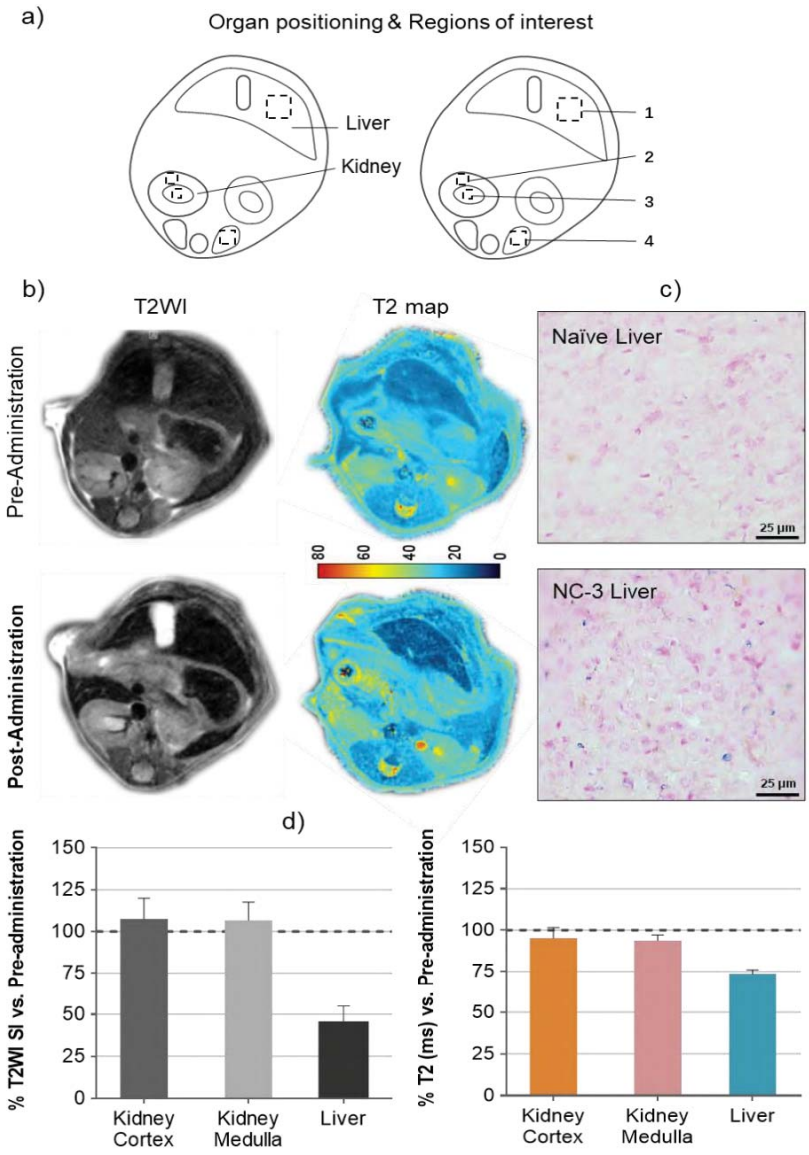

Figure 2-17. *In vivo* mouse MRI and *ex vivo* Prussian blue iron-stain for the tracking of NC-3. a) Representation of the abdominal region with organ positioning and regions of interest (ROIs) quantification in the kidney and liver (1: liver, 2: kidney cortex, 3: kidney medulla, 4: paravertebral muscle used for normalization); b) Representative abdominal images of T2W and T2 map pre- and post- NC-3 administration; c) Representative images of Prussian blue stain for ferric iron in liver sections of naïve and treated animals administered with NC-3 in the MRI study (blue spots); d) Signal intensity (SI) and relaxation time (msec) are calculated for each region of interest (ROI) corresponding to the analyzed anatomical structures which are then corrected by muscle ROI SI. Final data is represented as post-administration SI or T2 relaxation as the percentage of the pre-administration values (n=2).

2.2.2 Biosafety study of the NCs

In vitro and *in vivo* safety studies of NC-3 wereconducted considering that this formula is the optimal therapeutic formulation for magnetically targeted delivery. The cell proliferation/viability effect of NC-3 were tested at VHIR using human endothelial cells lining the blood vessels, which are the first NCs target following their *i.v.* administration. Thus, human brain endothelial cells (hCMEC/D3 cell line) derived from brain microcirculation, and primary cultures of human $CD34^+$ derived endothelial cells are exposed to NC-3 and its cytotoxicity is evaluated by performing an MTT assay at VHIR and Artois University, respectively. As shown in **Figure 2-18**, the cells do not exhibit a decrease in viability after being exposed for 48 h to the NCs from 25 to 100 µg/mL, and the differences in cell viability between groups are not significant (ANOVA >0.05), thus our results suggest that the NCs are biocompatible for the studied range of concentrations and time, *in vitro*.

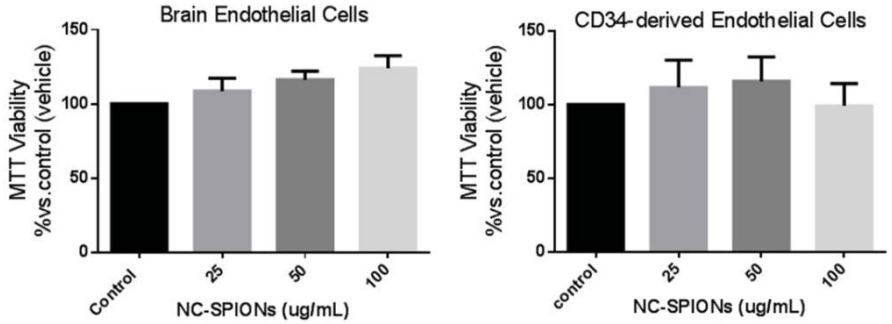

Figure 2-18. *In vitro* safety of the NCs (NC-3). Cell viability after exposure to an increasing dose of NCs for 48 h, expressed as a percentage of the untreated cells (control media), determined by MTT assay (n = 3, mean ± SEM).

Thereafter, the systemic effect of NCs *via i.v.* administration was evaluated at VHIR. **Figure 2-19a** shows that after the injection of NCs, all animals maintain the body weight within normal values for two weeks (no differences between groups at the end of the experimental period), with no significant morbidity and no potential adverse effects. At the same time, blood sample tests to monitor potential liver and pancreatic toxicity show that none of the biomarker enzymes are significantly different between groups and similar to those measured in non-treated mice (**Figure 2-19b**; ANOVA >0.05), suggesting a normal activity of these organs. All the above results reinforce the biosafety of this formulation of nanocarriers for future clinical translational practice.

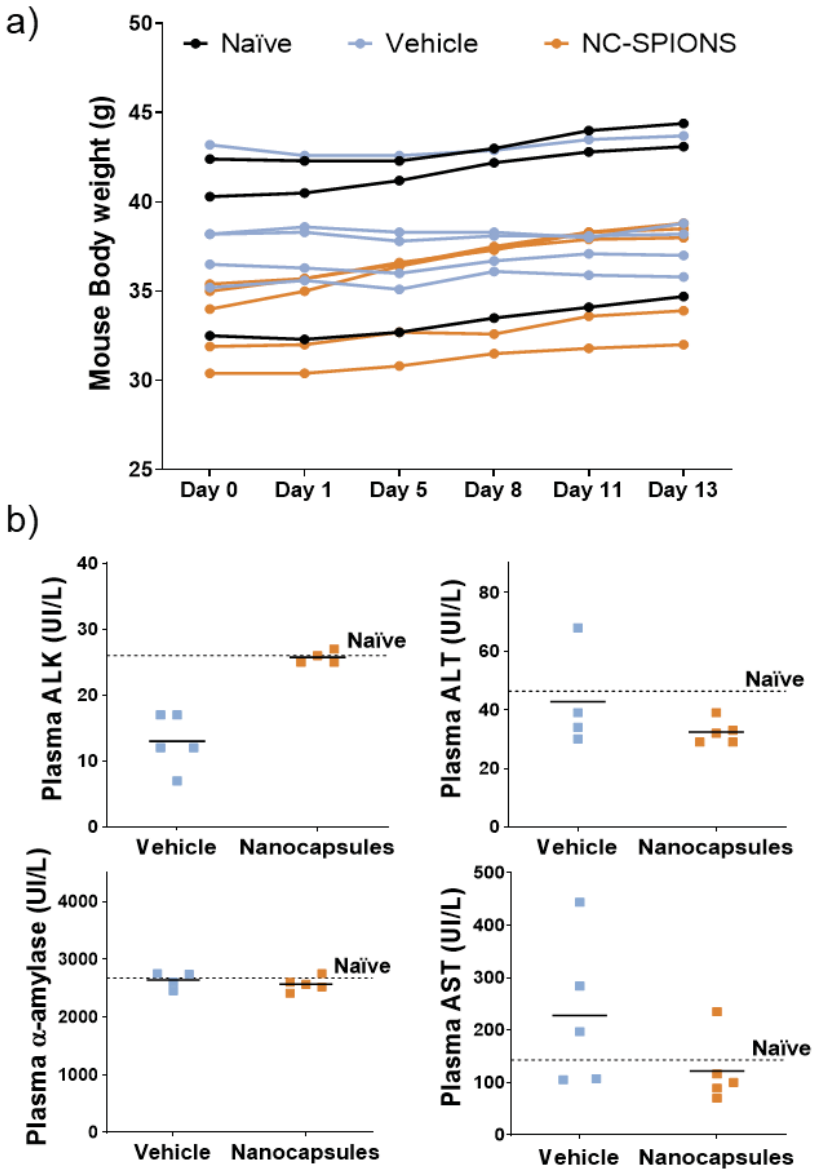

Figure 2-19. *In vivo* safety of the NCs (NC-3). a) The curve of body weight of the observed mice throughout the experiment, the naïve group was not treated serving as control (n = 3), the vehicle group received 150 µL of saline (n = 5) and the NCs group received 0.84 mg of NCs in 150 µL of saline (n = 5); b) Liver and pancreatic toxicity after 13 days of NC injection based on specific enzyme levels in plasma: alkaline phosphatase (ALK), alanine aminotransferase (ALT), α-amylase and aspartate aminotransferase (AST).

2.3 Quality control of the established PLGA NC formulation

It is important to monitor the quality of the NCs fabricated before *in*

vitro and *in vivo* studies to ensure reliable and reproducible results. The NCs should maintain a monodispersed spherical morphology before use since the formation of aggregates could disturb the *in vitro* and *in vivo* experiments. Efforts have been made to maintain the quality of NCs and determine the conditions which would affect this quality. For that, NCs size (DLS) and morphology (SEM) were monitored at several time points in particular after the synthesis, ultra freeze procedure, lyophilization, and long-term storage.

Note that after the organic solvent evaporation step, NCs are formed and then washed to remove the PVA used as surfactant. Then, fresh NCs dispersed in water are frozen at -80°C for future use. It is found that NCs aggregation can be observed after 1 month in the frozen state (**Figure 2-20b**) and that the NCs cannot be redispersed. Differently, NCs maintain their monodispersity after being frozen for 7 weeks when 2 mg/mL of trehalose is added (**Figure 2-20a**), confirming the role of trehalose as a cryoprotectant.

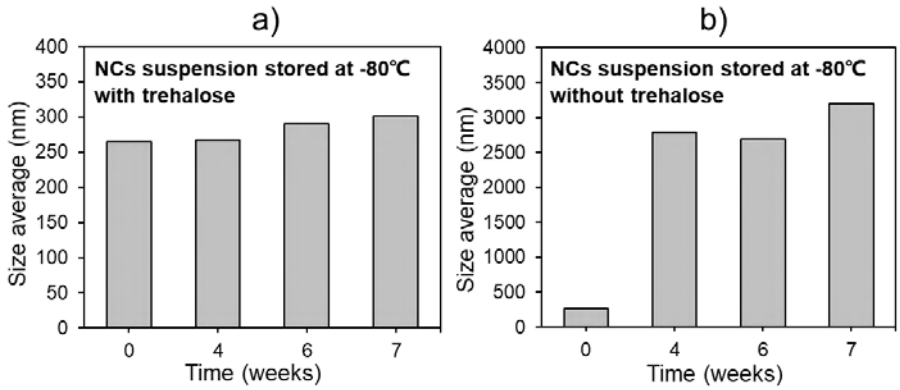

Figure 2-20. Effect of the trehalose for the frozen storage of the NCs. After the washing step NCs water suspension is stored at -80°C and DLS average size of the NCs is monitored at different time points. a) NCs suspension with 2 mg/mL of trehalose; b) NCs suspension without trehalose.

If we need to quantify the amount (mg) of NCs produced in each batch, the frozen NCs need to be lyophilized to weight the NC as dry powder. Lyophilized NCs are then preserved at 4°C with desiccant. I observe that the sample lyophilized with trehalose maintains the quality up to 45 days without apparent aggregations as monitored by SEM and DLS. While after 60 days some of the NCs attach to each other and cannot well redispersed in water suspension which is demonstrated by the increase of polydispersity index (PdI) and the average size of the NCs (**Figure 2-21** NCs with trehalose). Conversely, NCs lyophilized without trehalose show very short

self-life, after 15 days NCs appear to aggregate and after 30 days massive aggregation is observed by SEM (**Figure 2-21** NCs without trehalose).

The *in vitro* and *in vivo* investigations of the NCs usually need cooperation between different research groups, thus the manipulation and transfer of the dry powder sample at room temperature is unavoidable. Study shows that the NCs can maintain the quality at room temperature for 5 days and that after 10 days a decay in quality is observed (**Figure 2-22**), which means the transfer or delivery of NCs between research groups is better done in 5 days at room temperature but cold-chain transportation is advisable.

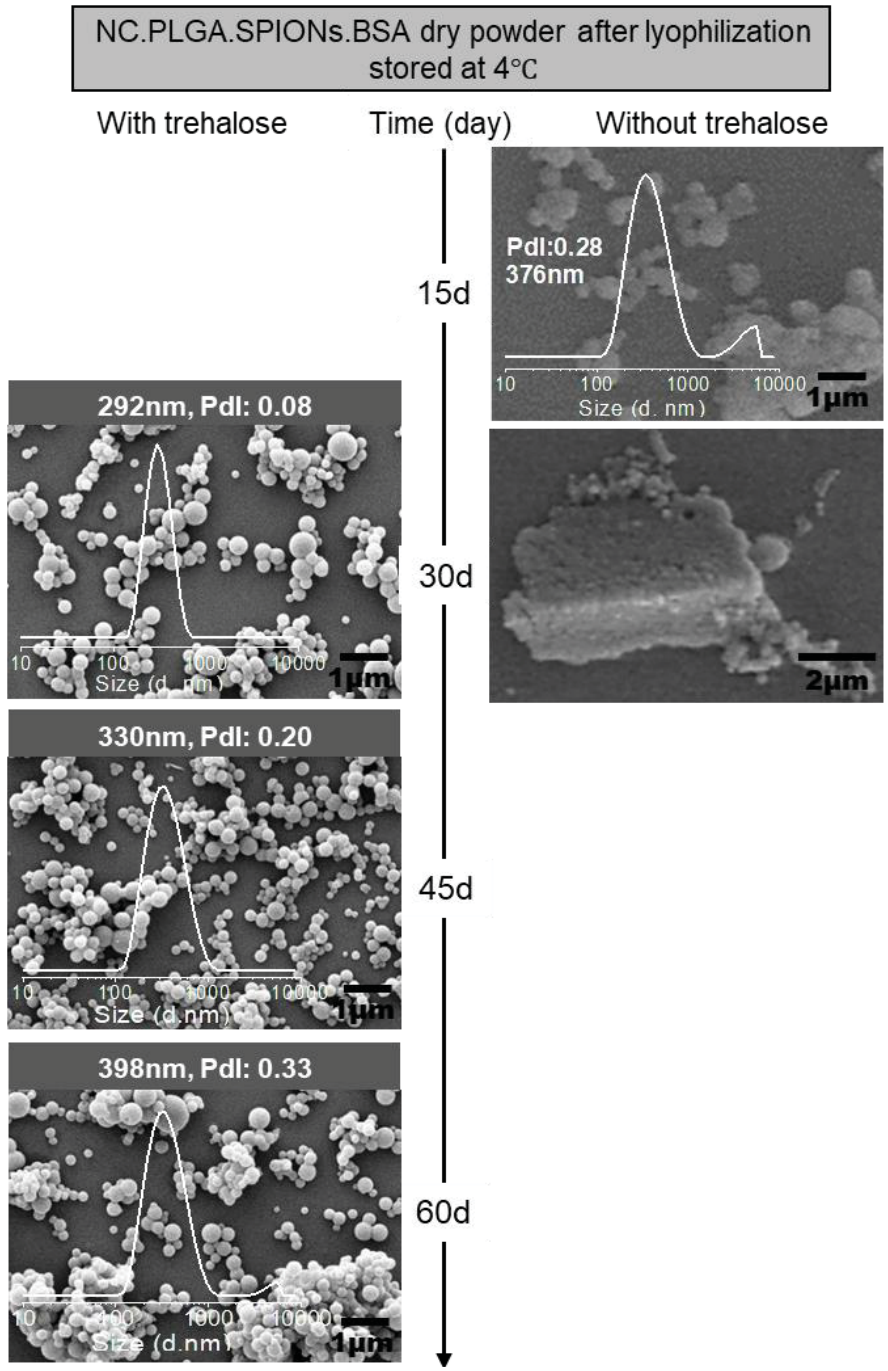

Figure 2-21. Effect of the trehalose for the lyophilized storage of NCs (NC-3). The NCs frozen suspension with or without trehalose (2 mg/mL) is lyophilized and the dry powder sample is stored at 4℃ with desiccant. The SEM morphology and DLS size distribution (Y-axis: intensity%) of the dry powder samples with or without trehalose are monitored at different time points.

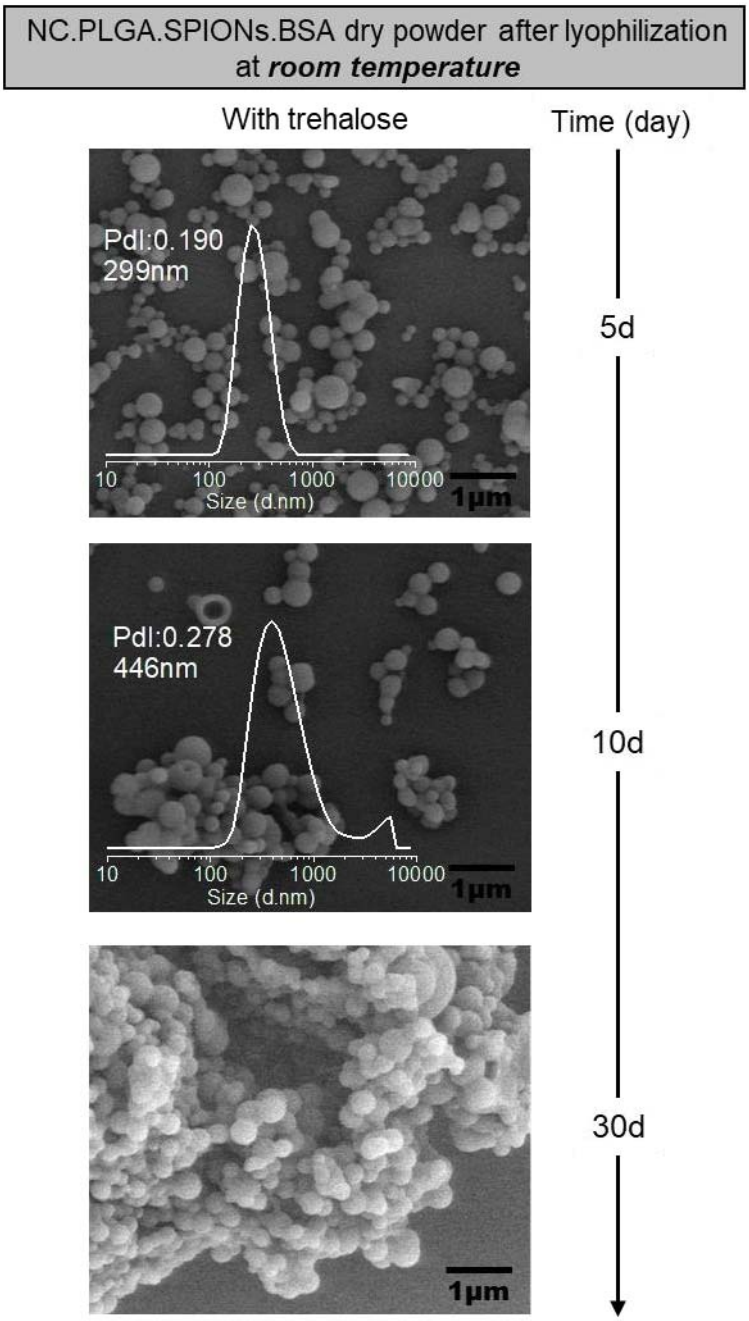

Figure 2-22. The durability of NCs (NC-3) at room temperature illustrated by the SEM morphology and DLS size distribution (Y-axis: intensity%) along time.

The above discussion confirms the role of trehalose as an excellent stabilizer for PLGA NCs in their frozen storage and after lyophilization preservation, the mechanism by which this

stabilization occurs is not fully understood. According to some theories been proposed[15], we consider that in the PLGA-NCs trehalose solution, trehalose molecules preferentially form hydrogen bonds with the PLGA carboxylic ending and thus substitute those water molecules interaction with the NCs[15]. Therefore, the formation of ice crystal around NC is hindered by the trehalose layer around NC. This hypothesis is consistent with the experimental results. Frozen NCs keep monodispersed with the protection of trehalose (**Figure 2-20**), while without trehalose adjacent NCs may be compressed and attached to ice crystal formed during the ultra-freezing process and after a long storage time cannot be separated. For NCs as dry powder after lyophilization in trehalose solution, the formed glassy coating of trehalose can be viewed as a cocoon that traps the NC inside according to the ‘‘immobilization theory’’[16], thus the NCs can be preserved for a longer time than those without trehalose coating (**Figure 2-21)**. At room temperature that near the glass transition temperature (Tg) of PLGA (Tg 42-46 °C), NCs aggregate much faster than those stored at 4°C (**Figure 2-22**), indicating the more viscous PLGA at room temperature facilitates the adherence of NCs with defective trehalose coating.

2.4 Chapter summary

We synthesized OA-SPIONs_9 nm with enhanced Ms of 75 emu/g dispersable in an organic phase. A high load of SPIONs (6 wt%) provided the obtained PLGA NCs with enhanced magnetic retention (Ms 4 emu/g) and MRI performance (r_2 = 336 mM^{-1} s^{-1}). Moreover, the NCs maintained a monodisperse size (~270 d.nm) after the integration of SPIONs and PEG (3 wt%). PEGylation improved the stability of the NCs dispersion in an aqueous phase.

An abdominal MRI performed in mice showed a dominant liver accumulation of the *i.v.* administered NCs, whereas the NCs show no toxicity *in vitro* or *in vivo*. In this regard, the NCs did not affect the viability of two different human endothelial cells (brain endothelial cells and CD34+ derived endothelial cells) for concentration up to 100 μg/mL. *In vivo* biosafety was shown based on the lack of morbidity of mice for 2 weeks after the systemic NC administration and the fact that none of the biomarker enzymes monitored were significantly different between groups and similar to those measured in non-treated mice.

Finally, to maintain the quality of the obtained monodispersed NCs, trehalose (2 mg/mL) as a cryoprotectant was used to enable the frozen storage of NCs as long as 7 weeks. Besides, the quality of the lyophilized NC as dry powder can be maintained for up to 45 days when preserved at 4 ℃ with desiccant.

2.5 Annex of Chapter 2

2.5.1 Synthesis of OA-SPIONs

The SPIONs were synthesized by microwave-assisted thermal decomposition[17] in a microwave oven (Discover SP, CEM Corporation, Matthews, NC, USA), and then coated by OA. The process to obtain homogeneous OA-SPIONs with an average diameter of 9 nm under Condition-2 (**Figure 2-2**) is as follows; 3.5 mmol of iron precursor $Fe(acac)_3$ are dissolved in 4.5 mL of benzyl alcohol in a microwave reaction glass tube. Microwave irradiation was initiated at 60 °C for 5 min to fully dissolve the precursor and, subsequently, the irradiation is kept at 210 °C for 30 min then, the reaction was stopped and fast cooled down to room temperature. 4 mL of OA in toluene (0.8 mmol/mL) is added immediately into the as-synthesized SPIONs dispersion followed by incubation under ultrasounds for 1 h. Subsequently, the obtained OA-SPIONs are separated by centrifugation in ten-fold of acetone. The pellet is redispersed in 4 mL of toluene in a glass vial and a magnet was attached on the wall for 5 s, The un-adsorbed suspension containing SPIONs with smaller size are discarded and the adsorbed pellet is redispersed in 6 mL of dichloromethane (DCM), followed by centrifugation at 4000 rpm for 5 min to sediment the unstable big particles. Finally, stable OA-SPIONs (9 nm) dispersion in DCM is centrifugated in ten-fold of acetone and the pellet product is dried under vacuum and redispersed in DCM at the concentration required for use. For OA-SPIONs of 6 nm under Condition-1 (**Figure 2-2**) is as follows: 0.35 mmol of $Fe(acac)_3$ in 4.5 mL of benzyl alcohol are irradiated at 60 °C for 5 min and subsequently, the irradiation is kept at 200 °C for 15 min, the reaction is then stopped and fast cooled down to room temperature. 0.4 mL of OA in toluene (0.8 mmol/mL) are added immediately to the as-synthesized SPIONs dispersion followed by incubation under ultrasound for 1 h. Subsequently, the obtained OA-SPIONs are separated by centrifugation in ten-fold of acetone. Finally, the pellet product is dried under vacuum and redispersed in DCM at the concentration required for use.

2.5.2 Fabrication of NCs

PLGA NCs encapsulating BSA are prepared by a double emulsion solvent evaporation method. Briefly, 50 µL of inner aqueous phase (W1) containing BSA (30 mg/mL) is emulsified in 500 µL of DCM organic phase (O) that is composed of 50 mg of PLGA (RG502H, Mn

12,000) and a certain amount of OA-SPIONs (2 mg for 3 wt% loading and 4 mg for 6wt% loading) by sonication (VC505, Sonics & Materials Inc., Newtown, CT, USA) at 200 W for 28 s to form the first emulsion (W1/O). Afterward, 2 mL of external aqueous phase (W2) with polyvinyl alcohol (PVA) (20 mg/mL) is added and the second emulsion (W1/O/W2) is formed by sonication for another 28 s. The temperature during the whole emulsion process is kept at 4 °C by using an ice bath. The resulting double emulsion is poured into 50 mL of MilliQ water and mechanically stirred at RT for 2 h to allow for complete evaporation of the organic solvent DCM and the formation of NCs. Finally, the NCs are washed three times with MilliQ water and lyophilized in 6 mL of trehalose aqueous solution (2 mg/mL). The as-obtained powder is stored at 4 °C with desiccant silica gel. For the PEGylated NCs, different proportions of PLGA-PEG copolymer are mixed in the organic phase while keeping the total amount of PLGA plus PLGA-PEG at 50 mg.

All the aqueous and organic solutions were sterilized by filtration (0.2 μm PTFE syringe filter) and all used materials were autoclaved before use. All the manipulations were done in sterile biohood to avoid contamination.

2.5.3 Thermogravimetric analysis (TGA)

Around 2 mg of SPIONs/OA-SPIONs sample and 15 mg of NCs were measured on a SETSYS Evolution TGA (Setaram) from room temperature to 700 °C at a heating rate of 10 °C/min and under dynamic dry airflow.

For the determination of OA fraction of OA-SPIONs samples, we considered that in air at 700 °C the difference of residual mass between SPIONs and OA-SPIONs can be attributed to the degradation and evaporation of the OA molecules. Here, we designate the SPIONs mass fraction of OA-SPIONs samples as **x**, mass of OA-SPIONs as **a** gram and residual mass fraction of SPIONs and OA-SPIONs samples at 700 °C as **b** and **c** respectively (**b** and **c** are given by TGA data in **Figure 2-5**). There is:

$$a \cdot x \cdot b = a \cdot c, \quad x = c/b$$

Then SPIONs_6 nm in OA-SPIONs: 82.1 wt% (OA 17.9 wt%), SPIONs_9 nm in OA-SPIONs: 86.3% (OA 13.7 wt%).

For the determination of $wt\%_{SPIONs}$ in the NCs samples: the SPIONs

and the NCs are heated to 700°C under air atmosphere and the residuals of them are considered to be the same substance. If **A** gram of pure NCs (the lyophilized NCs powder contains cryoprotectant trehalose, denote the percentage of pure NCs as **c**) contains **B** gram of SPIONs, there is:

$$\frac{A}{c} \cdot d = B \cdot e$$

where **d** is the residual mass (wt%) of NCs and **e** is the residual mass (wt%) of SPIONs. Then the experimental SPIONs loading ($wt\%_{SPIONs}$) can be calculated as:

$$wt\%_{SPIONs}\ (TGA) = \frac{B}{A} = \frac{d}{e} \cdot \frac{1}{c} \times 100\%$$

For NC-1 in Figure 2-9a, **d** is 1.9 wt%, **e** is 89.5 wt%, **c** is 75.8 wt%, so the calculated $wt\%_{SPIONs}$ of NC-1 is 2.8 wt%.

2.5.4 Magnetometry (SQUID)

Superconductive quantum interference device (SQUID, MPMS5XL, Quantum Design, San Diego, CA, USA) is used to measure the magnetization of NCs and SPIONs. A gelatin capsule filled with SPIONs or NC samples together with some cotton wool is inserted into the SQUID magnetometer sample holder and the hysteresis loop is measured from −50 kOe to 50 kOe.

For the determination of SPIONs loading ($wt\%_{SPIONs}$) of NCs samples: the Mr of the magnetic NCs (emu/g NCs) and of SPIONs (emu/g SPIONs) at 5 K is used:

$$wt\%_{SPIONs}\ (SQUID) = \frac{M_{r,\ NCs}}{M_{r,\ SPIONs}} \times 100\%$$

Here the Mr is used instead of the Ms to calculate the SPIONs loading because at 5 K when the external magnetic field backs to 0 the Mr of the sample is considered to come from the SPIONs with less noise than the Ms especially when the used mass is very low and the diamagnetic signal of cotton and gelatin capsule might interfere with the measure. For NC-1 in Figure 2-9b, the calculated $wt\%_{SPIONs}$ from SQUID is 2.9 wt%.

The entrapment efficiency of SPIONs ($EE\%_{SPIONs}$) can be calculated as:

$$EE\%_{SPIONs} = \frac{Experimental\ \text{wt}\%SPIONs}{Nominal\ \text{wt}\%SPIONs} \times 100\%$$

2.5.5 Dynamic light scattering (DLS)

DLS (Zetasizer Nano ZS, Malvern Panalytical, Madrid, Spain) measurement of the hydrodynamic diameter and size distribution of NCs is performed by redispersing 0.5 mg of lyophilized NCs powder into 1 mL of MilliQ water. For the SPIONs, very diluted OA-SPIONs DCM dispersion is measured.

2.5.6 Turbiscan

Turbiscan (Turbiscan Lab, Formulation, Toulouse, France) is used to detect the destabilization of the NCs suspension. 15 mL of 2 mg/mL NCs in the Turbiscan cell is scanned at all heights of the suspension with a time interval of 2 min for 24 h. The backscattering signals at different heights of the cell were recorded and the delta of backscattering intensity calculated by subtracting the signal at time = 0 s. The bottom part is defined as 1/5 of the liquid level.

2.5.7 Electron microscopies (SEM/TEM)

Field emitting scanning electron microscope (SEM, FEI Quanta 200 FEG, Thermo Fisher Scientific, Oregon, USA) and transmission electron microscope (TEM, JEM-1210, JEOL Ltd., Tokyo, Japan) are used to study the morphologies of SPIONs and NCs. For the SEM sample preparation of NCs, 0.5 mg of lyophilized NCs powder were redispersed into 1 mL of MilliQ water and centrifuged at 4000 rpm for 10 min to remove the trehalose (used for cryopreserving during lyophilization) in the supernatant. Then the pellet of NCs were redispersed in 1 mL of fresh water with ultrasound. Finally, 6 µL of the slightly turbid suspension was deposited onto a small piece of a silicon wafer stuck on the top of a carbon layer and dried at room temperature overnight. The sample was then sputtered with Au-Pd (20 mA 2 min, Emitech K550, Quorum Technologies Ltd., East Sussex, UK). The frozen NCs or NCs in media were washed with MilliQ water before the sample preparation. TEM samples were prepared by placing and drying one drop of the corresponding NCs or SPIONs dispersion on a copper grid at room temperature.

2.5.8 *In vitro* and *in vivo* MRI of the NCs

In vitro agarose phantoms of NCs were prepared by filling a series of glass microtubes with solutions of 0.63% agarose in water (Conda,

Madrid), into which different amounts of NCs are admixed. The corresponding iron doses (mmol/L) are calculated according to the wt% of SPIONs in each sample. T2 weighted images (T2WI) of the phantoms are acquired at 7 T in a 70/30 Bruker USR Biospec system (Bruker GmbH, Ettlingen) as follows: multi-slice multi-echo (MSME) sequence with echo time (TE) = 8 ms, repetition time (TR) = 2600 ms, average N = 2, matrix size = 160 × 160, field of view (FOV) = 24 x 24 mm, 14 slices of 1 mm thickness, and spectrometer bandwidth (BW) of 474 Hz per pixel. Quantitative T2 values are obtained from hand-drawn regions of interest (ROIs) by using curve fitting in the Image Sequence Analysis (ISA) Tool (ParaVision v.5.1).

Balb/c female mice (16–17 weeks of age, n = 2) were anesthetized with isoflurane (IsoFlo; Abbott Laboratories). T2WI are acquired pre- and 15–20 min post-administration of NCs (1.6 mg in 150 μL of saline through tail vein) using the following imaging parameters: MSME pulse sequence, 20 echo times with ΔTE = 8 ms, TR = 2.6 s, n = 2 averages, a matrix of 256 × 256 points covering a FOV of 25.6 × 25.6 mm^2, giving a resolution of 100 μm in plane, 14 continuous slices of 1 mm thickness, and BW = 75 kHz. The images were acquired with a respiratory gating by using an SAII Model 1030 monitoring & gating system (Smal Animals Instruments, Stony Brook, NY, USA). Fat suppression is achieved by a saturation pulse of 1050 Hz. T2 maps are constructed off-line using Image-J 1.50b (National Institutes of Health), and data are fitted to a three parameter exponential decay equation ($S = A + S_0 \exp(-TE/T2)$, where S represents signal intensity, A, S_0 and T2 are the fitting parameters), achieved by the "exponential decay with offset" equation of the fitting routine of ImageJ. Signal intensities in T2WI and T2 maps are quantified manually in selected ROIs using ImageJ. Afterward, mice are euthanized and organs are preserved for histological analyses.

2.5.9 Prussian blue stain

Liver samples from the mice subjected to MRI were embedded in an optimal cutting temperature (OCT) compound and kept at −80 °C until sliced in 8 μm sections with a cryostat. After rehydration, the sections were stained with a Prussian blue iron stain kit (Polysciences Inc, USA) following the manufacturer's protocol. Images are acquired after dehydration with a transmitted light microscope (Leica, Germany).

2.5.10 *In vitro* and *in vivo* toxicity evaluation of the NCs

The toxicity of the NCs on human brain endothelial cells (hCMEC/D3) and CD34+ endothelial cells[18, 19] is assessed by performing a viability assay with 3-(4-5-dimethylthiazol-2-yl)-2,5-diphenyl tetrazolium bromide (MTT). For the hCMEC/D3 cells, 2×10^4 viable cells were distributed on a 24-well plate in 400 µL Endothelial Growth Media (EGM2 from Lonza with 2% fetal bovine serum and half the amount of the growth factors included in the kit) whereas 5×10^3 viable CD34+ endothelial cells were seeded on a 96-well plate in complete media. Both cell types were incubated for 24 h at 37 °C and 5% of CO_2. After this period, culture supernatants were substituted with basal cell culture media (serum-free medium) containing increasing doses of NCs at concentrations of 25 µg/mL, 50 µg/mL, and 100 µg/mL (n = 3, triplicate). The MTT assay was performed after 48 h of incubation, and the absorbance of the resulting formazan crystals diluted in DMSO was determined at 540 nm. Cell viability is referred to as the percentage of viability compared with the control conditions (without NC).

Body weights of mice were monitored periodically at 0 d, 1 d, 5 d, 8 d, 11 d and 13 d after i.v. injection of NCs in 150 µL of saline at a dose of 0.84 mg Fe per kg (n = 5), where the vehicle group received 150 µL of saline (n = 5) and the naïve group without treatment served as control (n = 3). At the end of 13 days blood samples are collected and liver/pancreas toxicity based on specific enzyme levels in plasma is analyzed in all groups: alanine aminotransferase (ALT), alkaline phosphatase (ALK), aspartate aminotransferase (AST) and α -amylase using an Olympus AU5800 clinical chemistry analyzer.

2.6 Chapter references

[1] Y.-w. Jun, Y.-M. Huh, J.-s. Choi, J.-H. Lee, H.-T. Song, S. Kim, S. Kim, S. Yoon, K.-S. Kim, J.-S. Shin, Nanoscale size effect of magnetic nanocrystals and their utilization for cancer diagnosis via magnetic resonance imaging, *Journal of the American Chemical Society* 127(16) (2005) 5732-5733.

[2] R. Gref, M. Lück, P. Quellec, M. Marchand, E. Dellacherie, S. Harnisch, T. Blunk, R. Müller, 'Stealth'corona-core nanoparticles surface modified by polyethylene glycol (PEG): influences of the corona (PEG chain length and surface density) and of the core composition on phagocytic uptake and plasma protein adsorption, *Colloids and Surfaces B: Biointerfaces* 18(3-4) (2000) 301-313.

[3] E. Carenza, O. Jordan, P. Martinez-San Segundo, R. Jiřík, Z. Starčuk Jr, G. Borchard, A. Rosell, A. Roig, Encapsulation of VEGF 165 into magnetic PLGA nanocapsules for potential local delivery and bioactivity in human brain endothelial cells, *Journal of Materials Chemistry B* 3(12) (2015) 2538-2544.

[4] Y. Cui, M. Zhang, F. Zeng, H. Jin, Q. Xu, Y. Huang, Dual-targeting magnetic PLGA nanoparticles for codelivery of paclitaxel and curcumin for brain tumor therapy, ACS *Applied Materials & Interfaces* 8(47) (2016) 32159-32169.

[5] N. Butoescu, C.A. Seemayer, G. Palmer, P.-A. Guerne, C. Gabay, E. Doelker, O. Jordan, Magnetically retainable microparticles for drug delivery to the joint: efficacy studies in an antigen-induced arthritis model in mice, *Arthritis Research & Therapy* 11(3) (2009) R72.

[6] F. Esmaeili, M.H. Ghahremani, B. Esmaeili, M.R. Khoshayand, F. Atyabi, R. Dinarvand, PLGA nanoparticles of different surface properties: preparation and evaluation of their body distribution, *International Journal of Pharmaceutics* 349(1-2) (2008) 249-255.

[7] E. Swider, O. Koshkina, J. Tel, L.J. Cruz, I.J.M. de Vries, M. Srinivas, Customizing poly (lactic-co-glycolic acid) particles for biomedical applications, *Acta Biomaterialia* 73 (2018) 38-51.

[8] S. Schöttler, K. Landfester, V. Mailänder, Controlling the stealth effect of nanocarriers through understanding the protein corona, *Angewandte Chemie International Edition* 55(31) (2016) 8806-8815.

[9] T. Simón-Yarza, F.R. Formiga, E. Tamayo, B. Pelacho, F. Prosper, M.J. Blanco-Prieto, PEGylated-PLGA microparticles containing VEGF for long term drug delivery, *International Journal of Pharmaceutics* 440(1) (2013) 13-18.

[10] Y.-P. Li, Y.-Y. Pei, X.-Y. Zhang, Z.-H. Gu, Z.-H. Zhou, W.-F. Yuan, J.-J. Zhou, J.-H. Zhu, X.-J. Gao, PEGylated PLGA nanoparticles as protein carriers: synthesis, preparation and biodistribution in rats, *Journal of Controlled Release* 71(2) (2001) 203-211.

[11] A. Beletsi, Z. Panagi, K. Avgoustakis, Biodistribution properties of nanoparticles based on mixtures of PLGA with PLGA–PEG diblock copolymers, *International Journal of Pharmaceutics* 298(1) (2005) 233-241.

[12] Z. Panagi, A. Beletsi, G. Evangelatos, E. Livaniou, D. Ithakissios, K. Avgoustakis, Effect of dose on the biodistribution and pharmacokinetics of PLGA and PLGA–mPEG nanoparticles, *International Journal of Pharmaceutics* 221(1-2) (2001) 143-152.

[13] E. Taboada, R. Solanas, E. Rodríguez, R. Weissleder, A. Roig, Supercritical-fluid-assisted one-pot synthesis of biocompatible core (γ-Fe2O3)/shell (SiO2) nanoparticles as high relaxivity T2-contrast agents for magnetic resonance imaging, *Advanced Functional Materials* 19(14) (2009) 2319-2324.

[14] Y.-X.J. Wang, Superparamagnetic iron oxide based MRI contrast agents: Current status of clinical application, *Quantitative Imaging in Medicine and Surgery* 1(1) (2011) 35.

[15] C. Branca, S. Maccarrone, S. Magazu, G. Maisano, S. Bennington, J. Taylor, Tetrahedral order in homologous disaccharide-water mixtures, *The Journal of Chemical Physics* 122(17) (2005) 174513.

[16] Q. Liu, R. Schmidt, B. Teo, P. Karplus, J. Brady, Molecular dynamics studies of the hydration of α, α-trehalose, *Journal of the American Chemical Society* 119(33) (1997) 7851-7862.

[17] E. Carenza, V. Barceló, A. Morancho, J. Montaner, A. Rosell, A. Roig, Rapid synthesis of water-dispersible superparamagnetic iron oxide nanoparticles by a microwave-assisted route for safe labeling of endothelial progenitor cells, *Acta Biomaterialia* 10(8) (2014) 3775-3785.

[18] R. Cecchelli, S. Aday, E. Sevin, C. Almeida, M. Culot, L. Dehouck, C. Coisne, B. Engelhardt, M.-P. Dehouck, L. Ferreira, A stable and reproducible human blood-brain barrier model derived from hematopoietic stem cells, *PloS One* 9(6) (2014).

[19] F. Shimizu, Y. Sano, M.a. Abe, T. Maeda, S. Ohtsuki, T. Terasaki, T. Kanda, Peripheral nerve pericytes modify the blood–nerve barrier function and tight junctional molecules through the secretion of various soluble factors, *Journal of Cellular Physiology* 226(1) (2011) 255-266.

3

Functionalization of the NC formulation with fluorescence imaging modalities

PLGA-based nanocarriers have already been used as drug delivery systems to administer proteins[1, 2], DNA[3], and anticancer drugs[4-6]. Nonetheless, despite their compositional similarities, any novel PLGA-based drug delivery system will require a thorough evaluation to address potential toxicity issues and study its specific pharmacokinetics and pharmacodynamics. Such preclinical *in vitro* and *in vivo* studies, comprising multiple biological characterization phases, could be expedited by endowing the carrier with complementary imaging capacities. For instance, *in vitro* cellular uptake can be easily imaged with fluorescence[7, 8] while radioimaging[9, 10] or NIR fluorescence imaging[4, 11] is well suited for *in vivo* biodistribution studies.

However, the simultaneous incorporation of all these imaging probes into a single nanocarrier unnecessarily increases the complexity of the systemhindering its translation to the clinics. Moreover, any additional component of the theranostic carrier will have an enormous impact on the manufacturing process, production cost and complying with the medical regulations. In this sense, a drug delivery nanocarrier easily adaptable to incorporate one or several imaging moieties in a modular approach can be a smart strategy to guide the carrier alongside its preclinical development while guaranteeing that a simpler formula will be used for the final product. This modular approach and the use of FDA approved materials has been the strategy followed in my work. Note that this approach is suitable only when the inclusion or removal of the imaging probes does not affect the size, shape and main compositional traits of the final carrier. Thus, after each carrier modification to include a specific imaging probe, the monitoring of the morphological characteristics of the NCs will be carried out.

Furthermore, conventional approaches to physically blend the imaging probes within the carrier can lead to incomplete conclusions

or misinterpretations on the carrier's biodistribution[12, 13]. For example, loading two different molecules as probes into the same carrier led to opposite conclusions regarding the kinetics of brain-specific delivery[13]. A growing body of evidence suggests that new methods will be required to monitor nanocarriers' biodistribution avoiding interference of the imaging moieties with the encapsulated drug or the leaching of the imaging probes[13, 14].

In this chapter, I report on the modification of PLGA NCs for multichannel fluorescence imaging demand. I describe the chemical synthetic routes to covalently label the PLGA with biocompatible small molecule fluorophores at different emitting wavelengths (blue, green, red and NIR), and the fabrication of PLGA-SPIONs NCs incorporating these fluorescent molecules for their *in vitro* and *in vivo* optical imaging, as summarized in **Figure 3-1**.

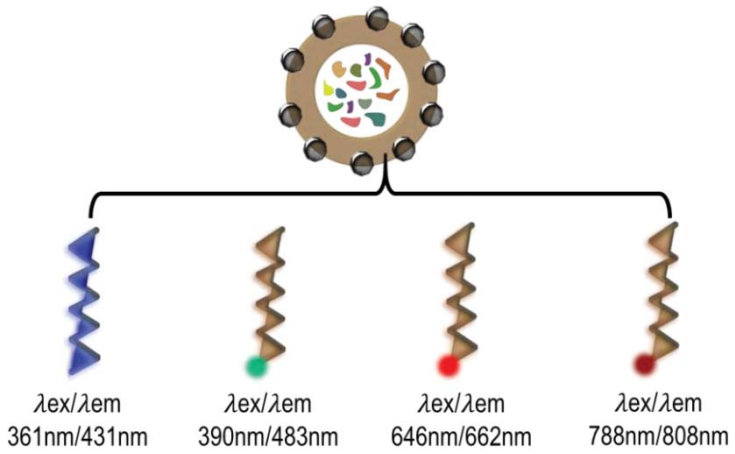

Figure 3-1. Schematic illustration of incorporation of different wavelength emitting fluorophores labeled PLGA (excitation and emission wavelengths of the modified PLGA are shown).

As mentioned, we will show that the inclusion or removal of the imaging probes does not affect the size, shape and main compositional traits of the final carrier, which offers a modular approach to guide the carrier preclinical development while guaranteeing that a simpler formula is used for the final product. In all cases, the imaging moieties are chemically attached to the PLGA shell matrix as opposed to being entrapped in the core of the nanocapsule[7-9, 11]. This approach is advantageous to avoid interferences of the imaging moieties with the cargo in the core[15]. This is especially important for delicate payloads such as proteins, enzymes or microRNAs.

3.1 NCs functionalized with blue fluorescence

3.1.1 PLGA-BPLP polymer

To date, large efforts have been devoted to conjugating PLGA with semiconducting quantum dots and organic dyes to create photoluminescent PLGA nanocarriers[16-18]. However, the inevitable photobleaching and low dye-to-polymer labeling ratios of organic dyes and the innate toxicity of quantum dots prevent their practical use *in vivo*[19, 20]. Recently, a series of biodegradable photoluminescent (PL) polyesters (BPLPs) with inherently photoluminescent and PLGA-BPLP copolymers were developed with excellent biocompatibility, tunable luminescence, degradation rates, and good thermal and mechanical properties, thus expanding the biomedical applications of PLGA in optical imaging[21, 22]. BPLPs are degradable oligomers that can be synthesized from biocompatible monomers, including citric acid, aliphatic diols, and various amino acids via a convenient and cost-effective polycondensation reaction. BPLPs presents some advantages over the traditional fluorescent organic dyes and quantum dots due to their cytocompatibility, minimal chronic inflammatory responses, controlled degradability, and excellent fluorescence properties[21].

In this work, I selected L-cysteine as the amino acid monomer and introduce it into the polyester structure that is made of monomers of citric acid and aliphatic 1,8-octanediol, since previously reported BPLP from this starting amino acid exhibited the highest quantum yield (62.3%)[21]. The fluorophore structure of BPLP has been determined as a fused ring structure (5-oxo-3,5-dihydro-thiazolopyridine-3,7-dicarboxylic acid, TPA) as previously reported[23]. In the synthesis described here, I first obtain the BPLP with a weight-average molecular weight (Mw) of 1044 g/mol determined by MALDI-TOF-MS (Section 3.6.1), then the BPLP oligomer was used as a macroinitiator to react with L-lactide and glycolide *via* a ring-opening polymerization to produce PLGA-BPLP[22]. The as-synthesized PLGA-BPLP (75:25):1 with molar ratios equal to 75:25 for L-lactide to glycolide and equal to 1:100 for BPLP to total L-lactide and glycolide were reported to have desirable glass transition temperature (Tg, 32.5 °C), mechanical properties, fluorescence properties, and degradation rate[22]. We have here proved that the 75:25 formulation is also suitable for the fabrication of NCs by the double emulsion method when compared to

the PLGA-BPLP (50:50):1 one, as shown in the following section.

ATR-FTIR spectra of the as-synthesized BPLP and the PLGA-BPLP copolymer confirm their chemical structures and the successful synthesis (**Figure 3-2**). For the BPLP, strong absorptions from the molecular backbone of the polyester are observed i.e., peaks at 1044 cm^{-1}, 1176 cm^{-1}, and 1716 cm^{-1} are attributed to the C=O stretch, C–O asymmetrical, and symmetrical stretches of the ester bond, respectively, the peaks at 2930 cm^{-1} and 2856 cm^{-1} are attributed to the C-H stretches of alkane from 1,8-octanediol and the band near 3467 cm^{-1} is from the −OH. NH bending of the secondary amide at 1527 cm^{-1} and −SH at 2575 cm^{-1} confirm that L-cysteine is chemically bound to the poly(diol citrate) chain. The shoulder band near 1635 cm^{-1} is attributed to the C=O stretching of the tertiary amide from the TPA ring. For the PLGA-BPLP copolymer, the bands and shapes are coincident with the ones of commercial PLGA, for instance, bands at 1084 cm^{-1}, 1165cm^{-1}, and 1747 cm^{-1} from the ester bonds of the PLGA. Note that BPLP is a very small portion of the PLGA-BPLP copolymer and their bands cannot be identified. **Figure 3-2b inset** exhibits the inherent photoluminescence of PLGA-BPLP from BPLP.

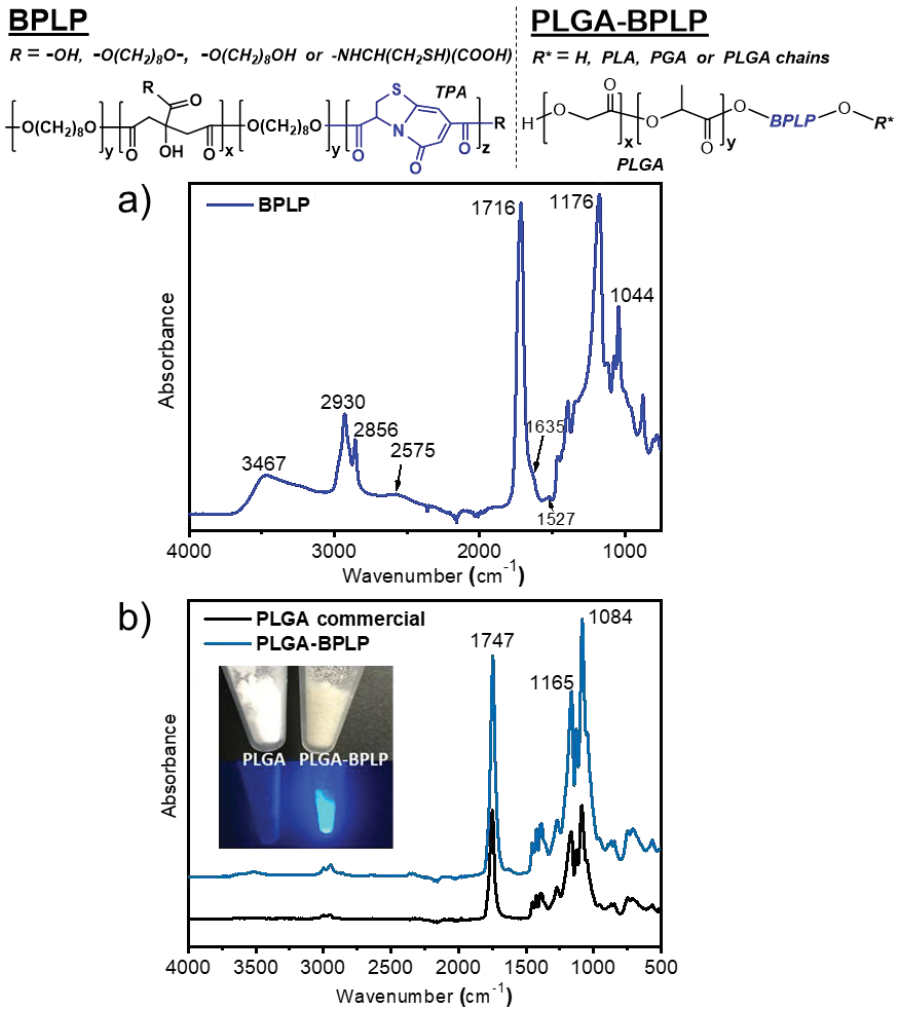

Figure 3-2. ATR-FTIR spectra of the as-synthesized BPLP and the PLGA-BPLP copolymer confirming their chemical structures and the successful synthesis. a) BPLP; b) PLGA-BPLP and commercial PLGA as reference. Inset: fluorescence of PLGA-BPLP observed under a UV lamp.

Next, the fluorescence of the as-synthesized BPLP and PLGA-BPLP is evaluated. The similar excitation and emission spectra depicted in **Figure 3-3** further confirm the inherent photoluminescence of PLGA-BPLP from BPLP.

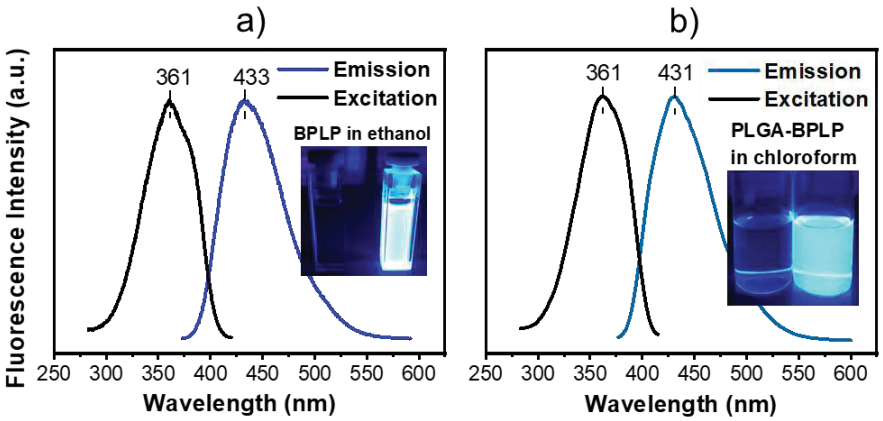

Figure 3-3. a) and b) excitation and emission spectra of the as-synthesized BPLP and PLGA-BPLP. Insets fluorescence of the polymers observed under UV lamp with the solvents as control.

Importantly, the fluorescence intensity of PLGA-BPLP only has a 10% decrease after 10 min of continuous illumination under a confocal microscope at 10% of laser power (0.40 ± 0.01 μW) (**Figure 3-4a**). Considering that the laser power used to observe stained cells is, in general, less than 10%, it is safe to assume that this photoluminescent polymer should exhibit good photostability for *in vitro* cell imaging. The calculated high quantum yields of BPLP (64%) and PLGA-BPLP (33%) from **Figure 3-4b** are consistent with previously reported values[21, 22].

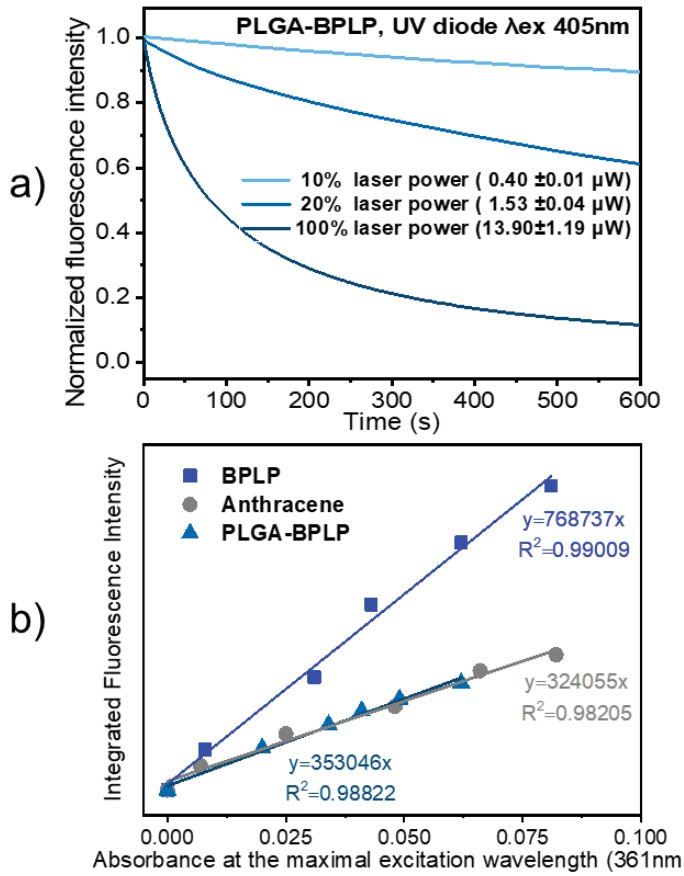

Figure 3-4. a) photostability evaluation of PLGA-BPLP powder under a confocal microscope at different laser power, fluorescence intensity expressed as the percentage vs. time 0; b) integrated fluorescence intensity-absorbance curves of BPLP, PLGA-BPLP and reference anthracene for quantum yield calculations.

The remarkable fluorescence properties shown here endow the PLGA-BPLP copolymer with high potential for the fabrication of functional photoluminescent NCs.

3.1.2 PLGA-BPLP NCs

The as-synthesized PLGA-BPLP is here used to fabricate NCs by the same double emulsion solvent evaporation method described in Section 2.1.2. The blue fluorescence moiety of PLGA-BPLP, together with other moieties, such as PLGA-PEG and SPIONs are incorporated into the organic phase with the unmodified PLGA. As listed in **Table 3-1**, both the non-PEGylated and PEGylated PLGA-BPLP NCs contain ~6 wt% of SPIONs and show

homogeneous size distributions (d.nm ~270) being similar to the non-PEGylated and PEGylated PLGA NCs listed in **Table 2-7** and indicating that the incorporation of fluorophore BPLP does not affect the size nor magnetism of the NCs.

Table 3-1. Summary of the non-PEGylated/PEGylated formulations for the PLGA-BPLP NCs.

NCs Type	Shell Polymers (wt%)			SPIONs Loading (wt%)	M_S (eum/g)	Size (DLS)	
	PLGA	PLGA-BPLP*	PLGA-PEG			d. nm	PdI
NC-5.non-PEGylated	10	90	/	6.0	4.0	272	0.11
NC-6.PEGylated	3	90	7	6.2	4.2	265	0.05

* PLGA-BPLP from initial molar ratios (LA:GA):BPLP = (75:25):1.

The representative morphology of the PLGA-BPLP NCs is shown in **Figure 3-5a**. The incorporation of BPLP did not affect the homogeneous spherical morphology of the NCs. The upper inset in **Figure 3-5a** shows a representative broken NC exposing the hollow core where the protein drug is loaded and the lower inset a TEM image of three NCs with the SPIONs visible as black spots well distributed in the polymer matrix. The magnetic loading up to 6 wt% of SPIONs (M_S 4 emu/g NCs) can be maintained without affecting the NCs morphology (**Figure 3-5b**), indicating the magnetic retention and MRI behavior of the NCs can be maintained as compared to the PLGA NCs.

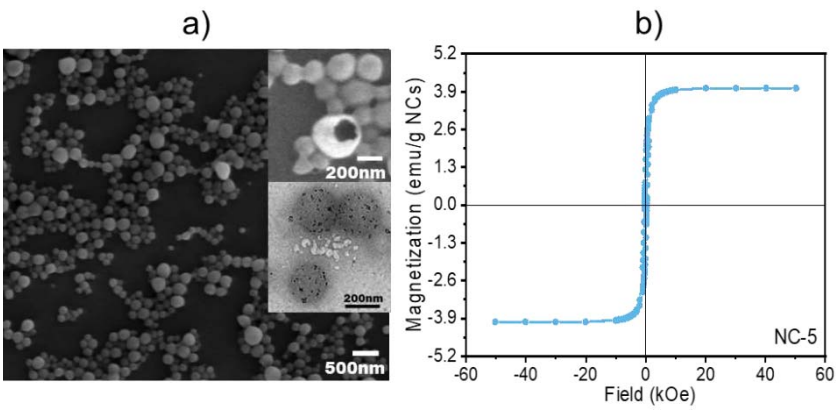

Figure 3-5. a) representative SEM image of lyophilized PLGA-BPLP NCs (NC-5) with the upper inset showing the hollow core of a NC and lower inset a TEM image of three NCs with the SPIONs visible as black spots well distributed in the polymer matrix; b) hysteresis loop (5 K) for the lyophilized NC-5.

Figure 3-6a shows that NC morphology is not affected even when using 100 wt% of PLGA-BPLP (75:25):1. Even though, a formulation with 90 wt% of PLGA-BPLP (75:25):1 is selected (NC-5) to allow for NC PEGylation by the addition of 7 wt% of PLGA-PEG (NC-6) (see **Figure 3-6b**). The PLGA-BPLP (50:50):1 polymer from the initial molar ratio of LA:GA = 50:50 and BPLP:(LA + GA) = 1:100 was proved less suitable for the fabrication of NCs. NCs with homogeneous morphology and narrow size distribution could be attained only up to a maximum of 30 wt% of PLGA-BPLP (50:50):1 (**Figure 3-6c**) and without the possibility of further adding PLGA-PEG, from which a majority of polymers do not form NCs (**Figure 3-6d**). When larger fractions of PLGA-BPLP (50:50):1 are used, for instance with 40 wt%, the size distribution of the NCs is good but many of the NCs are half-broken (**Figure 3-6d**) and with 50 wt%, the monodispersed NCs cannot form (**Figure 3-6f**). These results are in accordance with the higher glass transition temperature and better mechanical properties of PLGA-BPLP (75:25):1 over those of PLGA-BPLP (50:50):1[22]. Note that 7 wt% of PLGA-PEG (3 wt% PEG) was also determined as the maximum amount that can be mixed in the organic phase during the NCs fabrication process, for a larger wt% of PLGA-PEG, the morphology and size of NCs were not maintained, which is consistent with the PEGylation result without integrating BPLP, further confirming that the amphiphilic property of PLGA-PEG does affect the fabrication of PLGA NCs.

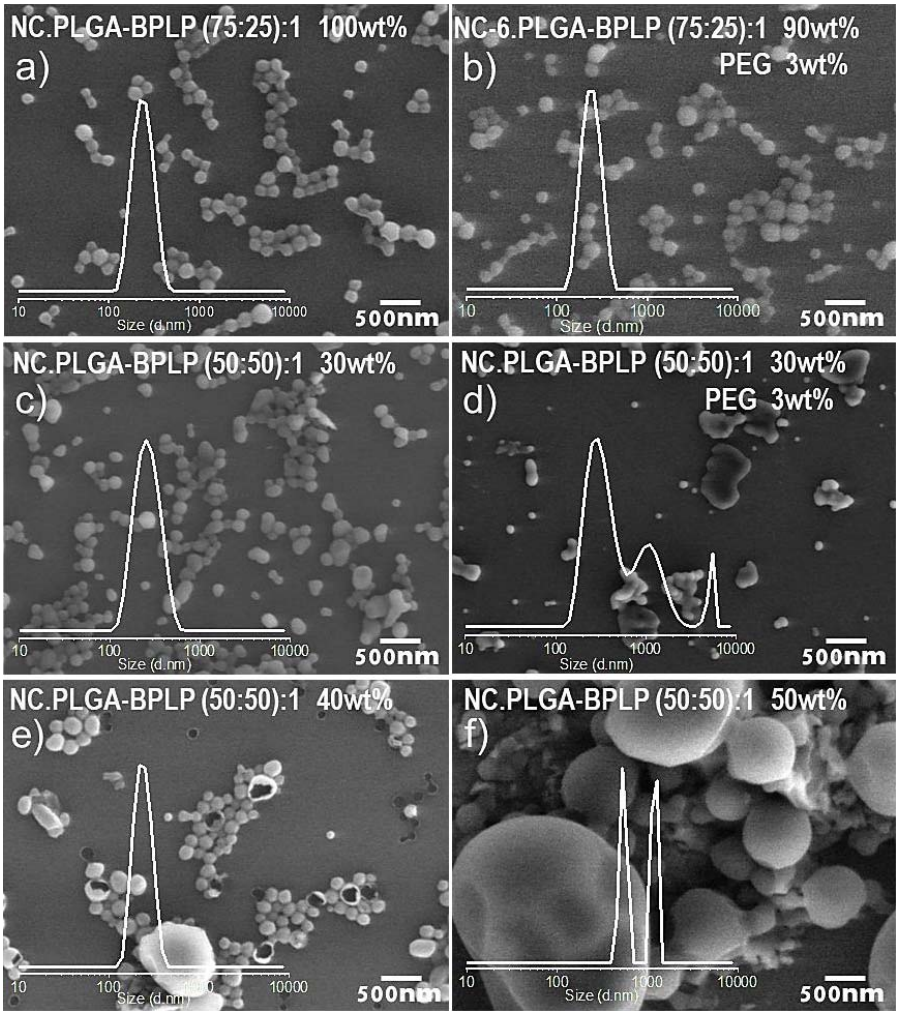

Figure 3-6. SEM images and DLS size distributions (Y-axis: intensity%) of NCs fabricated by different types of PLGA-BPLP.

As expected, the NCs fabricated with a higher fraction of PLGA-BPLP (75:25):1 (NC-5, 90 wt%) show higher fluorescence intensity than the ones obtained with 30 wt% of PLGA-BPLP (50:50):1 at the same concentration (**Figure 3-7**).

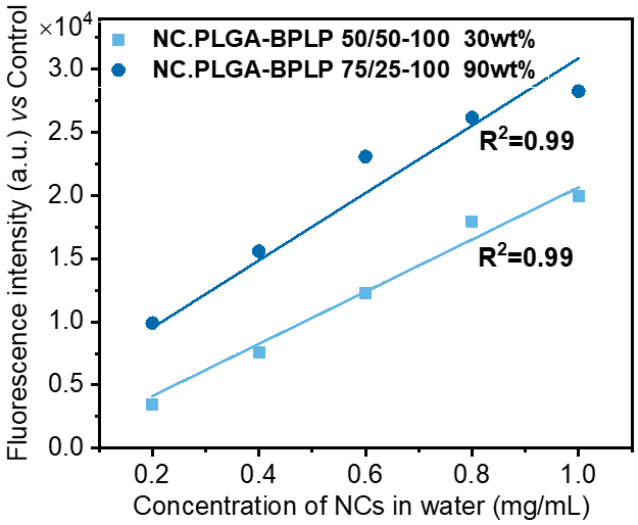

Figure 3-7. Fluorescence intensity of different concentrations of NCs at the maximal emission wavelengths (values have subtracted values of control non-fluorescence NCs).

The successful surface modification with PEG (3 wt%) for PLGA-BPLP NCs (NC-6) is also confirmed by Turbiscan which, as-mentioned, evaluates the flocculation regime of NCs by a protocol similar to that shown in section 2.3 except a physiological concentration of BSA (0.5 mM) is added to the NC PBS suspension. **Figure 3-8a** shows that, as NCs sedimentation progresses, the backscattering signal of the bottom part of the suspension increases from an increasingly higher concentration of NCs, while the signal of the top part decreases. The sedimentation rates of non-PEGylated and PEGylated NCs are compared with or without a physiological concentration of BSA (0.5 mM) in **Figure 3-8b**, as expected the bottom backscattering signal of the PEGylated NCs media increases at a slower rate than the non-PEGylated ones both with and without BSA, which demonstrates a better dispersibility of the NCs due to the surface hydrophilic PEG chains. Note that the sedimentation rates of non-PEGylated and PEGylated NCs both slow down with the physiological concentration of BSA probably due to the interaction of NCs with the dense BSA solution. Additionally, in **Figure 3-8a**, the backscattering signal of the middle part does not vary with time, which means that the NCs are monodispersed at the physiological concentration of BSA and flocculation or coalescence does not occur during the 24 h period. This is consistent with the DLS size distribution results that are shown in **Figure 3-8c**, both non-PEGylated and PEGylated NCs remain monodisperse at the

physiological concentration of BSA for 24 h, which is of great advantage for the *i.v.* administration and *in vivo* blood circulation.

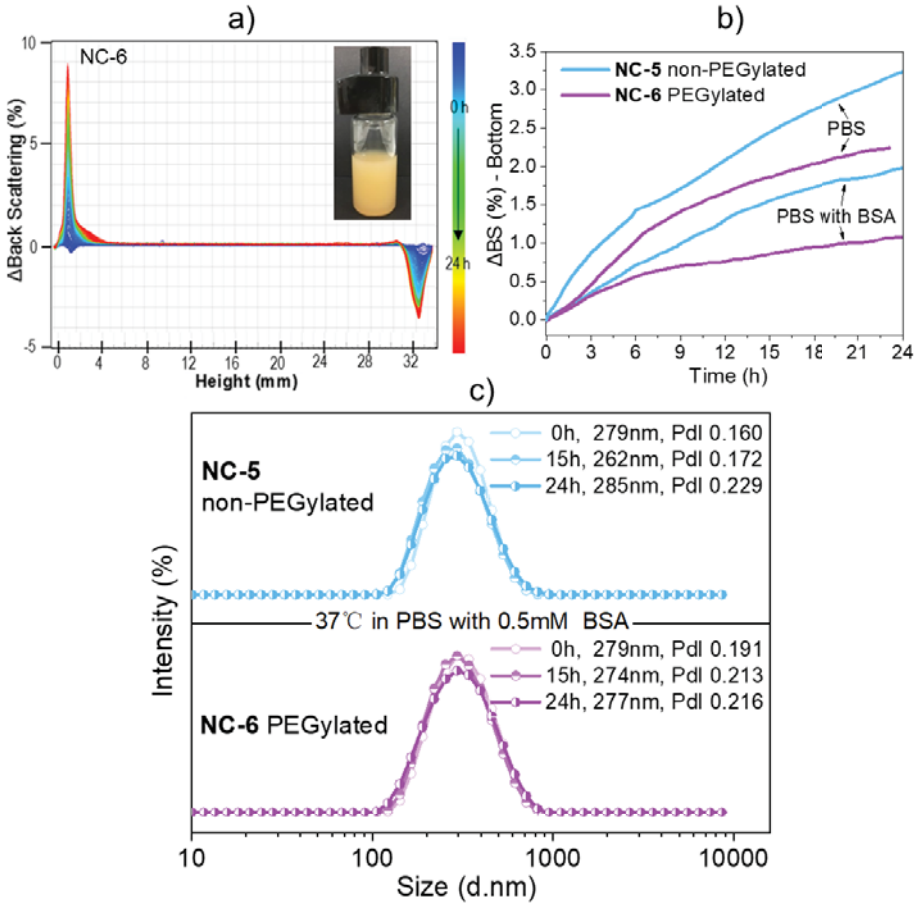

Figure 3-8. a) Backscattering intensity change at several heights of the vial for 24 h of the NC-6 PBS suspension (shown inset) containing 0.5 mM of BSA measured by Turbiscan; b) quantified backscattering intensity change of the bottom part of the vial for 24 h for NC suspension in different media; c) DLS size distributions of NC-5 and NC-6 PBS suspensions with 0.5 mM of BSA for 24 h.

Nanosight was used as an additional technique for the determination of size and the concentration of the NCs (**Figure 3-9**). The results show a similar size distribution as obtained by DLS. From the number concentration of the NCs, we can determine a mean mass of 1.06×10^{-11} mg/NCs.

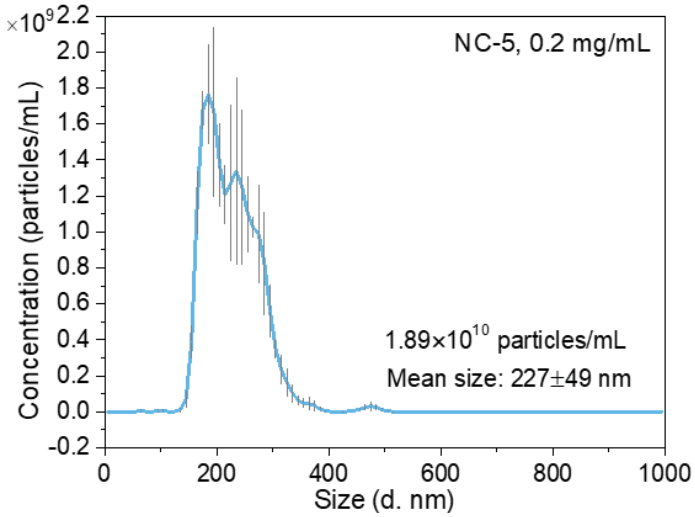

Figure 3-9. Quantitative number concentration and size distribution of the NCs measured by Nanosight (n = 3, mean ± SD with error bar).

Next, fluorescence characteristics of the NCs were evaluated. **Figure 3-10a** depicts the NCs excitation and emission spectra. The spectra are similar to those of the PLGA-BPLP polymer shown in **Figure 3-3a**. Importantly, the incorporation of SPIONs in the polymer matrix does not quench the fluorescence of NCs. Note that a small displacement of the emission peak wavelength is observed for aqueous dispersed fluorescent NCs when compared to the emission peak of the polymer in a chloroform solution (**Figure 3-3a**), which we ascribe to the different interaction of the fluorescent probe with the two solvents. The fluorescence intensities of NCs show a linear dependency on the NCs concentration within a range of 0.1 to 1.0 mg/mL; at higher concentrations, the fluorescence shows a trend towards saturation (**Figure 3-10b**). NCs can be clearly imaged with a fluorescence confocal microscope and they show a very good photostability while using 10% of laser power used for imaging *in vitro* cellular uptake (**Figure 3-10c**).

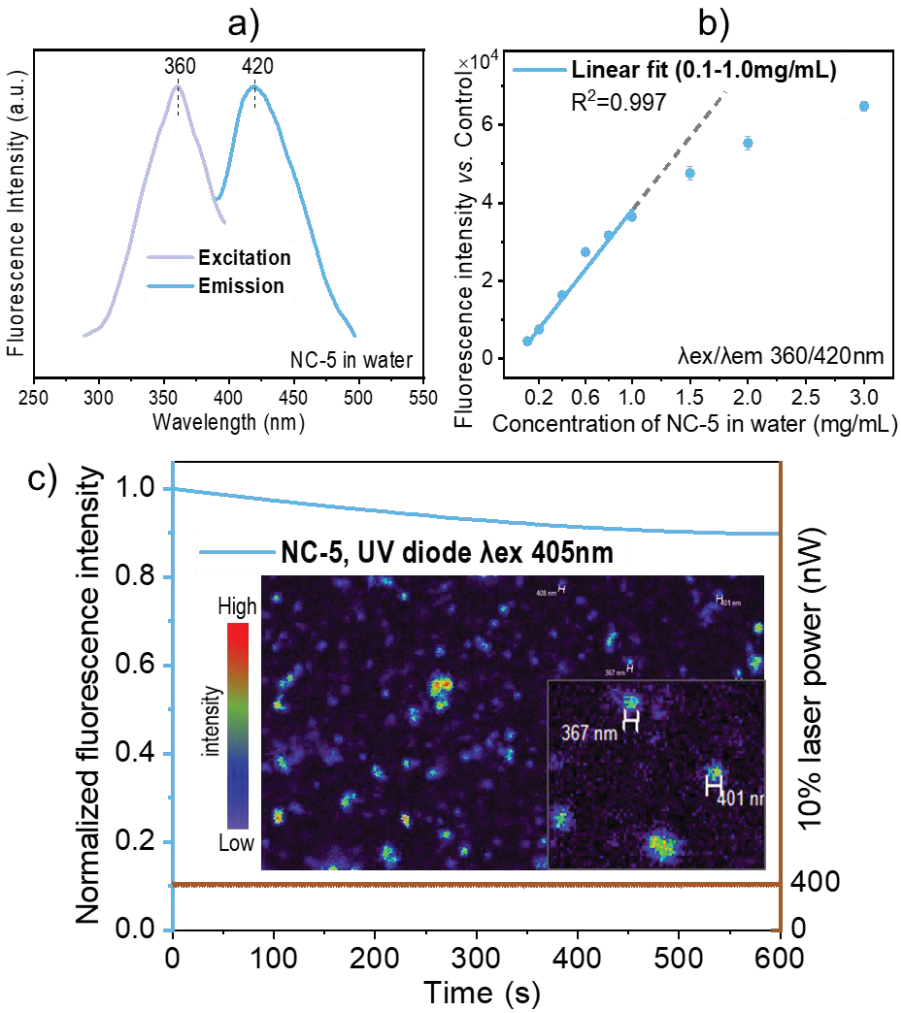

Figure 3-10. a) Excitation and emission spectra of the NCs water suspension; b) fluorescence intensity of 100 µL of different concentrations of NCs (values have subtracted values of control non-fluorescence NCs); c) photostability evaluation of NCs under confocal microscope at 10% laser power, fluorescence intensity expressed as the percentage *vs*. the value at the initial time, inset: NC-5 water suspension observed at 60× lens.

The strategy used here confers intrinsic photoluminescence to the PLGA NCs without introducing any cytotoxic quantum dots or photo-bleaching organic dyes when compared to other more conventional approaches that physically blend imaging probes within the carrier that can lead to misinterpretations on the tracing of the carrier[12, 13], which may greatly expand the applications of this drug carrier.

In Chapter 2 we have established the simple formulation and architecture of the NC.PLGA.SPIONs protein delivery carrier for potential clinical translation with intrinsic MRI modality. Here, by the incorporation of BPLP it has endowed the system with an additional blue fluorescence imaging modality which could benefit the *in vitro* development stage of the PLGA NCs. Besides, the SPIONs loading of this type of NCs, after the incorporation of PLGA-BPLP, was no affected by the modification of the PLGA. An MRI phantom study was conducted to demonstrate the dual-modal imaging performance of these PLGA-BPLP NCs. Phantoms of NCs that were dispersed in agarose gel at various concentrations are prepared (**Figure 3-11a**). Spin-spin relaxation time (T2) maps clearly exhibit signal decay in a concentration dependent manner. The calculated transverse relaxivity (r2) values at 7 Tesla of both non-PEGylated NC-5 (263 $mM^{-1}s^{-1}$) and PEGylated NC-6 (237 $mM^{-1}s^{-1}$) are similar as those seen in **Figure 3-11b**, as expected, further demonstrating the similar loading and distribution of SPIONs in the polymer shell matrix for both systems. And MRI/fluorescence dual-modal imaging is successfully achieved with different imaging moieties co-existing in the PLGA shell.

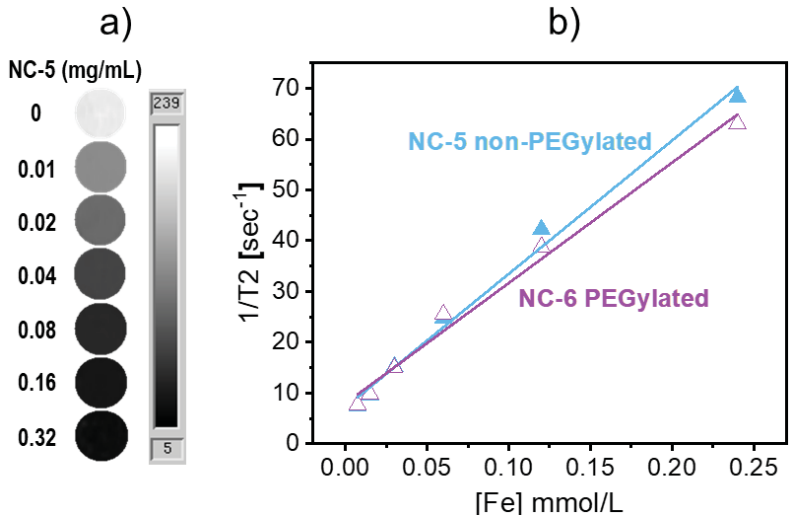

Figure 3-11. a) T2 maps of a series of concentrations of NCs in agarose phantoms; b) r2 relaxivity evaluation for the NCs.

The fluorescence capacity of the NCs is then applied to observe the cellular uptake. NCs are incorporated by brain endothelial cells after several hours in culture, as seen in **Figure 3-12a**, with cytoplasmic localization of the NCs in perinuclear structures compatible with

Golgi bodies and endosomes. This subcellular localization is confirmed by Z-stack images (**Figure 3-12b**).

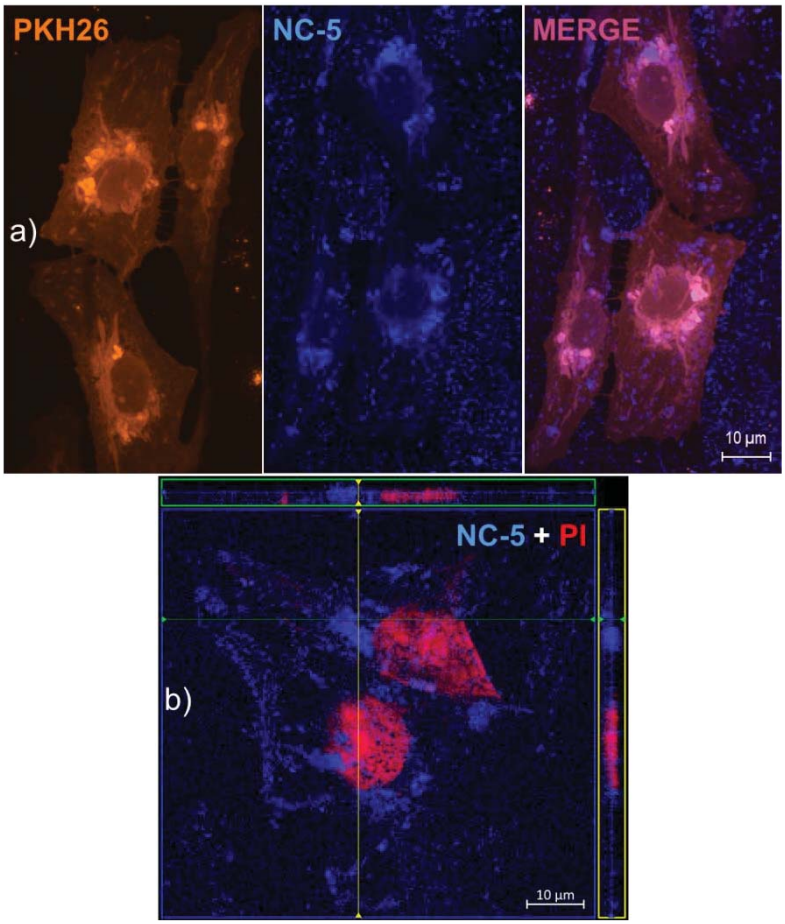

Figure 3-12. NCs uptake in human brain endothelial cells observed with a confocal microscope. a) Representative images of hCEMC/d3 cells stained with membrane dye PHK26 (orange) and exposed to 50 µg/mL of NC-5 (Blue) for 24 h (60× lens); b) Orthogonal view of a Z-stack of Propidium Iodide (PI) stained cells (showing the cell nuclei in red) and the blue NCs.

Importantly, this cellular uptake is biocompatible for endothelial cells, as the main exposed cells during NCs circulation in blood vessels, since viability tests do not show signs of cell toxicity at a wide range of NCs concentrations up to 500 µg/mL (**Figure 3-13**) and 48 h exposure. Note that the concentration of PLGA-BPLP NCs tested here is much higher than that of PLGA NCs (100 µg/mL, **Figure 2-18**), which has improved our knowledge that our NC formulation is biocompatible at a wide range of concentrations despite the existence of the fluorophore. Only an extremely high dose (1000 µg/mL) with

noticeable occupying space difficulties for cell culturing shows a significant reduction in cell viability and number.

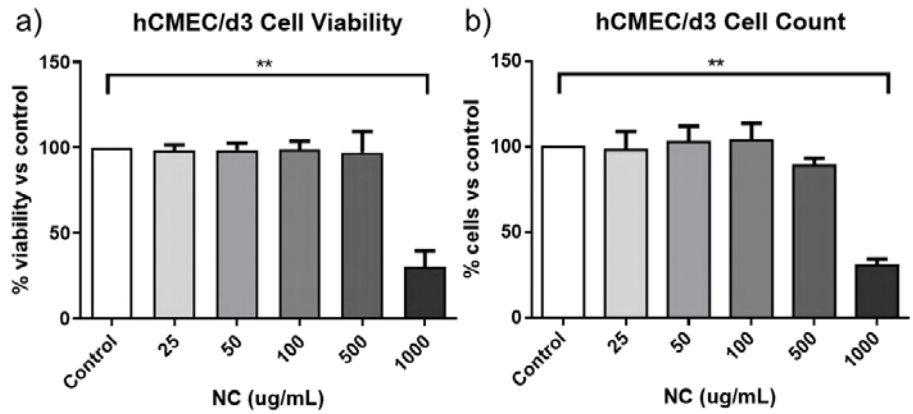

Figure 3-13. Cytotoxicity of NCs on human brain endothelial cells. a) and b) hCEMC/d3 cells are treated for 48 h with different concentrations of NC-5 and cell viability is determined with WST-8 reduction assay or tripsinized and counted in a Neubauer chamber (n = 3–4, values represent mean ± SEM, ** $P < 0.01$).

3.2 NCs functionalized with green fluorescence

3.2.1 PLGA-Fluram polymer

Currently, there are two major classes of biodegradable fluorescent polymers.[24] One class shows intrinsic photoluminescence by carrying integral fluorescent chemical structures in their polymer backbone, such as green fluorescent protein (GFP) and the PLGA-BPLP showed in Section 3.1.1. The other class is achieved by a combination of non-fluorescent biodegradable polymers and fluorescent agents such as organic dyes and quantum dots.

In this section, I show the route and advantages of conjugating a fluram derived green fluorophore to the end of PLGA molecular chain. Fluram is a non-fluorescent compound that reacts quickly and almost quantitatively with primary amines ($R\text{-}NH_2$) to form a fluorescent derivative, which emits strong fluorescence at around 480 nm when excited at 390 nm[25]. We design a route to combine this fluorescent derivative with PLGA through which the carboxylic acid-terminated commercial PLGA (PLGA-COOH) is firstly aminated to PLGA-NH_2 and then the fluram is anchored to the -NH_2 end. The conjugation of fluram to the –NH_2 end of PLGA for fluorescence application is very advantageous considering that

neither free fluram itself nor its hydrolysis product show fluorescence, the fluorescence signal detected can be attributed to the PLGA conjugate which forms NCs, thus having low background.

Figure 3-15 shows the schematic representation for terminal amination and fluram functionalization of the PLGA. Firstly, the carboxylic acid end group of PLGA is activated with N,N'-dicyclohexylcarbodiimide (DCC) and N-hydroxysuccinimide (NHS) to conjugate ethylenediamine and form PLGA-NH_2, bearing a free primary amine group in the PLGA end (**Figure 3-15a**). An excess amount of ethylenediamine (6:1 ethylenediamine:PLGA mole ratio) is used to suppress the coupling reaction of PLGA–PLGA that could occur due to the homo-functional crosslinker ethylenediamine. Subsequently, the fluram with amine-reactive group could be integrated at the end of the PLGA molecule to form a green fluorescent derivative (**Figure 3-15b**).

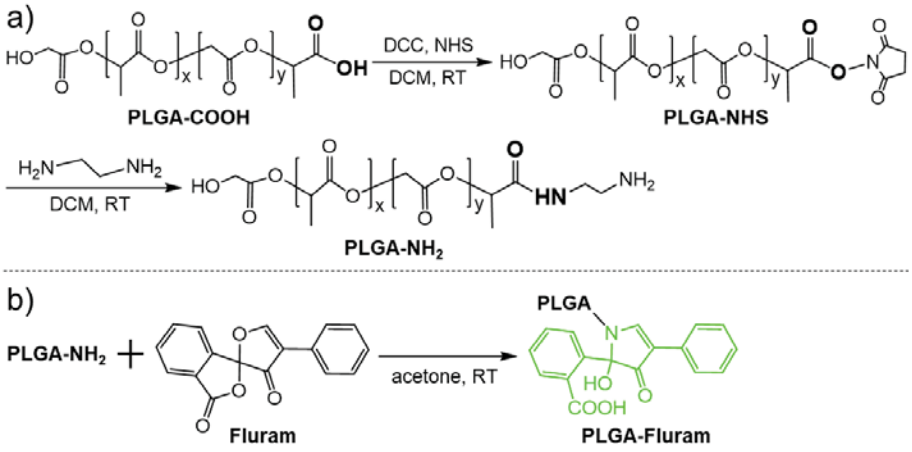

Figure 3-15. Synthetic schemes of terminal modification and functionalization of the commercial PLGA-COOH to obtain PLGA-Fluram.

ATR-FTIR spectra of the commercial PLGA-COOH and the PLGA-NH_2 product confirm their similar chemical structure and successful modification (Figure 3-16). Both of PLGA and PLGA-NH_2 show the typical bands at 1084 cm^{-1}, 1165cm^{-1} and 1747 cm^{-1} attributed to the C=O stretch and C-O asymmetrical and symmetrical stretches of the ester chain of the PLGA, and the C-H stretch bands of the alkane near 2951 cm^{-1}. The bands and shapes similarities of the two spectra imply that the main molecular chain of PLGA is not affected by the modification. Some new peaks appear in the spectrum of PLGA-NH_2, a band at 1542 cm^{-1} associated with the

NH bending of the secondary amide II, at 1683 cm^{-1} associated to the C=O stretching of the secondary amide I, at 3529 cm^{-1} and 3403 cm^{-1} shown in the inset attributed to the asymmetrical and symmetrical stretches of -NH_2. These correlation absorption bands successfully demonstrate the formation of a secondary amide at the -COOH terminal of PLGA with one -NH_2 group of ethylenediamine, meanwhile the -NH_2 group on the other side of ethylenediamine serves as the terminal functional group of PLGA chain.

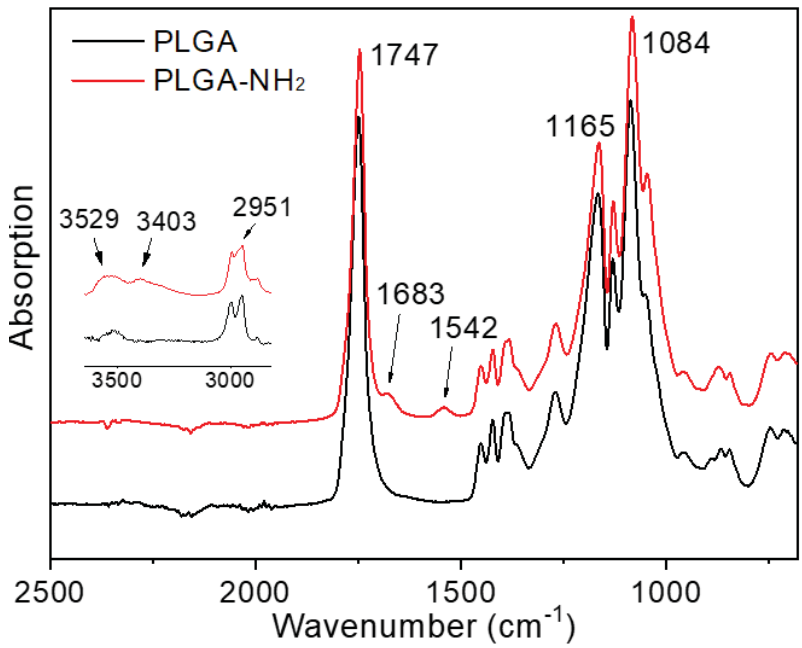

Figure 3-16. ATR-FTIR spectra of commercial PLGA and modified PLGA-NH_2 product confirming their similar chemical structures and the successful modification. Inset is the magnified spectra of the 3500-3000 cm^{-1} range.

The reaction efficiency of PLGA-COOH to PLGA-NH_2 is quantified by measuring the absorbance of the product at 390 nm after reaction with an excess amount of fluram (**Figure 3-17b**). The absorbance is converted to the amount of –NH_2 groups in the product by comparing with a standard absorbance/-NH_2 concentration calibration curve constructed from different concentrations of ethylenediamine reacted with fluram under the same conditions (**Figure 3-17a**). A reaction efficiency of 86% of PLGA-COOH to PLGA-NH_2 is estimated, which means that the molar fraction of pure PLGA-NH_2 in the product is 86%.

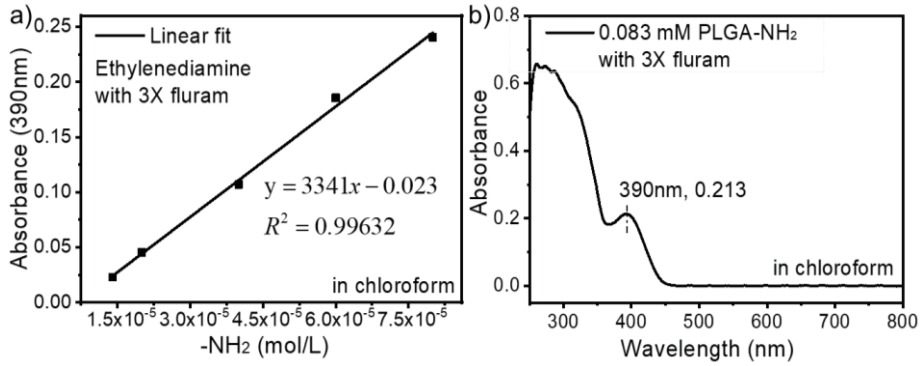

Figure 3-17. a) Absorbance-concentration calibration curve of ethylenediamine (expressed as the concentration of $-NH_2$) at the maximal absorbance wavelength (390nm) after reaction with an excess amount of fluram; b) Absorption curve of 0.083 mM of PLGA-NH_2 product after reaction with an excess amount of fluram.

The formation of PLGA-Fluram conjugate is characterized by the occurrence of an absorption peak of the fluorophore at 390 nm in the UV-Vis spectrum, and this characteristic peak is not observed either in PLGA-NH_2 or in fluram (**Figure 3-18a**). This is consistent with the fluorescent images of the corresponding polymer solutions as seen in **Figure 3-19** in which only PLGA-Fluram shows green fluorescence under the UV lamp. Note that the disappearance of the 309 nm absorption band of fluram in the PLGA-Fluram product (**Figure 3-18a**) indicates that the purification process removes the vast majority of free fluram. The fluorescence of the obtained PLGA-Fluram is evaluated and the excitation and emission spectra are depicted in **Figure 3-18b**. Importantly, the fluorescence intensity of PLGA-Fluram decreases only slightly (<5%) after continuous UV excitation at the maximum excitation wavelength for 3 h, thus exhibiting a photostability just slightly lower (2%) than rhodamine-B, a widely used commercial fluorescent dye (**Figure 3-18c**). Note that the calculated quantum yield of PLGA-Fluram (18%) from (Figure 3-18d) is much higher than the values reported for fluorescent proteins such as green fluorescent protein (GFP) (7.3%) and its blue variants (7.9%)[26], and similar to other polymeric fluorescent materials such as poly(amido amine)[27, 28]. The remarkable fluorescence properties of PLGA-Fluram shown here offer us the option to fabricate NCs with green fluorescence for *in vitro* tracking studies.

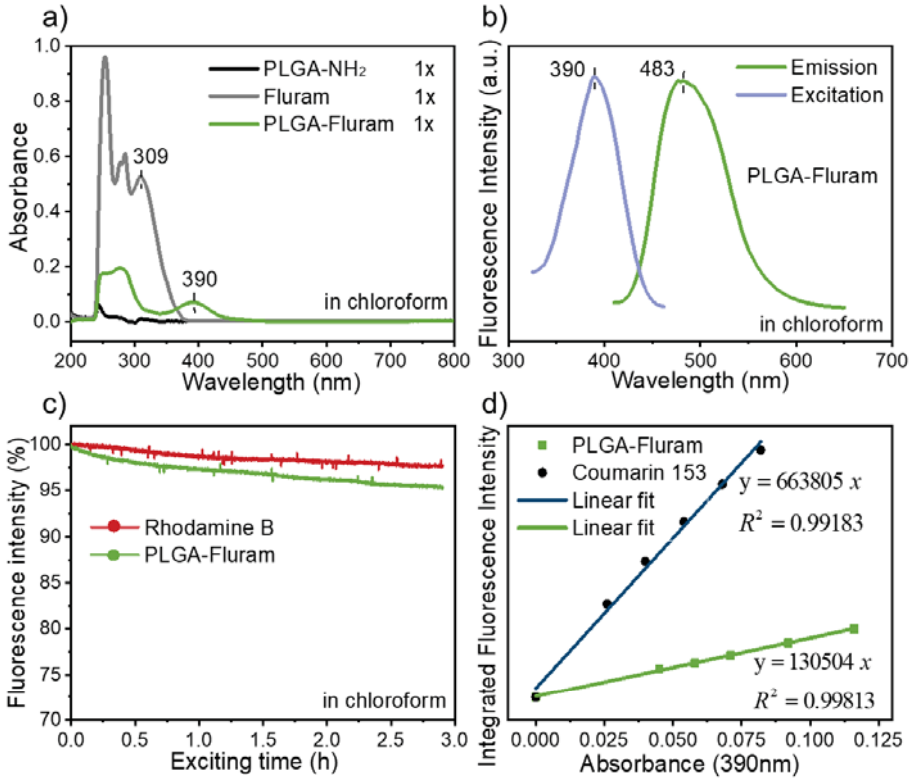

Figure 3-18. a) UV-Vis absorption spectra of PLGA/Fluram samples; b) excitation and emission spectra of PLGA-Fluram; c) photostability evaluation of PLGA-Fluram and control dye rhodamine B, fluorescence intensity expressed as the percentage vs. time 0; d) fluorescence intensity-absorbance curves of PLGA-Fluram and reference Coumarin 153 for quantum yield measurements.

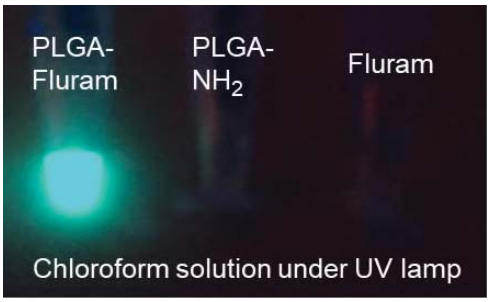

Figure 3-19. The corresponding polymer solutions under UV lamp. Only PLGA-Fluram shows green fluorescence.

3.2.2 PLGA-Fluram NCs

PLGA-Fluram is then used to fabricate NCs by the double emulsion solvent evaporation method described in Section 2.1.2. The

PLGA-Fluram, PLGA-PEG and SPIONs were incorporated into the organic phase together with unmodified PLGA. As listed in **Table 3-2**, both the non-PEGylated and PEGylated PLGA-Fluram NCs contain ~6 wt% of SPIONs and maintain size distributions very similar to the other NCs presented so far (d.nm ~275), indicating that the incorporation of the fluorophore does not affect the size nor magnetism of the NCs.

Table 3-2. Summary of the non-PEGylated/PEGylated formulations for the PLGA-Fluram NCs.

NCs Type	Shell Polymers (wt%)			SPIONs Loading (wt%)	M_S (eum/g)	Size (DLS)	
	PLGA	PLGA-Fluram	PLGA-PEG			d. nm	PdI
NC-7.non-PEGylated	50	50	/	6.2	4.7	260	0.15
NC-8.PEGylated	43	50	7	5.7	4.1	290	0.13

The representative SEM morphologies of the PLGA-Fluram NCs are shown in **Figure 3-20**.

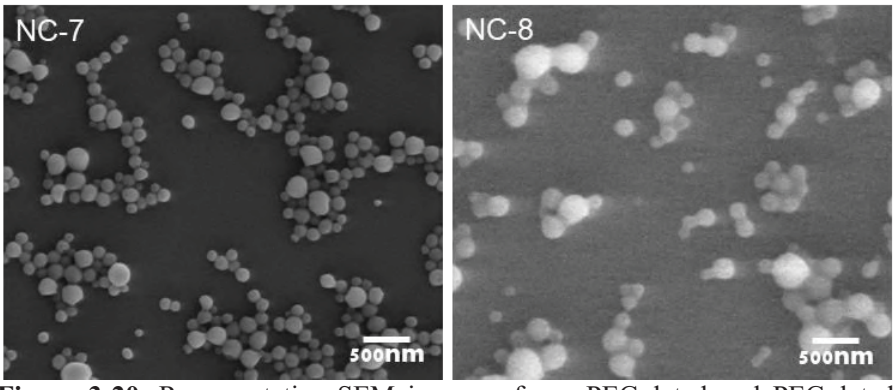

Figure 3-20. Representative SEM images of non-PEGylated and PEGylated PLGA-Fluram NCs after lyophilization.

The above presented fluorescent NCs are fabricated by pre-synthesized PLGA-Fluram polymer (synthesis route illustrated in **Figure 3-21a**). In addition to this route, I also tried to firstly fabricate the surface amino-enriched NCs using PLGA-NH_2 polymer and then use fluram to label the NCs in water suspension (route illustrated in **Figure 3-21b**).

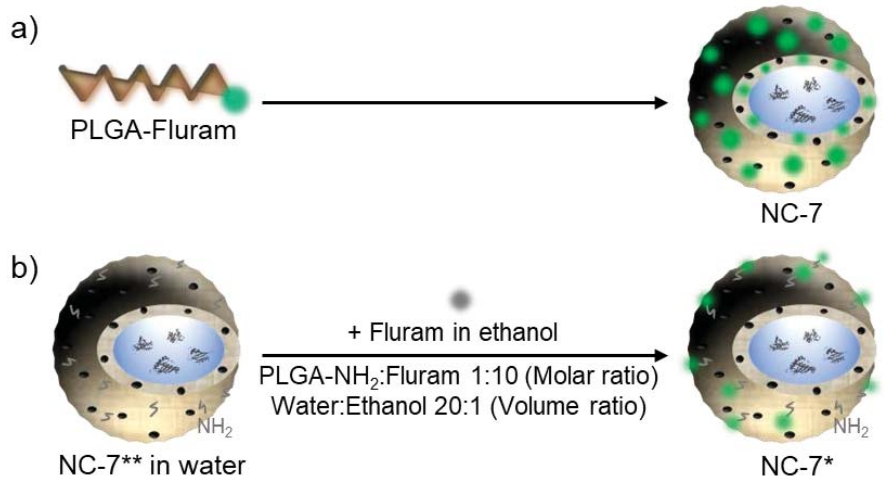

Figure 3-21. Schematic illustration of the two routes to fabricate PLGA-Fluram NCs. a) NC-7 uses pre-synthesized PLGA-Fluram polymer; b) NC-7* obtained by forming NCs, NC-7**, containing amino (-NH_2) functionalities at the surface and subsequently labelling them with fluram in water suspension.

The route schematized in **Figure 3-21b** is intended to show the feasibility of labeling surface amino-enriched NCs (SEM in **Figure 3-22**) in aqueous media.

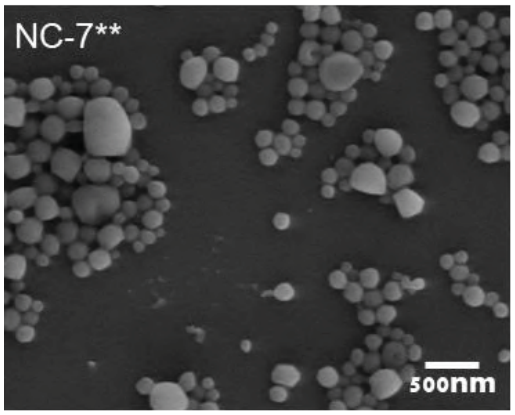

Figure 3-22. Representative SEM image of the lyophilized surface amino-enriched NCs (NC-7**, PLGA:PLGA-NH_2 50:50).

Figure 3-23 depicts the excitation and emission spectra of the fluorescent NCs obtained by the two routes. The spectra are similar to those of the PLGA-Fluram polymer shown in **Figure 3-18b**. However, the fluorescence intensity of NC-7 is much higher than that of NC-7* at the same concentration, indicating the availability of amino groups on NCs (NC-7**) is low in aqueous media. Consequently, the route using pre-synthesized fluorescent polymer to

fabricate NCs (**Figure 3-21a**) is preferable since can make full use of the amino groups and produce an inherent and more intense fluorescent shell. It also provides us with the opportunity for the conjugation of other amino-reactive functional moieties on the NCs.

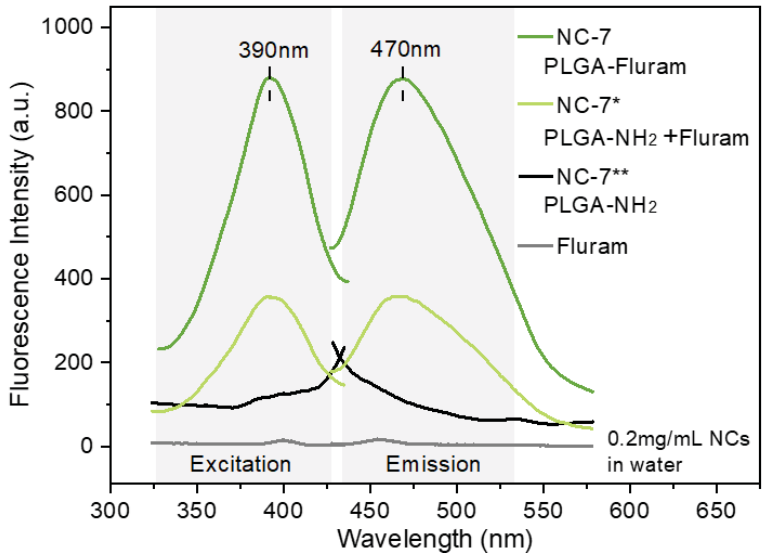

Figure 3-23. Excitation and emission spectra of PLGA-Fluram NCs obtained through the two routes shown in Figure 3-21 (NC-7 and NC-7*). Fluram and NC-7** without fluram labeling used as references. Fluorescence intensity of the NCs at same concentration (0.2 mg/mL) is compared.

The fluorescence intensity of the PLGA-Fluram NCs (NC-7) shows a linear dependency on the NCs concentration (**Figure 3-24a**). NCs can be imaged with a fluorescence confocal microscope and they show a very good photostability while using 10% of laser power (401 nW), the fluorescence intensity decreases by only 13% after 10 min of continuous illumination with a time interval of 1 s (**Figure 3-24b**). Considering the laser power applied to observe stained cells is generally less than 10%, our fluorescent NCs would exhibit good photostability under *in vitro* conditions.

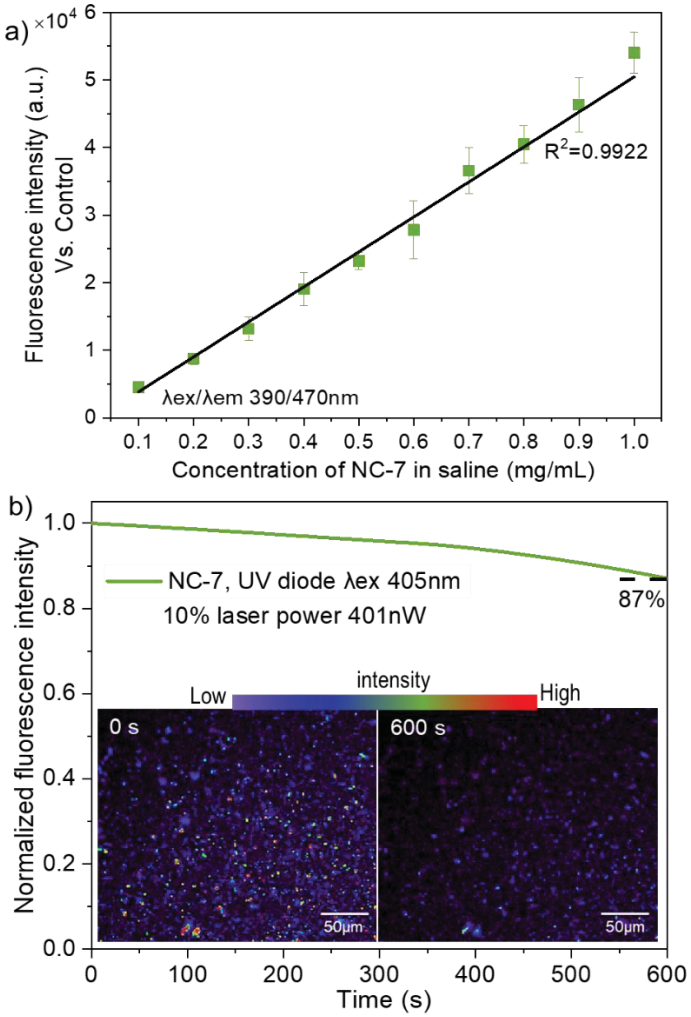

Figure 3-24. a) Fluorescence intensity of different concentrations of PLGA-Fluram NCs (NC-7) in 100 µL of saline measured by microplate reader (values have subtracted values of control non-fluorescence NCs, n = 3, mean ± SEM); b) Photostability evaluation of PLGA-Fluram NCs under confocal microscope at 10% laser power, fluorescence intensity expressed as the percentage vs. time 0 s. Inset: NC-7 water suspension observed at 60× lens.

3.3 NCs functionalized with red fluorescence

3.3.1 PLGA-Cy5 polymer

Cyanine (Cy) is the non-systematic name of a synthetic dye family belonging to the polymethine group. Cyanine dyes are molecules containing polymethine bridge between two nitrogen atoms with a delocalized charge [29] as seen in the structure in **Figure 3-28**. Due to

their structure, cyanines have outstandingly high extinction coefficients often exceeding 100000 L/mol·cm and can advantageously replace conventional dyes such as fluorescein and rhodamines because they yield brighter and more stable fluorescence. Importantly, absorbance and fluorescence wavelength can be controlled by a choice of polymethine bridge length: longer cyanines possess higher absorbance and emission wavelengths up to the NIR region. Correspondingly Cy3, Cy5 or Cy7 nomenclature is proposed where the number designates the count of the methines. While the side chains bound to the two nitrogen atoms are unspecified, both nitrogens may each be an independent part of a heteroaromatic moiety, such as pyrrole, imidazole, thiazole, pyridine, quinoline, indole, benzothiazole, etc. and can be bound with different functional R groups.

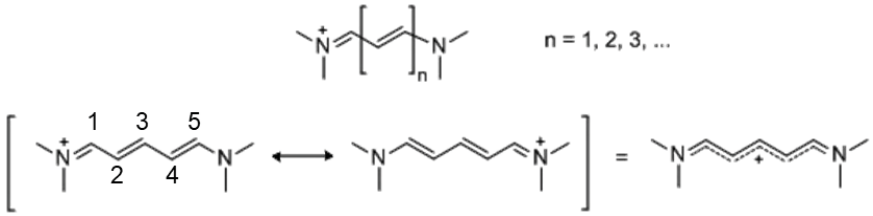

Figure 3-28. Main fluorophore structure of the cyanine dyes and the corresponding nomenclature.

The most popular cyanine dyes for biomedical imaging were introduced by A. Waggoner *et al.* in the early 1990s[29]. They all contain two indolenine rings flanking the polymethine chain exhibiting low non-specific binding to biomolecules and have bright fluorescence owing it to their huge extinction coefficients and good quantum yields. The R groups on either one or both of the nitrogen ends are modified to short aliphatic chains ending in various highly reactive moieties such as NHS esters, maleimides, azides, so that the modified cyanine dyes can be chemically linked to other entities such as nucleic acids or protein molecules for imaging. Here I choose a Cy5 (red emission) NHS ester derivative which is reactive for the labeling of all kinds of amino groups and aim to conjugate it at the amino end of the as-synthesized PLGA-NH_2 to produce red fluorescent PLGA-Cy5, and using this pre-synthesized fluorescent polymer to fabricate NCs, the same route used for the PLGA-Fluram NCs (**Figure 3-21a**, NC-7) which can result in higher fluorescence intensity. The synthetic steps of PLGA-Cy5 are shown in **Figure 3-29**.

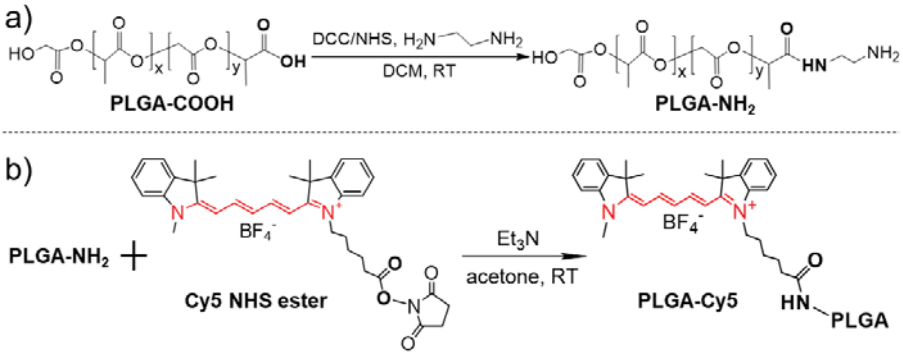

Figure 3-29. Synthetic schemes of terminal modification and functionalization of the commercial PLGA-COOH to obtain PLGA-Cy5.

The successful conjugation of Cy5 to PLGA is characterized by the occurrence of the absorption band of the fluorophore in the absorption spectrum of the purified PLGA-Cy5 product. As seen in **Figure 3-30a** the absorption spectra of PLGA-Cy5 product and Cy5 NHS ester are similar, with the maximal absorbance wavelengths at 655 nm belonging to the Cy5 fluorophore, while this absorption band does not appear in the spectrum of PLGA-NH_2. The reaction efficiency of PLGA-NH_2 to PLGA-Cy5 was quantified by measuring the conjugated amount of Cy5 in the PLGA-Cy5 product. An absorbance of 0.053 (655 nm) which attributes to Cy5 is obtained for PLGA-Cy5 product at the concentration of 7.0×10^{-7} mol/L (**Figure 3-30**a), after comparing with the absorbance-Cy5 concentration standard curve (**Figure 3-30b**) a Cy5 concentration of 5.1×10^{-7} mol/L is calculated for the PLGA-Cy5 product with the concentration of 7.0×10^{-7} mol/L, thus a molar fraction of 73% of pure PLGA-Cy5 in the product is obtained. Considering the fraction of pure PLGA-NH_2 in the reactant is 86%, a conjugation efficiency of 85% of the Cy5 NHS ester to PLGA-NH_2 is determined. This high conjugation efficiency would benefit the fluorescence property of the NCs fabricated.

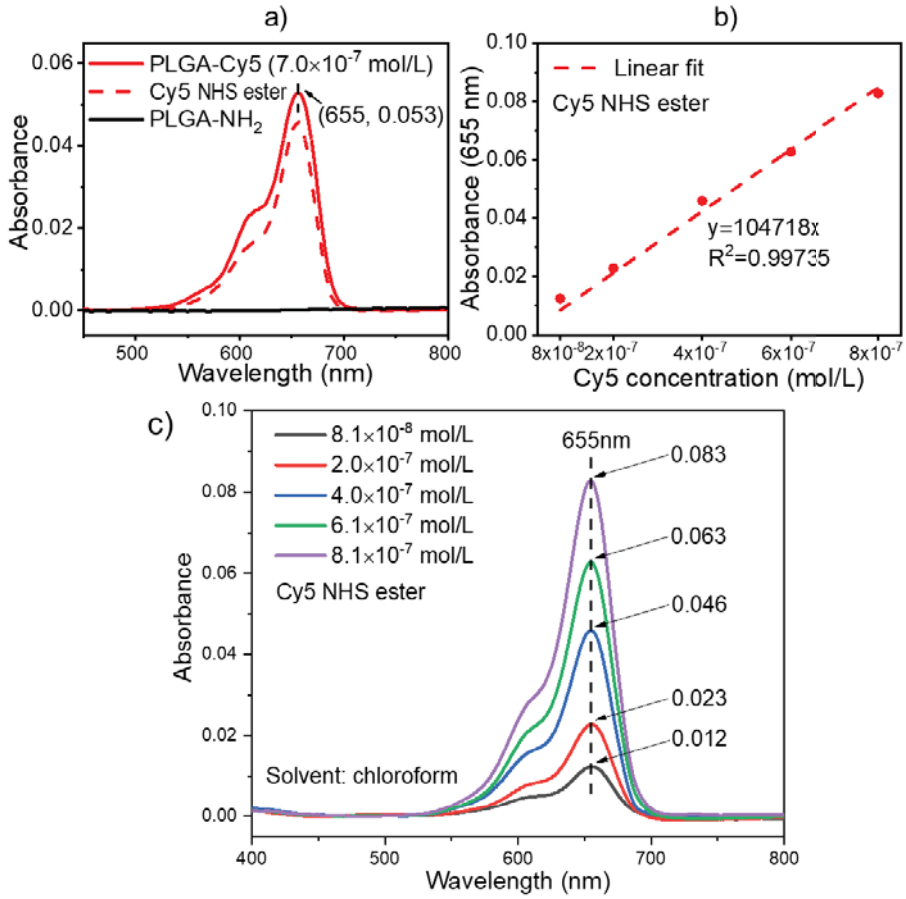

Figure 3-30. a) Absorption spectra of PLGA/Cy5 samples; b) absorbance-concentration calibration curve of Cy5 NHS ester at the maximal absorbance wavelength (655 nm); c) absorption spectra of a series concentrations of Cy5 NHS ester for the plotting of the calibration curve. All spectra are measured in solvent chloroform.

The fluorescence of the obtained PLGA-Cy5 is evaluated and the excitation and emission spectra are depicted in **Figure 3-31**. As expected, the spectra are almost the same when compared to those of the Cy5 NHS ester, indicating the PLGA-Cy5 has fully inherited the fluorescence property from free Cy5.

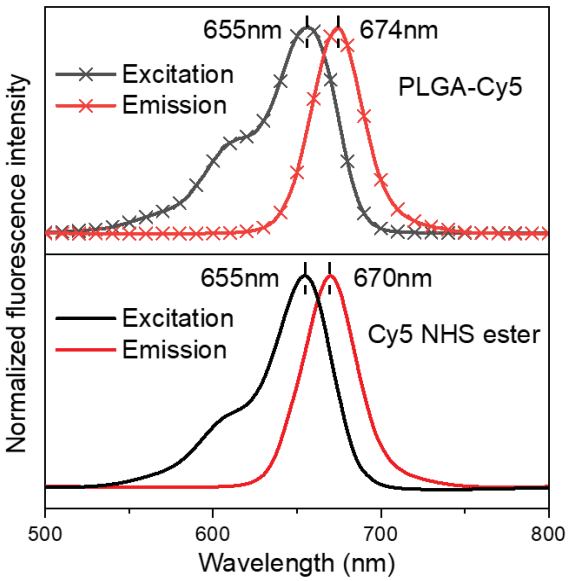

Figure 3-31. Excitation and emission spectra of PLGA-Cy5 (upper panel) and Cy5 NHS ester, measured in solvent chloroform (lower panel) .

3.3.2 PLGA-Cy5 NCs

As-synthesized PLGA-Cy5 is then used to fabricate NCs. Resulting PLGA-Cy5 NCs contain ~6 wt% of SPIONs and maintain homogeneous size distributions (d.nm ~275) as the same as the other types of NCs, indicating the incorporation of this fluorophore does not affect the size nor magnetism of the NCs. Representative SEM morphology of the PLGA-Cy5 NCs is shown in **Figure 3-32**, the incorporation of the fluorophore does not affect the homogeneous spherical morphology of the NCs.

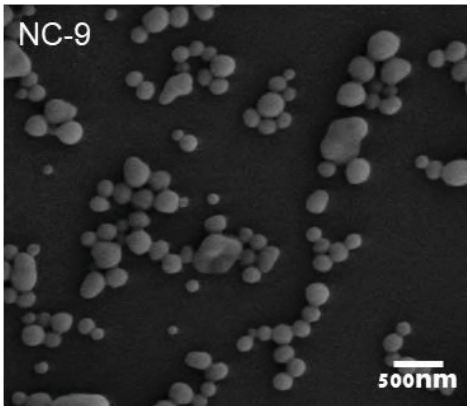

Figure 3-32. Representative SEM image of the lyophilized PLGA-Cy5 NCs.

Figure 3-33a depicts the excitation and emission spectra of the

PLGA-Cy5 NCs. The spectra are similar to those of the PLGA-Cy5 polymer shown in **Figure 3-31**. Small displacements of the spectra are also observed for the aqueous dispersed NCs when compared to the spectra of the polymer in a chloroform solution. It is interesting to note that the NCs containing SPIONs are green in color while those without SPIONs are blue presenting the initial color of the Cy5 dye, as seen in the inset images of **Figure 3-33a**. After measuring the emission spectrum of the NCs without SPIONs (**Figure 3-33a upright**), it is been confirmed that the SPIONs in the polymer matrix do not quench or shift the emission of the NCs even they change the color of the NCs. Red fluorescence of the NCs is observed on a fluorescent microscope as shown in **Figure 3-33b**.

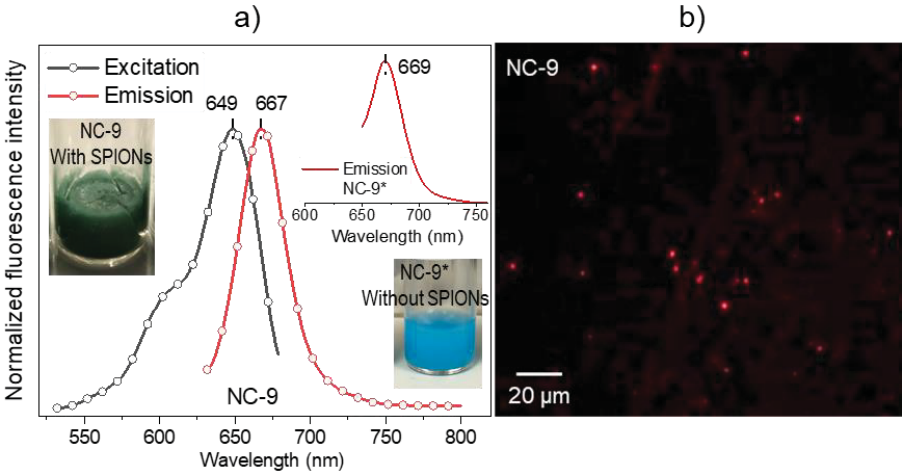

Figure 3-33. a) Excitation and emission spectra of the PLGA-Cy5 NCs (NC-9) in water. The upright curve shows the emission spectrum of the NCs (NC-9*) without SPIONs. Inset: pictures of green lyophilized NC-9 with SPIONs and blue suspension of NC-9* without SPIONs; b) NC-9 water suspension observed under a fluorescent microscope.

The fluorescence capacity of the NCs developed is then applied to observe the *in vitro* cell uptake. For that, macrophage-like cells differentiated from THP-1 cell line were used. As expected cells show low background at this red emission range (**Figure 3-34a**) which does not interfere with cells self-fluorescence as in the case of fluoram. (**Figure 3-26**). Interestingly, after 30 min incubation NC.PLGA-Cy5.SPIONs (NC-9) with a negative surface charge (-23 mV) shows a relatively much lower cellular uptake (**Figure 3-34b**) when compared to positively charged NC-9** (12 mV, **Figure 3-34c**), indicating the surface charge of NPs greatly affects cell-nanoparticle interaction[30, 31].

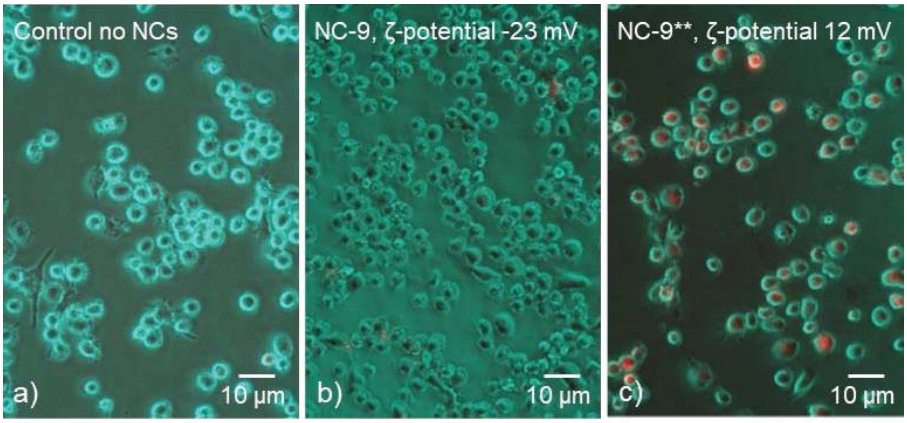

Figure 3-34. Cell uptake (macrophage-like cells differentiated from THP-1 cell line) of PLGA-Cy5 NCs observed by fluorescent microscope. a) Cells in 1mL of PBS without NCs as negative control; b) and c) Cells co-incubated with 0.6 mg/mL of NCs for 30 min: b) NC-9 with negative surface charge; c) NC-9** with positive surface charge fabricated by using 1:1 of PLGA-NH_2 and PLGA-Cy5.

Considering that the final target of the NCs is the ischemic brain, this fluorescent NC.PLGA-Cy5.SPIONs is useful for one of our partners (F. Gosselet, Artois University) to track the interactions of NCs with BBB in an *in vitro* BBB model. For instance, to evaluate the passage of NCs across the BBB, NCs need to be incubated in the *in vitro* BBB model in Ringer-Hepes medium for 3 h. To evaluate NCs endocytosis/uptake, NCs need to be incubated with cells in ECM+5% FCS medium for 24 h. These two studies rely on fluorescence signal visualization and quantification of NCs. With these considerations in mind, I include below a brief study intended to investigate the morphological integrity and fluorescence stability upon NCs incubation in these two media. As seen in **Figure 3-35b**, after incubating in Ringer-Hepes for 3 h, the NCs maintain the spherical morphology and good size distribution, and the fluorescence intensity is still acceptable with a decrease of around 17% (**Figure 3-35e**). Based on this information, we will be able to correlate the detected fluorescence signal with the amount of NCs across the BBB. For NCs incubated in ECM+5% FCS after 24 h, some NCs show holes on the shell (**Figure 3-35c**), fragments of the detached polymer are also observed (**Figure 3-35d**). The fast erosion of NCs in the cell culture media may benefit the release of drugs loaded while the uptake behavior may not change because most of them maintain the monodispersed spherical morphology. Fluorescence is quite stable in ECM+5% FCS medium with only a slight decrease of around 5%

(**Figure 3-35e**) after 24 h, which is good for the quantification of cell uptake.

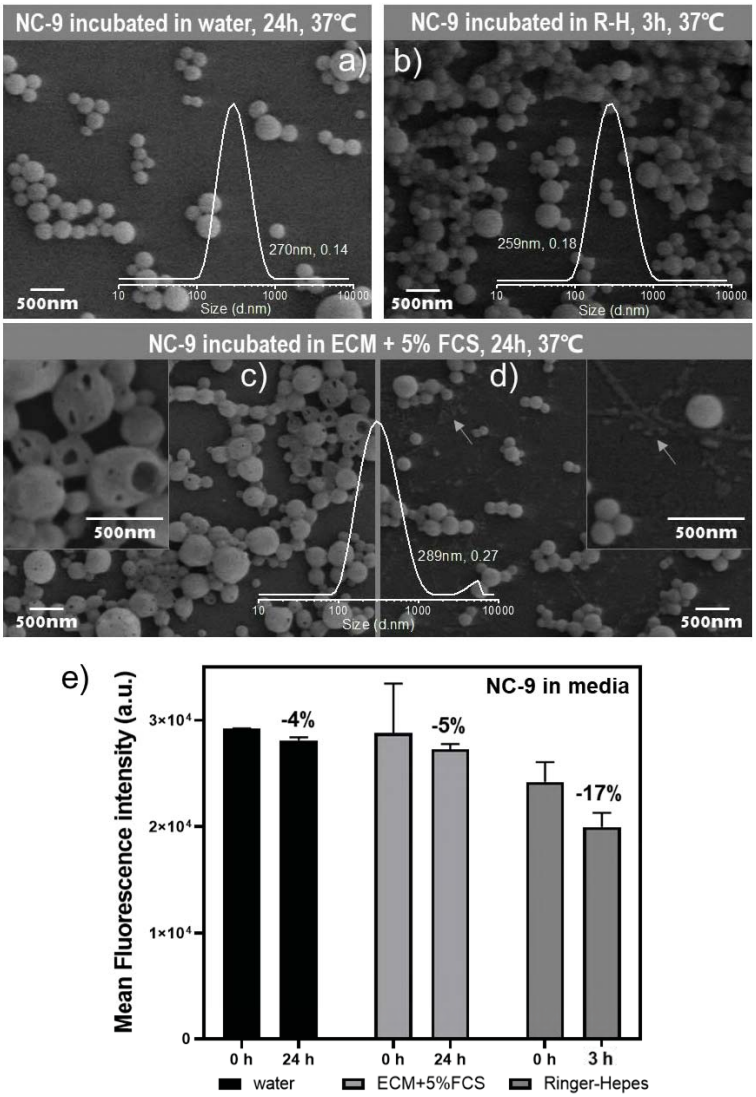

Figure 3-35. a)-d) SEM morphologies and DLS size distributions (d.nm, PdI) of NC.PLGA-Cy5.SPIONs (NC-9) after incubating in different media for several hours; e) The fluorescence intensities of NC-9 in different media before and after incubation, the decrease percentage as compared to time = 0 h is noted. 200 µL of 0.5 mg/mL of NCs in each medium (n=3) is measured by a microplate reader (λex/λem 600/670 nm) and results are expressed as mean ± SEM.

3.4 NCs functionalized with NIR fluorescence

3.4.1 PLGA-Cy7.5 Polymer

In this section Cy7.5 with seven carbon atoms between indolenine groups (long polymethine length) and benzo-fused (noted as suffix .5) is selected, which has the most NIR shifted absorption and emission wavelengths among cyanine dyes. Its absorption spectrum and structure closely resemble those of indocyanine green (ICG) that has been much used as a contrast agent *in vivo*, even in humans, while Cy7.5 possesses better quantum yield than ICG because of a structural modification[32]. In our case, the amine-reactive derivative Cy7.5 NHS ester is used as shown in **Figure 3-36** for the labeling of the as-synthesized PLGA-NH_2. Then the PLGA-Cy7.5 product is used for the fabricating of NCs with NIR radiation, which can readily penetrate tissues and facilitate the *in vivo* preclinical biodistribution study by NIR imaging.

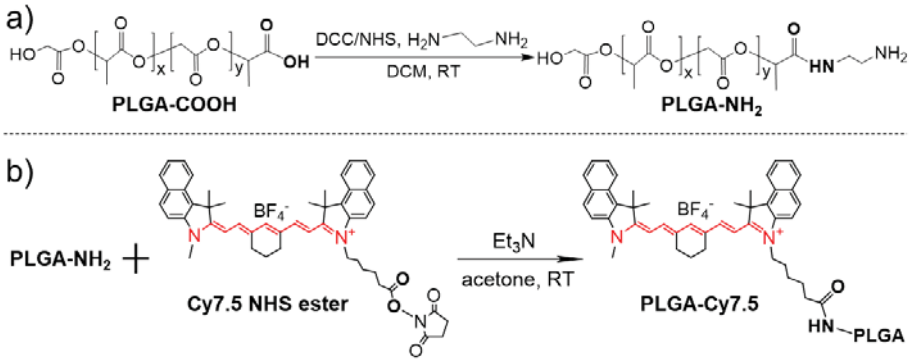

Figure 3-36. Synthetic schemes of terminal modification and functionalization of the commercial PLGA-COOH to obtain PLGA-Cy7.5.

The formation of PLGA-Cy7.5 conjugate is characterized by the occurrence of the absorption band of the fluorophore in the absorption spectrum of the purified PLGA-Cy7.5 product. As seen in **Figure 3-37a** the absorption band from Cy7.5 NHS ester appears in the spectra of PLGA-Cy7.5 product, and as control, the absorption spectrum of PLGA-NH_2 does not have this band. The reaction efficiency of PLGA-NH_2 to PLGA-Cy7.5 is quantified by measuring the conjugated amount of Cy7.5 in the PLGA-Cy7.5 product. An absorbance of 0.628 (800 nm) which attributes to Cy7.5 is obtained for PLGA-Cy7.5 product at the concentration of 6.5×10^{-6} mol/L (**Figure 3-37a**), after comparing with the absorbance-Cy5 concentration standard curve (**Figure 3-37b**) a Cy7.5 concentration

of 4.6×10^{-6} mol/L is calculated for the PLGA-Cy5 product with the concentration of 6.5×10^{-6} mol/L, thus a molar fraction of 71% of pure PLGA-Cy7.5 in the product is calculated. Considering the fraction of pure PLGA-NH_2 in the reactant is 86%, a conjugation efficiency of 83% of the Cy7.5 NHS ester to PLGA-NH_2 is calculated. This high conjugation efficiency would benefit the fluorescence property of the NCs fabricated.

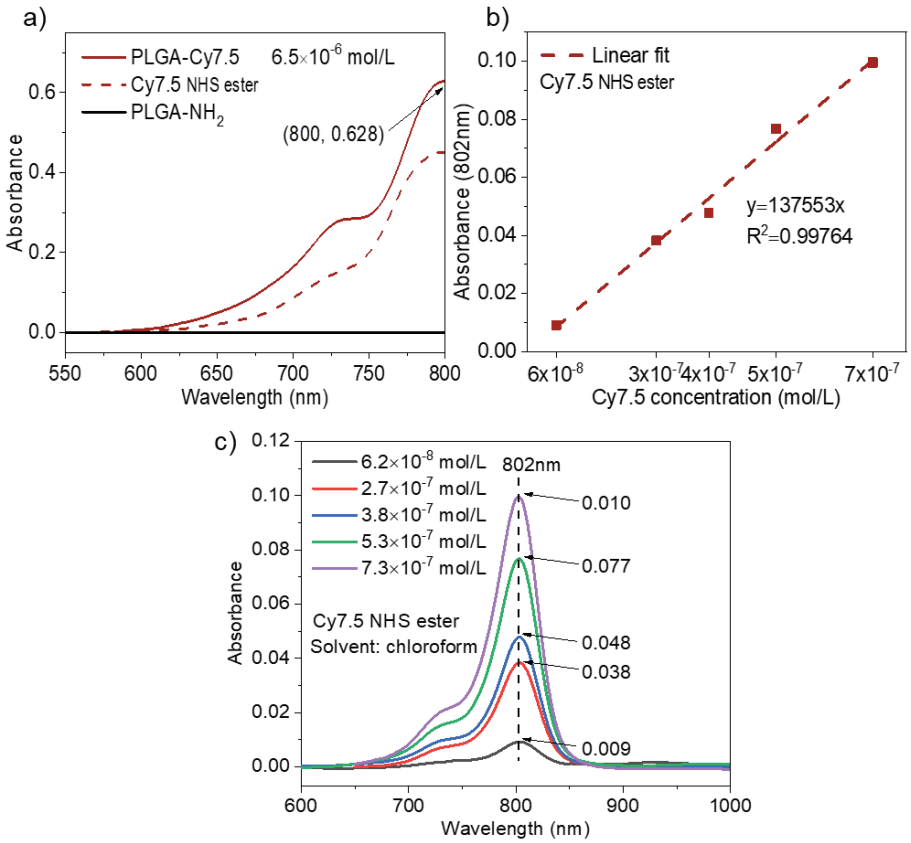

Figure 3-37. a) Absorption spectra of PLGA/Cy7.5 samples; b) absorbance-concentration calibration curve of Cy5 NHS ester at the maximal absorbance wavelength (802 nm); c) absorption spectra of a series concentrations of Cy7.5 NHS ester for the plotting of the calibration curve. All spectra are measured in solvent chloroform.

The fluorescence of the synthesized PLGA-Cy7.5 is well imaged by an *in vivo* imaging system (Xenogen IVIS®) as shown in **Figure 3-38**. Also in this way by comparing the fluorescence intensity with free Cy7.5 a molar fraction of 65% of pure PLGA-Cy7.5 in the product is estimated, and then a conjugation efficiency of 76% of the Cy7.5 NHS ester to PLGA-NH_2 is calculated considering that the fraction of

pure PLGA-NH_2 for reaction is 86%, this efficiency estimated by fluorescence is similar with the value obtained by the absorbance method.

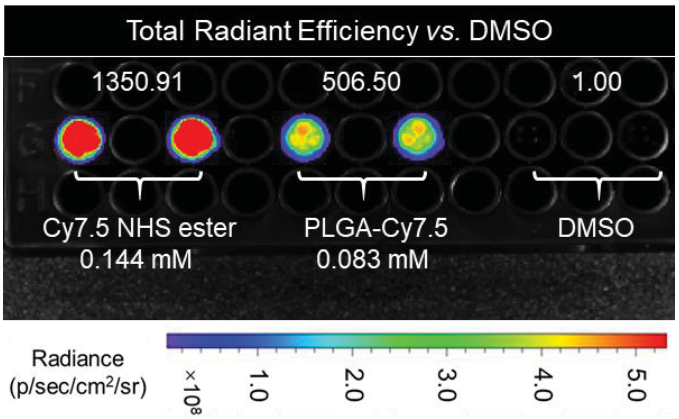

Figure 3-38. Quantification of fluorescence intensity of PLGA-Cy7.5 and free Cy7.5 in DMSO by IVIS at the λex/λem of 710/820 nm. DMSO is used as control.

3.4.2 PLGA-Cy7.5 NCs

The as-synthesized PLGA-Cy7.5 is then used to fabricate NCs. Both the non-PEGylated and PEGylated PLGA-Cy7.5 NCs contain ~6 wt% of SPIONs and maintain homogeneous size distributions (d.nm ~250) as the same as the other types of NCs. Representative SEM morphologies of the PLGA-Cy7.5 NCs are shown in **Figure 3-39**, the incorporation of the fluorophore does not affect the homogeneous spherical morphology of the non-PEGylated/PEGylated NCs, which is expected to not affect the in *vitro*/*in vivo* behavior of the NCs. **Figure 3-40** depicts the excitation and emission spectra of the PLGA-Cy7.5 NCs with the maximal emission at around 820 nm which is in the NIR range as expected.

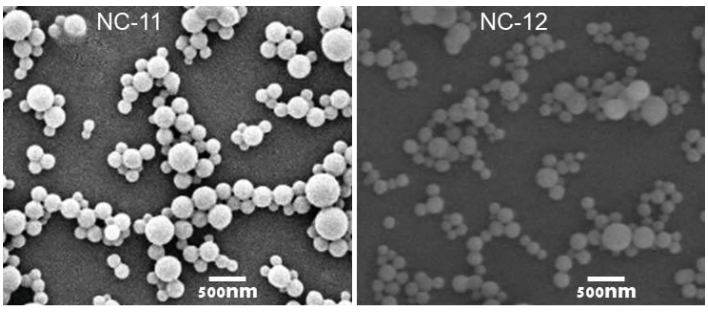

Figure 3-39. Representative SEM images of the lyophilized non-PEGylated (NC-11) and PEGylated (NC-12) NC.PLGA-Cy7.5.SPIONs.

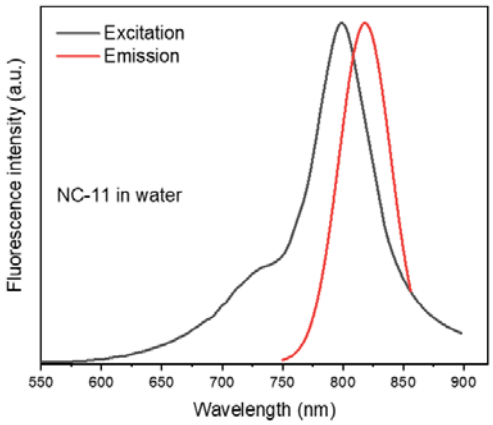

Figure 3-40. Excitation and emission spectra of NC.PLGA-Cy7.5.SPIONs (NC-11) in water.

Before administration of the NCs *in vivo* for biodistribution study, the optimal λex/λem wavelength setting of the imaging equipment for the fluorescence signal acquisition is firstly confirmed. As listed in **Table 3-3**, when the λex is set at 710 nm which is farther to the maximal λem of 820 nm than the λex setting at 745 nm, we obtain the higher fluorescence signal with lower noise, and at the maximal emission wavelength we obtain the best signal. So the setting of λex/λem at 710/820 nm is selected for the imaging of NCs. **Figure 3-41** shows the *in vitro* fluorescence performance of the NCs at this wavelength setting. The fluorescence intensity of NC-11 suspension in saline is linearly dependent on the concentrations of NCs, showing strong fluorescence and no quenching up to a high level of 1 mg/mL. Also, the mouse plasma shows no autofluorescence at this emission range and the NCs are well observed in the plasma (**Figure 3-41 up left inset image**). These make the formulation of PLGA-Cy7.5 NCs feasible for *in vivo* NIRF imaging.

Table 3-3. Quantification of NIRF intensity of NC.PLGA-Cy7.5.SPIONs (NC-11) water suspension at a series concentrations and determination of the optimal λex/λem wavelength with the highest fluorescence signal.

λex/λem (nm)	Replicate	Signal/water ratio of NCs at different concentrations (mg/mL)				
		1	0.75	0.5	0.25	0.1
710/800	1	52	26	25	13	6
	2	53	38	26	13	5
710/820	1	123	55	51	25	12
	2	126	80	52	26	11
710/840	1	86	35	32	15	8
	2	89	51	33	16	7
745/800	1	6	3	3	2	2
	2	6	4	3	2	1
745/820	1	26	12	11	6	3
	2	26	17	12	6	3
745/840	1	27	12	11	5	3
	2	28	17	11	6	3

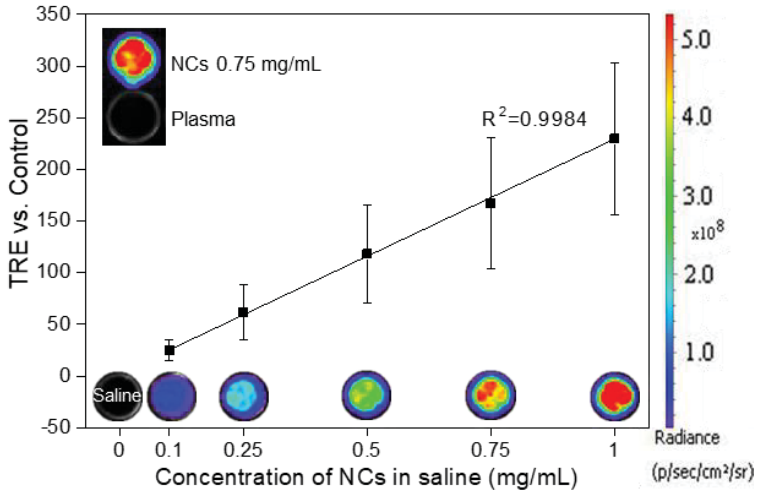

Figure 3-41. Quantitative curve of *in vitro* NIRF intensity of different concentrations of NC.PLGA-Cy7.5.SPIONs (NC-11) vs. control saline (n=3, mean ± SEM) and on the bottom representative images of NCs in the well. NIRF image of NCs *ex vivo* in mouse plasma is also shown on the up left, plasma without NCs is also shown as control. The fluorescence intensity is quantified as Total Radiant Efficiency (TRE) measured by IVIS with λex/λem of 710/820 nm.

3.4.3 Biodistribution investigation of the *i.v.* injected NCs by IVIS

Real-time whole-body imaging (**Figure 3-42a**) reveals a dominant abdominal distribution of the NCs with a total radiant efficiency

(TRE) of ~42.40 *vs.* control at 3 h post-injection (p.i.). At the end of the observation, main organs including brain, heart, lungs, liver, spleen, kidneys, and bladder are collected. **Figure 3-42b** shows the *ex vivo* fluorescence of those organs and **Figure 3-42c** shows the quantified result of the biodistribution of the NCs. Dominant abdominal signal is observed in accordance with the liver, spleen and lung accumulation and matching with the data acquired with MRI (Section 2.2.1). However, significant accumulation in the targeted brain area is not observed, indicating that the accumulation in the brain is not occurring after the *i.v.* administration, further efforts need to be made as discussed in Section 5.1. Note that we do see the bladder signal during the real-time imaging, this phenomenon is also observed and further discussed in Section 4.2 using more sensitive PET imaging, and we attribute the bladder signal to the detached polymer fragments from the eroded NCs at the early stage post-injection. The unobservable *ex vivo* bladder signal may result from the uncontrolled urination and urine sample collection.

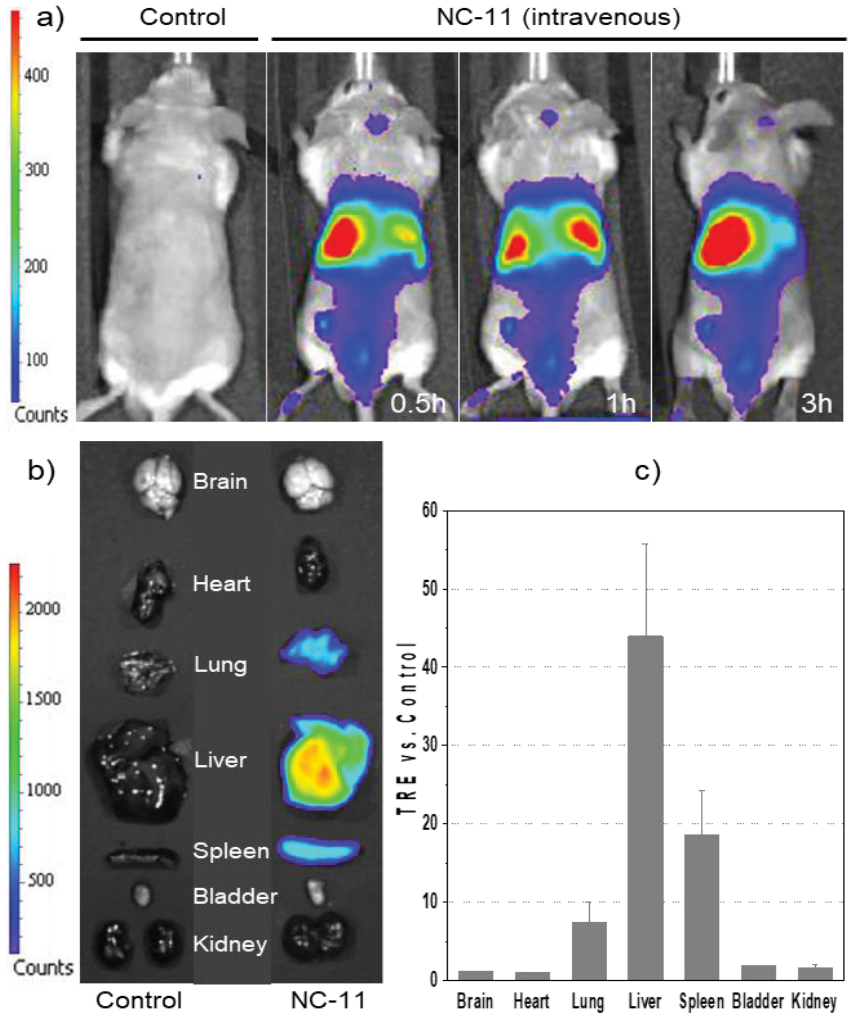

Figure 3-42. a) Representative whole-body *in vivo* NIRF images obtained at different time points after i.v. injection of NCs; b) representative *ex vivo* images of excised organs at the end of the *in vivo* experiment; c) *ex vivo* quantification of the distribution of NCs expressed as the averaged organ TRE *vs.* the control mouse (n = 2, mean ± SEM).

3.5 Chapter summary

I synthesized various fluorescent PLGA polymers with several emitting wavelengths, *e.g.* PLGA-BPLP (max. λex/λem 361/431 nm), PLGA-Fluram (max. λex/λem 390/483 nm), PLGA-Cy5 (max. λex/λem 646/662 nm) and PLGA-Cy7.5 (max. λex/λem 788/808 nm).

I demonstrated that the route to obtained fluorescent polymers to fabricate fluorescent PLGA NCs is a modular approach. Selective inclusion of the imaging probes can be achieved by integrating different types of fluorescent PLGA, and the size, shape and main compositional traits of the NCs are not affected. Also, cationic NCs with positive surface charge (12mV) can be obtained by using PLGA-NH_2.

Good fluorescence imaging performances of the multichannel PLGA NC formulations (blue, green, red and NIR) are demonstrated for *in vitro/in vivo* tracking. Interestingly, the positively charged NCs (12 mV) shows a relatively much higher cellular uptake when compared to negatively charged NCs (-23 mV), indicating the surface charge of NPs greatly affects cell-nanoparticle interaction. Biodistribution by real-time whole-body NIRF imaging showed a dominant liver, spleen and lung accumulation of the *i.v.* administered NCs.

3.6 Annex of Chapter 3

3.6.1 Synthesis of PLGA-BPLP Copolymer

Step one involves the synthesis of a hydroxyl-terminated BPLP pre-polymer. Briefly, citric acid, 1,8-octanediol, and L-cysteine with the molar ratio of 1:1:0.2 (5.76 g, 4.38 g, 0.72 g) are added into a flask of 50 mL with a stirring bar. Under a constant flow of argon, the reactants are melted by heating to 140 °C until a clear solution is formed. The solution was allowed to react at this temperature for 80 min and then stopped before the stirring bar stopped stirring completely in the increasingly viscous solution by adding 25 mL of 1,4-dioxane to dilute the produced prepolymer. The product is purified by dropwise precipitation from the 1,4-dioxane solution in water to remove the unreacted monomers. The final BPLP product is collected by centrifugation and then lyophilized.

In the second step, the PLGA-BPLP copolymer is synthesized while using the BPLP as a macroinitiator to react with L-lactide and glycolide via a ring-opening polymerization that is catalyzed by Tin (II) 2-ethylhexanoate ($Sn(OCt)_2$). Briefly, L-lactide, glycolide and BPLP with the molar ratios of (75:25):1 or (50:50):1 are added into a reaction tube. Subsequently, $Sn(OCt)_2$ (0.1 wt% of L-lactide and glycolide mixture) is added as a solution in dichloromethane which is then evaporated in vacuum. The tube is flushed with argon and capped and subsequently immersed in a 160 °C oil bath for 48 h. The obtained product is dissolved in chloroform and then purified by dropwise precipitation into pure ethanol to remove unreacted raw materials. Finally, the PLGA-BPLP copolymer is recovered by centrifugation and then dried in vacuum at room temperature. All of the PLGA-BPLP mentioned in the text are with molar ratios of (75:25):1, unless specified otherwise.

Matrix-assisted laser desorption/ionization-time of flight mass spectroscopy (MALDI-TOF-MS) is used to determine the average molecular weight (Mw) of BPLP. The BPLP sample is dissolved in ethanol at a concentration of 6 mg/mL and spotted in a MALDI plate with 1, 8, 9-Antracenotriol (Ditranol) at 1:1 and analyzed using a mass spectrometer (Bruker Daltonics Ultraflex TOF/TOF) in reflection mode, the mass spectrum is shown in **Figure 3-43**.

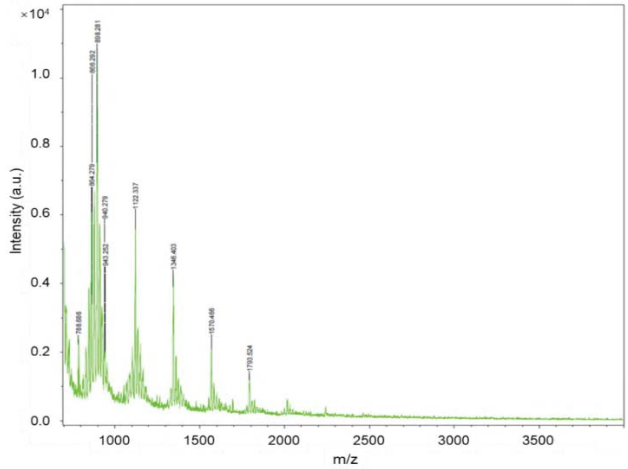

Figure 3-43. Mass spectrum of BPLP measured by MALDI-TOF-MS.

The weight-average molecular weight $\langle M \rangle_w$ is calculated from the mass distribution values of BPLP (Table 3-4), as follows:

$$\langle M \rangle_w = \frac{\sum w_i M_i}{\sum w_i}, \qquad w_i = \frac{M_i I_i}{\sum M_i I_i}$$

where w_i is the weight fraction of a certain molecular weight of BPLP.

Table 3-4. Mass distribution values of BPLP extracted from the mass spectrum.

m/z (M_i)	Intensity (I_i)	m/z (M_i)	Intensity (I_i)
832	1429	923	1882
846	2125	926	2154
848	2588	928	1571
850	1279	943	1515
862	2602	943	1501
864	4534	1103	1251
866	2523	1105	1421
876	1718	1119	2061
878	3430	1121	4249
880	4925	1123	3065
882	2986	1133	1582
884	1469	1136	1995
892	1781	1138	1242
893	1910	1149	1336
894	3552	1152	1360
895	2014	1167	1099
896	3618	1343	1207
897	5052	1345	2975
898	5837	1347	1777
900	2051	1360	1304
906	1475	1375	1074
908	2270	1567	923
910	3119	1569	1342
912	3336	1571	956
914	2530	1584	849
921	1300	1791	627

3.6.2 Synthesis of PLGA-NH_2

To introduce a terminal amine group into PLGA, the carboxylic acid

terminal group of commercial PLGA (lactic:glycolic ratio 50:50, RG502H, Mw 12000) is activated and reacted with ethylenediamine. The carboxylic groups are firstly activated with DCC and NHS. 0.025 mmol of PLGA is dissolved in 8 ml of DCM, and then 0.1 mmol of DCC in 1 mL of DCM and 0.1 mmol of NHS in 0.5 mL of acetone are added into the polymer solution under magnetic stirring. PLGA-NHS activation is achieved after 4 h at room temperature (RT). The coupling reaction is accomplished by adding an excess amount of ethylenediamine (0.15 mmol) in 1 mL of DCM to the solution and further stirring for 2 h. The majority of the insoluble by-product, dicyclohexylurea, is removed by centrifuging the solution after reaction at 9391 rcf for 15 min at 4 °C and discarding the pellet. The supernatant is filtered (0.2 μm PTFE syringe filter) to remove any trace of the insoluble by-product. PLGA-NH_2 is precipitated by slowly pouring the supernatant into an excess amount of ethanol (10-fold), where the un-reacted NHS/DCC/ethylenediamine is separated from PLGA-NH_2 due to their solubility in ethanol. Precipitated PLGA-NH_2 is redissolved in DCM and reprecipitated in ethanol twice for purification. The purified PLGA-NH_2 is dried under vacuum.

3.6.3 Synthesis of PLGA-Fluram

Fluram (fluorescamine) is a non-fluorescent compound that reacts with primary amines (R-NH_2) fast and near completely forming the fluorophore of fluram derivative which emits strong fluorescence at λem = 465 nm (λex = 390 nm). 0.025 mmol of the as-synthesized PLGA-NH_2 and 0.075 mmol of fluram are mixed and dissolved in 4 mL of acetone and the reaction takes place in a dark room after 2 h at RT under magnetic stirring. Then the solution is slowly dropped into an excess amount of ethanol (10-fold) to precipitate the product PLGA-Fluram. The PLGA-Fluram is collected by centrifugation, redissolved in acetone and reprecipitated in ethanol twice for purification. The purified PLGA-Fluram is dried under vacuum.

3.6.4 Synthesis of PLGA-Cy5

Red fluorophore cyanine 5 is introduced at the end of PLGA-NH_2 by forming an amide bond between the PLGA terminal amine group and amine-reactive Cy5 NHS ester (Lumiprobe GmbH, Hannover, Germany). 0.025 mmol of the as-synthesized PLGA-NH_2 and 0.05 mmol of Cy5 NHS ester are mixed and dissolved in 4 mL of acetone and 0.05 mmol of Et_3N is added as the catalyst. The reaction takes

place in the dark after 6 h at RT under magnetic stirring. Then the solution is slowly poured into an excess amount of ethanol (10-fold) to precipitate PLGA-Cy5. The product is collected by centrifugation, redissolved in acetone and precipitated in ethanol twice for purification. The purified PLGA-Cy5 is dried under vacuum.

3.6.5 Synthesis of PLGA-Cy7.5

NIR fluorophore cyanine 7.5 is introduced at the end of PLGA-NH_2 by forming an amide bond between the PLGA terminal amine group and amine-reactive Cy7.5 NHS ester (Lumiprobe GmbH, Hannover, Germany). 0.025 mmol of the as-synthesized PLGA-NH_2 and 0.05 mmol of Cy7.5 NHS ester are mixed and dissolved in 4 mL of acetone and 0.05 mmol of Et_3N is added as the catalyst. The reaction takes place in the dark after 6 h at RT under magnetic stirring. Then the solution is slowly poured into an excess amount of ethanol (10-fold) to precipitate PLGA-Cy7.5. The product is collected by centrifugation, redissolved in acetone and precipitated in ethanol twice for purification. The purified PLGA-Cy7.5 is dried under vacuum.

3.6.6 Absorption spectroscopy of the polymers

Attenuated total reflectance-Fourier transform infrared (ATR-FTIR) characterization of the polymers is performed on a Bruker Vertex 70 FTIR spectrometer with a Pike Miracle Single-Bounce diamond crystal plate accessory at room temperature. The FTIR spectra are recorded over a wavelength range of 4000–500 cm^{-1} with a resolution of 4 cm^{-1}. UV-Vis absorbance spectra of the fluorescent polymers are recorded on a Varian Cary-5000 UV-Vis spectrophotometer using a quartz cuvette with an optical path of 1 cm.

3.6.7 Fluorescence properties

Fluorescence spectra of the polymers and NCs are acquired on a spectrofluorometer (LS45, PerkinElmer Inc., Waltham, MA, USA). The excitation and emission slit widths are both set at 10 nm.

The quantum yields of BPLP/PLGA-BPLP/PLGA-Fluram are measured by the Williams' method[21]. Briefly, a series of solutions are prepared with gradient concentrations in the corresponding solvents. Maximal excitation wavelength is determined, which generates the highest emission intensity. The fluorescence emission

spectra are collected for the series of solutions in the 10 mm fluorescence cuvette (**Figure 3-44** and **Figure 3-45**). The integrated fluorescence intensity, which is the area of the fluorescence spectrum, is calculated and then noted. Afterwards, the UV-Vis absorbance spectra are collected with the same solutions and the absorbance at the maximal excitation wavelength within the range of 0.01–0.1 Abs units is noted (**Figure 3-44** and **Figure 3-45)**. The graphs of integrated fluorescence intensity vs. absorbance are plotted (**Figure 3-4b** and **Figure 3-18d**). The quantum yield is calculated according to the equation: $\Phi s = \Phi_r(\frac{\text{Slope}_s}{\text{Slope}_r})(\frac{n_s}{n_r})^2$

where, Φ = quantum yield; Slope = slope of the straight line obtained from the plot of intensity vs absorbance (Figure 3-4b and Figure 3-18d); n = refractive index of the solvent; s-subscript denotes the sample; and, r-subscript denotes the reference used. Here, anthracene (Φ = 27% in ethanol) and courmarin 153 (Φ = 90% in cyclohexane) are used as the references[33].

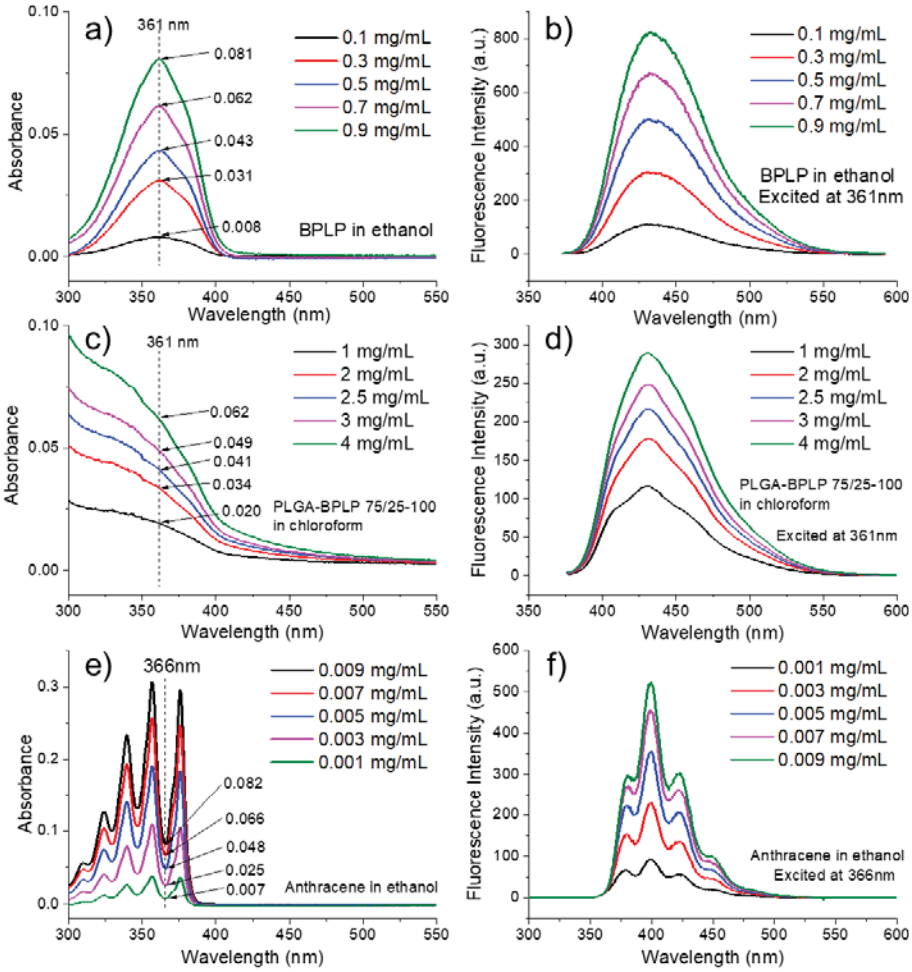

Figure 3-44. UV-Vis absorption spectra and fluorescence emission spectra of the as-synthesized a/b) BPLP, c/d) PLGA-BPLP and e/f) reference anthracene at series concentrations for fluorescence quantum yield calculation.

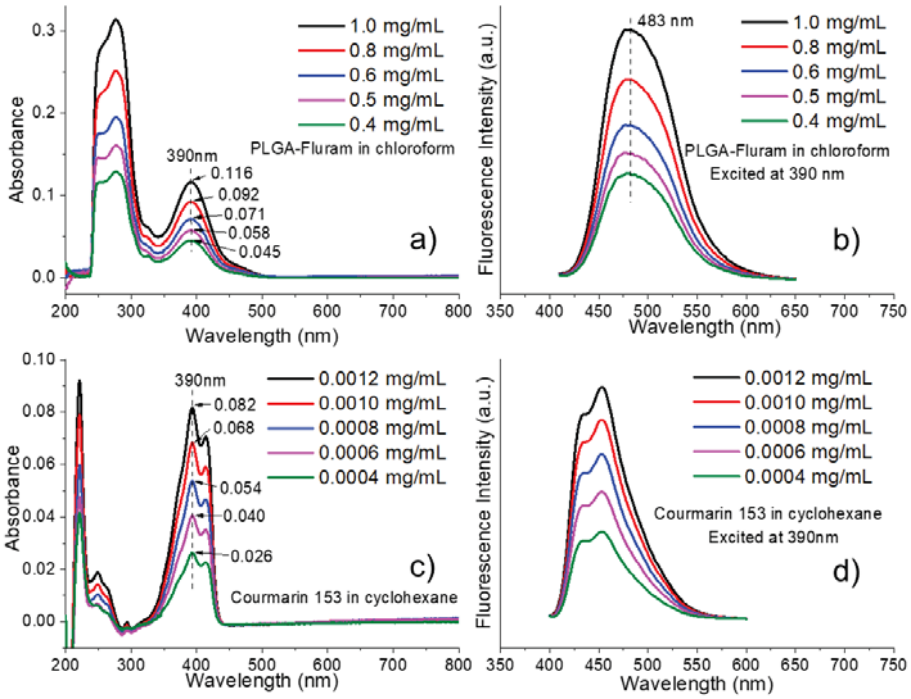

Figure 3-45. UV-Vis absorption spectra and fluorescence emission spectra of the as-synthesized a/b) PLGA-Fluram and c/d) reference courmarin 153 at series concentrations for fluorescence quantum yield calculation.

Photostability is measured by continuously illuminating the polymer or NCs in a fluorescent confocal microscope (Leica SP5, Leica Microsistemas S.L.U., Barcelona, Spain) while using UV diode 405 nm excitation at different laser power (10%, 20%, 100%). The fluorescence images are acquired within the emission range of 420-565 nm at a time interval of 1 s for 10 min., changes of mean fluorescence intensity of six regions of interests (ROIs) in 10 min. are calculated while using software Las AF. The real laser power (W) at different percentages for 10 min. is monitored using a laser power meter. The photostability of the PLGA-Fluram in organic solution is also compared with the commercial dye rhodamine B using the spectrofluorometer LS45. The PLGA-Fluram solution is continuously illuminated with excitation light at 390 nm and the resulting emission at 483 nm is monitored for 3 h at a time interval of 1 s. The photostability of rhodamine B as a reference is tested with its maximum excitation at 540 nm and maximum emission at 625 nm for the same 3 h in aqueous solution.

The fluorescence intensity of NCs aqueous suspension is quantified

in a 96-well by a microplate reader (Spark, Tecan Group Ltd., Männedorf, Switzerland). The fluorescence signal is collected by area scan at the maximal emission wavelength. For NIR PLGA-Cy7.5 NCs in the well plate, they are imaged using a Xenogen IVIS® spectrum (λex/λem 710/820 nm) and fluorescence intensity is acquired from the image.

3.6.8 Nanosight

Nanosight (NS300, Malvern Panalytical, Madrid, Spain) is used to measure the averaged size and concentration of the NCs water suspension. 0.2 mg/mL of NCs with 50 times dilution is pumped into the cell and the data are acquired and analyzed through the Nanoparticle Tracking Analysis (NTA) software along with the instrument.

3.6.9 *In vitro* cell uptake and toxicity of the NCs

The hCMEC/D3 endothelial cells are seeded in cover-slips that are pre-treated with collagen (2×10^4 cells/well in 24 well plates) and 24 h later are exposed to 50 μg/mL of PLGA-BPLP NCs. After an additional 24 h of culture, the wells are washed with PBS, fixated with 4% paraformaldehyde, and mounted with Vectashield antifade mounting medium (Vector Laboratories) with propidium iodide for nucleic acid counterstaining. Additionally, some of the cells are stained with PKH26 lipophilic fluorescent dye for cell membrane labeling according to the manufacturer's protocol. Images at 60× are obtained on a fluorescent confocal microscope (LSM 980 with Airyscan 2 detector, Zeiss, Oberkochen, Germany).

Two parallel methods assessed the toxicity of the PLGA-BPLP NCs on human brain endothelial cells (hCMEC/D3): a viability assay based on WST-8 tetrazolium salt reduction (cell counting Kit-8, Dojindo) and direct cell counting. First, 10^4 viable cells per well are seeded on a 24-well plate pre-treated with collagen (rat tail type I, Corning) in 400 μL of endothelial growth medium (EGM2 from Lonza with 2% fetal bovine serum and half the amount of the growth factors that are included in the kit). After incubation for 72 h at 37 °C with 5% of CO_2, the cells are at 80–90% confluence and the medium is changed to endothelial basal medium (EBM2, Lonza) containing NCs at 25, 50, 100, 500, and 1000 μg/mL. After 48 h, the cells are washed and incubated with 10% WST-8 solution for two hours. Culture supernatants are centrifuged at 20,000 rpm for 5 min. to

remove NCs detritus that could interfere with the dye absorption before determining the absorbance at 450 nm. Cells are trypsinized and resuspended in growth medium and diluted 1:1 in Trypan Blue in order to perform cell counting in a Neubauer chamber. Cell viability and count are expressed as the percentage of absorbance or number of cells as compared with the control (vehicle without NCs). ANOVA test and Dunnett's multiple comparisons post-hoc test is performed vs. the control.

To observe the fluorescent PLGA-Fluram and PLGA-Cy5 NCs in the cell culture, "macrophage-like" cells (differentiated from THP-1 cell line which are human monocytic cells derived from an acute monocytic leukemic patient) are used. Cells are seeded in a 12-well plate at 2×10^4 cells/well and co-incubated with different concentrations of NCs for 30 min. After this capture period, the wells are imaged by a fluorescence microscope (Inverted microscope Leica DMI 4000B) at λex 380nm for PLGA-Fluram NCs and at λex 620 nm for PLGA-Cy5 NCs.

3.6.10 *In/ex vivo* fluorescence imaging of the NCs

For the PLGA-Cy7.5 NCs, BALB/c AnNRj mice are anesthetized with isoflurane and injected *via* the tail vein with NCs at a dose of 1.6 mg in 200 µL of saline. The whole-body *in vivo* NIRF images are acquired on a Xenogen IVIS® spectrum imaging system at 0.5 h, 1 h and 3 h post injection (λex/λem of 710/820 nm). At the end of the 3 h scan, the mice are euthanized to image the signal intensity of the principal organs *ex vivo* (λex/λem of 745/820 nm). Control animals are used for each *in vivo* and *ex vivo* acquisition groups as a background measurement. For quantification, ROIs are drawn and TRE [photons/s]/[µW/cm²]) is measured using the Living Image software and corrected by the TRE from the corresponding ROI in the control animal.

3.7 Chapter references

[1] M.M. Pakulska, I.E. Donaghue, J.M. Obermeyer, A. Tuladhar, C.K. McLaughlin, T.N. Shendruk, M.S. Shoichet, Encapsulation-free controlled release: Electrostatic adsorption eliminates the need for protein encapsulation in PLGA nanoparticles, *Science Advances* 2(5) (2016) e1600519.

[2] X. Qin, C. Yu, J. Wei, L. Li, C. Zhang, Q. Wu, J. Liu, S.Q. Yao, W. Huang, Rational Design of Nanocarriers for Intracellular Protein Delivery, *Advanced Materials* 31(46) (2019) 1902791.

[3] A. Harguindey, D.W. Domaille, B.D. Fairbanks, J. Wagner, C.N. Bowman, J.N. Cha, Synthesis and Assembly of Click-Nucleic-Acid-Containing PEG–PLGA Nanoparticles for DNA Delivery, *Advanced Materials* 29(24) (2017) 1700743.

[4] R. Klippstein, J.T.W. Wang, R.I. El-Gogary, J. Bai, F. Mustafa, N. Rubio, S. Bansal, W.T. Al-Jamal, K.T. Al-Jamal, Passively Targeted Curcumin-Loaded PEGylated PLGA Nanocapsules for Colon Cancer Therapy In Vivo, *Small* 11(36) (2015) 4704-4722.

[5] C.J. Bowerman, J.D. Byrne, K.S. Chu, A.N. Schorzman, A.W. Keeler, C.A. Sherwood, J.L. Perry, J.C. Luft, D.B. Darr, A.M. Deal, Docetaxel-loaded PLGA nanoparticles improve efficacy in taxane-resistant triple-negative breast cancer, *Nano Letters* 17(1) (2017) 242-248.

[6] B. Colzani, L. Pandolfi, A. Hoti, P.A. Iovene, A. Natalello, S. Avvakumova, M. Colombo, D. Prosperi, Investigation of antitumor activities of trastuzumab delivered by PLGA nanoparticles, *International Journal of Nanomedicine* 13 (2018) 957.

[7] W. Tao, X. Zeng, J. Wu, X. Zhu, X. Yu, X. Zhang, J. Zhang, G. Liu, L. Mei, Polydopamine-based surface modification of novel nanoparticle-aptamer bioconjugates for in vivo breast cancer targeting and enhanced therapeutic effects, *Theranostics* 6(4) (2016) 470.

[8] P. Kumar, T. Van Treuren, A.P. Ranjan, P. Chaudhary, J.K. Vishwanatha, In vivo imaging and biodistribution of near infrared dye loaded brain-metastatic-breast-cancer-cell-membrane coated polymeric nanoparticles, *Nanotechnology* 30(26) (2019) 265101.

[9] A. Souza, A.d. Nascimento, N. de Vasconcelos, M. Jerônimo, I. Siqueira, L. R-Santos, D. Cintra, L. Fuscaldi, O.P. Júnior, R. Titze-de-Almeida, Activity and in vivo tracking of Amphotericin B loaded PLGA nanoparticles, *European Journal of Medicinal Chemistry* 95 (2015) 267-276.

[10] J. Llop, P. Jiang, M. Marradi, V. Gomez-Vallejo, M. Echeverria, S. Yu, M. Puigivila, Z. Baz, B. Szczupak, C. Perez-Campana, Visualisation of dual radiolabelled poly (lactide-co-glycolide) nanoparticle degradation in vivo using energy-discriminant SPECT, *Journal of Materials Chemistry B* 3(30) (2015) 6293-6300.

[11] L.J. Cruz, M.A. Stammes, I. Que, E.R. van Beek, V.T. Knol-Blankevoort, T.J. Snoeks, A. Chan, E.L. Kaijzel, C.W. Löwik, Effect of PLGA NP size on

efficiency to target traumatic brain injury, *Journal of Controlled Release* 223 (2016) 31-41.

[12] M.M. Abdel-Mottaleb, A. Beduneau, Y. Pellequer, A. Lamprecht, Stability of fluorescent labels in PLGA polymeric nanoparticles: quantum dots versus organic dyes, *International Journal of Pharmaceutics* 494(1) (2015) 471-478.

[13] R.L. Cook, K.T. Householder, E.P. Chung, A.V. Prakapenka, D.M. DiPerna, R.W. Sirianni, A critical evaluation of drug delivery from ligand modified nanoparticles: Confounding small molecule distribution and efficacy in the central nervous system, *Journal of Controlled Release* 220 (2015) 89-97.

[14] S. Florinas, M. Liu, R. Fleming, L. Van Vlerken-Ysla, J. Ayriss, R. Gilbreth, N. Dimasi, C. Gao, H. Wu, Z.-Q. Xu, A nanoparticle platform to evaluate bioconjugation and receptor-mediated cell uptake using cross-linked polyion complex micelles bearing antibody fragments, *Biomacromolecules* 17(5) (2016) 1818-1833.

[15] K. Qian, J. Wu, E. Zhang, Y. Zhang, A. Fu, Biodegradable double nanocapsule as a novel multifunctional carrier for drug delivery and cell imaging, *International Journal of Nanomedicine* 10 (2015) 4149.

[16] R. Yang, J. Xu, L. Xu, X. Sun, Q. Chen, Y. Zhao, R. Peng, Z. Liu, Cancer cell membrane-coated adjuvant nanoparticles with mannose modification for effective anticancer vaccination, *Acs Nano* 12(6) (2018) 5121-5129.

[17] D.X. Medina, K.T. Householder, R. Ceton, T. Kovalik, J.M. Heffernan, R.V. Shankar, R.P. Bowser, R.J. Wechsler-Reya, R.W. Sirianni, Optical barcoding of PLGA for multispectral analysis of nanoparticle fate in vivo, *Journal of Controlled Release* 253 (2017) 172-182.

[18] J.-K. Park, T. Utsumi, Y.-E. Seo, Y. Deng, A. Satoh, W.M. Saltzman, Y. Iwakiri, Cellular distribution of injected PLGA-nanoparticles in the liver, Nanomedicine: Nanotechnology, *Biology and Medicine* 12(5) (2016) 1365-1374.

[19] J.K. Jaiswal, H. Mattoussi, J.M. Mauro, S.M. Simon, Long-term multiple color imaging of live cells using quantum dot bioconjugates, *Nature Biotechnology* 21(1) (2003) 47-51.

[20] T. Jamieson, R. Bakhshi, D. Petrova, R. Pocock, M. Imani, A.M. Seifalian, Biological applications of quantum dots, *Biomaterials* 28(31) (2007) 4717-4732.

[21] J. Yang, Y. Zhang, S. Gautam, L. Liu, J. Dey, W. Chen, R.P. Mason, C.A. Serrano, K.A. Schug, L. Tang, Development of aliphatic biodegradable photoluminescent polymers, *Proceedings of the National Academy of Sciences* 106(25) (2009) 10086-10091.

[22] J. Hu, J. Guo, Z. Xie, D. Shan, E. Gerhard, G. Qian, J. Yang, Fluorescence imaging enabled poly (lactide-co-glycolide), *Acta Biomaterialia* 29 (2016) 307-319.

[23] W. Kasprzyk, S. Bednarz, D. Bogdał, Luminescence phenomena of biodegradable photoluminescent poly (diol citrates), *Chemical Communications* 49(57) (2013) 6445-6447.

[24] Y. Zhang, J. Yang, Design strategies for fluorescent biodegradable polymeric biomaterials, *Journal of Materials Chemistry B* 1(2) (2013) 132-148.

[25] S. Udenfriend, S. Stein, P. Boehlen, W. Dairman, W. Leimgruber, M. Weigele, Fluorescamine: a reagent for assay of amino acids, peptides, proteins, and primary amines in the picomole range, *Science* 178(4063) (1972) 871-872.

[26] K. Mauring, V. Krasnenko, S. Miller, Photophysics of the blue fluorescent protein, *Journal of Luminescence* 122 (2007) 291-293.

[27] D. Wang, T. Imae, M. Miki, Fluorescence emission from PAMAM and PPI dendrimers, *Journal of Colloid and Interface Science* 306(2) (2007) 222-227.

[28] W. Yang, C.Y. Pan, Synthesis and fluorescent properties of biodegradable hyperbranched poly (amido amine) s, *Macromolecular Rapid Communications* 30(24) (2009) 2096-2101.

[29] Cyanine dyes, Lumiprobe GmbH, GE Healthcare, https://www.lumiprobe.com/tech/cyanine-dyes.

[30] E. Fröhlich, The role of surface charge in cellular uptake and cytotoxicity of medical nanoparticles, *International Journal of Nanomedicine* 7 (2012) 5577.

[31] C. Foged, B. Brodin, S. Frokjaer, A. Sundblad, Particle size and surface charge affect particle uptake by human dendritic cells in an in vitro model, *International Journal of Pharmaceutics* 298(2) (2005) 315-322.

[32] Cyanine 7.5, Lumiprobe GmbH, GE Healthcare, https://www.lumiprobe.com/t/fluorophores/cy75.

[33] A.M. Brouwer, Standards for photoluminescence quantum yield measurements in solution (IUPAC Technical Report), *Pure and Applied Chemistry* 83(12) (2011) 2213-2228.

4

Functionalization of the NC formulation with PET imaging modality

PET is a nuclear imaging technique showing great advantages regarding the study of the *in vivo* fate of nanomedicines. Nanoformulations labelled with radioisotopes can be detected and quantified by PET in a non-invasive fashion with high sensitivity once administered. Importantly, this technique is fully translational and enables the evaluation of the pharmacokinetics of nanoformulations in both preclinical and clinical stages[1-4].

The principle of detection and localization of a radioisotope by PET is shown in **Figure 4-1**. The radioisotopes used by PET are positron emitters such as ^{18}F, ^{11}C, ^{13}N, ^{68}Ga and ^{89}Zr, etc. with different half-lives that emit one positron during their disintegration. The positron interacts with other charged particles in the tissue randomly and progressively loses its kinetic energy during its short lifetime, and finally annihilates with an electron of a surrounding atom which results in the emission of a pair of gamma rays with energy of 511 keV each traveling 180° apart (**Figure 4-1a**). The distance between the locations where the disintegration and the annihilation occur is called positron range and is typically of a few millimeters in water. Those pairs of gamma rays with linear directions reach the back-to-back detectors and simultaneously excite two opposed scintillation crystals where the gamma-ray signal is converted to visible wavelengths, detected by a photodetector (**Figure 4-1b**). The stationary full-ring array of detectors record the directions and intensities of all pairs of gamma rays and then feed mathematical reconstruction algorithms to obtain tomographic datasets, from which the position and concentration of the radionuclide can be reconstructed and visualized.

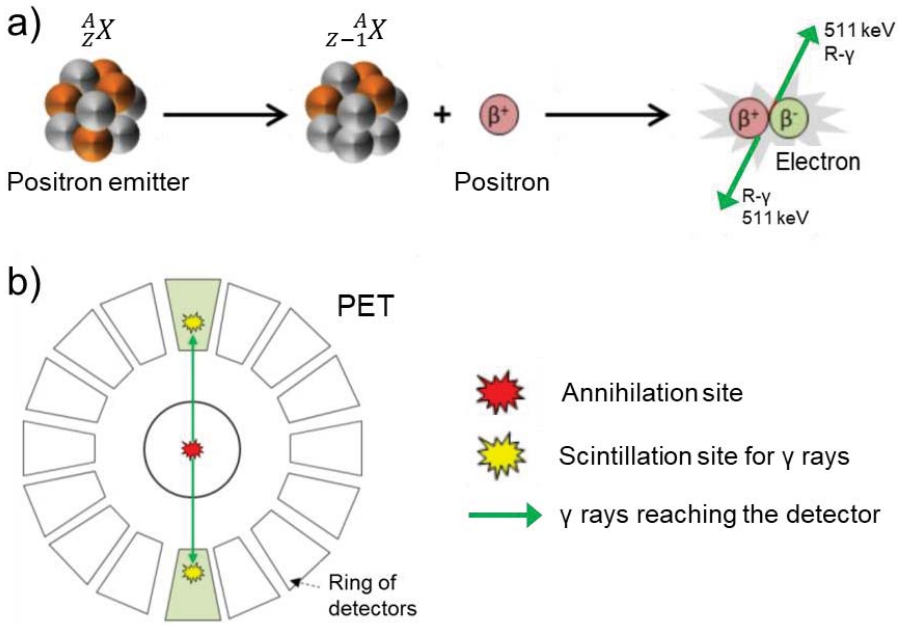

Figure 4-1. Schematic illustration of a) positron emission and gamma ray generation, b) photon detection and localization using PET scanner.[5]

As discussed above, PET enables the localization and quantification of the concentration of a radionuclide over time. Once administered *in vivo,* and in combination with another imaging modality such as computed tomography (CT) that shows a co-registered image of the structures of the organism, the radionuclide's information acquired by PET can be matched with its distribution in the PET-CT merged image. In this manner, the distribution of the studied NC within a living organism can be assessed as long as the radioisotope remains chemically bound to it.

In this chapter, we achieve the radiolabeling of the fabricated PLGA NCs by using a bifunctional chelator (p-NCS-Bz-DFO) as a bridge between the NC and the radionuclide (**Figure 4-2**). One functional group in the chelator allows us to anchor the chelator to the surface of the NCs while the other enables the entrapment of a metallic radionuclide. This strategy has some clear advantages; i) the NCs designed can already integrate the chelator before the radiolabeling and can undergo full characterization and ii) the chelation reaction for incorporating the radioisotope can be done at the very last stage just before conducting the PET acquisition, and it usually takes place under mild reaction conditions which are expected not to

significantly alter the NC properties. In this chapter, the biodistributions of the radiolabeled non-PEGylated/PEGylated NCs after *i.v.* administration are studied.

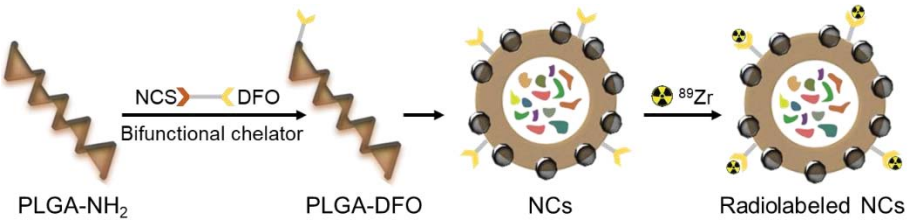

Figure 4-2. Schematic illustration of the strategy to obtain chelator anchored PLGA NCs and radiolabeling.

4.1 NCs functionalized with radioisotope ^{89}Zr

4.1.1 PLGA-DFO polymer

Deferoxamine (DFO) is a bacterial siderophore that can be isolated from *Streptomyces pilosus*. It can form metallic complexes with heavy metals like iron, aluminum or zirconium and it is used as a chelating agent[6] in diseases characterized by high levels of circulating iron or aluminum[7, 8]. Here we choose the DFO chelator aiming to entrap the metallic radionuclide ^{89}Zr for PET imaging where the bifunctional derivative p-NCS-Bz-DFO is used as a bridge to modify the NCs. In practice, the NCs are firstly labeled with "empty" DFO and subsequently the radionuclides are captured, as illustrated in **Figure 4-2**.

To achieve the DFO labeling of NCs, a route to first synthesize the PLGA-DFO polymer and subsequently fabricates NCs using the PLGA-DFO is selected similarly to other types of NCs discussed in Section 3.2.2 and shown in Figure 3-21a. In fact, the poor solubility of p-NCS-Bz-DFO would make it much more difficult to follow a route to directly anchor p-NCS-Bz-DFO to the -NH_2 enriched surface of pre-fabricated NCs. **Figure 4-3** illustrates the synthetic scheme to obtain PLGA-DFO, the -NCS group in p-NCS-Bz-DFO reacts with the -NH_2 group at the terminal of PLGA, by forming a thiocarbamide bond the DFO is introduced to the end of PLGA.

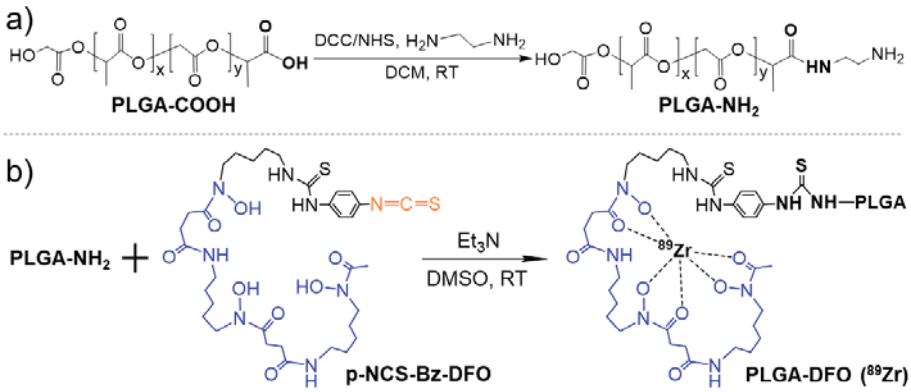

Figure 4-3. Synthetic sequence of terminal modification and functionalization of the commercial PLGA-COOH to obtain PLGA-DFO and the chelation of ^{89}Zr.

ATR-FTIR spectra of the PLGA-NH_2 and the chelator labeled PLGA-DFO product confirms their similar chemical structure and successful modification (**Figure 4-4**). Both PLGA-NH_2 and PLGA-DFO show the typical bands at 1084 cm^{-1}, 1165cm^{-1} and 1747 cm^{-1} attributed to the C=O stretch and C-O asymmetrical and symmetrical stretches of the ester chain of the PLGA, and the C-H stretch bands of the alkane near 2951 cm^{-1}. The bands and shapes similarities of the two spectra imply that the main molecular chain of PLGA is not affected by the modifications. The characteristic peaks attribute to -NH_2 in the spectra of PLGA-NH_2 was previously discussed in Figure 3-16. After the incorporation of DFO, some new bands appear. Bands at 1618 cm^{-1}, 1554 cm^{-1} and 1503 cm^{-1} attribute to the C=C stretching of the backbone of the aromatic ring, the band at 3310 cm^{-1} corresponds to the NH stretching of the secondary amide, all these structure information are consistent with those in commercial p-NCS-Bz-DFO (**Figure 4-4 upper left inset**), indicating the successful conjugation of DFO. The disappearance of N=C=S stretching band at 2130 cm-1 in the PLGA-DFO spectrum also demonstrates the reaction of –NCS with –NH_2.

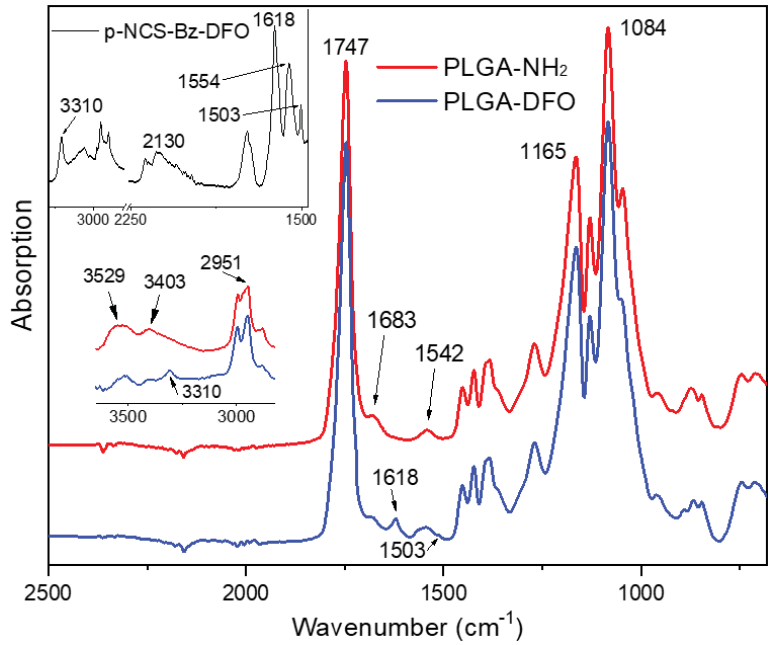

Figure 4-4. ATR-FTIR spectra of PLGA-NH_2 and chelator labeled PLGA-DFO product confirming their similar chemical structures and the successful modification. Left lower inset is the magnified spectra of the 3500-3000 cm^{-1} range, left upper inset is the spectra of p-NCS-Bz-DFO.

The amount of conjugated DFO in the PLGA-DFO product is quantified indirectly by measuring the amount of unreacted PLGA-NH_2 through the fluram method. As shown in **Figure 4-5**, after reaction with an excess amount of fluram, the absorption band at 390 nm appears resulting from the conjugation of fluram to the unreacted -NH_2. The absorbance value is compared with the absorbance-amino concentration standard curve established in **Figure 3-17a**, and a molar fraction of 11% of unreacted PLGA-NH_2 in the PLGA-DFO product is calculated. Considering the fraction of pure PLGA-NH_2 in the reactant is 86%, a fraction of 75% of pure PLGA-DFO (reacted PLGA-NH_2) in the product is estimated and a conjugation efficiency of 87% of p-NCS-Bz-DFO to PLGA-NH_2 was calculated.

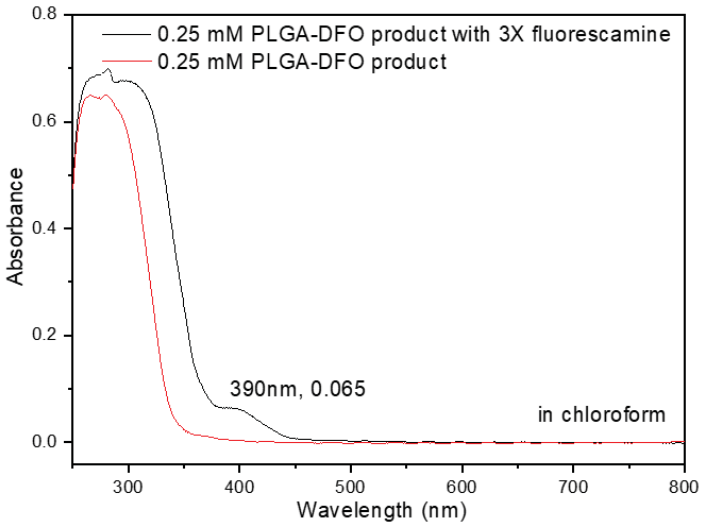

Figure 4-5. Absorption curves of 0.25 mM of PLGA-DFO product before and after reaction with an excess amount of fluram.

4.1.2 PLGA-DFO NCs labeled with ^{89}Zr

The as-synthesized PLGA-DFO is then used to fabricate NCs. The ^{89}Zr chelating moiety of PLGA-DFO together with other functional moieties of PLGA-PEG and SPIONs are incorporated into the organic phase with pure PLGA. As listed in **Table 4-1** both the non-PEGylated and PEGylated PLGA-DFO NCs contain ~6 wt% of SPIONs.

Table 4-1. Non-PEGylated/PEGylated formulations for the PLGA-DFO NCs.

NCs Type	Shell Polymers (wt%)			SPIONs Loading (wt%)	M_S (eum/g)	Size (DLS)	
	PLGA	PLGA-DFO	PLGA-PEG			d. nm	PdI
NC-13.non-PEGylated	60	40	/	6.3	4.3	271	0.19
NC-14.PEGylated	53	40	7	6.0	4.7	258	0.17

Representative SEM morphologies of the PLGA-DFO NCs are shown in **Figure 4-6**, the incorporation of the DFO does not affect the homogeneous spherical morphology of the non-PEGylated/ PEGylated NCs.

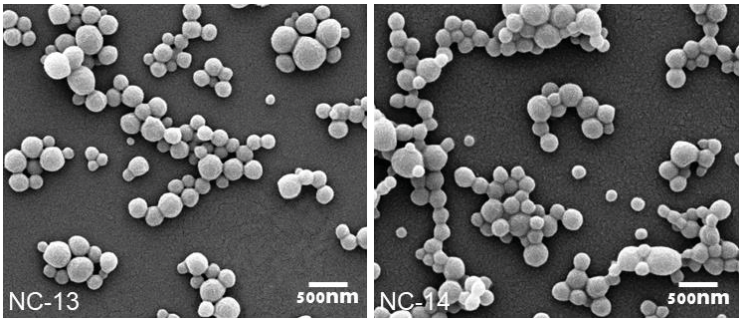

Figure 4-6. Representative SEM images of the lyophilized non-PEGylated and PEGylated PLGA-DFO NCs.

Our results show that ^{89}Zr-labeling has a yield of about 70% for PLGA-DFO NCs after overnight incubation at room temperature (experimental condition: 3.2 mg/mL of NCs in 500 μL of ^{89}Zr solution with initial radioactivity of 39.0 MBq). A DFO challenge study has been reported to demonstrate the radiostability of ^{89}Zr-labeled NPs.[9] In our study, the as-obtained PLGA-DFO-^{89}Zr NCs are suspended in 1 mM DFO aqueous solution and incubated at 37 °C for 23 h. Then the NCs are separated by centrifugation and 100% are still labelled, with no presence of ^{89}Zr-DFO in the supernatant, demonstrating a strong binding affinity of ^{89}Zr to the PLGA-DFO NCs.

4.2 Biodistribution investigation of the *i.v.* injected NCs by PET

With a ~3 day half-life, ^{89}Zr-PET imaging holds great potential as a useful tool for long-term monitoring of the dynamic biodistribution, biodegradation and clearance pathway of NPs *in vivo*.[10]

4.2.1 PEGylation effect

^{89}Zr labeled PLGA-DFO-^{89}Zr NCs were injected *via* the tail vein with the same dosage as for the MRI and IVIS study to anesthetized mice. Static whole-body PET-CT images were acquired at 1 h, 4 h, 23 h and 47 h p.i. for both non-PEGylated and PEGylated NCs as shown in **Figure 4-7**. Dominant liver, spleen and lung uptake is observed (**Figure 4-7**) and confirmed by the quantitative ROI analysis (**Figure 4-8**) for both non-PEGylated and PEGylated NCs within two days, which can be related to phagocytic cell uptake by the mononuclear phagocyte system[11], as expected for *i.v.* injected PLGA NPs of this size[12]. As the PEGylated NCs are expected to have longer blood circulation time and less immune cell uptake than the non-PEGylated ones, the organ accumulation data of these two types of NCs are

further compared as shown in **Figure 4-9**. The PEGylated NCs do show less accumulation in liver and lung after one day which may imply a longer blood circulation time (**Figure 4-9a & b**) but we can not find an easiyexplanation of why the PEGylated NCs show a much higher accumulation in spleen (**Figure 4-9c**). Further experiments would be needed to be repeated to confirm the results and give a final assessment of the PEGylation effect of our NCs. Moreover, methods to improve the PEGylation density on the nanoparticle surface should be also evaluated[13].

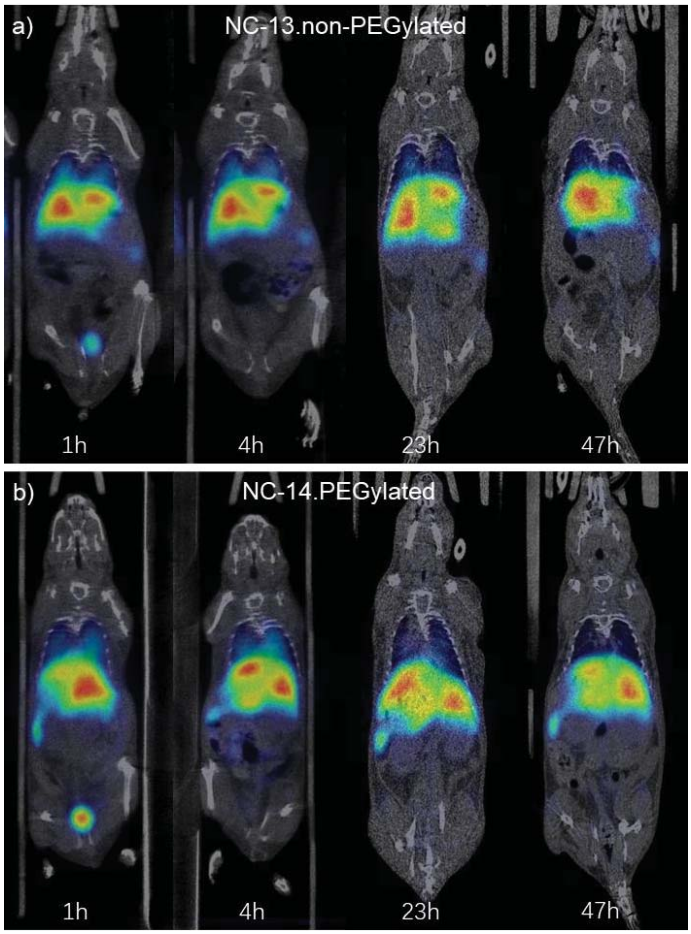

Figure 4-7. Representative PET-CT coronal images of mice obtained at different time points after *i.v.* administration of a) non-PEGylated and b) PEGylated PLGA-DFO-^{89}Zr NCs. PET images have been co-registered with CT images (slices) of the same animals for localization of the radioactive signal.

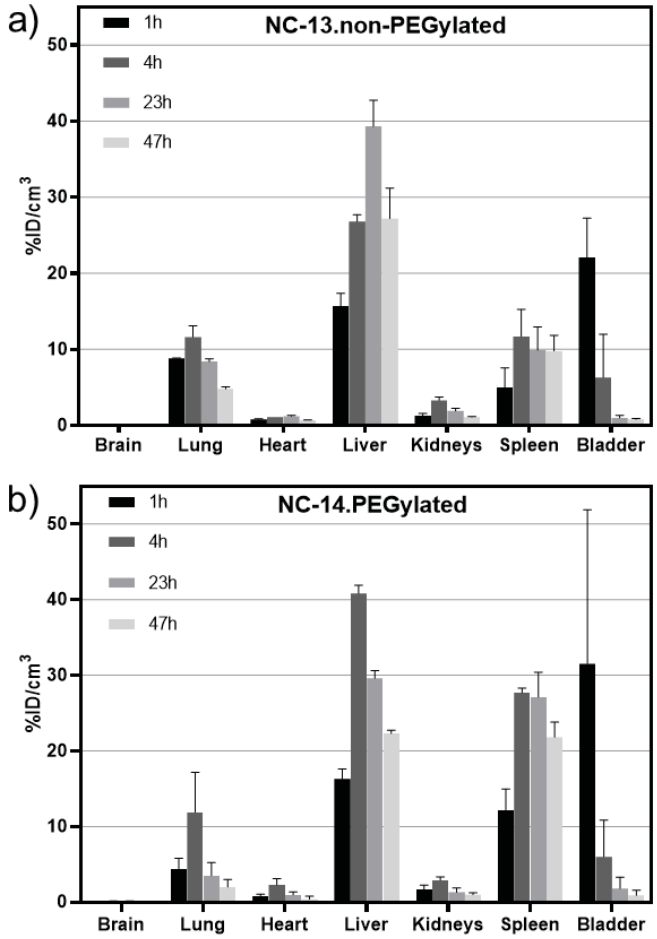

Figure 4-8. Quantification of biodistribution of a) non-PEGylated and b) PEGylated PLGA-DFO-^{89}Zr NCs at 1 h, 4 h, 23 h and 47 h p.i. (mean ± SEM of n = 2) determined by the PET images analysis in Figure 4-7. Radioactivity expressed as a percentage of injected dose per cm^3 of tissue (%ID/cm^{-3}).

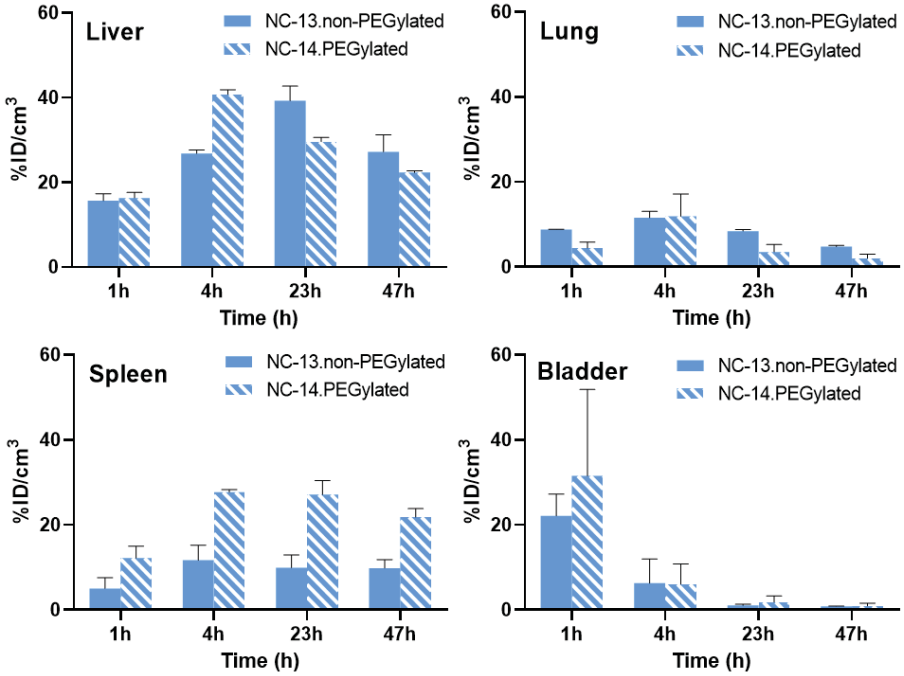

Figure 4-9. Comparison of organ accumulation between non-PEGylated and PEGylated PLGA-DFO-^{89}Zr NCs at 1 h, 4 h, 23 h and 47 h p.i. (mean ± SEM of n = 2). Data extracted from Figure 4-8.

Interestingly, noticeable bladder accumulations are observed at 1 h p.i. for both non-PEGylated and PEGylated NCs, with a sharp decrease at 4 h p.i. likely due to uncontrolled animals' urination between scans (**Figure 4-9**). It is hard to assign the activity in the urine to the detachment of free ^{89}Zr from the NCs, since detached free ^{89}Zr is a well-known osteophilic cation with a fast and retained uptake in bones[10, 14], which is not detectable in our case. In the study of Chen et al.[10], for both free ^{89}Zr-oxalate or ^{89}Zr labeled SiO_2 NPs, fast and sustained uptake of free/detached ^{89}Zr in bones and joints is observed from the first few hours up to three weeks, while the accumulation in the bladder is negligible. We thus hypothesize that the erosion of the soft polymeric NCs has happened at an early stage in the complex blood circulation environment. The detached ^{89}Zr-molecular fragments from the NCs, either by degradation of ester bonds in PLGA molecular chains or thiocarbamide bonds between PLGA and DFO or by mechanical force, with a size smaller than 15 nm[15] undergo renal clearance and are observed in the bladder. Erosion of NCs is clearly observed after *in vitro* incubation in mouse plasma at 37 °C for 24 h (**Figure 4-10**). Small holes appeared on the NCs while

under the same conditions NCs incubated in saline do not show the same eroded surface. Considering the *in vivo* blood circulation setting, the erosion of PLGA NCs would be much faster as reported by Swider *et al.*[16]. Not surprisingly, at late time points, the radioactivity in the bladder decreases likely due to the fast accumulation of the NCs in the liver/spleen.

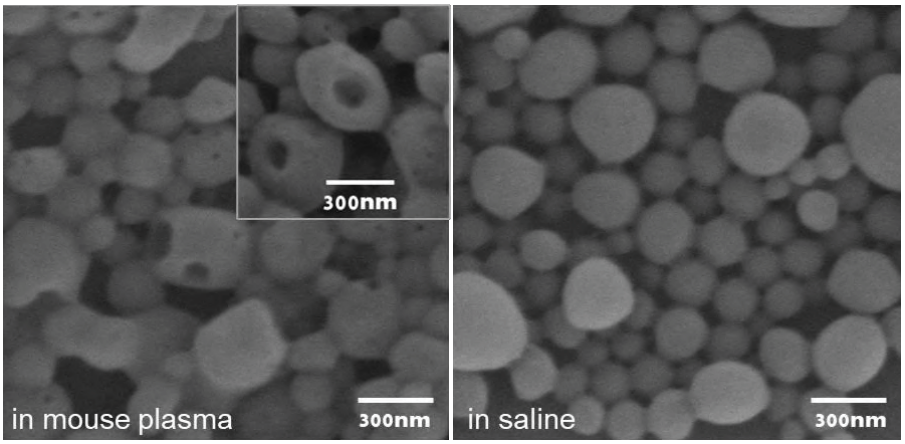

Figure 4-10. SEM images of the NCs after incubation for 24 h at 37 °C in mouse plasma or saline. Inset is another SEM area of the NCs in mouse plasma with clear holes.

4.2.2 Trial with magnet implant

As mentioned, the final application of the NC formulation is to achieve brain delivery for neurorepair treatment after an ischemic stroke. The preliminary PET biodistribution results shown in **Figure 4-7** and **Figure 4-8** indicated that no significant brain accumulation of NCs occurs through *i.v.* administration. We have also shown that the NC formulation can be magnetically retained as discussed in Section 2.1.3. Here we show a very preliminary *in vivo* experiment to study whether the use of an external magnetic field can improve retention of NCs in the brain area.

NCs were injected *i.v.* (tail vein) into the mice without implantation of a magnet, with a magnet on the left brain and with a magnet on the right brain respectively. Then, continuous whole-body PET acquisition was done for 150 min and co-registered with one CT image acquired at the end of the scan, aiming to observe the ipsilateral hemisphere retention of NCs resulting from the external magnetic field. Unfortunately, the brain PET signals were low with noise and no significant difference could be observed between the

three, dominant liver, spleen and lung uptake is still observed (**Figure 4-11**a). The quantification data of brain radioactivity in **Figure 4-11**b clearly shows the signals during 150 min are tiny for all the animals without a significant retention effect from the magnet. Two important facts could be learned from this initial experiment; i) magnet design applying higher magnetic forces would be needed and ii) the magnet should be detached from the skull before the PET/CT imaging since it exerts some image distortion when PET imaging the brain impacting in the accuracy of ROI quantification.

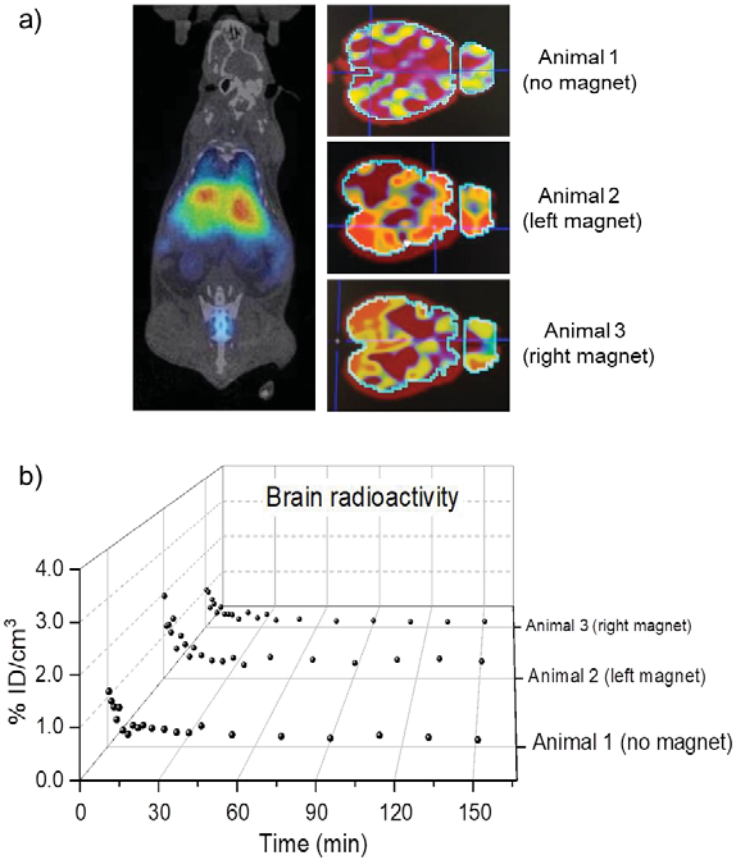

Figure 4-11. Dynamic whole-body PET acquisition during 150 min after i.v. injection of NCs (NC-13) with a magnet on one hemisphere of the mouse brain. a) A representative PET-CT coronal image of the mouse which corresponds to all frames summed during 150 min, PET images co-registered with one CT image acquired at the end of the scan. The signal in the brain area has been magnified to compare the difference of NCs injected without magnet and with a magnet on the left or right of the brain; b) dynamic quantification of the brain radioactivity (% of injected dose per cm^3 of tissue) during 150 min of the animal without magnet and with the magnet on the left or right of the brain.

Similarly, the early-stage bladder activity is also observed and shows a linear increase within 150 min p.i. (**Figure 4-12)**, which is in line with the results discussed in the last section, indicating the fast erosion of NCs in blood circulation.

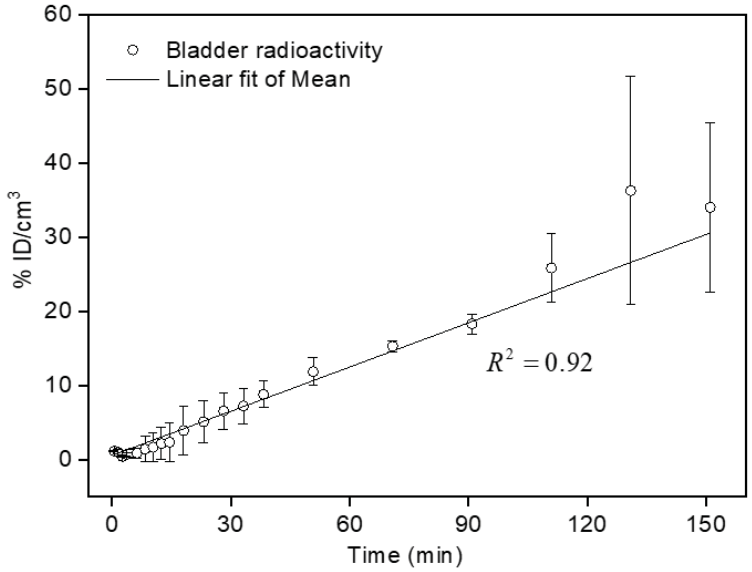

Figure 4-12. Dynamic quantification of the bladder radioactivity (% of injected dose per cm^3 of tissue) during 150 min upon *i.v.* injection of the NCs (mean ± SEM of n = 3). Values determined by the PET images analysis.

4.3 Chapter summary

I conjugated the chelator DFO to the end of the PLGA molecule and then fabricated the PLGA-DFO NCs. Similarly, neither conjugation nor the PEGylation modifications affected the morphology and magnetization of the obtained NCs. The NCs were successfully labeled by ^{89}Zr with high radiostability.

Biodistribution study by PET imaging showed a dominant liver, spleen and lung accumulation of the *i.v.* administered NCs, significant brain accumulation of NCs was not observed with this sensitive imaging technique, the results were consistent with those obtained by NIRF. Moreover, the PEGylated NCs showed less accumulation in liver and lung after one day which may imply a longer blood circulation time. A preliminary assay with magnet implantation on the mouse skull did not show a significant retention effect for the *i.v.* administered NCs to the brain.

Finally, early stage bladder activity was confirmed by PET which was also observed by NIRF, indicating the fast erosion of NCs in blood circulation.

4.4 Annex of Chapter 4

4.4.1 Synthesis of PLGA-DFO

^{89}Zr chelator deferoxamine (DFO) is introduced at the terminal amine of PLGA-NH_2 by forming a thiocarbamide bond between -NH_2 and the amine-reactive -NCS group in the p-NCS-Bz-DFO (CheMatech, Dijon, France). 0.025 mmol of the as-synthesized PLGA-NH_2 and 0.05 mmol of p-NCS-Bz-DFO are mixed and dissolved in 4 mL of DMSO (note that p-NCS-Bz-DFO is insoluble in common solvents such as DCM, chloroform, acetone and ethyl acetate in which PLGA dissolves well), and 0.05 mmol of Et_3N is added as the catalyst. The reaction is accomplished after 12 h at RT under magnetic stirring. Then the DMSO solution is mixed with an equal proportion of DCM and slowly dropped into 10-fold diethyl ether (pure DMSO is immiscible with diethyl ether) to precipitate the PLGA-DFO product and the unreacted p-NCS-Bz-DFO as well, which are collected by centrifugation at 9391 rcf for 10 min. The PLGA-DFO/p-NCS-Bz-DFO mixture pellet is dissolved in 1.5 mL of DCM and centrifuged at 13 171 rcf for 60 min to remove the insoluble p-NCS-Bz-DFO. The supernatant is further filtered (0.2 μm PTFE syringe filter) to remove the traces of p-NCS-Bz-DFO. Finally, the PLGA-DFO product is precipitated by slowly dropping the supernatant into 10-fold diethyl ether, collected by centrifugation and dried under vacuum.

4.4.2 ^{89}Zr labeling of the PLGA-DFO NCs and *in vivo* PET imaging

The protocols and experiments described below were performed by Jordi Llop and co-workers at the CIC-Biomagune using dedicated radiolabeling chemistry and preclinical PET-CT facilities.

PLGA-DFO NCs was labelled with ^{89}Zr as follows: 1500 μL of 1 M oxalic acid containing ^{89}Zr (8.2 mCi, 303.4 MBq) was produced in house and neutralized with 2 M sodium carbonate (pH = 7.2) and the volume adjusted to 3.5 mL with 0.5 M HEPES buffer. Each aliquot (1.6 mg) of the lyophilized NCs was dispersed in 50 μL MQ-water, and 450 μL of the freshly prepared ^{89}Zr-solution added to each and mixed well by sonication.After incubating overnight at room temperature, the NCs were purified by centrifugation and washed two times with MQ-water followed by one wash with saline to remove all non-bound ^{89}Zr. The pellet of the last wash was dispersed in 120 μL

of saline with an average calculated radiochemical yield of 70.1% (decay-corrected, obtained by dividing the radioactivity of the pellet by that of the initial incubating solution). As the achieved samples are too active, a one to one dilution with non-labelled NCs was performed. The final injections (1.6 mg) was administered *i.v. via* the tail vein of healthy female mice (Crl : CD1(ICR)). The magnet was implanted on the top of the skull and below the skin with the position on one hemisphere (**Figure 4-13**), PET-CT was acquired in the presence of magnet.

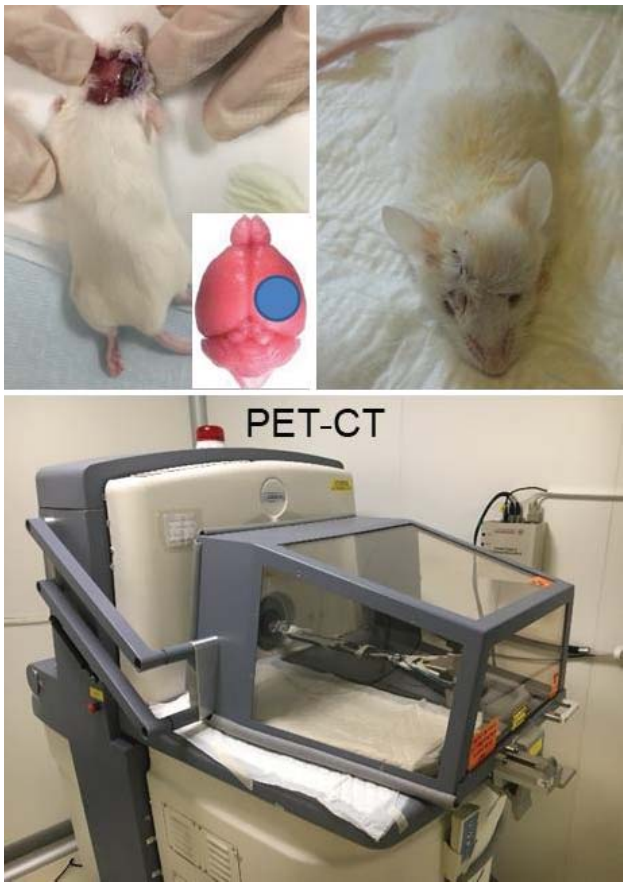

Figure 4-13. Images of magnet implantation on the top of the skull and below the skin. The magnet was adhered on one hemisphere.

PET-CT was conducted using the β- and X-cube microsystem of Molecubes. Static or dynamic whole-body images (1 bed) are acquired in a 511 keV ± 30% energetic window post-injection. PET images were analyzed using PMOD image analysis software (PMOD Technologies Ltd, Zurich, Switzerland) and counts per second and

per cm^3 in the ROIs were obtained. By using a calibration fraction obtained by acquiring images of a vial containing a known concentration of radioactivity, the concentration of radioactivity in the ROI is determined in $\mu Ci/cm^3$. Then, this number is divided by the injected activity and multiply by 100 to obtain the percentage of injected dose per cm^3 of tissue ($\%ID/cm^{-3}$), the final expressed radioactivity.

All animal experiments followed the Spanish policy for animal protection (RD53/2013). All experimental procedures were approved by the Ethical Committee of CIC biomaGUNE and authorized by the local authorities. All animals were housed in ventilated cages and fed on a standard diet *ad libitum*.

4.5 Chapter references

[1] N.K. Devaraj, E.J. Keliher, G.M. Thurber, M. Nahrendorf, R. Weissleder, 18F labeled nanoparticles for in vivo PET-CT imaging, *Bioconjugate Chemistry* 20(2) (2009) 397-401.

[2] E.D. Pressly, R. Rossin, A. Hagooly, K.-i. Fukukawa, B.W. Messmore, M.J. Welch, K.L. Wooley, M.S. Lamm, R.A. Hule, D.J. Pochan, Structural effects on the biodistribution and positron emission tomography (PET) imaging of well-defined 64Cu-labeled nanoparticles comprised of amphiphilic block graft copolymers, *Biomacromolecules* 8(10) (2007) 3126-3134.

[3] S. Rojas, J.D. Gispert, R. Martín, S. Abad, C. Menchon, D. Pareto, V.c.M. Víctor, M. Alvaro, H. García, J.R. Herance, Biodistribution of amino-functionalized diamond nanoparticles. in vivo studies based on 18F radionuclide emission, *ACS Nano* 5(7) (2011) 5552-5559.

[4] T. Schluep, J. Hwang, I.J. Hildebrandt, J. Czernin, C.H.J. Choi, C.A. Alabi, B.C. Mack, M.E. Davis, Pharmacokinetics and tumor dynamics of the nanoparticle IT-101 from PET imaging and tumor histological measurements, *Proceedings of the National Academy of Sciences* 106(27) (2009) 11394-11399.

[5] U.C. Arrieta, Radiolabelling and preclinical evaluation of nanoparticles as drug delivery systems: Application to infectious pulmonary diseases, Doctoral thesis, University of Basque Country, 2018.

[6] W.L. Steinmetz, M.R. Glick, T. Oei, Modified aca method for determination of iron chelated by deferoxamine and other chelators, *Clinical Chemistry* 26(11) (1980) 1593-1597.

[7] E.J. Neufeld, Update on iron chelators in thalassemia, Hematology 2010, the American Society of Hematology Education Program Book 2010(1) (2010) 451-455.

[8] M.C. Stuart, M. Kouimtzi, S.R. Hill, WHO model formulary 2008, World Health Organization 2009.

[9] E. Boros, A.M. Bowen, L. Josephson, N. Vasdev, J.P. Holland, Chelate-free metal ion binding and heat-induced radiolabeling of iron oxide nanoparticles, *Chemical Science* 6(1) (2015) 225-236.

[10] F. Chen, S. Goel, H.F. Valdovinos, H. Luo, R. Hernandez, T.E. Barnhart, W. Cai, In vivo integrity and biological fate of chelator-free zirconium-89-labeled mesoporous silica nanoparticles, *ACS Nano* 9(8) (2015) 7950-7959.

[11] R. Klippstein, J.T.W. Wang, R.I. El-Gogary, J. Bai, F. Mustafa, N. Rubio, S. Bansal, W.T. Al-Jamal, K.T. Al-Jamal, Passively Targeted Curcumin-Loaded PEGylated PLGA Nanocapsules for Colon Cancer Therapy *In Vivo*, *Small* 11(36) (2015) 4704-4722.

[12] L.J. Cruz, M.A. Stammes, I. Que, E.R. van Beek, V.T. Knol-Blankevoort, T.J. Snoeks, A. Chan, E.L. Kaijzel, C.W. Löwik, Effect of PLGA NP size on efficiency to target traumatic brain injury, *Journal of Controlled Release* 223 (2016) 31-41.

[13] N. Bertrand, P. Grenier, M. Mahmoudi, E.M. Lima, E.A. Appel, F. Dormont, J.M. Lim, R. Karnik, R. Langer, O.C. Farokhzad, Mechanistic understanding of in vivo protein corona formation on polymeric nanoparticles and impact on pharmacokinetics, *Nature Communication* 8(1) (2017) 777.

[14] D.S. Abou, T. Ku, P.M. Smith-Jones, In vivo biodistribution and accumulation of 89Zr in mice, *Nuclear Medicine and Biology* 38(5) (2011) 675-681.

[15] M. Cataldi, C. Vigliotti, T. Mosca, M. Cammarota, D. Capone, Emerging role of the spleen in the pharmacokinetics of monoclonal antibodies, nanoparticles and exosomes, *International Journal of Molecular Sciences* 18(6) (2017) 1249.

[16] E. Swider, S. Maharjan, K. Houkes, N.K. van Riessen, C. Figdor, M. Srinivas, O. Tagit, Fo ¨ rster Resonance Energy Transfer-Based Stability Assessment of PLGA Nanoparticles in Vitro and in Vivo, *ACS Applied Biomaterials* 2(3) (2019) 1131-1140.

5

Towards the brain targeting theranostic NC formulation

The biodistribution studies of the *i.v.* administered NCs through MRI (Section 2.2.1), NIRF (Section 3.4.3) and PET (Section 4.2) have shown that most of NCs are initially accumulated in the liver, spleen and lung. In this chapter we explored improved administration protocols to guarantee a better brain delivery according to the data collected in the previous chapters. The intra-arterial (*i.a.*) administration is used as a more efficient route for NC delivery to the brain, as NCs following this route directly reach the middle cerebral artery (MCA) and before reaching the pulmonary circulation. NCs with NIRF and MRI modalities are used to investigate the biodistribution of NCs through this route and improved brain accumulation is confirmed. Furthermore, the protein loading and release kinetics of the NC formulation are evaluated and efforts are made to increase the loading of the therapeutic secretome.

5.1 Improvement of brain accumulation

Recent years new endovascular thrombectomies conducted in stroke patients use the *i.a.* route to reach the brain vasculature and remove the clot. The developments motivate our project partners at the Vall d'Hebron Research Institute to try this *i.a.* approach for the brain delivery of NCs. Preclinical *i.a.* administration in animal models[1-3] also demonstrated the feasibility of this approach. The schematic illustration of the *i.a.* administration of NCs is shown in **Figure 5-1.**

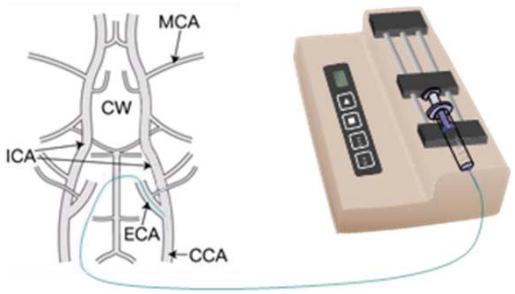

Figure 5-1. Schematic illustration of the intra-arterial infusion of NCs.

Firstly, NIRF imaging was use to investigate the biodistribution of NCs through *i.a.* route. PLGA-Cy7.5 NC formulation was selected. Despite the major signal comes from the abdomen, a strong brain signal in the brain is observed after the infusion of the NCs through the right internal carotid artery (ICA) (**Figure 5-2a**). The quantitative analysis shown in **Figure 5-2b** indicates that the retention of NCs in the brain is fast with an intense signal observed after 15 min post injection (p.i.), and within 3 h the brain signal decreases only slightly and maintains an average TRE of ~5 vs. control. At the end of the observation, main organs including brain, heart, lungs, liver, spleen, kidneys, and bladder are collected.

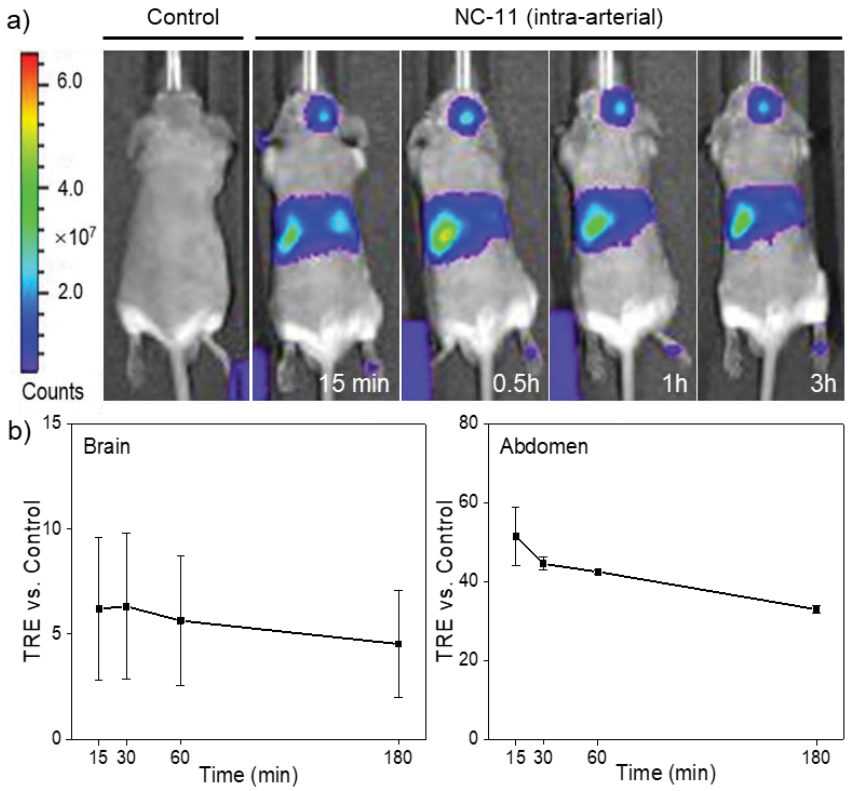

Figure 5-2. a) Representative whole-body *in vivo* NIRF images obtained at different time points after intracarotid infusion of NCs; b) Quantification of the *in vivo* brain and abdomen signals of NCs along time expressed as the averaged organ TRE *vs.* the control mouse (n = 2, mean ± SEM).

Figure 5-3a shows a representative *ex vivo* fluorescence image of those organs and **Figure 5-3b** shows the quantified result of the biodistribution of the NCs. Ipsilateral brain hemisphere accumulation is seen and dominant liver and spleen accumulation is observed.

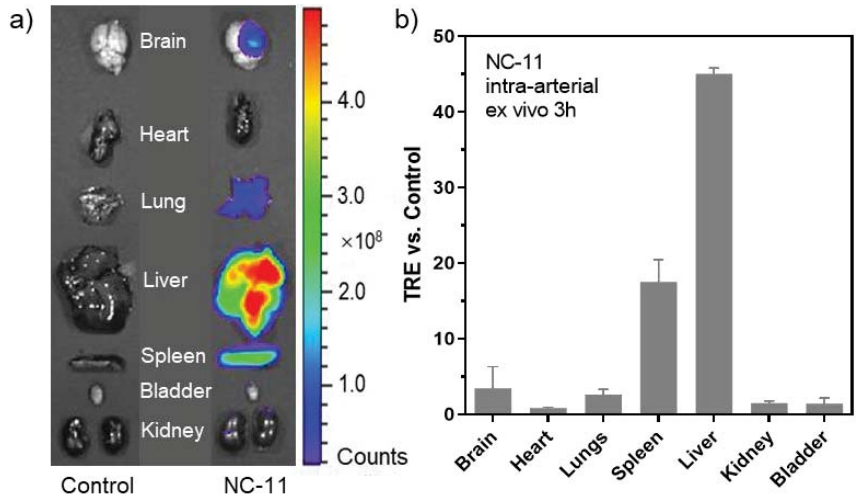

Figure 5-3. a) representative *ex vivo* NIRF images of excised organs at the end of the *in vivo* experiment; b) *ex vivo* quantification of the distribution of NCs expressed as the averaged organ TRE *vs.* the control mouse (n = 2, mean ± SEM).

Secondly, MRI was used to support the accumulation of NCs in the ipsilateral brain, as the MRI monitors the signal from the SPIONs, another component of the NCs, and has higher spatial resolution than NIRF. In **Figure 5-4**, the biodistribution of NCs through *i.v.* and *i.a.* administration is compared. The T2 weighted MRI images of the mouse head in **Figure 5-4b** clearly show the contrast from SPIONs as black dots in the ipsilateral brain resulted from *i.a.* administration of NCs (right image), while this is not observed by *i.v.* administration (left image). MRI results are consistent with the *ex vivo* NIRF imaging result shown in **Figure 5-4a**, the brain TRE increases by ~ 4-fold when using *i.a.* route and the brain slices clearly show the ipsilateral location of the NCs. Note that the lung TRE decreases by ~ 2-fold compared to *i.v.* injection, indicating that the amount of NCs reaching the pulmonary circulation might be reduced through the *i.a.* route.

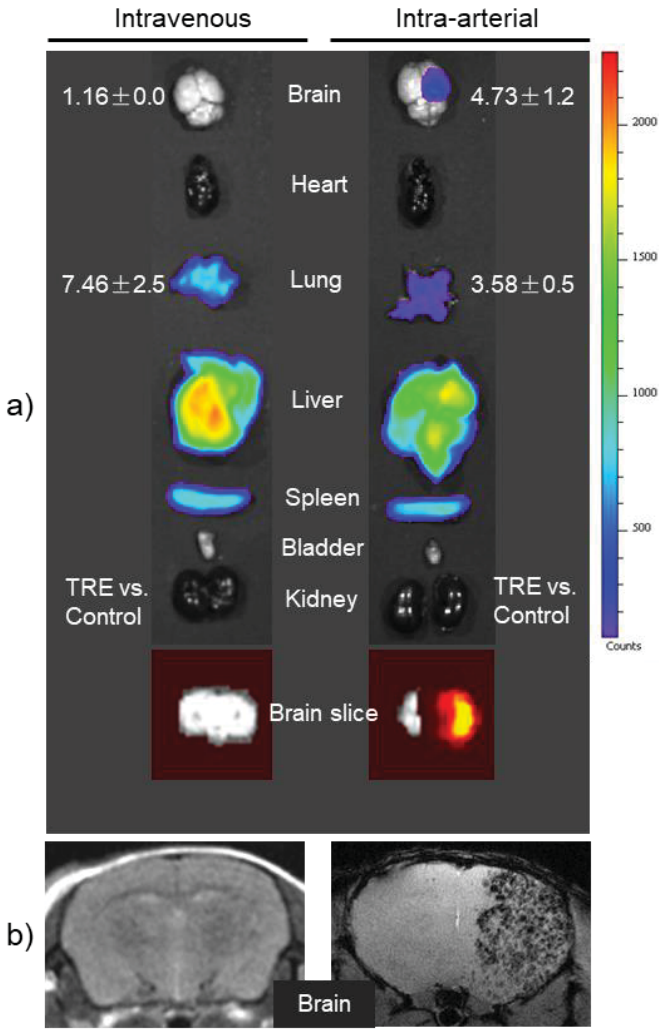

Figure 5-4. Comparison of the biodistribution of NCs through different administration routes, tail vein and intracarotid respectively. a) representative *ex vivo* NIRF images of excised organs at the end of the *in vivo* experiment and the quantitative values; b) representative *in vivo* T2 weighted MRI images of the mouse head after the administration of NCs (left *i.v.*, right *i.a.*).

In general, the mutual support information from MRI and NIRF imaging by monitoring different components of the NC formulation successfully confirms the improvement of brain accumulation. Further experiments need to be conducted regarding magnet implantation to study the magnetic retention effect. Also, the MRI can be combined with NIRF and PET imaging to make a match of the localization of NCs monitored by the different imaging components.

5.2 Evaluation of the therapeutic NC formulation

5.2.1 Protein loading and release profile using BSA

Table 5-1 describes some of the assays we have cinducted to have quantitative total protein loading and encapsulation efficiency values of EPCs-secretome encapsulated in the PLGA NCs. Unfortunately, many protein quantification methods available in the market show interference either with the EBM (the EPCs-secretome media), e.g., BCA assay/CBQCA assay, or with the nanocarrier itself, e.g., Bradford assay. It is also difficult to find a lysis protocol that ensures a total release of the proteins from inside the NCs being at the same time compatible with the protein assay method. Besides, even though some sensitive enzyme immunoassays can quantify specific proteins, the large amount of proteins in the secretome required high-sensitivity methods.

As mentioned, **Table 5-1** I briefly summarize and explain some of the lysis protocols we have essayed and the encountered difficulties with the protein quantification methods. Finally, the Lysis protocol-4 combined with CBQCA protein assay was selected and BSA as a model protein cargo was used to estimate the protein loading ability and release kinetics of the NCs. It provided a simple protein quantification approach to mimic the loading and release conditions of therapeutic proteins in the NC formulation.

Empty NCs (NC.PLGA_6wt%SPIONs_H_2O) with water encapsulated during synthesis were first lysed following Lysis protocol-4 and measured by CBQCA assay to be used as a control. Then NCs loaded with BSA (NC.PLGA_6wt%SPIONs_BSA) were tested. As listed in **Table 5-2**, when 0.05 mL of 30 mg/mL BSA is used for encapsulation, the final measured BSA loading is around 11 μg/mg NCs (1.1 wt%) with an encapsulation efficiency (EE%) *circa* to 40%. The protein loading is much higher than the reported value (0.03 wt%) of vessel endothelial growth factor loaded PLGA NCs[4] and the EE% is comparable to the PLGA NCs loaded with neurotrophin-3 (47 ± 2%) or brain-derived neurotrophic factor (47 ± 7%)[5].

Table 5-1. Lysis protocols studied to break the NCs and release the secretome loaded. The corresponding compatibility of the protocols with several protein quantification methods is summarized.

Lysis protocol-1	10 mg NCs in 1 mL DMSO + 5 mL H_2O (1% SDS, 0.1 M NaOH).
	Bradford assay: SDS interferes, DMSO interferes (>10%).
Lysis protocol-2	10 mg NCs in 0.5 mL DMSO + 5 mL PBS, concentrate the solution with 3 kDa centrifugal filter.
	Bradford assay: No signal differences between EBM and CM loaded NC samples, the protein concentration may below the detection limit.
Lysis protocol-3	10 mg NCs in 0.1 mL DMSO + 1 mL PBS, concentrate the solution with 3 kDa centrifugal filter.
	Bradford assay: The protein can be detected in the lysis media but the hard eliminated SPIONs in the media add positive signal.
Lysis protocol-4	10 mg NCs in 0.1 mL DMSO.
	CBQCA assay: This lysis protocol is simple and NCs fully dissolved with a much higher concentration. Neither the nanocarrier nor the solvent interferes. Only the EBM loaded interferes.
Comments	BCA assay interferes with EBM where the secretome is in, and it is hard to find a proper lysis protocol to break the NCs. Bradford assay does not interfere with EBM, but it's also hard to find a proper lysis protocol that the protein concentration in the lysis media is enough to detect without the interference of the nanocarrier. CBQCA assay is compatible with DMSO which can fully dissolve and break the NCs, and the nanocarrier itself does not interfere. So if the incompatible EBM can be eliminated, Lysis protocol-4 will be a good option.
Selected Process	By using Lysis protocol-4 and CBQCA protein assay, it would be a simple way to use a stable and cost-effective model protein BSA as cargo to estimate the protein loading ability and release kinetics of the NCs.

Table 5-2. Protein loading and encapsulation efficiency (EE%) of NC.PLGA_6wt%SPIONs_BSA (n=6) measured by CBQCA assay using Lysis protocol-4. Centrifugation for 3x times of 15 min at 9391 rcf is used to wash and recover the NC product.

A	B	C	D	E	F	G	H	I	J
CBQCA protein quantification (100mg NCs/mL DMSO)		**NCs per batch**				**BSA calculations**			
Sample	[BSA] measured (ug/mL DMSO)	NCs (mg)	Pure NCs (mg)[a]	BSA added for encapsulation[b]		BSA measured (ug/NCs batch)	BSA theorical loading (ug/mg NCs)[c]	BSA measured loading (ug/mg NCs)	BSA EE%
				ug/mL	ug				
					*E*0.05*	*B/100*C*	*F/(50+4+F/1000)*	*G/D*	*I/H*
n1	882	43	31	29415	1471	376	27	12	46%
n2	965	43	31	30150	1508	416	27	13	49%
n3	911	41	29	30150	1508	377	27	13	47%
n4	544	43	31	29703	1485	236	27	8	28%
n5	574	43	31	29703	1485	248	27	8	30%
n6	731	45	33	29703	1485	328	27	10	37%
Mean	768	43	31	29804	1490	330	27	11	40%
SD	180	1	1	291	15	74	0	3	9%
NCs recovery method: 3x 15min at 9391 rcf.[d]									

[a]Every NCs batch contains 12mg of trehalose which used as a cryoprotectant during the lyophilizing process.

[b]0.05 mL of 30 mg/mL BSA is added for encapsulation, [BSA] here is double checked by CBQCA.

[c]50 mg of PLGA and 4 mg of SPIONs are added for the NCs fabrication.

[d]After the organic solvent evaporation step the NCs is centrifugated and washed 3 times to remove the PVA.

Table 5-3. Protein loading and encapsulation efficiency (EE%) of NC.PLGA_6wt%SPIONs_BSA (n=6) measured by CBQCA assay using Lysis protocol-4. Centrifugation for 3x times of 30 min at 9391 rcf is used to wash and recover the NC product.

A	B	C	D	E	F	G	H	I	J
CBQCA protein quantification (100mg NCs/mL DMSO)		**NCs per batch**				**BSA calculations**			
Sample	[BSA] measured (ug/mL DMSO)	NCs (mg)	Pure NCs (mg)[a]	BSA added for encapsulation[b]		BSA measured (ug/NCs batch)	BSA theorical loading (ug/mg NCs)[c]	BSA measured loading (ug/mg NCs)	BSA EE%
				ug/mL	ug				
					*E*0.05*	*B/100*C*	*F/(50+4+F/1000)*	*G/D*	*I/H*
n1	831	46	34	29415	1471	386	27	11	42%
n2	847	47	35	30150	1508	399	27	11	42%
n3	771	49	37	30150	1508	382	27	10	38%
n4	427	48	36	28543	1427	206	26	6	22%
n5	451	48	36	28543	1427	218	26	6	23%
n6	400	48	36	29670	1483	193	27	5	20%
Mean	621	48	36	29412	1471	297	27	8	31%
SD	216	1	1	730	37	101	1	3	10%
NCs recovery method: 3x 30min at 9391 rcf.[d]									

[a]Every NCs batch contains 12mg of trehalose which used as a cryoprotectant during the lyophilizing process.

[b]0.05 mL of 30 mg/mL BSA is added for encapsulation, [BSA] here is double checked by CBQCA.

[c]50 mg of PLGA and 4 mg of SPIONs are added for the NCs fabrication.

[d]After the organic solvent evaporation step the NCs is centrifugated and washed 3 times to remove the PVA.

As 50 mg of PLGA and 4 mg of OA-SPIONs are used to fabricate NCs and the pure NCs obtained per batch is around 31 mg (**Table 5-2**), a NC yield around 57% is calculated. To recover more product a longer centrifugation time at the NC washing and recovering step was also tried. As shown in **Table 5-3**, a longer time (3x, 30 min) is used compared to the normal time (3x, 15 min) in **Table 5-2**. As expected an average of 5 mg more NCs is recovered without affecting the morphology and size distribution of NCs (see SEM and DLS data in **Figure 5-9**). However, the measured BSA loading (~ 8 μg/mg NCs) and EE% (~ 31%) are not improved. We hypothesize that with a longer centrifugation time the increased mass comes from the lighter particles in the supernatant, these lighter particles formed after the second emulsification process and might be defective or just consisting of solid PLGA decreasing the final EE%. So the NC recovery protocol is fixed as 3x times of 15 min centrifugation (**Table 5-2**).

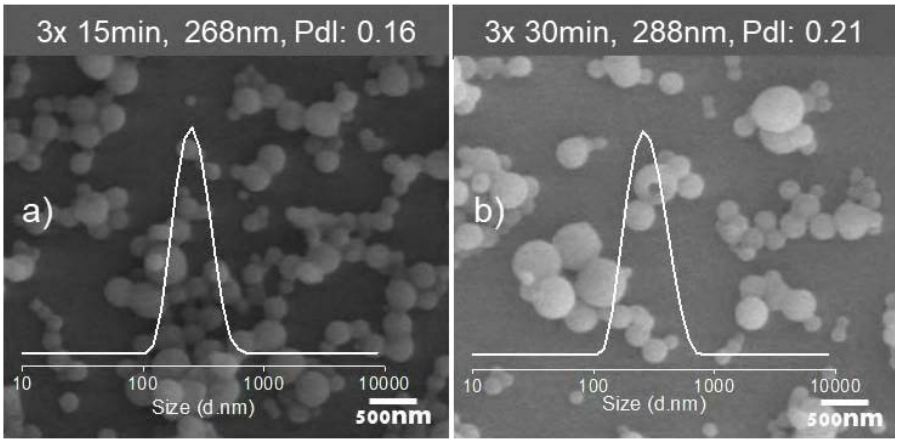

Figure 5-9. SEM morphologies and DLS size distributions of lyophilized NCs recovered from different centrifugation times at the washing step. a)3x 15 min; b) 3x 30 min.

The protein release profile is then studied *in vitro* for two weeks by incubating NCs in PBS under constant rotation at 37°C. Results showed a sustained BSA release with almost ~ 51% of the total cargo discharged over a period of two weeks (**Figure 5-10a**), the process was faster during the first week (48% discharged). The monitored morphologies of NCs by SEM at different incubating time points (**Figure 5-10c**) offer us a visual understanding of the degrading dynamics of the NCs and the release profile. At day 1, holes began to appear on the PLGA shell while after 7 days more and bigger holes

could be visualized and the size of NCs increased by 48% in diameter (**Figure 5-10b**). This significant increase of the NC size after 7 days may be due to the permeation of water through the cracks and holes of the PLGA shell and the simultaneous swelling of the PLGA together with the diffusion of protein outside of the NCs. As seen in **Figure 5-10a** and **b**, the noticeable protein release during the first week is in good agreement with the increase of NCs size during this time. From day 7 to day 14, the NCs size does not vary resulting from the already fully water filling of the core and the fully wetting of the PLGA shell after 7 days, in which process the majority of protein has been discharged decreasing the release rate after 7 days. After 14 days completely broken NCs were observed and after 21 days the spherical morphology of NCs was destroyed. The observed incomplete release may result from the adsorption of protein on PLGA[6, 7].

It is noteworthy that the erosion rates of NCs are quite different when compared NCs evolution in different media. For instance, in EBM (**Figure 5-10c inset**) many more holes appear on the NCs as compared to PBS at the same incubation condition, meaning a faster release in EBM. Considering a much more different environment *in vivo*, it is extremely difficult to mimic and understand the real release situation *in vivo*.

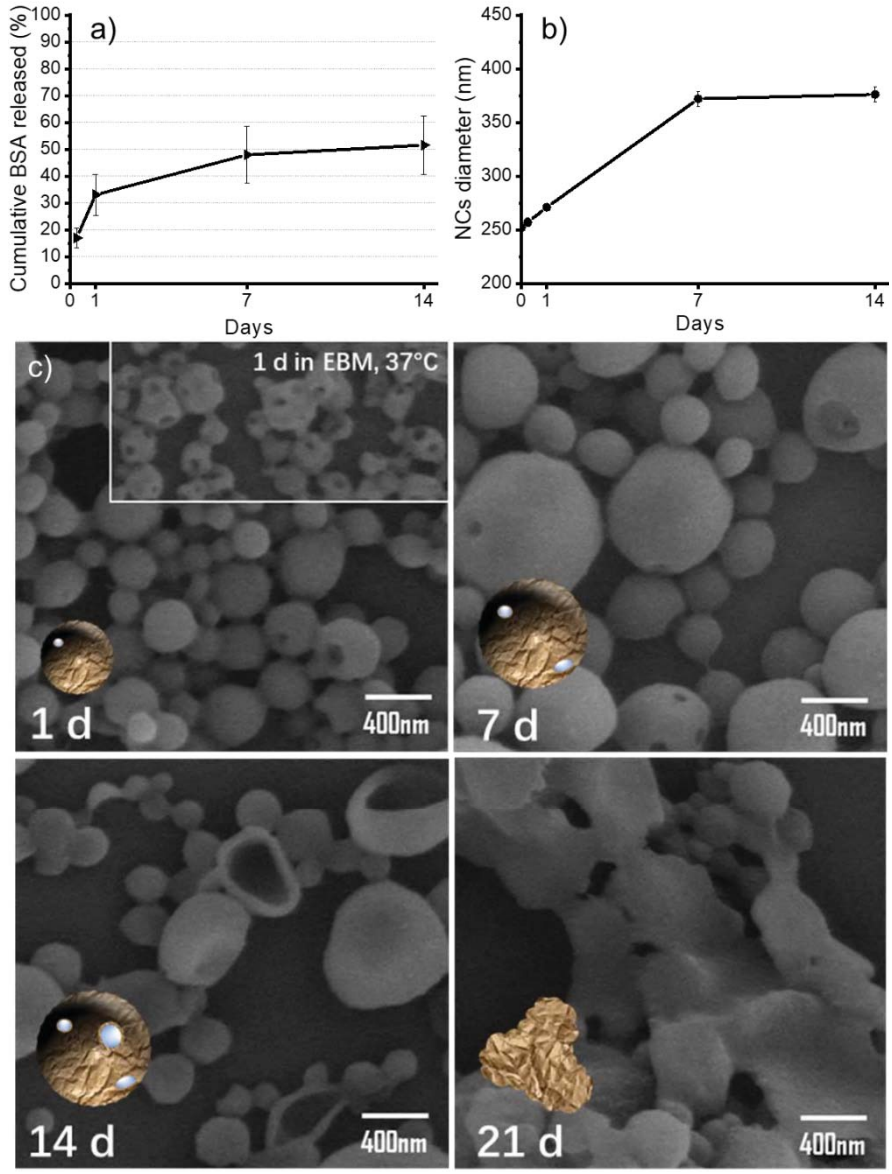

Figure 5-10. a) *In vitro* protein release profile of NC.PLGA_6wt%SPIONs_BSA incubated in PBS under constant rotation at 37°C (n = 6, mean ± SEM); b) The corresponding average size of NCs at each incubating time point obtained from SEM images (NCs counted = 300, mean ± SEM); c) The corresponding SEM morphologies of the NCs obtained after each incubating time point. Inset is the NCs incubated in EBM in the same condition.

Even though our simple formulation of magnetic PLGA NCs loaded with therapeutic proteins will be used as the drug delivery system for

potential clinical translation, it is also helpful to know if the imaging functionalization of the NC formulation affects the protein loading and release. I have already shown that the size and morphology of the NC formulation are not affected by all the imaging functionalization. Here, I select the PLGA-BPLP NCs system as representative of PLGA modified system to evaluate the protein loading and release profiles since PLGA-BPLP is a synthetic polymer with BPLP in the molecular backbone, which may significantly alter the properties of pure PLGA.

The protein loading of PLGA-BPLP NCs (NC.90wt%PLGA-BPLP_ 6wt%SPIONs_BSA) was determined using the same Lysis protocol-4 combined with CBQCA protein assay. The measured BSA loading content is ~10 μg BSA/mg NCs (1 wt%) with an EE% of around 40%, values of which are very similar to those of the PLGA NCs (NC.PLGA_6wt%SPIONs_BSA) shown in **Table 5-2**, indicating the incorporation of PLGA-BPLP polymer as high as 90wt% in the NC shell does not affect the protein encapsulation. The *in vitro* release experiment shows that 32% of total encapsulated protein mass is released in one week with a faster release at the early stages (**Figure 5-11**), without significant difference compared to the PLGA NCs. The amount of released protein in one week is similar when indirectly measured from the pellet retained protein (**Figure 5-11b&c**), although the release profile shows a more sustained pattern over time, which could be associated with the protein that is trapped within the PLGA polymer. In conclusion, the protein loading and release profile of the imaging functionalized NC formulation also do not change, which are crucial for the theranostic study of the NC formulation at the preclinical stage.

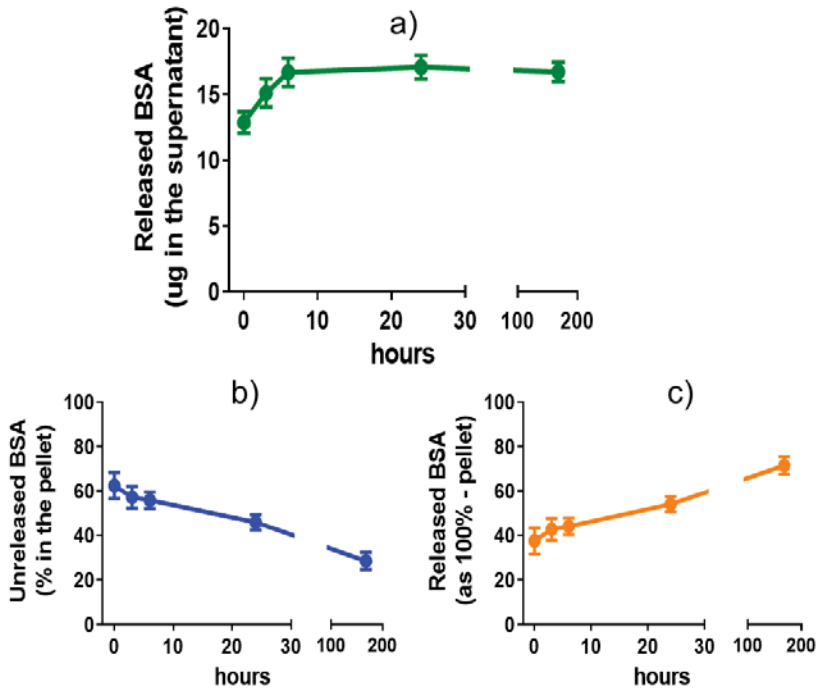

Figure 5-11. Protein release temporal profile of the NCs. a) to c) NC-5 in PBS (10 mg/mL) are incubated at 37 °C in rotation. a) the released BSA is quantified as total mass of protein released in the supernatant; b) and c) BSA content in the remaining NCs pellet by DMSO lysis and the released BSA calculated indirectly from the pellet values, the percentage is calculated versus intact unreleased NCs lysated also in DMSO (n = 8, values represent mean ± SEM).

5.2.2 EPCs secretome encapsulation and the angiogenesis effect

As introduced in Section 1.1.2, the utilization of EPCs secretome might be a safe and effective cell-free option among therapeutic strategies for ischemic stroke but at the same time is a very complex therapeutic agent. The secretome is harvested in the conditioned medium (CM) as illustrated in **Figure 5-12**. The VHIR group has realized proteomics analysis of the EPC-secretome showing the abundance of many different proteins, with more than 1,000 proteins being identified (unpublished data). Numerous factors of potential relevance in angiogenesis[8, 9] were detected such as tissue plasminogen activator, ephrin receptors and matrix metalloproteinases. Also, several growth factors (GF) were identified including VEGF, insulin-like GF, connective tissue GF and hepatoma derived GF. Moreover, previous *in vivo* work showed significant

enhancement of angiogenesis in CM treated animals with vessel density increase in peri-infarct tissue at two weeks.[10]

To load a high amount of secretome in the PLGA nanocarrier, the harvested CM was concentrated two times using centrifugal filter to get concentrated CM (cCM) and super concentrated CM (scCM), as shown in **Figure 5-12**. Compared to the initial CM, the cCM and scCM is of ~25x and ~70x more concentrated respectively.

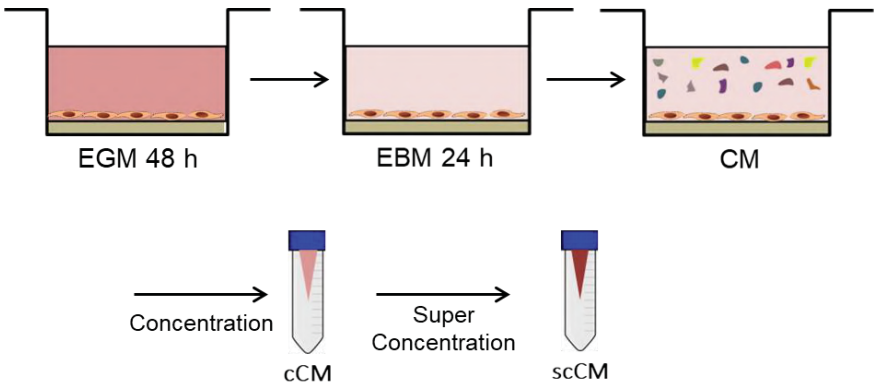

Figure 5-12. Schematic illustration of the processes of harvest and concentration of EPCs-secretome. EGM: endothelial growth medium, EBM: endothelial basal medium, CM: conditioned medium.

Then the obtained scCM was encapsulated into the PLGA NCs using the same double emulsion solvent evaporation method as elaborated in Section 2.1.2, scEBM without secretome was also encapsulated as control. Importantly, the lyophilized NCs present homogeneous spherical morphologies (**Figure 5-14**) which are similar to those NCs encapsulating BSA.

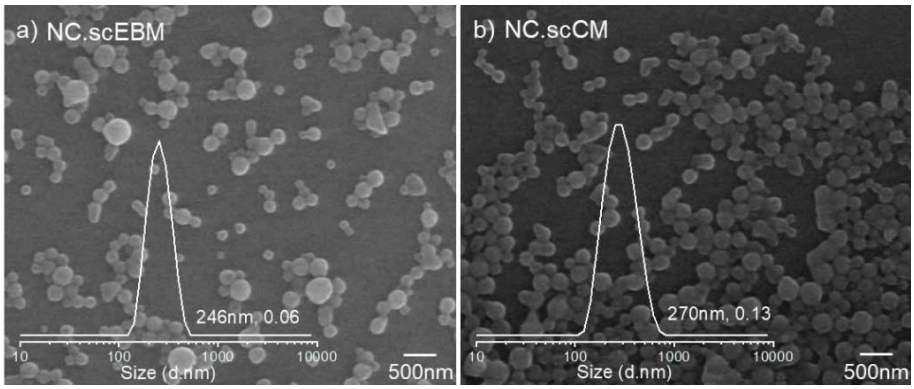

Figure 5-14. Representative SEM morphologies of the lyophilized NCs loaded with scEBM/scCM. Insets are the DLS size distributions (average d.nm, PdI) of the NCs by % intensity.

Then, *in vitro* cell proliferation of CM and CM loaded NCs on human brain endothelial cells were investigated as shown in **Figure 5-15a&b**. As expected, both cCM and scCM show human brain endothelial cells proliferation (**Figure 5-15a**), which is an indicator for angiogenesis[4]. Surprisingly both the scEBM and scCM loaded NCs show cell proliferation at different concentrations compared to the vehicle cells treated with scEBM (**Figure 5-15b**), and the cell proliferation effect derives from scCM NCs cannot be extracted. We thus hypothesize that the nanoparticle itself can stimulate the proliferation of cells, and the amount of loaded scCM is not high enough to produce a significant cell proliferation. As demonstrated in **Figure 5-15c**, compared to the vehicle both empty NCs with and without SPIONs show a certain degree of cell proliferation. By monitoring the PLGA NCs in EBM (**Figure 5-15d**), degraded PLGA was observed which may serve as a carbon source for the cells under *in vitro* condition. As has been claimed by V. Préat *et al.*, the lactate, one of the hydrolysis products of PLGA, has a key role in biochemical pathways and could exert therapeutic effects such as angiogenesis[11, 12]. This deserves further investigations.

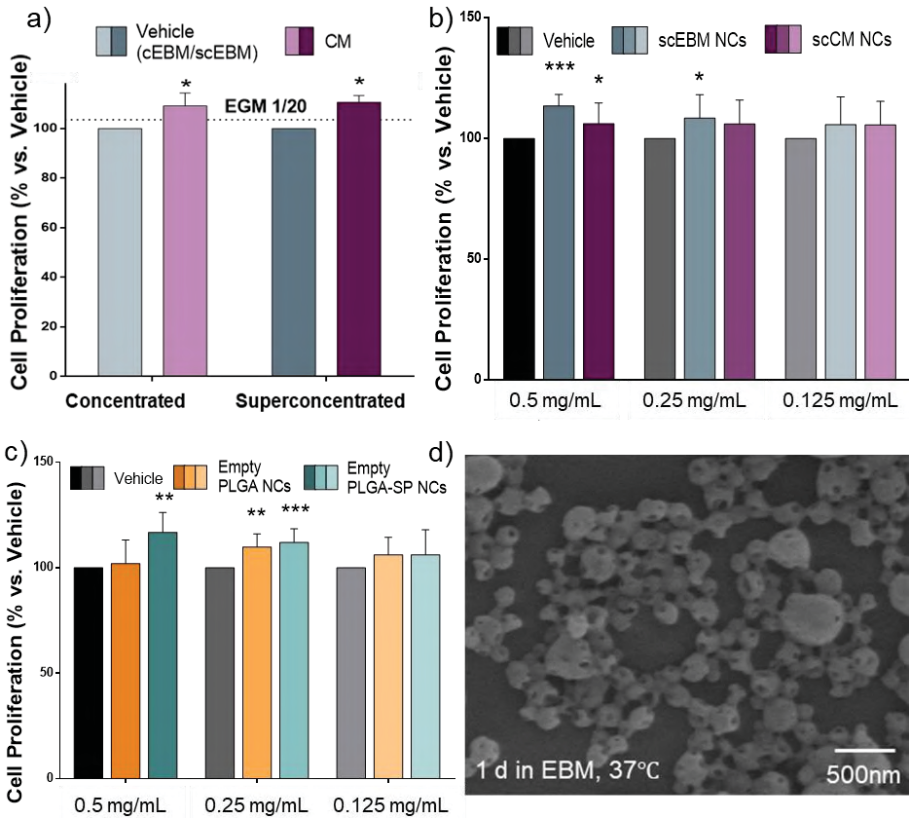

Figure 5-15. Proliferation of human brain endothelial cells (hCMEC/D3 cell line) in EBM treated by a) cEBM/cCM (n=6) and scEBM/scCM (n=5); b) scEBM/scCM loaded NCs (n=8) and c) empty NCs with (n=5) or without (n=7) SPIONs. Values represent mean ± SEM. Cells treated by scEBM is used as vehicle. d) Representative SEM morphology of NCs incubated in EBM after 1 day at 37°C.

Previous work on isolated VEGF encapsulation and subsequent administration to cell culture has yielded an increased rate in endothelial cell proliferation and viability[4]. Nevertheless, in those assays, a larger initial amount of a well-established angiogenic inducer VEGF is employed. Therefore, and taking into account that not all the proteins present in EPCs-secretome play a role in angiogenesis, we speculate on a too low bioactive content inside the NCs as a possible cause of the observed mild effect in the *in vitro* assays. This is probably due to the fact that current protein, or other bioactive molecules, concentration in the scCM is still too low for encapsulation purposes. To circumvent this issue, we propose to lyophilize the collect after the two times' concentration by centrifugal filter and re-suspend it in a smaller volume to further concentrate the

secretome and then do the encapsulation. Meanwhile, Pure Biologics Inc., a collaborator in this project, is trying to improve the cell culture protocol to increase the production of secretome.

Assays to increase secretome load are listed in **Table 5-5**, scCM is further concentrated for 10x (~4mg/mL protein measured) and 20x (~10mg/mL) by lyophilizing and re-suspending in a smaller volume and then used for NC fabrication, scEBM is equally done as control.

Table 5-5. Summary of the effect of lyophilizing concentration times of the encapsulated scEBM/scCM on the morphology of the NCs. The protein concentration of the medium is determined by Bradford assay.

NC sample	NC Morphology	Medium used for encapsulation (50 μL)[a]	
		Concentration times	Protein concentration (pre-/post- lyophilization)
NC.scEBM-10X	GOOD	10X	—
NC.scCM-10X	GOOD		0.4/4 mg/mL
NC.scEBM-20X	BAD	20X	—
NC.scCM-20X	BAD		0.5/10 mg/mL

[a] The scCM is lyophilized and re-suspended in a smaller volume to further concentrate the protein, 50 μL of the further concentrated medium is used for encapsulation. The scEBM is lyophilized equally and encapsulated as control.

However, the NCs lost the integrity of the spherical shell membrane when encapsulating scCM/scEBM-20x, as observed from the SEM images in **Figure 5-16c&d**, which means that such highly concentrated secretome cannot be well encapsulated. Considering the protein concentration of scCM-20x (~10mg/mL) is much less than that of the BSA solution (~30mg/mL) we use for encapsulation, and even the scEBM-20x has no protein, we exclude the possibility that the higher protein concentration in post-lyophilized media affects the formation of NCs. Probably at a much high density, certain amphiphilic ingredients (confidential) in the commercial EBM may interrupt the formation of clear inner water-oil interface at the first emulsion step during NC fabrication, or certain macromolecules in the medium at a high density could increase the viscosity of the inner water phase and change the condition to be emulsified and encapsulated. The ingredients in EBM are clearly seen in a solid form after lyophilization of scEBM/scCM (**Figure 5-16e**). And a faster erosion speed of NCs incubated in EBM is also observed with bigger holes appear on the surface of NCs (**Figure 5-15d**), which indicates

the EBM does have an impact on the PLGA shell. At a relatively lower concentration of 10x post-lyophilization, the morphologies of NCs are maintained (**Figure 5-16a&b**).

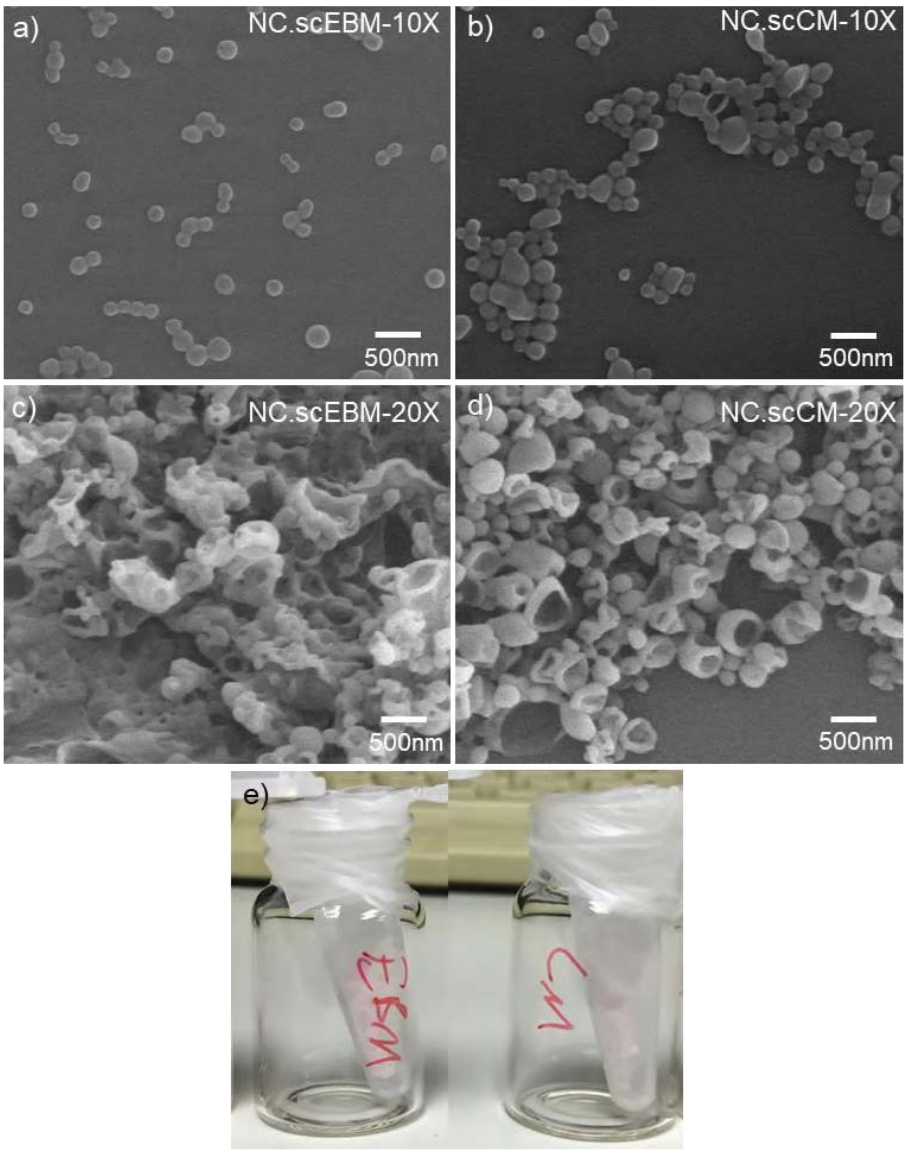

Figure 5-16. a)-d) representative SEM morphologies of the NCs loaded with lyophilized further concentrated scEBM/scCM as listed in Table 5-5; e) images of the lyophilized dry EBM/CM.

Then we use the CM produced by Pure Biologics Inc. (PBCM) with a higher initial protein concentration (~3mg/mL) to do the lyophilizing concentration (5x, ~15mg/mL) and encapsulation. As discussed in

Table 5-1, it is not so easy to find a NC lysis protocol and protein quantification method to measure the total protein amount in the secretome loaded NCs. However, we concentrate in detecting several specific proteins from the secretome in the NC lysate using the Lysis protocol-4 combined with multiplex magnetic immunoassay. This kind of immunoassay can quantify several secreted proteins simultaneously and is proved to be compatible with the NC lysate. As listed in **Table 5-6**, four secreted proteins, VEGF, pentraxin 3 (PTX3), granulocyte-macrophage colony-stimulating factor (GM-CSF) and angiogenin (Ang) were monitored for both PBCM and PBCM loaded NCs. The detected concentrations of the four proteins in the CM are multiplied and consistent with the increase in protein concentrations of PBCM (3mg/mL) to PBCM-5x (15mg/mL), indicating a coherence of the Bradford assay and the multiplex magnetic immunoassay. For the CM loaded NCs, the loads of these four proteins show well multiplying increase for NC.PBCM-5x as compared to NC.PBCM (**Table 5-6**). A previous study by F. Felice *et al.* (2018) using multiblock α-methoxy-ω-2-(N,N-diethanolamino) ethyl *-co-* poly(ethylene glycol) *-co-* polylactide *-co-* pyromellitic dianhydride (mE2N-PEG-PLA-PMDA) copolymeric NPs to deliver EPCs secretome to ischemic hindlimb showed a VEFG loading of 5.3 pg/mg NPs and a significant increase of blood perfusion in the hindlimb after 2 weeks.[14] Thus our EPCs secretome loaded NC.PBCM-5x with a detected VEGF load of 13.7 pg/mg NCs which is much higher than the load of 5.3 pg/mg NPs reported is expected to have a promising therapeutic effect considering the higher secretome load.

Table 5-6. PBCM and lyophilizing concentrated PBCM-5x were loaded into the NCs. The selected four proteins (VEGF, PTX3, GM-CSF, Ang) in the EPCs secretome were monitored for both PBCM and PBCM loaded NCs by multiplex magnetic immunoassay.

	VEGF	PTX3	GM-CSF	Ang
	NC (pg/mg NC),		PBCM (pg/mL CM)	
NC.PBCM	3.5	8.0	1.8	8.3
PBCM (3mg/mL)	1280.6	35204.1	755.1	1678.6
NC.PBCM-5X	13.7	32.1	5.3	32.5
PBCM (15mg/mL)	2894.7	83345.9	1729.3	5614.0

The SEM morphologies of the PBCM encapsulated NCs are shown in **Figure 5-17**, NCs maintain the integrity.

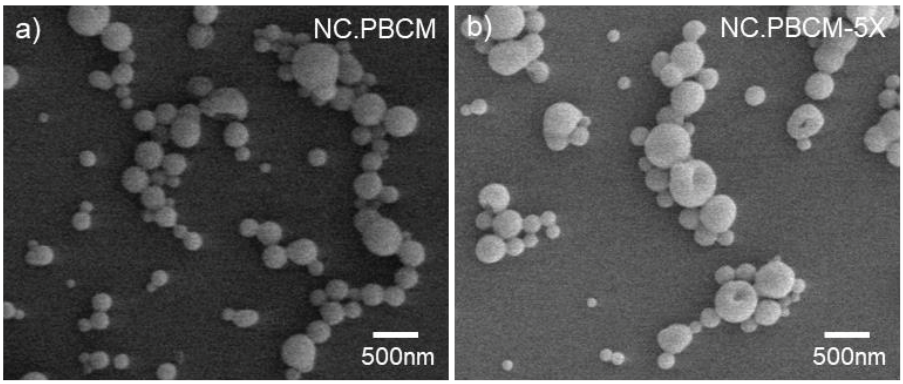

Figure 5-17. a)-c) representative SEM morphologies of the NCs loaded with PBCM as listed in Table 5-6.

Loading of EPCs-secretome into PLGA NCs has scarcely been done before and we do meet many problems regarding the quantification of secretome loading and release. Even though, we obtained reasonable results regarding the four proteins' loading amounts of NC.PBCM and NC.PBCM-5x by multiplex magnetic immunoassay (**Table 5-6**). Problems also occur for the *in vitro* secretome release study in PBS, even though we detected the existence of secretome in the release medium but the expected increasing accumulative release did not occur (data not shown) as we have observed in the case of NCs loaded with BSA. We believe this may be due to the limitation of the protein detection methods and further experiments need to be done to localize the interferences and reconfirm the results obtained. At least, by using the model protein BSA discussed in the last section, we have acquired understandings about the protein loading ability and release profile of the PLGA NCs.

At present, the NC.PBCM-5x (15mg/mL) listed in **Table 5-6** shows the best secretome loading performance with detected reasonable higher proteins load. Taking into account that PLGA NCs have a fast erosion rate in EBM, the loaded secretome is expected to be well released in cell culture media. Future experiments will be directed to investigate the cell proliferation effect and bioactivity of this improved therapeutic NC formulation.

5.3 Chapter summary

The developed multimodal imaging functionalized PLGA NC formulation was successfully used for *in vivo* tracking. The mutual support information from MRI and NIRF by monitoring different components of the NC formulation proved the higher NC brain accumulation through the *i.a.* administration route.

The measured protein loading content is ~10 µg BSA/mg NCs (1 wt%) with an EE% *circa* 40%. The *in vitro* protein release study in PBS showed a sustained BSA release with almost ~51% of the total cargo discharged over a period of two weeks. Moreover, the imaging functionalization does not affect the protein loading and release profile of the NCs.

Finally, we could concentrate the harvested therapeutic EPCs-secretome medium by two methods: through centrifugal filter and a 10-times concentration by lyophilizing and redispersing in a smaller volume without affecting the NC morphology after encapsulation. The encapsulation of condensed therapeutic secretome (15mg/mL) resulted in a higher protein loading of NCs. And several proteins (VEGF, PTX3, GM-CSF, Ang) could be successfully detected in the secretome encapsulated NCs with improved loads. Based on the fast erosion rate of NCs in cell culture medium (EBM) we expect that most of the secretome will be quickly released and the *in vitro* endothelial cell proliferation of the therapeutic NCs will be detected.

5.4 Annex of Chapter 5

5.4.1 Intra-arterial administration and *in vivo* NIRF and MRI

The surgical procedures and NIRF imaging experiments were performed at the Vall d'Hebron Research Institute (VHIR) by Dr. Anna Rosell and co-workers, and the MRI at the Nuclear Magnetic Resonance Service from the Universitat Autònoma de Barcelona (SeRMN-UAB). All procedures are approved by the Ethics Committee for Animal Experimentation of VHIR and conducted in compliance with the Spanish legislation and in accordance with the Directives of the European Union.

Intra-arterial administration is performed in BALB/c AnNRj mice (n=2) through the internal carotid artery (ICA) route as described previously[14]. All animals are anesthetized with isoflurane (5% for induction and 1.5% for maintenance in air, 79% N_2:21% O_2) and body temperature is maintained at 37°C. After surgical exposure of the right common carotid artery (CCA) bifurcation into the external carotid artery (ECA) and the internal carotid artery (ICA), the ECA is cannulated with a polyimide micro-catheter (0.2-0.22 mm OD, 0.14-0.15 mm ID) directed to the ICA and connected to an infusion pump at an infusion rate of 75 µL/min (1.6 mg of NCs in 150 µL of saline). After infusion, the micro-catheter is removed, blood flow from the CCA is restored towards the ICA and the arteriotomy site is ligated, the skin is closed and the animal is allowed to recover from anesthesia.

Near-infrared fluorescence (NIRF) imaging is then performed to track the NCs *in vivo* and *ex vivo* after *i.a.* administration using a Xenogen IVIS® spectrum. Mice are anesthetized with isoflurane *via* facemask and images are acquired at 15 min, 30 min, 1h and 3h after administration (λex/λem of 710/820 nm) in dorsal and ventral views of the whole body. After the last scan *in vivo*, animals are euthanized by cervical dislocation and major organs are collected for the *ex vivo* acquisition (λex/λem of 745/820 nm) in dorsal and ventral views of all organs. Control animals are used for each *in vivo* and *ex vivo* acquisition groups as a background measurement. For quantification, ROIs are drawn and TRE [photons/s]/[µW/cm²]) is measured using the Living Image software and corrected by the TRE from the corresponding ROI in the control animal.

MRI is performed as a pilot study to track the NCs *in vivo* after *i.a.*

administration. One BALB/c AnNRj mouse received 1.6 mg of NCs in 150 µL of saline *i.a.* following the protocol mentioned above. For the image acquisition, the animal is anesthetized with isoflurane *via* facemask and temperature is controlled using a heating pad. Coronal T2-weighted images (T2WI) (TR/TE = 8/350 ms, α = 40º, MTX 320x320, slice thickness 0.5mm) are acquired on the whole brain.

5.4.2 BSA loading amount of the NCs and release kinetics

The BSA content of the NC is directly determined using the CBQCA protein assay kit (Invitrogen™ ref. C6667), which determines the protein concentration based on the production of fluorescent products measurable at λex/λem = 450 nm/550 nm via non-covalent interaction between CBQCA and primary aliphatic amines of proteins. This highly sensitive fluorescence-based method shows compatibility with DMSO, SPIONs, detergents, and other substances that interfere with other commonly used protein determination methods. Lyophilized NCs encapsulating albumin as well as empty NCs as control are fully dissolved in DMSO at 100 mg/mL. The protein contents in the NCs lysates are measured and calculated based on the difference in fluorescence with the control and a calibration curve drawn with standard albumin solutions, the protein contents in the BSA solutions used for encapsulation are also measured. All of the measurements are performed in duplicate for each NC batch. The experimental BSA loading in the NCs is expressed as µg of BSA per mg of NCs (µg/mg) or the wt% of the NCs, and the BSA EE% is calculated, as follows:

$$EE\%\ BSA = \frac{Experimentally\ measured\ BSA\ loading}{Nominal\ BSA\ loading} \times 100\%$$

For the release studies, lyophilized NCs are resuspended in phosphate buffered saline (PBS) (pH 7.4, Sigma ref. D1408) at 10 mg/mL in low protein binding microcentrifuge tubes (Thermo Scientific© ref. 90410). NCs solutions are incubated at 37 °C in a vertical rotator for different time measures to simulate the *in vivo* environment: right after the resuspension (time=0s), and after 3 h, 6 h, one day, and seven days of incubation. In all cases, an aliquot of 200 µL is frozen at −80 °C until protein determination. Before the CBQCA assay, the aliquots are centrifuged at 15,000× g rcf to separate the supernatant. The amount of protein released is directly calculated as the percentage of total released protein in the supernatant compared with the intact NCs fully dissolved in DMSO used as the 100% release set

up. BSA-loaded NCs batches and one H_2O-NCs batch as control are used and measures are done in duplicate. The release profiles are expressed in terms of cumulative release and plotted vs. time.

5.4.3 Harvest of EPCs-secretome and *in vitro* cell proliferation

This was performed at the Vall d'Hebron Research Institute by Dr. Anna Rosell and co-workers.

Human EPC cultures are obtained from blood samples of stroke patients as detailed elsewhere[16]. EPCs are seeded in a fibronectin-coated flask in Endothelial Cell Growth Medium (EGM, Lonza) complemented with 10% FBS and kept in a 5% CO_2 incubator at 37°C. When EPCs reach a ~80% confluence, they are thoroughly washed with PBS and kept in Endothelial Basal Medium (EBM, Lonza) for 24h. Then, all the extracellular medium is collected and concentrated by two centrifugation steps with 3K filter (Amicon Ultra, Merck Millipore, Germany) to obtain the concentrated CM (cCM) and super concentrated CM (scCM). The products are kept at -80°C until use.

The cell proliferation effect of CM and CM loaded NCs on human brain endothelial cells (hCMEC/D3) is assessed by performing a viability assay with 3-(4-5-dimethylthiazol-2-yl)-2,5-diphenyl tetrazolium bromide (MTT). In short, 2×10^4 viable cells are distributed on a 24-well plate in 400 µL endothelial growth media (EGM2 from Lonza with 2% fetal bovine serum and half the amount of the growth factors included in the kit) and incubated for 24 h at 37 °C and 5% of CO_2. After this period, culture supernatants are substituted with basal cell culture media (EBM, serum free) containing CM or NCs at different concentrations. The MTT assay is performed after 48 h of incubation, and the absorbance of the resulting formazan crystals diluted in DMSO is determined at 540 nm. Cell viability is referred to as the percentage of viability compared with the control conditions.

5.4.4 Multiplex immunoassay of the secretome loaded NCs

Four secreted proteins, VEGF, PTX3, GM-CSF and Ang in the secretome were analyzed using the multiplex immunoassay (R&D Systems, Inc.). This assay utilizes a mixture of color-coded superparamagnetic beads coated with different analyte-specific capture antibodies. After adding the sample to the mixture, the magnetic beads capturing analytes in the sample are detected using a

cocktail of biotinylated detection antibodies and a streptavidin-phycoerythrin conjugate, and read using the Luminex MAGPIX® Analyzer. The samples of lyophilized NCs encapsulating secretome were fully dissolved in DMSO at 100 mg/mL. The contents of the four proteins in the NC lysates were measured and calculated based on a calibration curve drawn with standard protein solutions, the four proteins' contents in the initial CM media used for encapsulation were also measured.

5.5 Chapter references

[1] J. Lundberg, E. Södersten, E. Sundström, K. Le Blanc, T. Andersson, O. Hermanson, S. Holmin, Targeted intra-arterial transplantation of stem cells to the injured CNS is more effective than intravenous administration: engraftment is dependent on cell type and adhesion molecule expression, *Cell Transplantation* 21(1) (2012) 333-343.

[2] V. Misra, M.M. Ritchie, L.L. Stone, W.C. Low, V. Janardhan, Stem cell therapy in ischemic stroke: role of IV and intra-arterial therapy, *Neurology* 79(13 Supplement 1) (2012) S207-S212.

[3] L. Li, Q. Jiang, G. Ding, L. Zhang, Z.G. Zhang, Q. Li, S. Panda, M. Lu, J.R. Ewing, M. Chopp, Effects of administration route on migration and distribution of neural progenitor cells transplanted into rats with focal cerebral ischemia, an MRI study, *Journal of Cerebral Blood Flow & Metabolism* 30(3) (2010) 653-662.

[4] E. Carenza, O. Jordan, P. Martinez-San Segundo, R. Jiřík, Z. Starčuk Jr, G. Borchard, A. Rosell, A. Roig, Encapsulation of VEGF 165 into magnetic PLGA nanocapsules for potential local delivery and bioactivity in human brain endothelial cells, *Journal of Materials Chemistry B* 3(12) (2015) 2538-2544.

[5] M.M. Pakulska, I.E. Donaghue, J.M. Obermeyer, A. Tuladhar, C.K. McLaughlin, T.N. Shendruk, M.S. Shoichet, Encapsulation-free controlled release: Electrostatic adsorption eliminates the need for protein encapsulation in PLGA nanoparticles, *Science Advances* 2(5) (2016) e1600519.

[6] S. Fredenberg, M. Wahlgren, M. Reslow, A. Axelsson, The mechanisms of drug release in poly (lactic-co-glycolic acid)-based drug delivery systems—a review, *International Journal of Pharmaceutics* 415(1-2) (2011) 34-52.

[7] Y. Wei, Y.X. Wang, W. Wang, S.V. Ho, F. Qi, G.H. Ma, Z.G. Su, Microcosmic mechanisms for protein incomplete release and stability of various amphiphilic mPEG-PLA microspheres, *Langmuir* 28(39) (2012) 13984-13992.

[8] D. Bouïs, Y. Kusumanto, C. Meijer, N.H. Mulder, G.A. Hospers, A review on pro-and anti-angiogenic factors as targets of clinical intervention, *Pharmacological Research* 53(2) (2006) 89-103.

[9] G. Pula, U. Mayr, C. Evans, M. Prokopi, D.S. Vara, X. Yin, Z. Astroulakis, Q. Xiao, J. Hill, Q. Xu, Proteomics identifies thymidine phosphorylase as a key regulator of the angiogenic potential of colony-forming units and endothelial progenitor cell cultures, *Circulation Research* 104(1) (2009) 32-40.

[10] A. Rosell, A. Morancho, M. Navarro-Sobrino, E. Martínez-Saez, M. Hernández-Guillamon, S. Lope-Piedrafita, V. Barceló, F. Borras, A. Penalba, L. Garcia-Bonilla, Factors secreted by endothelial progenitor cells enhance neurorepair responses after cerebral ischemia in mice, *PloS One* 8(9) (2013).

[11] K.K. Chereddy, V.L. Payen, V. Préat, PLGA: From a classic drug carrier to a novel therapeutic activity contributor, *Journal of Controlled Release* 289 (2018) 10-13.

[12] K.K. Chereddy, A. Lopes, S. Koussoroplis, V. Payen, C. Moia, H. Zhu, P. Sonveaux, P. Carmeliet, A. des Rieux, G. Vandermeulen, Combined effects of PLGA and vascular endothelial growth factor promote the healing of non-diabetic and diabetic wounds, *Nanomedicine: Nanotechnology, Biology and Medicine* 11(8) (2015) 1975-1984.

[13] F. Felice, A.M. Piras, S. Rocchiccioli, M.C. Barsotti, T. Santoni, A. Pucci, S. Burchielli, F. Chiellini, N. Ucciferri, R. Solaro, A. Altomare, A. Cecchettini, R. Di Stefano, Endothelial progenitor cell secretome delivered by novel polymeric nanoparticles in ischemic hindlimb, *Internationl Journal of Pharmaceutics* 542(1-2) (2018) 82-89.

[14] M. Janowski, A. Lyczek, C. Engels, J. Xu, B. Lukomska, J.W. Bulte, P. Walczak, Cell size and velocity of injection are major determinants of the safety of intracarotid stem cell transplantation, *Journal of Cerebral Blood Flow & Metabolism* 33(6) (2013) 921-927.

[15] A. Rosell, K. Arai, J. Lok, T. He, S. Guo, M. Navarro, J. Montaner, Z.S. Katusic, E.H. Lo, Interleukin-1β augments angiogenic responses of murine endothelial progenitor cells in vitro, *Journal of Cerebral Blood Flow & Metabolism* 29(5) (2009) 933-943.

6

Conclusions and future perspectives

6.1 General Conclusions

We proposed a nanoformulation of magnetic PLGA NCs (~270 d.nm) with therapeutic proteins encapsulation as drug delivery system for potential clinical translation. The magnetic component, the SPIONs, integrated in the PLGA shell matrix and responsible for the magnetic targeting and MRI were optimized in terms of size (9 nm) and loading (6wt%) endowing the nanocarrier with improved magnetic retention effect (Ms 4 eum/g) and MRI performance (r_2 =336 mM^{-1} s^{-1}). The PLGA NC formulation was demonstrated to be biosafe *in vitro* and *in vivo*. The quality of the PLGA NC was monitored at the different stages of the study.

We functionalized the PLGA NC formulation with multimodal imaging moieties. By covalently bonding PLGA with fluorescent small molecules and radioligands as well as by incorporating SPIONs we could propose a modular approach to fabricate tailor-made NCs with modalities of several emitting wavelengths for fluorescence imaging (blue, green, red and NIR), MRI and PET. In all cases, the imaging moieties are integrated into the PLGA shell matrix and with minimal interaction with the encapsulated drug thus avoiding leaching and interferences with the therapeutic agent. Moreover, all types of NC formulations can be PEGylated (3 wt% PEG) to endow the NCs with potential stealth effect, and surface charge of NC formulations can be modified by integrating PLGA-NH_2 to tune the cellular uptake. The modular approach offers the selective inclusion or removal of the functional moieties without affecting the size, shape and main compositional traits of the final carrier, to guide the carrier alongside its preclinical development while guaranteeing that a simpler formula is used for the final product in views of its potential translation to the clinics.

We applied the developed multimodal imaging PLGA NC formulation to *in vitro*/*in vivo* tracking. The good fluorescent performance of NCs was demonstrated for *in vitro* studies. *In vivo*

biodistribution monitored by MRI/NIRF/PET showed the dominant liver, spleen and lung accumulation of the *intra venu.* administered NCs, and proved the higher NC brain accumulation through *intra arterial* administration route. The combination of different modalities to monitor different components of the NC formulation provided complementary information.

We evaluated the therapeutic aspects of the PLGA NC formulation in terms of protein loading content and release kinetics, and the *in vitro* human brain endothelial cell proliferation effect. The NCs can be loaded with a moderate protein load (~10 µg BSA/mg NCs) and achieve sustained release with ~51% of the total cargo discharged over a period of two weeks in PBS. Similarly, the encapsulation of concentrated therapeutic endothelial progenitor cells-secretome (~15 mg/mL) could be achieved and a protein loading with detected improved loads of several proteins (VEGF 13.7, PTX3 32.1, GM-CSF 5.3 and Ang 32.5 pg/mg NCs) was measured. Regarding the cell proliferation, we found a fast erosion rate of NCs in cell culture medium (EBM) and the degraded PLGA itself contributed to the cell proliferation.

6.2 Future perspectives

The developed multimodal imaging functionalization is a powerful tool for the tracking of PLGA-based nanocarriers. To fully transform the PLGA nanocarrier into a theranostic platform, further active targeting strategies through the attachment of specific ligands to the PLGA nanocarrier could be exploited and study the synergistic effect of this biological targeting with the magnetic one.

Surface modification of the PLGA nanocarrier for a better stealth effect and a longer blood circulation time, for instance by PEGylation, needs to be further studied to improve the availability of NCs in the brain area. Moreover, a combination of *i.a.* administration and external magnetic field to improve NC brain accumulation should be investigated. The blood-brain barrier behavior of the NCs is also worthy to study and the modification can be adjusted according to the desired purpose.

The protein quantification method and release protocols for therapeutic secretome loaded NCs need to be refined to better monitor the loaded secretome. After optimizing the brain targeting and therapeutic secretome load, the preclinical pro-angiogenesis and

neurorepair effect of the drug delivery system can be studied in an animal model of ischemic stroke.

List of publications

Zhang Y, García-Gabilondo M, Grayston A, ... Rosell A* & Roig A*. (2020). PLGA protein nanocarriers with tailor-made fluorescence/MRI/PET imaging modalities. *Nanoscale*, 12(8), 4988-5002.

Zhang Y, García-Gabilondo M, Rosell A* & Roig A*. (2020). MRI/Photoluminescence dual-modal imaging magnetic PLGA nanocapsules for theranostics. *Pharmaceutics*, 12(1), 16.

Nanoscale

ROYAL SOCIETY OF CHEMISTRY

PAPER

Cite this: *Nanoscale*, 2020, **12**, 4988

PLGA protein nanocarriers with tailor-made fluorescence/MRI/PET imaging modalities†

Yajie Zhang,[a] Miguel García-Gabilondo,[b] Alba Grayston,[b] Irene V. J. Feiner,[c] Irene Anton-Sales,[a] Rodrigo A. Loiola,[d] Jordi Llop,[c,e] Pedro Ramos-Cabrer,[f,g] Ignasi Barba,[h] David Garcia-Dorado,‡[h] Fabien Gosselet,[d] Anna Rosell*[b] and Anna Roig*[a]

Designing theranostic nanocarriers with high protein payload and multimodality tracking without cross interferences between the different imaging probes and the delicate protein cargo is challenging. Here, chemical modifications of poly(lactic-*co*-glycolic acid) (PLGA) to produce nanocapsules (NCs) that incorporate several imaging moieties are reported. The biocompatible and biodegradable PLGA-NCs can be endowed with a magnetic resonance imaging (MRI) reporter, two fluorescence imaging probes (blue/NIR) and a positron emission tomography (PET) reporter. The modular integration of these imaging moieties into the shell of the NCs is successfully achieved without affecting the morphochemical properties of the nanocarrier or the protein loading capacity. *In vivo* biodistribution of the NCs is monitored by MRI, PET and NIRF and the results from different techniques are analyzed comparatively. The viabilities of two different human endothelial cells *in vitro* show no toxicity for NC concentration up to 100 μg mL^{-1}. The morbidity of mice for 2 weeks after systemic administration and the hepatic/pancreatic enzymes at the plasma level indicate their *in vivo* biosafety. In summary, the new theranostic PLGA nanoplatform presented here shows versatile *in vitro*/*in vivo* multimodal imaging capabilities, excellent biosafety and over 1 wt% protein loading.

Received 16th December 2019,
Accepted 20th January 2020

DOI: 10.1039/c9nr10620k

rsc.li/nanoscale

Introduction

Drug delivery nanocarriers can be extremely advantageous to administer insoluble, sensitive or multi-component drugs by protecting the encapsulated therapeutic molecules from clearance, inactivation or degradation, as well as by reducing potential toxicity, increasing blood circulation time or tissue specificity.[1–5] Poly(lactic-*co*-glycolic acid) (PLGA) has demonstrated optimal properties for the encapsulation of a large variety of therapeutic agents and it is extensively employed in nanomedicine.[6,7] Moreover, PLGA-based nanocarriers have been used as drug delivery systems to administer proteins,[8,9] DNA[10] and anticancer drugs among others.[1,11,12] Nonetheless, despite their compositional similarities, any novel PLGA-based drug delivery system will require a thorough evaluation to address potential toxicity issues and study the pharmacokinetics and the pharmacodynamics of each specific carrier. Such preclinical *in vitro* and *in vivo* studies, comprising multiple biological characterization phases, could be expedited by endowing the carrier with complementary imaging capacities. For instance, *in vitro* cellular uptake can be easily imaged with fluorescence[13,14] while radioimaging[15,16] or near infrared (NIR) imaging[1,17] are well suited for *in vivo* biodistribution studies. However, the simultaneous incorporation of all these imaging probes into a single nanocarrier unnecessarily increases the complexity of the system, potentially limiting translation to the clinics. Moreover, any additional component of the theranostic carrier will have an enormous impact on the manufacturing process, production cost and in complying with the medical regulations. In this sense, a drug delivery nanocarrier easily

[a]*Institut de Ciència de Materials de Barcelona (ICMAB-CSIC), 08193 BellaterraCatalonia, Spain. E-mail: anna.roig@csic.es*
[b]*Neurovascular Research Laboratory, Vall d'Hebron Institut de Recerca, Universitat Autònoma de Barcelona, 08035 BarcelonaCatalonia, Spain. E-mail: anna.rosell@vhir.org*
[c]*Radiochemistry and Nuclear Imaging Group, CIC biomaGUNE, Basque Research and Technology Alliance (BRTA), 20014 San Sebastian, Guipúzcoa, Spain*
[d]*University of Artois, Blood-Brain Barrier Laboratory (BBB Lab), UR2465, F-62300 Lens, France*
[e]*CIBERES, Centro de Investigación Biomédica en Red, 28029 Madrid, Spain*
[f]*Magnetic Resonance Imaging Laboratory, CIC biomaGUNE, Basque Research and Technology Alliance (BRTA), 20014 San Sebastian, Guipúzcoa, Spain*
[g]*Ikerbasque, Basque Foundation for Science, 48013 Bilbao, Spain*
[h]*Cardiovascular Diseases Research Group, Vall d'Hebron University Hospital and Research Institute, Universitat Autònoma de Barcelona, 08035 Barcelona, Spain*

†Electronic supplementary information (ESI) available. See DOI: 10.1039/c9nr10620k

‡In memory of our colleague Dr Garcia-Dorado who passed away on August 16th 2019.

adaptable to incorporate one or several imaging moieties in a modular approach can be a smart strategy to guide the carrier preclinical development while guaranteeing that a simpler formula is used for the final product. However, this strategy is suitable only when the inclusion or removal of the imaging probes do not affect the size, shape and main compositional traits of the final carrier.

Furthermore, conventional approaches to physically blend imaging probes within the carrier can lead to incomplete conclusions or misinterpretations on the carrier's biodistribution.[18,19] For example, loading two different molecules as probes into the same carrier led to opposite conclusions regarding the kinetics of brain-specific delivery.[19] A growing body of evidence suggests that new methods will be required to monitor nanocarriers' biodistribution avoiding interference of the imaging moieties with the encapsulated drug or leaching of the imaging probes.[19,20]

Here, we report on PLGA nanocapsules (NCs) as a multimodal theranostic platform for *in vivo* drug delivery. We describe the chemical synthetic routes to covalently label the PLGA with biocompatible small molecule fluorophores or radioligands. It involves the fabrication of PLGA NCs integrating several moieties for their *in vitro* and *in vivo* imaging. Specifically, superparamagnetic iron oxide nanoparticles (SPIONs) enabled magnetic resonance imaging (MRI), fluorescence imaging at different emitting wavelengths (blue and NIR) and ^{89}Zr-labeling enabled positron emission tomography (PET) imaging. We show that the morphology and size of PLGA NCs are not altered by either the incorporation or the removal of one of the several imaging probes. In all cases, the imaging moieties are chemically attached to the PLGA shell matrix as opposed to being entrapped in the core of the nanocapsule.[13–15,17] This approach is advantageous to avoid interferences of the imaging moieties with the cargo in the core.[21] This is especially important for delicate payloads such as proteins, enzymes or microRNAs. For this, we have used bovine serum albumin (BSA) as a model protein to evaluate the protein loading capability.

Experimental section

All reagents were purchased from Sigma Aldrich unless otherwise specified. The Ethics Committee of Animal Experimentation of the Vall d'Hebron Research Institute approved all experimental animal procedures (protocol number 70.18), which were performed in accordance with the Spanish legislation and the Directives of the European Union. Experiments performed at CIC biomaGUNE were approved by the Ethical Committee of the Institution and by the corresponding authorities (Departamento de Promoción Económica, Turismo y Medio Rural, Diputación Foral de Guipúzcoa; project codes PRO-AE-SS-059 and PRO-AE-SS-067).

Modification and functionalization of the commercial PLGA

Synthesis of –NH$_2$ terminated PLGA (PLGA-NH$_2$). In order to introduce a terminal amine group into PLGA, the carboxylic acid terminal group of PLGA (lactic : glycolic ratio 50 : 50, RG502H, M_w 12 000) was activated and reacted with ethylenediamine. The carboxylic groups were firstly activated with *N*,*N*′-dicyclohexylcarbodiimide (DCC) and *N*-hydroxysuccinimide (NHS). 0.025 mmol of PLGA was dissolved in 8 ml of dichloromethane (DCM), and then 0.1 mmol of DCC in 1 mL of DCM and 0.1 mmol of NHS in 0.5 mL of acetone were added into the polymer solution under magnetic stirring. PLGA-NHS activation was achieved after 4 h at room temperature (RT). The coupling reaction was accomplished by adding an excess amount of ethylenediamine (0.15 mmol) in 1 mL of DCM to the solution and further stirring for 2 h. The majority of the insoluble by-product, dicyclohexylurea, was removed by centrifuging the solution after reaction at 9391 rcf for 15 min at 4 °C and discarding the pellet. The supernatant was filtered (0.2 μm PTFE syringe filter) to remove any trace of the insoluble by-product. PLGA-NH$_2$ was precipitated by slowly pouring the supernatant into an excess amount of ethanol (10-fold), where the un-reacted NHS/DCC/ethylenediamine was separated from PLGA-NH$_2$ due to their solubility in ethanol. Precipitated PLGA-NH$_2$ was redissolved in DCM and reprecipitated in ethanol twice for purification. The purified PLGA-NH$_2$ was dried under vacuum.

Synthesis of fluorophore terminated PLGA using fluorescamine (PLGA-fluram). Fluorescamine (fluram) is a non-fluorescent compound that reacts with primary amines (R-NH$_2$) fast and near completely forming the fluorophore of fluram derivative which emits strong fluorescence at λ_{em} = 465 nm (λ_{ex} = 390 nm).[22] 0.025 mmol of the as-synthesized PLGA-NH$_2$ and 0.075 mmol of fluram were mixed and dissolved in 4 mL of acetone and the reaction took place in a dark room after 2 h at RT under magnetic stirring. Then the solution was slowly dropped into an excess amount of ethanol (10-fold) to precipitate the product PLGA-fluram. The PLGA-fluoram was collected by centrifugation, redissolved in acetone and reprecipitated in ethanol twice for purification. The purified PLGA-fluram was dried under vacuum.

Synthesis of fluorophore terminated PLGA using Cy7.5 (PLGA-Cy7.5). NIR fluorophore cyanine7.5 (λ_{em} = 808 nm, λ_{ex} = 788 nm) was introduced at the end of PLGA-NH$_2$ by forming an amide bond between the PLGA terminal amine group and amine reactive Cy7.5 NHS ester (Lumiprobe GmbH, Hannover, Germany). 0.025 mmol of the as-synthesized PLGA-NH$_2$ and 0.05 mmol of Cy7.5 NHS ester were mixed and dissolved in 4 mL of acetone and 0.05 mmol of Et$_3$N were added as the catalyst. The reaction took place in the dark after 6 h at RT under magnetic stirring. Then the solution was slowly poured into an excess amount of ethanol (10-fold) to precipitate PLGA-Cy7.5. The product was collected by centrifugation, redissolved in acetone and precipitated in ethanol twice for purification. The purified PLGA-Cy7.5 was dried under vacuum.

Synthesis of DFO terminated PLGA (PLGA-DFO). ^{89}Zr chelator deferoxamine (DFO) was introduced at the terminal amine of PLGA-NH$_2$ by forming a thiocarbamide bond between the PLGA terminal amine group and amine reactive p-NCS-Bz-DFO

(CheMatech, Dijon, France). 0.025 mmol of the as-synthesized PLGA-NH_2 and 0.05 mmol of p-NCS-Bz-DFO ester were mixed and dissolved in 4 mL of DMSO and 0.05 mmol of Et_3N were added as the catalyst. The reaction was accomplished after 12 h at RT under magnetic stirring. Then the DMSO solution was mixed with 2-fold DCM and slowly dropped into 10-fold diethyl ether to precipitate PLGA-DFO and unreacted p-NCS-Bz-DFO, which were collected by centrifugation at 9391 rcf for 10 min. The PLGA-DFO/p-NCS-Bz-DFO mixture pellet was dissolved in 1.5 mL of DCM and centrifuged at 13 171 rcf for 60 min to remove the insoluble p-NCS-Bz-DFO. The supernatant was further filtered (0.2 μm PTFE syringe filter) to remove the traces of p-NCS-Bz-DFO. Finally PLGA-DFO was precipitated by slowly dropping the supernatant into 10-fold diethyl ether, collected by centrifugation and dried under vacuum.

Synthesis of SPIONs coated with oleic acid (OA-SPIONs)

SPIONs were synthesized through a microwave assisted thermal decomposition in a microwave oven (Discover SP, CEM Corporation) at a frequency of 2.45 GHz and 300 W of power and then coated with oleic acid (OA).[23] Briefly, the process to obtain homogeneous OA-SPIONs with an average diameter of 9 nm was as follows. In a microwave reaction glass tube 3.5 mmol of iron precursor $Fe(acac)_3$ was dissolved in 4.5 mL of benzyl alcohol. The tube was closed and microwave irradiation occurred with the power set at 300 W. The solution was kept at 60 °C for 5 min to fully dissolve the precursor and subsequently heated to 210 °C and kept at this temperature for 30 min and then cooled down to room temperature. After the reaction, a black colored dispersion formed which suggested the formation of a magnetic material. Then 3.17 mmol of oleic acid in 4 mL of toluene was added to the product dispersion and sonicated for 1 h. Then 5-fold of acetone was added followed by centrifugation to sediment the product pellet. The pellet was redispersed in 4 mL of toluene and transferred into a glass vial, a magnet was attached on the wall and after 5 s the suspension containing SPIONs with smaller size and lower magnetization was discarded. Then the pellet was redispersed in 6 mL of DCM followed by centrifugation at 1075 rcf for 5 min to sediment the unstable big particles. The OA-SPIONs of 9 nm stable in DCM were precipitated by adding 5-fold acetone and centrifugation. The final black product was dried under vacuum and redispersed in DCM at the concentration required for use.

Fabrication of PLGA-based NCs and encapsulation of BSA

BSA encapsulated PLGA-based NCs were prepared by the double emulsion solvent evaporation method. Briefly, 50 μL of the inner aqueous phase (W_1) containing BSA (30 mg mL^{-1}) was emulsified in 500 μL of DCM organic phase (O) composed of 50 mg of different proportions of PLGA/functional PLGA and a certain amount of OA-SPIONs by sonication at 200 W for 28 s (VC505, Sonics & Materials, Inc., USA) to form the first emulsion (W_1/O). Then 2 ml of external aqueous phase (W_2) with PVA (20 mg mL^{-1}) was added and the second emulsion (W_1/O/W_2) was formed by sonication for an additional 28 s. The temperature during the whole emulsion process was kept at 4 °C by using an ice bath. The resulting double emulsion was poured into 50 mL of MilliQ water and mechanically stirred at RT for 2 h to allow complete evaporation of the organic solvent and formation of NCs. Finally, the NC pellet was obtained by centrifugation at 9391 rcf for 15 min and washed three times with 50 mL of MilliQ water and then lyophilized in 6 mL of trehalose (2 mg mL^{-1}) aqueous solution. The as-obtained powder was stored at 4 °C with desiccant silica gel.

Physicochemical characterization of the polymers, SPIONs and PLGA-NC

ATR-FTIR, UV/Vis, TG, DLS. Attenuated total reflectance-Fourier transform infrared (ATR-FTIR) characterization of the polymers was performed on a Bruker Vertex 70 FTIR spectrometer with a Pike Miracle Single-Bounce diamond crystal plate accessory at room temperature. FTIR spectra were recorded over a wavelength range of 4000–500 cm^{-1} with a resolution of 4 cm^{-1}. The ultraviolet-visible infrared (UV/Vis) spectra of the fluorescent polymers were recorded on a Varian Cary-5000 UV/Vis spectrophotometer using a quartz cuvette with an optical path of 1 cm. Thermogravimetric (TG) analysis of oleic acid coated SPIONs was carried out on a SETSYS Evolution TGA (Setaram) from room temperature to 800 °C at a heating rate of 10 °C min^{-1} and under a dynamic dry air flow. Dynamic light scattering (DLS) (Malvern Zetasizer) measurements of the hydrodynamic diameter and size distribution of NCs by intensity were performed by redispersing 0.5 mg of lyophilized powder into 1 mL of MilliQ water.

Electron microscopies. A field emitting scanning electron microscope (SEM, FEI Quanta 200 FEG) and a transmission electron microscope (TEM, JEOL JEM-1210) were used to study the morphologies of SPIONs and NCs. For the SEM sample preparation of NCs, 0.5 mg of lyophilized powder was redispersed in 1 mL of MilliQ water and centrifuged at 4000 rpm for 10 min. Then the supernatant was discarded to remove the trehalose and 1 mL of fresh water was added, and the pellet of NCs was redispersed in water with ultrasound. Finally, 6 μL of the slightly turbid suspension was deposited onto a small slice of silicon wafer stuck on top of a carbon layer and dried at room temperature overnight. The sample was sputtered with Au–Pd (Emitech K550 Sputter Coater, 20 mA for 2 min). TEM samples were prepared by placing and drying one drop of the corresponding NC or SPION dispersion on a copper grid at room temperature.

SQUID. Superconductive quantum interference device (SQUID, Quantum Design MPMS5XL) was used to measure the magnetization of NCs and SPIONs and calculate the experimental SPION loading ($wt\%_{SPIONs}$) and $EE\%_{SPIONs}$ of NCs. A gelatin capsule filled with about 7 mg of samples topped with some cotton wool was inserted into the SQUID magnetometer sample holder and the hysteresis loop was measured from −50 kOe to 50 kOe at 5 K. The remnant magnetization of the magnetic NCs ($M_{R,\ NCs}$, emu g^{-1}) and of SPIONs ($M_{R,\ SPIONs}$, emu

g^{-1}) at 5 K was used to calculate $wt\%_{SPIONs}$ and $EE\%_{SPIONs}$ as follows:

$$wt\%_{SPIONs} = \frac{M_{R,NCs}}{M_{R,SPIONs}} \times 100\%$$

$$EE\%_{SPIONs} = \frac{\text{Experimental SPION loading}}{\text{Nominal SPION loading}} \times 100\%$$

Fluorescence properties. Fluorescence spectra of the polymer PLGA-fluram were acquired on a PerkinElmer LS45 spectrofluorometer. Both the excitation and emission-slit widths were set at 10 nm. The quantum yield of the polymer was measured by the Williams' method[24] shown in Fig. S3a.† The molar extinction coefficient (ε, mol^{-1} L cm^{-1}) of PLGA-fluram was calculated according to the Beer–Lambert law, $A = \varepsilon CL$. Here C and L are the concentration (mol L^{-1}) and length (cm) of the dye solution in a UV/Vis cuvette respectively. Brightness and photostability are two important intrinsic photophysical properties of fluorescent materials. The brightness intensity of PLGA-fluram can be calculated by the extinction coefficient multiplied by the quantum yield. Photostability was measured by continuously illuminating polymer solution with excitation light at 390 nm and measuring the resulting emission at 483 nm for 3 h. The photostability of rhodamine B as a reference was tested with its maximum excitation at 540 nm and maximum emission at 625 nm for the same 3 h in aqueous solution. Fluorescence signals of different concentrations of PLGA-fluram NC in saline were quantified in a 96-well plate by a microplate reader. The NCs were excited at the maximal excitation wavelength and the fluorescence signal was collected at the maximal emission wavelength.

In vitro and *in vivo* MRI of the NC·SPIONs

In vitro agarose phantoms of NCs were prepared by filling a series of glass microtubes with solutions of 0.63% agarose in water (Conda, Madrid), into which different amounts of NCs were admixed. The corresponding iron doses (mmol L^{-1}) were calculated according to the wt% of SPIONs in each sample. $T2$ weighted images (T2WI) of the phantoms were acquired at 7 T in a 70/30 Bruker USR Biospec system (Bruker GmbH, Ettlingen) as follows: multi-slice multi-echo (MSME) sequence with echo time (TE) = 8 ms, repetition time (TR) = 2600 ms, average N = 2, matrix size = 160 × 160, field of view (FOV) = 24 × 24 mm, 14 slices of 1 mm thickness, and spectrometer bandwidth (BW) of 474 Hz per pixel. Quantitative $T2$ values were obtained from hand-drawn regions of interest (ROIs) by using curve fitting in the Image Sequence Analysis (ISA) Tool (ParaVision v.5.1).

Balb/c female mice (16–17 weeks of age, n = 2) were anesthetized with isoflurane (IsoFlo; Abbott Laboratories). T2WI were acquired pre- and 15–20 min post-administration of NCs (1.6 mg in 150 μL of saline through tail vein) using the following imaging parameters: MSME pulse sequence, 20 echo times with ΔTE = 8 ms, TR = 2.6 s, N = 2 averages, a matrix of 256 × 256 points covering a FOV of 25.6 × 25.6 mm^2, giving a resolution of 100 μm in plane, 14 continuous slices of 1 mm thickness, and BW = 75 kHz. The images were acquired with a respiratory gating by using a SAII Model 1030 monitoring & gating system (Smal Animals Instruments, Stony Brook, NY, USA). Fat suppression was achieved by a saturation pulse of 1050 Hz. T2 maps were constructed off-line using Image-J 1.50b (National Institutes of Health), and data were fitted to a three parameter exponential decay equation ($S = A + S0 \exp(-TE/T2)$, where S represents signal intensity, A, $S0$ and $T2$ are the fitting parameters), achieved by the "exponential decay with offset" equation of the fitting routine of ImageJ. Signal intensities in T2WI and T2 maps were quantified manually in selected ROIs using ImageJ. Afterwards mice were euthanized and organs were preserved for histological analyses.

In vitro and *in vivo* NIRF imaging of NC·PLGA-Cy7.5

A series of concentrations of NCs in 100 μL of saline (n = 3) were prepared in a 96-well plate and imaged using a Xenogen IVIS® spectrum ($\lambda_{ex}/\lambda_{em}$ 710/820 nm). BALB/cAnNRj male mice (Janvier; 7–8 weeks of age, n = 2) were deeply anesthetized with isoflurane and were injected *via* the tail vein with NCs at a dose of 1.6 mg in 200 μL of saline. The NIRF images were acquired on a Xenogen IVIS® spectrum imaging system at 0.5 h, 1 h and 3 h post injection. At the end of the 3 h scan, the mice were euthanized to image the signal intensity of the principal organs *ex vivo* together with blood and urine.

In vivo PET imaging of ^{89}Zr labelled NC·PLGA-DFO

NC·PLGA-DFO were labelled with ^{89}Zr as follows: $[^{89}Zr]ZrC_2O_4$ was produced in house following a standard protocol. The as-obtained 1500 μL of 1 M oxalic acid containing ^{89}Zr (8.2 mCi, 303.4 MBq) were neutralized with 2 M sodium carbonate (pH = 7.2) and the volume was adjusted to 3.5 mL with 0.5 M HEPES buffer. Six aliquots (1.6 mg each) of the lyophilized particles were dispersed in 50 μL MQ-water, and 450 μL of the freshly prepared ^{89}Zr-solution was added to each and mixed well by sonication. After incubating overnight at room temperature the particles were purified by centrifugation and washed two times with MQ-water followed by one wash with saline to remove all non-bound ^{89}Zr. The pellet of the last wash was dispersed in 120 μL of saline with an average calculated radiochemical yield of 70.1% (decay-corrected). As the achieved samples were too high in activity, a one to one dilution with non-labelled particles was performed. The final injections (150 μL) were performed intravenously *via* the tail vein of healthy female mice (Crl : CD1(ICR)) with an average injected activity of 161 μCi (6.0 MBq).

Imaging studies were conducted using positron emission tomography (PET) in combination with computerized tomography (CT), using the β- and X-cube microsystem of Molecubes. Static whole body images (1 bed) were acquired in a 511 keV ± 30% energetic window at 1 h, 4 h, 23 h and 47 h post injection (acquisition time 5 min for 1 h and 4 h, 20 min for 23 h and 47 h). PET images were analyzed using PMOD image analysis software (PMOD Technologies Ltd, Zurich, Switzerland).

Prussian blue stain

Liver samples from the mice subjected to PET were embedded in an optimal cutting temperature (OCT) compound and kept at −80 °C until sliced in 8 μm sections with a cryostat. After rehydration, the sections were stained with a Prussian blue iron stain kit (Polysciences Inc, USA) following the manufacturer's protocol except that potassium ferrocyanide : hydrochloric acid solution was kept for a total of 40 minutes and nuclear Fast Red for 1 minute. Images were acquired after dehydration with a transmitted light microscope (Leica, Germany).

In vitro and *in vivo* toxicity evaluation of the NCs

Cell viability evaluation. The toxicity of the NCs on human brain endothelial cells (hCMEC/D3) and $CD34^+$ endothelial cells[25,26] was assessed by performing a viability assay with 3-(4-5-dimethylthiazol-2-yl)-2,5-diphenyl tetrazolium bromide (MTT). For the hCMEC/D3 cells, 2×10^4 viable cells were distributed on a 24-well plate in 400 μL Endothelial Growth Media (EGM2 from Lonza with 2% fetal bovine serum and half the amount of the growth factors included in the kit) whereas 5×10^3 viable $CD34^+$ endothelial cells were seeded on a 96-well plate in complete media. Both cell types were incubated for 24 h at 37 °C and 5% of CO_2. After this period, culture supernatants were substituted with basal cell culture media (serum-free medium) containing increasing doses of NCs at concentrations of 25 μg mL^{-1}, 50 μg mL^{-1}, and 100 μg mL^{-1} ($N = 3$, triplicate). The MTT assay was performed after 48 h of incubation, and the absorbance of the resulting formazan crystals diluted in DMSO was determined at 540 nm. Cell viability was referred to as the percentage of viability compared with the control conditions (without NC).

***In vivo* safety.** Body weights of mice were monitored periodically at 0 d, 1 d, 5 d, 8 d, 11 d and 13 d after i.v. injection of NCs in 150 μL of saline at a dose of 0.84 mg Fe per kg ($n = 5$), where the vehicle group received 150 μL of saline ($n = 5$) and the naïve group without treatment served as control ($n = 3$). At the end of 13 days blood samples were collected and liver/pancreas toxicity based on specific enzyme levels in plasma was analysed in all groups: alanine aminotransferase (ALT), alkaline phosphatase (ALK), aspartate aminotransferase (AST) and α-amylase using an Olympus AU5800 clinical chemistry analyser.

BSA loading content

The albumin content was determined directly using the CBQCA protein assay kit (Invitrogen™ ref. C6667), which determines the protein concentration based on the production of fluorescent products measurable at $\lambda_{ex}/\lambda_{em}$ = 450 nm/550 nm *via* non-covalent interaction between CBQCA and primary aliphatic amines of proteins. This highly sensitive fluorescence-based method showed compatibility with DMSO, SPIONs, detergents and other substances which interfere with many commonly used protein determination methods. Lyophilized NCs encapsulating albumin as well as empty NCs as control were fully dissolved in DMSO at 100 mg mL^{-1}. The protein contents in the NC lysates were measured and calculated based on the difference in fluorescence with control and a calibration curve drawn with standard albumin solutions, and the protein contents in the BSA solutions used for encapsulation were also measured. All determinations were performed in duplicate for each NC batch. The experimental BSA loading content was expressed as μg of BSA per mg of NCs (μg mg^{-1}). The encapsulation efficiency (EE%) was calculated as follows:

$$\text{EE\% BSA} = \frac{\text{Experimental BSA loading}}{\text{Nominal BSA loading}} \times 100\%$$

Results and discussion

PLGA NCs reported here incorporate several biocompatible multimodal imaging modalities (Fig. 1): fluram and cyanine 7.5 (Cy7.5) as fluorescent probes in the blue and the near-infrared (NIR) wavelengths, ^{89}Zr chelated with DFO as a radio imaging probe and SPIONs as a MRI contrast agent. The fluorescent probes and the DFO chelator were anchored to an aminated PLGA, PLGA-NH_2, resulting from the modification of the commercial carboxylic acid-terminated PLGA. BSA encapsulated PLGA NCs could then be prepared by a double emulsion solvent evaporation method where selected imaging moieties were incorporated into the PLGA shell by adding the desired

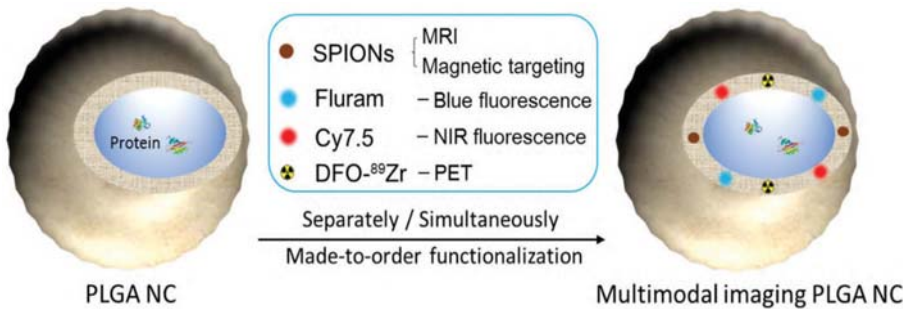

Fig. 1 Schematic illustration of a PLGA NC as a tailor-made multimodal theranostic platform.

proportions of a given functional PLGA and oleic acid coated SPIONs to the organic phase while the BSA was added to the aqueous phase.

Chemical modification of the PLGA with functional moieties

Fig. 2 shows the schematic representation for terminal modifications and functionalization of the PLGA. Firstly, the carboxylic acid end group of PLGA was activated with DCC and NHS to conjugate ethylenediamine and form PLGA-NH_2, bearing a free primary amine group in the PLGA end (Fig. 2a). An excess amount of ethylenediamine (6 : 1 ethylenediamine : PLGA mole ratio) was used to suppress the coupling reaction of PLGA–PLGA that could occur due to the homo-functional crosslinker ethylenediamine. Subsequently, the three functional moieties with amine-reactive groups (fluram, Cy7.5, DFO) could be respectively integrated at the end of the PLGA molecule through coupling reactions (Fig. 2b). Further details are reported in the Experimental section.

ATR-FTIR spectra of the commercial PLGA-COOH and the PLGA-NH_2 product confirmed their similar chemical structure and successful modification (Fig. S1 in the ESI†). The reaction efficiency of PLGA-COOH to PLGA-NH_2 was quantified by measuring the conjugated amount of fluram to the $-NH_2$ groups. The UV absorbance of the PLGA-NH_2 product (M_w 12 000 g mol^{-1}) in chloroform at 390 nm due to the conjugation of fluram was compared with a standard calibration curve constructed from different concentrations of ethylenediamine prepared under the same conditions (Fig. S2†). A reaction efficiency of 86% of PLGA-COOH to PLGA-NH_2 was estimated, which means that the molar fraction of pure PLGA-NH_2 in the product was 0.86.

Fluram is a non-fluorescent compound that reacts quickly and almost quantitatively with primary amines (R-NH_2) to form a fluorescent derivative, which emits strong fluorescence at around 480 nm when excited at 390 nm.[22] The conjugation of this compound to the $-NH_2$ end of PLGA for fluorescence application is very advantageous considering that neither free fluram itself nor its hydrolysis product show fluorescence. As shown in Fig. 3a, the characteristic absorption peak of the fluorophore at 390 nm occurred in the UV-Vis spectrum of the conjugation product PLGA-fluram but this was not observed either in PLGA-NH_2 or in fluram. The disappearance of the 309 nm absorption band of fluram in the PLGA-fluram product indicates that the purification process removes the vast majority of free fluram. The fluorescence of the obtained PLGA-fluram was evaluated and the excitation and emission spectra are depicted in Fig. 3b. Importantly, the fluorescence intensity of PLGA-fluram decreased only slightly (<5%) after continuous UV excitation at the maximum excitation wave-

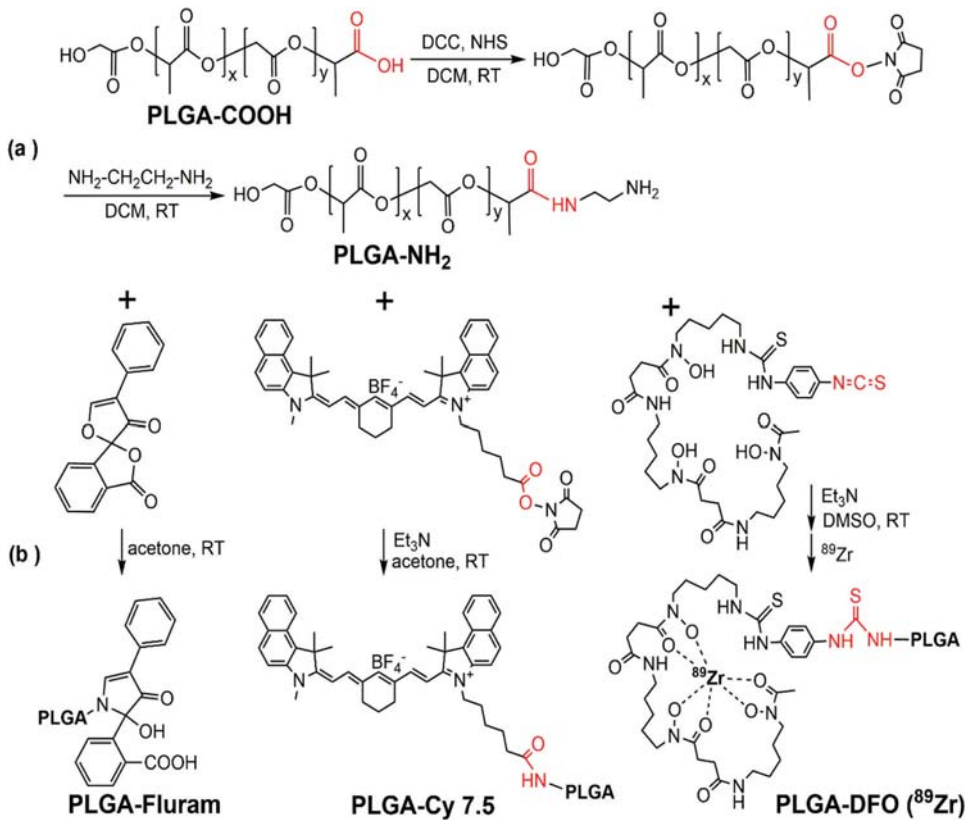

Fig. 2 PLGA chemical modifications. Synthetic schemes of terminal modifications and functionalization of the PLGA.

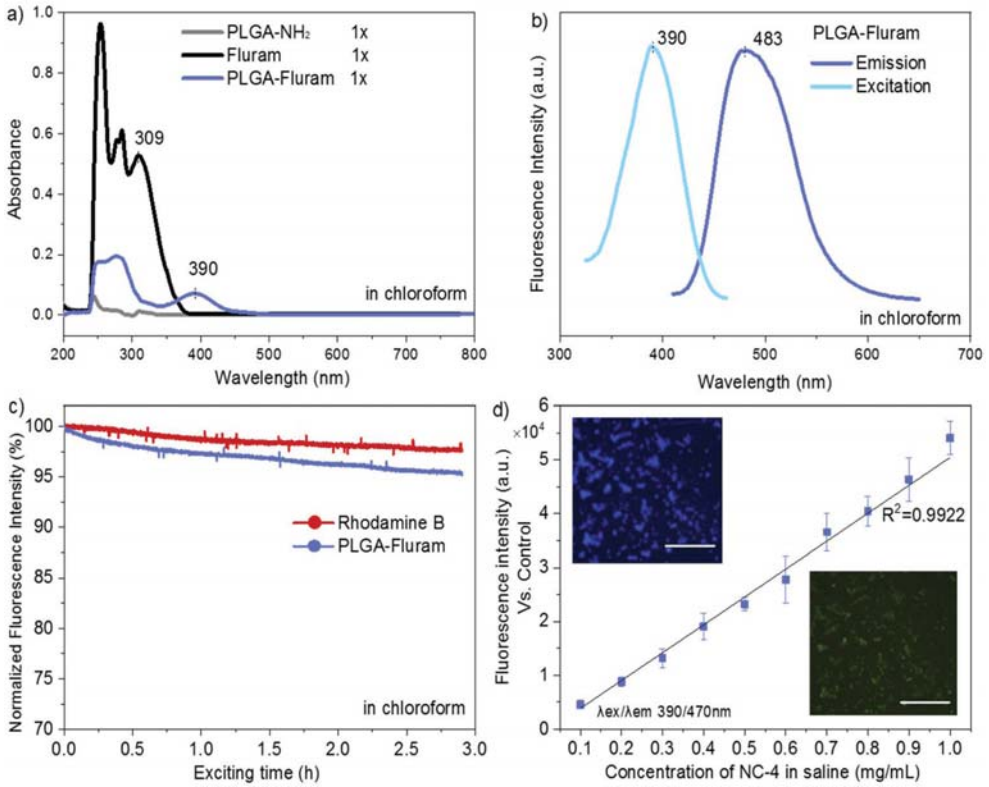

Fig. 3 PLGA-fluram system spectroscopic and fluorescence characterization. (a) UV-Vis absorption spectra of PLGA and PLGA/fluram samples; (b) excitation and emission spectra of PLGA-fluram; (c) photostability evaluation of PLGA-fluram and control dye rhodamine B, fluorescence intensity expressed as the percentage *vs.* time 0; (d) fluorescence intensity of different concentrations of NC·PLGA-fluram (NC-4) *vs.* NC-control (NC-3) measured by using a microplate reader (n = 3, values represent mean ± SEM); insert: lyophilized NC-4 observed under a fluorescence microscope with DAPI/GFP filters, scale bar 60 μm.

length for 3 h, thus exhibiting a photostability just slightly lower (2%) than rhodamine-B, a widely used commercial fluorescent dye (Fig. 3c). The photostability of PLGA-fluram using a confocal microscope configuration is also included in Fig. S3b.† The fluorescence intensity of NCs fabricated by PLGA-fluram decreased by only 13% after 10 min of continuous illumination at 10% of laser power (401 nW). Considering that the laser power applied to observe stained cells is generally less than 10%, our fluorescent NCs would exhibit good photostability under *in vitro* conditions. Note that the calculated quantum yield of PLGA-fluram (18%) (Fig. S3a†) is much higher than the values reported for fluorescent proteins such as green fluorescent protein (GFP) (7.3%) and its blue variants (7.9%),[27] and similar to other polymeric fluorescent materials such as poly(amido amine)s.[28,29] Finally, the calculated fluorescent brightness of PLGA-fluram (25056) is also much higher than that of other reported biodegradable photo-luminescent poly(lactide-*co*-glycolide) (BPLP-*co*-PLGA) (6550–19230)[30] and other frequently used small organic dyes such as Alexa Fluor 430 (8800) or DAPI (15660). The fluorescence intensities of the fabricated NCs show linear dependency on the NC concentration, and NCs can be clearly imaged with a fluorescence microscope (Fig. 3d). Although in this work we have focused on *in vivo* imaging modalities, the remarkable fluorescence properties shown here endow the PLGA-fluram system with very interesting features for *in vitro* fluorescence tracking studies.

Next, the NIR fluorophore Cy7.5 was introduced into the terminal amine of PLGA-NH_2 *via* an amide bond between the PLGA terminal amine group and amine-reactive Cy7.5 NHS ester. The absorption band of Cy7.5 appeared in the UV-Vis spectrum of the PLGA-Cy7.5 product, which confirmed the successful conjugation of Cy7.5 (Fig. S4a†). The amount of conjugated Cy7.5 in the PLGA-Cy7.5 product was quantified by comparing the fluorescence intensity of the PLGA-Cy7.5 product with freeCy7.5 (Fig. S4b†) in DMSO. Pure PLGA-Cy7.5 with a molar fraction of 0.65 was estimated in the product and a conjugation efficiency of 76% of the Cy7.5 NHS ester to PLGA-NH_2 was calculated considering that the fraction of pure PLGA-NH_2 is 0.86.

For radiolabelling functionalization the ^{89}Zr chelator DFO was introduced at the end of PLGA-NH_2 by forming a thiocarbamide bond between the PLGA terminal amine group and the amine reactive –NCS group in the DFO derivative

p-NCS-Bz-DFO. Compared to the IR spectrum of PLGA-NH_2, some new bands corresponding to the DFO conjugate appear in the spectrum of PLGA-DFO, indicating the successful conjugation of DFO (Fig. S1†). The amount of conjugated DFO in the PLGA-DFO product was quantified by measuring the amount of unreacted PLGA-NH_2 through the fluram method described above (Fig. S2c†). Pure PLGA-DFO with a molar fraction of 0.75 was estimated in the product, and a conjugation efficiency of 88% of p-NCS-Bz-DFO to PLGA-NH_2 was calculated considering that the fraction of pure PLGA-NH_2 is 0.86.

Fabrication of PLGA NCs with selected combinations of imaging moieties

PLGA NCs with encapsulated BSA were prepared by a double emulsion solvent evaporation method.[31] Imaging moieties were incorporated into the PLGA shell by adding to the organic phase various proportions of functionalized PLGA as well as the oleic acid (OA) coated SPIONs (Table 1). Compositional changes of the organic phase did not affect the encapsulation process, and all types of NCs prepared showed mean hydrodynamic sizes within a diameter range of 250–300 nm and a polydispersity index (PdI) <0.2. As seen in Table 1 from NC-1 to NC-3, neither increasing the SPION size nor increasing two-fold its loading affected the mean size of the NCs compared to plain PLGA NCs (NC-0). Note that for the same loading of SPIONs, the magnetization of NC-2 is much higher than that of NC-1 given the larger size of SPIONs for NC-2. Therefore optimal formulation regarding SPIONs (6 wt%, with 9 nm nanoparticles) yields an average saturation magnetization value of 4.06 emu g^{-1} NCs which is more than four-fold larger than our previously reported value (0.90 emu g^{-1}).[31] As will be shown later, the increase of the magnetic moment of NCs resulting from using larger size SPIONs and increasing their load will positively impact on the MRI signal intensity.[32]

Furthermore, the size of NCs as well as the encapsulation efficiency (EE%) of SPIONs were not affected when various proportions of PLGA-fluram (NC-4), PLGA-DFO (NC-5) or PLGA-Cy7.5 (NC-6) were incorporated into the PLGA matrix, even when incorporating various moieties simultaneously (NC-7). Importantly, we had found that the PLGA-based NCs can be fabricated using either up to 100 wt% of any modified PLGA (PLGA-DFO, PLGA-Cy7.5 or PLGA-fluram) or with any mixed proportion of them without affecting the morphology of NCs and EE% of SPIONs. This can be explained by the forming process of the NCs: the different functional moieties at the end of the comparatively extra-long PLGA molecules do not affect the film-forming of PLGA and the entrapment of SPIONs in the polymeric matrix. Finally, PEGylation of the PLGA NCs was achieved by adding a given amount of the commercial amphiphilic block copolymer PLGA-PEG (PEG M_n 5000 and PLGA M_n 7000) to the organic phase. The morphology and size of NCs (NC-8) are maintained up to a maximal fraction of 7 wt% amphiphilic PLGA-PEG (3 wt% PEG, Table 1) and are not affected when co-incorporating other hydrophobic modified PLGA (*i.e.*, PLGA-Fluram/PLGA-DFO/PLGA-Cy7.5) (data not shown).

Fig. 4 shows a representative scanning electron microscopy (SEM) image of the NCs (NC-3) presenting homogeneous spherical morphologies. The inset is a dynamic light scattering (DLS) size distribution histogram of lyophilized NCs redispersed in water. In this case, the mean hydrodynamic diameter of the NCs is 276 nm with a polydispersity index (PdI) of 0.18 reflecting good redispersibility of the NCs in water after the lyophilization process. As mentioned, all types of NCs listed in Table 1 had similar morphologies and sizes (Fig. S7†), which were considered to be suitable for intravenous administration.[33] The upper inset in Fig. 4 shows a representative broken NC, exposing the hollow core, ideal for the loading of protein drugs. The transmission electron microscopy (TEM)

Table 1 Summary of the formulations of PLGA-based NCs. Different proportions of modified PLGA and SPIONs were mixed in the organic phase during the double emulsion process

	PLGA information (wt%)					SPIONs					Size (DLS)	
Sample type	PLGA	PLGA-Fluram	PLGA-DFO	PLGA-Cy7.5	PLGA-PEG	Size[a] (nm)	Loading[b] (wt%)	EE%[b]	M_R (emu g^{-1})	M_S (emu g^{-1})	d.nm	PdI
NC-0	100	—	—	—	—	—	—	—	—	—	255	0.10
NC-1	100	—	—	—	—	6	2.9	92%	0.4	1.0	279	0.17
NC-2	100	—	—	—	—	9	3.0	90%	0.8	1.9	264	0.19
NC-3	100	—	—	—	—	9	6.1	95%	1.6	3.9	276	0.18
NC-4	50	50	—	—	—	9	6.2	95%	1.6	4.7	260	0.15
NC-5	40	—	60	—	—	9	6.3	97%	1.6	4.3	271	0.19
NC-6	40	—	—	60	—	9	5.9	91%	1.5	3.6	245	0.11
NC-7	—	50	50	—	—	9	5.9	91%	1.5	3.7	268	0.18
NC-8	93	—	—	—	7	9	6.0	92%	1.6	3.8	265	0.13
OA-SPIONs[c]						6			14.0	50.8		
						9			26.1	75.1		

[a] The size of SPIONs was determined by statistics from TEM images (Fig. S5†). [b] SPION loading and entrapment efficiency (EE%) were determined by SQUID measurements at 5 K. [c] The fraction of SPIONs in OA-SPIONs was determined by thermogravimetric analysis (TGA) and the magnetization is expressed as emu g^{-1} SPIONs (Fig. S6†).

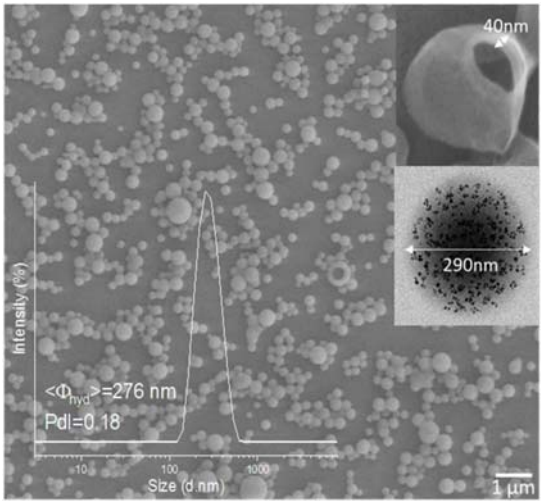

Fig. 4 Morphological data of a representative PLGA NC system (NC-3). SEM image of lyophilized PLGA based NCs with the upper inset showing the hollow core of the NC; lower inset TEM image shows a spherical NC with SPIONs visible as black spots, uniformly distributed in the polymer matrix; DLS curve of NC water suspension after lyophilization with a mean diameter of 276 nm and 0.18 polydispersity.

image in the lower inset revealed the embedding and finely homogeneous distribution of the SPIONs within the polymeric matrix.

NC magnetic properties, accumulation and biodistribution by MRI

The magnetic hysteresis loop at room temperature of lyophilized NC-3 is displayed in Fig. 5a showing the superparamagnetic character of the NCs (lack of coercivity). The superparamagnetic behavior of the NCs after SPION encapsulation is important since in the absence of an external magnetic field, it ensures lack of interactions among NCs thus minimizing the risk of embolization for i.v. administration. The magnetic retention of NCs is illustrated with the use of an external magnet. As seen in Fig. 5b, the colloidal water suspension of 2 mg mL^{-1} of NC-3 forms a round pellet next to the magnet after 7 h. The solution becomes completely clear indicating that a great majority of the NCs are retained by the magnet. Previous experiments using magnetic PLGA nanoparticles[34] or microparticles loaded with only 1 wt% iron oxide[35] already demonstrated magnetic retention in rodent brain or knees, indicating that our protein loaded magnetic NCs with a higher magnetic load (6 wt%, M_S = 4 emu g^{-1}) may still have better characteristics to address magnetic targeting.

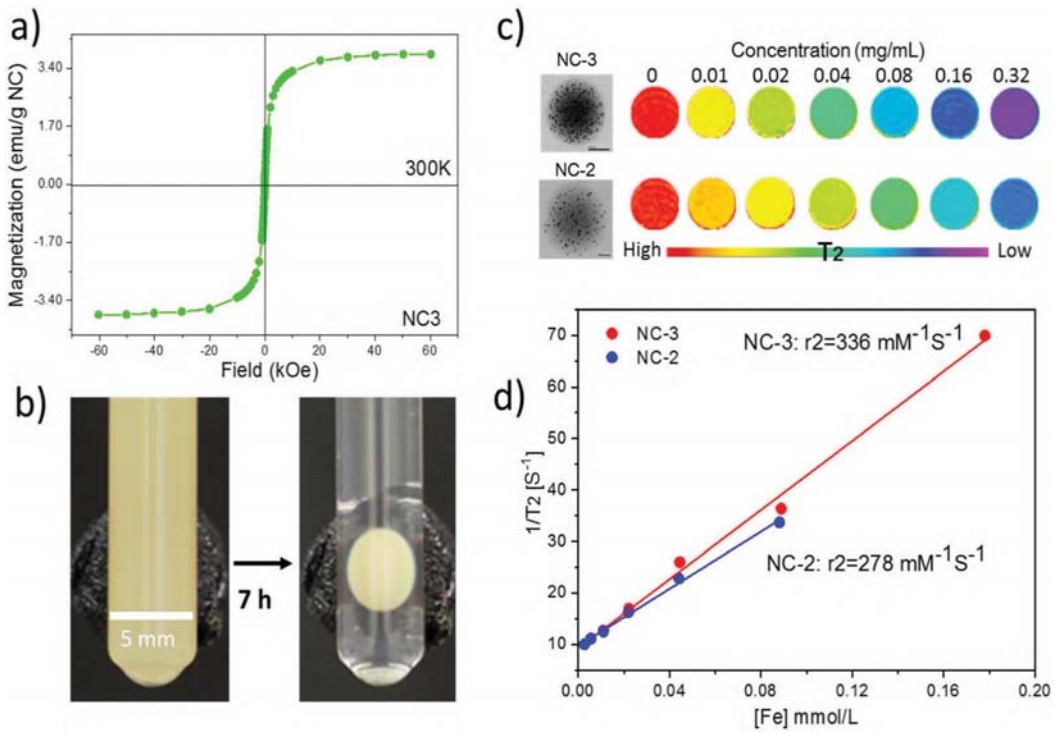

Fig. 5 Magnetic characterization, retention and MRI phantoms of PLGA–SPIONs NCs. (a) Hysteresis loop of the lyophilized batch NC-3 at 300 K, showing superparamagnetism at room temperature; (b) glass tube with water suspension of NC-3 at a concentration of 2 mg mL^{-1}. A permanent magnet (diameter 8 mm, surface field ~0.4 T) was placed on the wall. After 7 h, the NCs adsorbed to the tube wall on the magnet side; (c) *T*2-weighted phantoms obtained by mixing lyophilized NCs with agarose at increasing NC concentrations, on the left are TEM images of NCs; (d) evaluation of r_2 relaxivities for NC-3 and NC-2 (3 wt% and 6 wt%; 9 nm diameter).

Phantom studies were conducted to confirm the MRI performance of the NCs. Phantoms from two batches (NC-2 and NC-3) with different SPION loadings (3 wt% and 6 wt%; 9 nm diameter) at a series of concentrations were prepared (Fig. 5c). Spin–spin relaxation time (T_2) weighted color-coded MRI images clearly exhibit signal decay in a concentration dependent manner. Importantly, at the same concentration NC-3 with 6 wt% SPIONs showed a higher T_2 signal decay rate than NC-2 with 3 wt% SPIONs indicating that NC-3 will be easier to track *in vivo* by MRI. Furthermore, the transverse relaxivity (r_2) value at 7 Tesla of NC-3 (336 mM^{-1} s^{-1}) was higher, as expected, than that of NC-2 (278 mM^{-1} s^{-1}) as seen in Fig. 5d, indicating that the denser packing of SPIONs in a single NC of NC-3 endows the NCs with a larger magnetic moment and increases its efficiency as a spin–spin relaxation agent.[36] Compared with other clinically used SPION systems such as Feridex (98 mM^{-1} s^{-1}) and Resovist (151 mM^{-1} s^{-1}),[37] the much higher r_2 value in our final NC formula (6 wt% SPIONs of 9 nm in diameter) is expected to be useful for *in vivo* MRI tracking of the NCs.

As the representative abdominal images show in Fig. 6b, a much clearer increase of the contrast of the liver was observed in both T2WI and T2 maps after NC administration, illustrating the fast accumulation of NCs in the liver. Quantitative ROI analysis in Fig. 6c shows a 55% drop of signal intensity (SI) on T2W images and a 26% drop of *T*2 relaxation time in the liver, while a negligible signal drop was observed in the kidney, which further demonstrate the large accumulation of NCs in this organ. To further confirm the presence of NCs in the tissue, Prussian blue staining on liver sections confirmed the presence of ferric iron (Fig. 6d) after the *in vivo* MRI.

Biodistribution of the NCs monitored by PET

With a ~3 day half-life, ^{89}Zr-based PET imaging holds great potential as a useful tool for long-term monitoring of the dynamic biodistribution, biodegradation and clearance pathway of nanoparticles *in vivo.*[38] Our results showed that ^{89}Zr-labelling has a yield of about 70% for NC·PLGA-DFO (NC-5) after overnight incubation at room temperature at a concentration of 3 mg mL^{-1}. A DFO challenge study has been

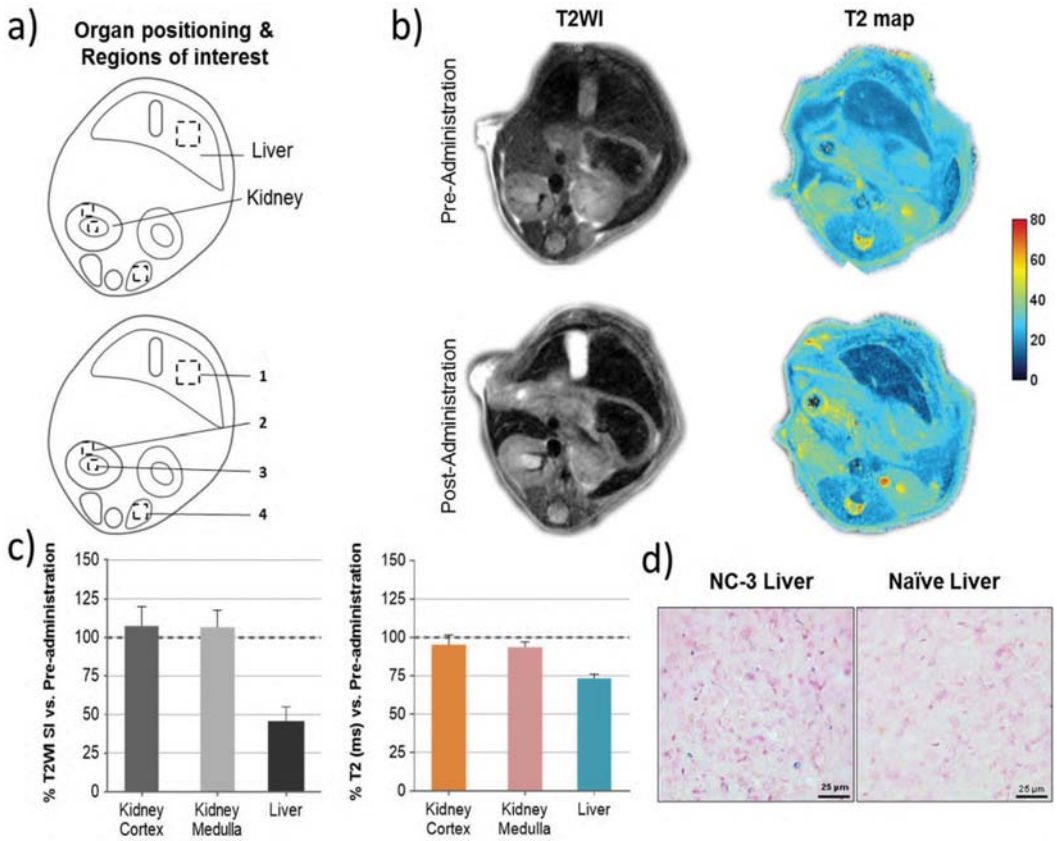

Fig. 6 *In vivo* mouse MRI of the PLGA–SPIONs NCs and liver Prussian blue iron-stain. (a) Representation of the abdominal region with organ positioning and ROI quantification in the kidney and liver (1: liver, 2: kidney cortex, 3: kidney medulla, 4: paravertebral muscle used for normalization). (b) Representative images of T2W and T2 maps before and after NC-3 administration. (c) Signal intensity (SI) and relaxation time (ms) were calculated for each ROI corresponding to the analyzed anatomical structures which were then corrected by muscle ROI SI. Final data are represented as post-administration SI or *T*2 relaxation as the percentage of the pre-administration values (mean ± SEM; n = 2). (d) Representative images of Prussian blue stain for ferric iron in liver sections of naïve and treated animals administered with NC-3 in the MRI study (blue spots).

reported to demonstrate the radiostability of ^{89}Zr-labelled nanoparticles.[39] In our study, the as-obtained NC·PLGA-DFO-^{89}Zr was suspended in 1 mM DFO aqueous solution and incubated at 37 °C for 23 h. Then the NCs were separated by centrifugation and 100% were still labelled, with no presence of ^{89}Zr-DFO in the supernatant, demonstrating a strong binding affinity of ^{89}Zr to the NC·PLGA-DFO.

^{89}Zr labelled NC·PLGA-SPIONs-DFO-^{89}Zr (NC-5) were then injected *via* the tail vein with the same iron dosage as for the MRI study (1.68 mg Fe per kg^{-}) to anesthetized mice. Static whole body PET-CT images were acquired at 1 h, 4 h, 23 h and 47 h p.i. Dominant liver, spleen and lung uptake was observed (Fig. 7a) and confirmed by the quantitative ROI analysis (Fig. 7b) within two days, which can be related to phagocytic cell uptake by the mononuclear phagocyte system,[1] as expected for i.v. injected PLGA nanoparticles of this size.[17] Interestingly, noticeable bladder accumulation (~22%ID cm^{-3}) was observed at 1 h p.i., with a sharp decrease at 4 h p.i. (~6%ID cm^{-3}) likely due to uncontrolled animals' urination between scans. The early stage activity in the bladder could also be confirmed by continuous PET-CT acquisition (Fig. S8†), which showed a linear increase of activity within 3 h p.i. It is hard to assign the activity in the urine to the detachment of free ^{89}Zr from the NCs, since detached free ^{89}Zr is a well-known osteophilic cation with a fast and retained uptake in bones,[38,40] which is not detectable in our case. In the study of Chen *et al.*,[38] for both free ^{89}Zr-oxalate or ^{89}Zr labelled SiO_2 nanoparticles, fast and sustained uptake of free/detached ^{89}Zr in bones and joints was observed from the first few hours up to three weeks, while the accumulation in the bladder was negligible. We thus hypothesized that the erosion of the soft polymeric NCs had happened at an early stage in the complex blood circulation environment. The detached ^{89}Zr-molecular fragments from the NCs, either by degradation of ester bonds in PLGA molecular chains or thiocarbamide bonds between PLGA and DFO or by mechanical force, with a size smaller than 15 nm (ref. 41) underwent renal clearance and were observed in the bladder. Additional experiments showed erosion of NCs clearly observed after *in vitro* incubation in mouse plasma at 37 °C for 24 h (Fig. 7c). Small holes appeared on the NCs while under the same conditions NCs incubated in saline did not show the same eroded surface (Fig. 7d). Considering the *in vivo* blood

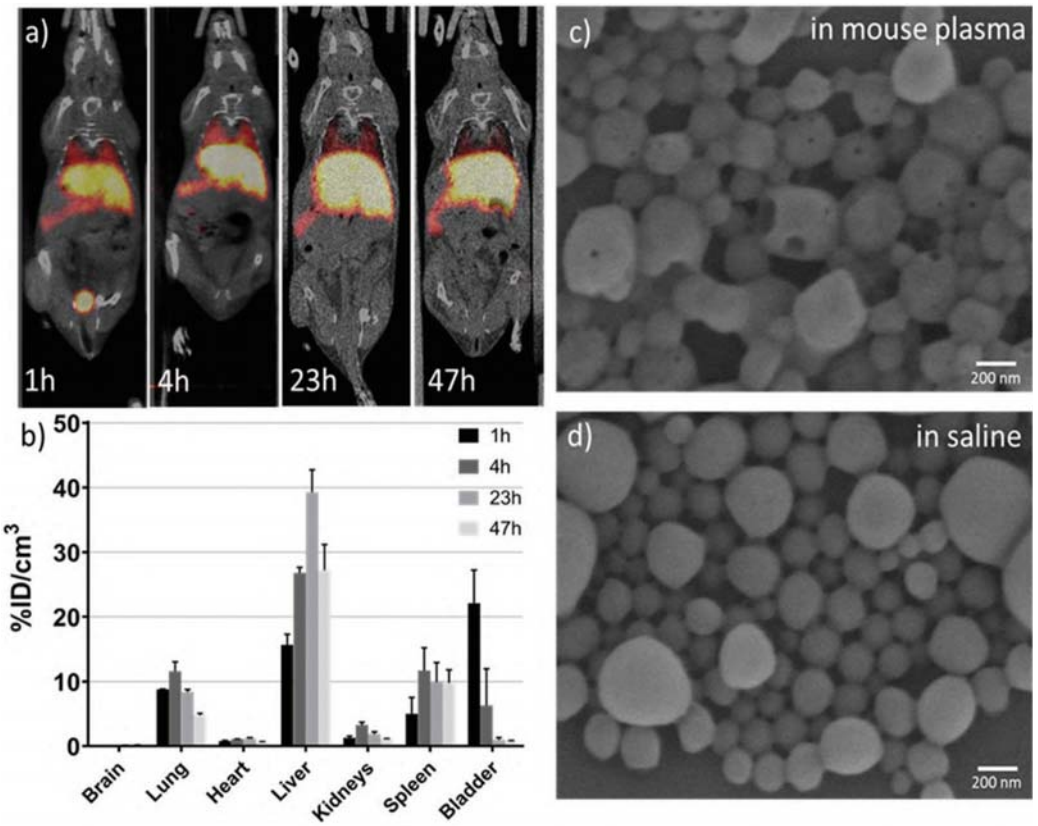

Fig. 7 PET biodistribution study of PLGA-SPIONs-DFO-89Zr NCs. (a) Representative PET-CT coronal images of mice obtained at different time points after intravenous (i.v.) administration of NC·PLGA-SPIONs-DFO-^{89}Zr (NC-5). PET images (maximum intensity projections) have been co-registered with CT images (slices) of the same animals for localization of the radioactive signal; (b) accumulation of radioactivity, expressed as a percentage of injected dose per cm^3 of tissue (%ID cm^{-3}) at 1 h, 4 h, 23 h and 47 h p.i. (mean ± SEM of n = 2); (c) and (d) SEM images of the NCs after incubation for 24 h at 37 °C in mouse plasma or saline.

circulation setting, the erosion of PLGA NCs would be much faster as reported by Swider.[42] Not surprisingly, at late time points the concentration of radioactivity in the bladder decreases likely due to the fast accumulation of the NCs in the liver/spleen.

NC biodistribution monitored by near infrared fluorescence (NIRF) imaging

To investigate the feasibility of the formulation of NC·PLGA-Cy7.5 (NC-6) for *in vivo* NIRF imaging, *in vitro* fluorescence performance was firstly checked. The *in vitro* fluorescence intensity of NC-6 was linearly dependent on the concentrations of NCs, showing strong fluorescence and no quenching up to a high level of 1 mg mL^{-1} (Fig. 8a). Real-time whole-body imaging revealed a dominant abdominal distribution of the NCs with a total radiant efficiency (TRE) of ~42.40 *vs.* control at 2 h p.i. At the end of the observation, main organs including brain, heart, lungs, liver, spleen, kidneys, and bladder were collected. Fig. 8c shows a representative *ex vivo* fluorescence picture of those organs and Fig. 8d shows the quantified result of the biodistribution of the NCs. Dominant liver, spleen and lung accumulation was observed which was consistent with the data acquired with PET. Note that we also did see the bladder signal during the real-time imaging, which further demonstrated that the erosion of NCs really occurred at the early stage p.i., considering that the NIRF imaging is less sensitive than PET. The unobservable *ex vivo* bladder signal may result from the uncontrolled urination and urine sample collection.

From the above discussion, similar biodistribution of the NCs with different imaging probes for MRI/PET/NIRF was evidenced. That was expected since the only difference among the NCs for these three imaging modalities is the existence or not of small molecule ^{89}Zr-DFO or Cy7.5 at the end of the PLGA molecular chain. As we have demonstrated, the imaging probes in the matrix of the PLGA shell do not affect the size of the NCs, which is a key attribute influencing the biodistribution and pharmacokinetics of the nanocarriers.[17,41,43] Thus, the incorporation or removal of these small molecules in the shell does not affect the NCs' *in vivo* biodistribution and tailor-made capsules can be fabricated with the appropriate imaging probe needed for each specific *in vivo* and *in vitro*

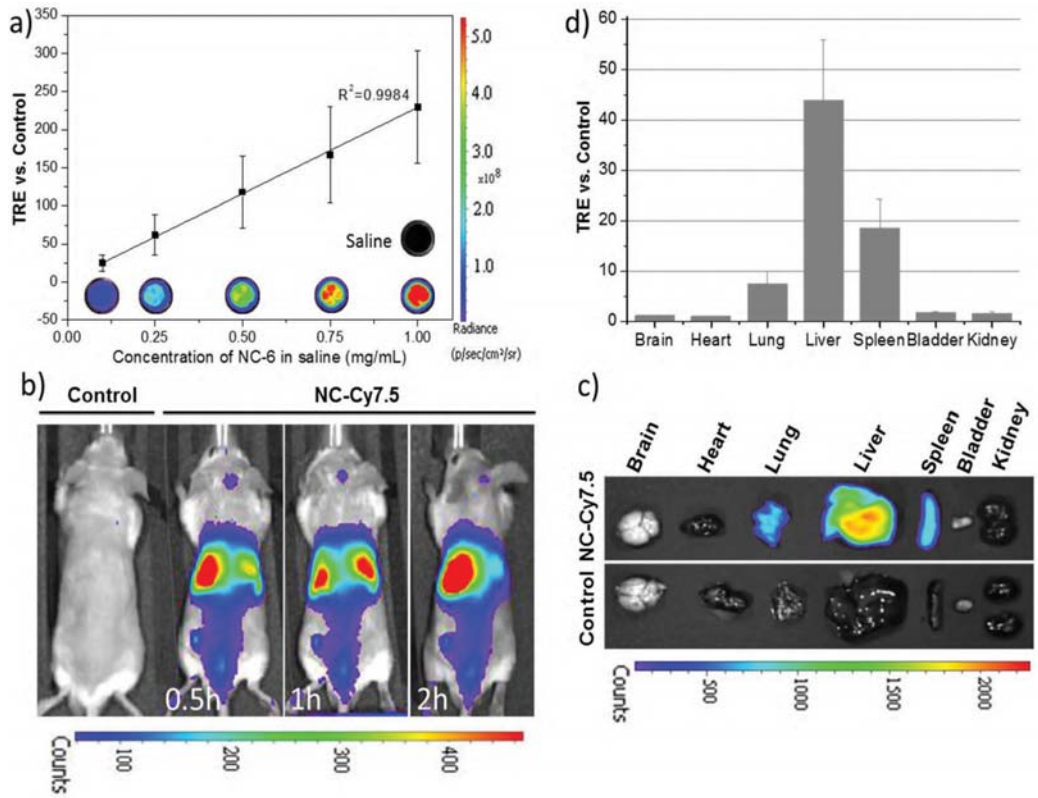

Fig. 8 Fluorescence molecular imaging of PLGA-SPIONs-Cy7.5 NCs. A Xenogen IVIS® imaging system ($\lambda_{ex}/\lambda_{em}$ 710/820 nm) was used to monitor the NIRF signal of NC-6, and the fluorescence intensity was quantified as total radiant efficiency (TRE) *vs.* the corresponding control. (a) Quantitative *in vitro* NIRF intensity of different concentrations of NCs *vs.* control saline (n = 3, mean ± SEM) and representative images of NCs in the well; (b) representative whole body *in vivo* images obtained at different time points after i.v. injection; (c) representative *ex vivo* images of excised organs at the end of the *in vivo* experiment; (d) *ex vivo* quantification of biodistribution of NCs determined by the averaged organ TRE *vs.* the control mouse (n = 2, mean ± SEM).

study. Moreover, simultaneous multimodal imaging is an option through custom-tuning the functional moieties in the capsules. Despite that bare (non-PEGylated) NCs were used here, the PLGA NCs can also be easily pegylated as shown for the NC-8 system (3 wt% PEG Mn 5000) and modify the blood circulation time of NCs. Moreover, the magnetic functionality could be exploited for magnetic targeting in a selected organ or tissue.

In vitro and *in vivo* safety studies of NCs

In vitro and *in vivo* safety studies of NC-3 (PLGA-SPIONs NCs) were conducted considering that this is the simplest therapeutic formulation for magnetically targeted delivery. We tested the effect of NC-3 on the proliferation/viability of human endothelial cells since endothelial cells lining the blood vessels are the first NC target following their intravenous administration. Thus, human brain endothelial cells (hCMEC/D3), a cell line derived from brain microcirculation, and primary cultures of human $CD34^{+}$-derived endothelial cells were exposed to NC-3 and its cytotoxicity was evaluated by performing a MTT assay. As shown in Fig. 9a, the cells did not exhibit a decrease in viability after being exposed for 48 h to the NCs from 25 to 100 μg mL^{-1}, and the differences in cell viability between groups were not significant (ANOVA >0.05), thus our results suggest that the NCs are biocompatible for the studied range of concentrations and time. Thereafter, the systemic effect of NCs *via* i.v. administration was evaluated. Fig. 9b shows that after injection of NCs, all animals maintained the body weight within normal values for two weeks (no differences between groups at the end of the experimental period), with no significant morbidity and no potential adverse effects. At the same time, blood sample tests to monitor potential liver and pancreatic toxicity showed that none of the biomarker enzymes were significantly different between groups and similar to those measured in non-treated mice (Fig. 9c; ANOVA >0.05), suggesting a normal activity of these organs. All the above results reinforce the biosafety of this formulation of nanocarriers for future clinical translational practice.

Protein loading

The protein loading content was determined as 11.3 ± 1.0 μg BSA per mg NCs (1.13 wt%) with an encapsulation efficiency of 46.0 ± 1.4%, the average of six different batches measured. The

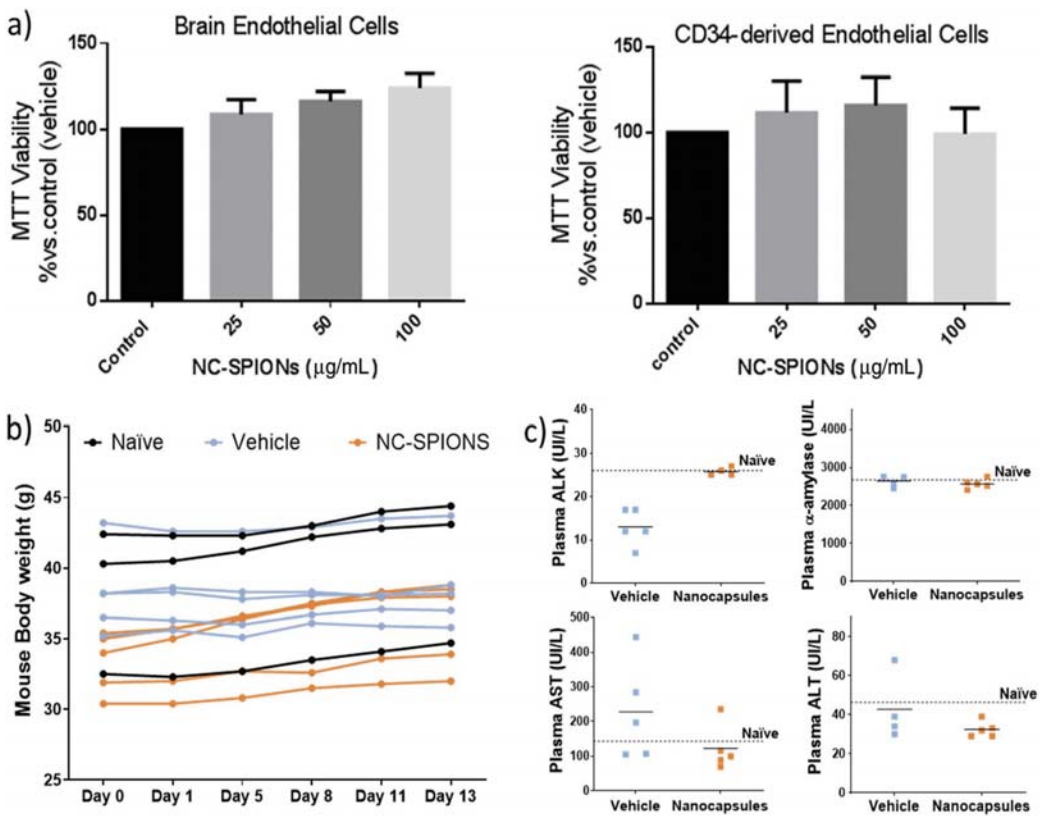

Fig. 9 *In vitro* and *in vivo* safety of PLGA–SPION NCs (NC-3). (a) Cell viability after exposing to an increasing dose of NCs for 48 h, expressed as a percentage of untreated cells (control media), determined by MTT assay (n = 3, mean ± SEM); (b) the curve of body weight of the observed mice throughout the experiment, the naïve group was not treated serving as control (n = 3), the vehicle group received 150 μL of saline (n = 5) and the NC group received 0.84 mg NCs in 150 μL of saline (n = 5); (c) liver and pancreatic toxicity after 13 days of NC injection based on specific enzyme levels in plasma: alanine aminotransferase (ALT), alkaline phosphatase (ALK), aspartate aminotransferase (AST) and α-amylase.

protein loading of 1.13 wt% is much higher than the reported value (0.03 wt%) of vessel endothelial growth factor loaded PLGA NCs[31] and the EE% is comparable to the PLGA NCs loaded with neurotrophin-3 (47 ± 2%) or brain-derived neurotrophic factor (47 ± 7%).[8]

Conclusions

By covalently bonding PLGA with small molecules of fluorophores and radioligands as well as by incorporating iron oxide nanoparticles we propose here chemical synthetic approaches to transform PLGA NCs into a sensitive, multimodal theranostic platform for drug delivery. We have shown that the size of PLGA NCs remained unaltered after incorporation or removal of one or several imaging moieties. We have proposed a modular approach for capsules with multimodal capacities to be used at several development phases and investigated by different imaging modalities including MRI, fluorescence at different emitting wavelengths (blue and NIR) or ^{89}Zr-labeling enabled positron emission tomography (PET) imaging. In all cases, the imaging moieties are chemically attached to the PLGA and with minimal interaction with the encapsulated drug thus avoiding leaching and interferences with the therapeutic agent.

The theranostic PLGA NCs show no toxicity *in vitro* or *in vivo*. In this regard, the NCs did not affect the viability of two different human endothelial cells (brain endothelial cells and CD34$^+$ derived endothelial cells) for concentration up to 100 μg mL^{-1}. *In vivo* biosafety was shown based on the lack of morbidity of mice for 2 weeks after the systemic NC administration and the fact that none of the biomarker enzymes monitored were significantly different between groups and similar to those measured in non-treated mice.

Finally, we have shown that the NCs can contain over 1 wt% of protein in their core achieved at the fabrication level. Interestingly, PLGA NCs decorated with iron oxide nanoparticles can be exploited for magnetic retention or magnetic guiding and biodistribution could be modified by using PEG-PLGA NCs.

Author contributions

Y. Zhang contributed to the experimental design, data acquisition and analysis, and manuscript writing. M. García contributed to protein loading and *in vitro* safety study. A. Grayston contributed to the *in vivo* safety and IVIS study. I. Feiner and J. Llop contributed to the radiolabelling and PET study. R. Loiola and F. Gosselet participated in the *in vitro* safety study. P. Cabrer, I. Barba and D. Dorado contributed to the MRI study. I. Anton participated in the NC preparation. A. Rosell and A. Roig contributed to the design of experiments, coordination of the study, and manuscript writing. All authors revised the manuscript.

Conflicts of interest

The authors declare no conflicts of interest.

Acknowledgements

The Acciones Complementarias program from the Instituto de Salud Carlos III, Spain, co-financed by the European Regional Development Fund (AC17/00004 grant) as part of the MAGBBRIS project (Euronanomed III 8th joint call), and the RETICS INVICTUS RD16/0019/0021 are acknowledged. The Miguel Servet program (CPII15/00003) and PFIS program (FI17/00073) from Fondo de Investigaciones Sanitarias-Instituto de Salud Carlos III and ERDF supported A. Rosell and A. G. research contracts. This work was also partially supported by the Spanish Ministry of Science, Innovation and Universities through the grants PCIN-2017-090, RTI2018-096273-B-I00, CTQ2017-87637-R, SAF2017-87670-R, SEV-2015-0496 and MDM-2017-0720 and by the Generalitat de Catalunya grants (2017SGR765 & 2017SGR1427). Yajie Zhang is supported by the China Scholarship Council (CSC). FG and RAL are supported by the French national agency (ANR) through the grant ANR-17-ENM3-0005-01. The authors thank Dr Vanessa Gómez-Vallejo, Dr Unai Cossío, Dr Xabier Rios and Zuriñe Baz for support in labelling and PET *in vivo* experimentation. We acknowledge support of the publication fee by the CSIC Open Access Publication Support Initiative through its Unit of Information Resources for Research (URICI).

References

1 R. Klippstein, J. T. W. Wang, R. I. El-Gogary, J. Bai, F. Mustafa, N. Rubio, S. Bansal, W. T. Al-Jamal and K. T. Al-Jamal, *Small*, 2015, **11**, 4704–4722.
2 T. Sudha, D. J. Bharali, M. Yalcin, N. H. Darwish, M. Debreli Coskun, K. A. Keating, H. Y. Lin, P. J. Davis and S. A. Mousa, *Int. J. Nanomed.*, 2017, **12**, 1305–1315.
3 R. Yang, J. Xu, L. Xu, X. Sun, Q. Chen, Y. Zhao, R. Peng and Z. Liu, *ACS Nano*, 2018, **12**, 5121–5129.
4 N. Bertrand, J. Wu, X. Xu, N. Kamaly and O. C. Farokhzad, *Adv. Drug Delivery Rev.*, 2014, **66**, 2–25.
5 Z. Ouyang, T. Tan, C. Liu, J. Duan, W. Wang, X. Guo, Q. Zhang, Z. Li, Q. Huang and P. Dou, *Biomaterials*, 2019, **205**, 50–63.
6 F. Danhier, E. Ansorena, J. M. Silva, R. Coco, A. Le Breton and V. Preat, *J. Controlled Release*, 2012, **161**, 505–522.
7 D. Bobo, K. J. Robinson, J. Islam, K. J. Thurecht and S. R. Corrie, *Pharm. Res.*, 2016, **33**, 2373–2387.
8 M. M. Pakulska, I. E. Donaghue, J. M. Obermeyer, A. Tuladhar, C. K. McLaughlin, T. N. Shendruk and M. S. Shoichet, *Sci. Adv.*, 2016, **2**, e1600519.
9 X. Qin, C. Yu, J. Wei, L. Li, C. Zhang, Q. Wu, J. Liu, S. Q. Yao and W. Huang, *Adv. Mater.*, 2019, **31**, 1902791.

10 A. Harguindey, D. W. Domaille, B. D. Fairbanks, J. Wagner, C. N. Bowman and J. N. Cha, *Adv. Mater.*, 2017, **29**, 1700743.

11 C. J. Bowerman, J. D. Byrne, K. S. Chu, A. N. Schorzman, A. W. Keeler, C. A. Sherwood, J. L. Perry, J. C. Luft, D. B. Darr, A. M. Deal, M. E. Napier, W. C. Zamboni, N. E. Sharpless, C. M. Perou and J. M. DeSimone, *Nano Lett.*, 2017, **17**, 242–248.

12 B. Colzani, L. Pandolfi, A. Hoti, P. A. Iovene, A. Natalello, S. Avvakumova, M. Colombo and D. Prosperi, *Int. J. Nanomed.*, 2018, **13**, 957–973.

13 W. Tao, X. Zeng, J. Wu, X. Zhu, X. Yu, X. Zhang, J. Zhang, G. Liu and L. Mei, *Theranostics*, 2016, **6**, 470–484.

14 P. Kumar, T. V. Treuren, A. P. Ranjan, P. Chaudhary and J. K. Vishwanatha, *Nanotechnology*, 2019, **30**, 265101.

15 A. C. Souza, A. L. Nascimento, N. M. de Vasconcelos, M. S. Jeronimo, I. M. Siqueira, L. R-Santos, D. O. Cintra, L. L. Fuscaldi, O. R. Pires Junior, R. Titze-de-Almeida, M. F. Borin, S. N. Bao, O. P. Martins, V. N. Cardoso, S. O. Fernandes, M. R. Mortari, A. C. Tedesco, A. C. Amaral, M. S. Felipe and A. L. Bocca, *Eur. J. Med. Chem.*, 2015, **95**, 267–276.

16 J. Llop, P. Jiang, M. Marradi, V. Gomez-Vallejo, M. Echeverria, S. Yu, M. Puigivila, Z. Baz, B. Szczupak and C. Perez-Campana, *J. Mater. Chem. B*, 2015, **3**, 6293–6300.

17 L. J. Cruz, M. A. Stammes, I. Que, E. R. van Beek, V. T. Knol-Blankevoort, T. J. A. Snoeks, A. Chan, E. L. Kaijzel and C. Lowik, *J. Controlled Release*, 2016, **223**, 31–41.

18 M. M. Abdel-Mottaleb, A. Beduneau, Y. Pellequer and A. Lamprecht, *Int. J. Pharm.*, 2015, **494**, 471–478.

19 R. L. Cook, K. T. Householder, E. P. Chung, A. V. Prakapenka, D. M. DiPerna and R. W. Sirianni, *J. Controlled Release*, 2015, **220**, 89–97.

20 S. Florinas, M. Liu, R. Fleming, L. Van Vlerken-Ysla, J. Ayriss, R. Gilbreth, N. Dimasi, C. Gao, H. Wu and Z.-Q. Xu, *Biomacromolecules*, 2016, **17**, 1818–1833.

21 K. Qian, J. Wu, E. Zhang, Y. Zhang and A. Fu, *Int. J. Nanomed.*, 2015, **10**, 4149.

22 S. Udenfriend, S. Stein, P. Bohlen, W. Dairman, W. Leimgruber and M. Weigele, *Science*, 1972, **178**, 871–872.

23 E. Carenza, V. Barcelo, A. Morancho, J. Montaner, A. Rosell and A. Roig, *Acta Biomater.*, 2014, **10**, 3775–3785.

24 J. Yang, Y. Zhang, S. Gautam, L. Liu, J. Dey, W. Chen, R. P. Mason, C. A. Serrano, K. A. Schug and L. Tang, *Proc. Natl. Acad. Sci. U. S. A.*, 2009, **106**, 10086–10091.

25 R. Cecchelli, S. Aday, E. Sevin, C. Almeida, M. Culot, L. Dehouck, C. Coisne, B. Engelhardt, M. P. Dehouck and L. Ferreira, *PLoS One*, 2014, **9**, e99733.

26 F. Shimizu, Y. Sano, M. a. Abe, T. Maeda, S. Ohtsuki, T. Terasaki and T. Kanda, *J. Cell. Physiol.*, 2011, **226**, 255–266.

27 K. Mauring, V. Krasnenko and S. Miller, *J. Lumin.*, 2007, **122**, 291–293.

28 D. Wang, T. Imae and M. Miki, *J. Colloid Interface Sci.*, 2007, **312**, 8–13.

29 W. Yang and C. Y. Pan, *Macromol. Rapid Commun.*, 2009, **30**, 2096–2101.

30 J. Hu, J. Guo, Z. Xie, D. Shan, E. Gerhard, G. Qian and J. Yang, *Acta Biomater.*, 2016, **29**, 307–319.

31 E. Carenza, O. Jordan, P. Martinez-San Segundo, R. Jiřík, Z. Starčuk Jr., G. Borchard, A. Rosell and A. Roig, *J. Mater. Chem. B*, 2015, **3**, 2538–2544.

32 Y.-w. Jun, Y.-M. Huh, J.-s. Choi, J.-H. Lee, H.-T. Song, S. Kim, S. Kim, S. Yoon, K.-S. Kim and J.-S. Shin, *J. Am. Chem. Soc.*, 2005, **127**, 5732–5733.

33 R. Gref, M. Lück, P. Quellec, M. Marchand, E. Dellacherie, S. Harnisch, T. Blunk and R. Müller, *Colloids Surf., B*, 2000, **18**, 301–313.

34 Y. Cui, M. Zhang, F. Zeng, H. Jin, Q. Xu and Y. Huang, *ACS Appl. Mater. Interfaces*, 2016, **8**, 32159–32169.

35 N. Butoescu, C. A. Seemayer, G. Palmer, P. A. Guerne, C. Gabay, E. Doelker and O. Jordan, *Arthritis Res. Ther.*, 2009, **11**, R72.

36 E. Taboada, R. Solanas, E. Rodríguez, R. Weissleder and A. Roig, *Adv. Funct. Mater.*, 2009, **19**, 2319–2324.

37 Y. X. Wang, *Quant. Imaging Med. Surg.*, 2011, **1**, 35–40.

38 F. Chen, S. Goel, H. F. Valdovinos, H. Luo, R. Hernandez, T. E. Barnhart and W. Cai, *ACS Nano*, 2015, **9**, 7950–7959.

39 E. Boros, A. M. Bowen, L. Josephson, N. Vasdev and J. P. Holland, *Chem. Sci.*, 2015, **6**, 225–236.

40 D. S. Abou, T. Ku and P. M. Smith-Jones, *Nucl. Med. Biol.*, 2011, **38**, 675–681.

41 M. Cataldi, C. Vigliotti, T. Mosca, M. Cammarota and D. Capone, *Int. J. Mol. Sci.*, 2017, **18**, 1249.

42 E. Swider, S. Maharjan, K. Houkes, N. K. van Riessen, C. G. Figdor, M. Srinivas and O. Tagit, *ACS Appl. Bio Mater.*, 2019, **2**(3), 1131–1140.

43 J. M. Caster, S. K. Yu, A. N. Patel, N. J. Newman, Z. J. Lee, S. B. Warner, K. T. Wagner, K. C. Roche, X. Tian, Y. Min and A. Z. Wang, *Nanomedicine*, 2017, **13**, 1673–1683.

pharmaceutics

MDPI

Article

MRI/Photoluminescence Dual-Modal Imaging Magnetic PLGA Nanocapsules for Theranostics

Yajie Zhang [1], Miguel García-Gabilondo [2], Anna Rosell [2,*] and Anna Roig [1,*]

[1] Institut de Ciència de Materials de Barcelona (ICMAB-CSIC), Campus UAB, 08193 Bellaterra, Catalonia, Spain; yzhang@icmab.es

[2] Neurovascular Research Laboratory, Vall d'Hebron Institut de Recerca, Universitat Autònoma de Barcelona, 08035 Barcelona, Catalonia, Spain; miguel.garcia@vhir.org

* Correspondence: anna.rosell@vhir.org (A.R.); roig@icmab.es (A.R.)

Received: 30 October 2019; Accepted: 17 December 2019; Published: 21 December 2019

Abstract: Developing multifunctional and biocompatible drug delivery nanoplatforms that integrate high drug loads and multiple imaging modalities avoiding cross-interferences is extremely challenging. Here we report on the successful chemical reaction of the high quantum yield biodegradable and photoluminescent polyester (BPLP) with the poly(lactic-co-glycolic acid) (PLGA) polymer to fabricate biocompatible photoluminescent nanocapsules (NCs). Furthermore, we transform the PLGA-BPLP NCs into a magnetic resonance (MR)/photoluminescence dual-modal imaging theranostic platform by incorporating superparamagnetic iron oxide nanoparticles (SPIONs) into the polymeric shell. In vitro phantoms confirmed the excellent MRI-r_2 relaxivity values of the NCs whilst the cellular uptake of these NCs was clearly observed by fluorescence optical imaging. Besides, the NCs (mean size ~270 nm) were loaded with ~1 wt% of a model protein (BSA) and their PEGylation provided a more hydrophilic surface. The NCs show biocompatibility in vitro, as hCMEC/D3 endothelial cells viability was not affected for particle concentration up to 500 μg/mL. Interestingly, NCs decorated with SPIONs can be exploited for magnetic guiding and retention.

Keywords: PLGA nanocapsules; magnetic resonance imaging; photoluminescence; drug delivery systems; magnetic targeting; multimodal imaging; theranostics

1. Introduction

Nanomedicine, which refers to the application of nanotechnology in medicine, offers valuable new tools for the diagnosis and treatment of many diseases. Nanoparticles are increasingly important by assisting to expedite the development of contrast agents, therapeutics, drug delivery vehicles, and theranostics in the context of nanomedicine [1]. Polymer-based nanoparticles are frequently proposed as drug carriers due to their biocompatibility and biodegradability, as well as the possibility of customizing their physicochemical properties for a specific drug or delivery route [2–4]. Among them, poly(lactic-co-glycolic acid) PLGA nanoparticles have gathered particular attention, since they encompass a number of interesting features: (i) FDA and European Medicine Agency approval in drug delivery systems for parenteral administration; (ii) well described formulations and methods of production adapted to various drugs i.e., hydrophilic or hydrophobic, small molecules, or macromolecules; (iii) protects the loaded drugs from degradation and possibility of sustained release; and, (iv) easy to modify to include targeted delivery or to provide tuned performance in a specific biological environment [5,6].

Theranostics is an emerging field that combines diagnostics and therapeutics into multifunction nanoparticle systems [7]. Drugs and nanocarriers in vitro/in vivo fate can be monitored while using noninvasive imaging techniques, such as magnetic resonance imaging (MRI) and fluorescent imaging,

in order to optimize the route of delivery, biodistribution, and drug accumulation, among other factors [4,8,9]. PLGA nanoparticles can be used in diagnostic and therapeutic imaging by the addition of the imaging moieties during the particle synthesis. To date, large efforts have been devoted to conjugating PLGA with semiconducting quantum dots and organic dyes to create photoluminescent PLGA nanocarriers [9–11]. However, conventional approaches for physically blending imaging probes within the nanoparticles can lead to incomplete conclusions or misinterpretations on the nanoparticles' biodistribution and fate [12,13]. Moreover, the inevitable photobleaching and low dye-to-polymer labeling ratios of organic dyes and the innate toxicity of quantum dots prevent their practical use in vivo [14,15]. Recently, a series of biodegradable photoluminescent (PL) polyesters (BPLPs) could derived inherently photoluminescent PLGA-BPLP copolymers with excellent biocompatibility, tunable luminescence and degradation rates, and good thermal and mechanical properties, thus expanding the biomedical applications of PLGA to highly desired optical imaging [16,17].

Here, we present PLGA nanocapsules (NCs) as a dual-modal imaging theranostic platform for magnetic targeting protein delivery (Figure 1). We report on the protocol for the fabrication of magnetic PLGA-BPLP NCs with intrinsic photoluminescence and MRI capacity being endowed by the incorporation of superparamagnetic iron oxide nanoparticles (SPIONs). Moreover, the NCs are functionalized with poly(ethylene glycol) (PEG), providing a hydrophilic surface that could result in an enhanced stealth effect. Unlike solid PLGA nanoparticles [4,18,19], in our NCs, the functional moieties are incorporated into the polymeric shell matrix to minimize interferences with the cargo being placed inside the NC; this is especially important for delicate payloads, such as proteins, enzymes, or microRNAs. In this study, bovine serum albumin (BSA) has been used as a model protein for evaluating the protein loading capability and release kinetics of the proposed nanocarrier.

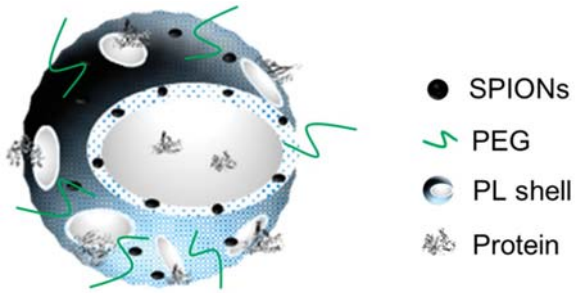

Figure 1. Schematic illustration of poly(lactic-co-glycolic acid)-biocompatible photoluminescent polymer nanocapsule (PLGA-BPLP NC) as a dual-modal imaging theranostic platform.

2. Experimental Section

All of the reagents were purchased from Sigma-Aldrich (Merck KGaA, Darmstadt, Germany) unless specified otherwise.

2.1. Synthesis of PLGA-BPLP Copolymer

The PLGA-BPLP copolymer was synthesized by a slight modification of Yang's method [16,17]. Step one involves the synthesis of a hydroxyl terminated BPLP pre-polymer. Briefly, citric acid, 1,8-octanediol, and L-cysteine with the molar ratio of 1:1:0.2 (5.76 g, 4.38 g, 0.72 g) were added into a flask of 50 mL with a stirring bar. Under a constant flow of argon, the reactants were melted by heating to 140 °C until a clear solution formed. The solution was allowed to react at this temperature for 80 min. and then stopped before the stirring bar stopped stirring completely in the increasingly viscous solution by adding 25 mL of 1,4-dioxane to dilute the produced prepolymer. The product was purified by dropwise precipitation from the 1,4-dioxane solution in water to remove the unreacted monomers. The final BPLP product was collected by centrifugation and then lyophilized.

In the second step, the PLGA-BPLP copolymer was synthesized while using the BPLP as a macroinitiator to react with L-lactide and glycolide via a ring-opening polymerization that was catalyzed by Tin (II) 2-ethylhexanoate ($Sn(OCt)_2$). Briefly, L-lactide, glycolide and BPLP with the molar ratios of (75:25):1 or (50:50):1 were added into a reaction tube. Subsequently, $Sn(OCt)_2$ (0.1 wt% of L-lactide and glycolide mixture) was added as a solution in dichloromethane which was then evaporated in vacuum. The tube was flushed with argon and capped and subsequently immersed in a 160 °C oil bath for 48 h. The obtained product was dissolved in chloroform and then purified by dropwise precipitation into pure ethanol to remove unreacted raw materials. Finally, the PLGA-BPLP copolymer was recovered by centrifugation and then dried in vacuum at room temperature. All of the PLGA-BPLP mentioned in the text were with molar ratios of (75:25):1, unless specified otherwise.

2.2. Synthesis of Oleic Acid Coated SPIONs

The SPIONs were synthesized by microwave assisted thermal decomposition in a microwave synthesizer (Discover SP, CEM Corporation, Matthews, NC, USA), and then coated by oleic acid (OA) [20]. The process to obtain homogeneous OA-SPIONs with an average diameter of 9 nm was as follows: 3.5 mmol of iron precursor $Fe(acac)_3$ was dissolved in 4.5 mL of benzyl alcohol in a microwave reaction glass tube. Microwave irradiation was initiated at 60 °C for 5 min. to fully dissolve the precursor and, subsequently, the irradiation was kept at 210 °C for 30 min., and the reaction was then stopped and cooled down to room temperature. 4 mL of oleic acid in toluene (0.8 mmol/mL) was added immediately into the as-synthesized SPIONs dispersion followed by incubation under ultrasound for 1 h. Subsequently, the obtained OA-SPIONs were separated by centrifugation in five-fold of acetone. The pellet was redispersed in 4 mL of toluene in a glass vial and a magnet was attached on the wall for 5 s, the un-adsorbed suspension containing SPIONs with smaller size was discarded and the adsorbed pellet was redispersed in 6 mL of dichloromethane (DCM), followed by centrifugation at 4000 rpm for 5 min. to sediment the unstable big particles. Finally, the stable OA-SPIONs (9 nm) dispersion in DCM was centrifugated in five-fold of acetone and the pellet product was dried under vacuum and redispersed in DCM at the concentration required for use.

2.3. Fabrication of Functional PLGA-BPLP NCs and Encapsulation of BSA

Functional PLGA NCs encapsulating BSA were prepared by a double emulsion solvent evaporation method. Briefly, 50 μL of inner aqueous phase (W1) containing BSA (30 mg/mL) was emulsified in 500 μL of DCM organic phase (O) that was composed of 50 mg of different proportions of PLGA (RG502H, Mn 12,000)/PLGA-BPLP/PLGA-PEG (PLGA Mn 7000, PEG Mn 5000) and a certain amount of OA-SPIONs by sonication (VC505, Sonics & Materials Inc., Newtown, CT, USA) at 200 W for 28 s to form the first emulsion (W1/O). Afterwards, 2 mL of external aqueous phase (W2) with polyvinyl alcohol (PVA) (20 mg/mL) was added and the second emulsion (W1/O/W2) was formed by sonication for another 28 s. The temperature during the whole emulsion process was kept at 4 °C by using an ice bath. The resulting double emulsion was poured into 50 mL of MilliQ water and mechanically stirred at RT for 2 h to allow for complete evaporation of the organic solvent DCM and the formation of NCs. Finally, the NCs were washed three times with MilliQ water and lyophilized in 6 mL of trehalose aqueous solution (2 mg/mL). The as-obtained powder was stored at 4 °C with desiccant silica gel.

The non-PEGylated and PEGylated NCs have been labelled, as follows: NC1.non PEGylated (90 wt% PLGA-BPLP + 10 wt% PLGA) and NC2.PEGylated (90 wt% PLGA-BPLP + 3 wt% PLGA + 7 wt% PLGA-PEG), both containing ~6 wt% of SPIONs, as gathered in Table 1.

Table 1. Summary of the two main formulations for the NCs. Oleic acid coated-SPIONs and PLGA-BPLP and PLGA-PEG were mixed in the organic phase during the double miniemulsion process.

NCs Type	Shell Polymers (wt%)			SPIONs Loading (wt%)	M_s (eum/g)	Size (DLS)		BSA Loading (wt%)	BSA EE%
	PLGA	PLGA-BPLP *	PLGA-PEG			d. nm	PdI		
NC1.non-PEGylated	10	90	/	5.7	4.0	272	0.11	0.96	38.5
NC2.PEGylated	3	90	7	6.0	4.2	265	0.05	1.01	41.3

* PLGA-BPLP from initial molar ratios (LA:GA):BPLP = (75:25):1.

2.4. Physicochemical Characterization of PLGA-BPLP, SPIONs, and NCs

2.4.1. Absorption Spectroscopies of the Polymers

Attenuated total reflectance-Fourier transform infrared (ATR-FTIR) characterization of the polymers was performed on a Bruker Vertex 70 FTIR spectrometer with a Pike Miracle Single-Bounce diamond crystal plate accessory at room temperature. The FTIR spectra were recorded over a wavelength range of 4000–500 cm^{-1} with a resolution of 4 cm^{-1}. UV-Vis absorbance of the fluorescent polymers was recorded on a Varian Cary-5000 UV-Vis spectrophotometer while using a quartz cuvette with an optical path of 1 cm.

2.4.2. Size Distribution and Disperse Stability of the NCs

Dynamic light scattering (DLS) (Zetasizer Nano ZS, Malvern Panalytical, Madrid, Spain) measurement of the hydrodynamic diameter and size distribution of NCs by intensity was performed by redispersing 0.5 mg of lyophilized NCs powder into 1 mL of MilliQ water.

Turbiscan (Turbiscan Lab, Formulaction, Toulouse, France) is used to detect the destabilization of the NCs suspension. 15 mL of 2 mg/mL NCs in the Turbiscan cell were scanned at all of the heights of the suspension with a time interval of 2 min. during 24 h. The back scattering signals at different heights of the cell were recorded and the delta of back scattering intensity was calculated by subtracting the reference time 0 s. The bottom part was defined as 1/5 of the liquid level.

Nanosight (NS300, Malvern Panalytical, Madrid, Spain) is used to measure the averaged size and concentration of the NCs water suspension. 0.2 mg/mL of NCs with 50 times dilution was pumped into the cell and the data were acquired and analyzed through the Nanoparticle Tracking Analysis (NTA) software along with the instrument.

2.4.3. Electron Microscopies

Field emitting scanning electron microscope (SEM, FEI Quanta 200 FEG, Thermo Fisher Scientific, OR, USA) and transmission electron microscope (TEM, JEM-1210, JEOL Ltd., Tokyo, Japan) were used to study the morphologies of SPIONs and NCs. 0.5 mg of lyophilized powder was redispersed into 1 mL of MilliQ water and centrifuged at 4000 rpm for 10 min. for the SEM sample preparation of NCs. Subsequently, the supernatant was discarded to remove the trehalose (used for cryopreserving during lyophilization) and 1 mL of fresh water was added, the pellet of NCs was redispersed in water with ultrasound. Finally, 6 L of the slightly turbid suspension was deposited onto a small slice of silicon wafer stuck on the top of a carbon layer and dried at room temperature overnight. The sample was sputtered with Au-Pd (20 mA 2 min, Emitech K550, Quorum Technologies Ltd., East Sussex, UK). The TEM samples were prepared by placing and drying one drop of the corresponding NCs or SPIONs dispersion on a copper grid at room temperature.

2.4.4. Magnetometry

Superconductive quantum interference device (SQUID, MPMS5XL, Quantum Design, San Diego, CA, USA) was used to measure the magnetization of NCs and SPIONs and calculate the SPIONs loading (wt%-SPIONs) of the magnetic NCs. Zero-field cooling and field cooling (ZFC-FC) measurement were used to determine the blocking temperature (T_B) of the SPIONs. A gelatin capsule filled with about

7 mg of samples, together with some cotton wool, was inserted into the SQUID magnetometer sample holder and the hysteresis loop was measured from −50 kOe to 50 kOe. The saturation magnetization of the NCs (M_S-NCs, emu/g) and of SPIONs (M_S-SPIONs, emu/g) was used to calculate wt%-SPIONs, as follows:

$$\text{wt\%-SPIONs} = M_S\text{-NCs}/M_S\text{-SPIONs} \times 100\%$$

2.4.5. Fluorescence Properties

Fluorescence spectra of the polymers and NCs were acquired on a spectrofluorometer (LS45, PerkinElmer Inc., Waltham, MA, USA). The excitation and emission slit widths were both set at 10 nm. The quantum yield of the polymers was measured by the Williams' method [16]. Briefly, a series of BPLP/PLGA-BPLP solutions in the corresponding solvents were prepared with gradient concentrations. Maximal excitation wavelength was determined, which generated the highest emission intensity. The fluorescence spectra were collected for the series of solutions in the 10 mm fluorescence cuvette (Figure S1). The integrated fluorescence intensity, which is the area of the fluorescence spectrum, was calculated and then noted. Afterwards, the UV-Vis absorbance spectra were collected with the same solutions and the absorbance at the maximal excitation wavelength within the range of 0.01–0.1 Abs units was noted (Figure S1). The graphs of integrated fluorescence intensity vs. absorbance were plotted. The quantum yield was calculated according to the equation:

$$\Phi s = \Phi_r \left(\frac{\text{Slope}_s}{\text{Slope}_r}\right)\left(\frac{n_s}{n_r}\right)^2$$

where, Φ = quantum yield; Slope = slope of the straight line obtained from the plot of intensity vs. absorbance; n = refractive index of the solvent; s = subscript denotes the sample; and, r = subscript denotes the reference used. Here, anthracene (Φ = 27% in ethanol when excited at 366 nm) was used as the reference.

The fluorescence intensities of different concentrations of NCs in water were quantified in a 96-well by a microplate reader (Spark, Tecan Group Ltd., Männedorf, Switzerland). The NCs were excited at the maximal excitation wavelength and the fluorescence signal was collected by area scan at the maximal emission wavelength.

Photostability was measured by continuously illuminating the polymer or NCs in a fluorescent confocal microscope (Leica SP5, Leica Microsistemas S.L.U., Barcelona, Spain) while using UV diode 405 nm excitation at different laser power (10%, 20%, 100%). The fluorescence images were acquired at a time interval of 1 s for 10 min., changes of mean fluorescence intensity of six region of interests (ROIs) in 10 min. were calculated while using software Las AF. The real laser power (W) at different percentage during 10 min. was monitored using a laser power meter.

2.5. MRI Phantoms of the NCs

In vitro agarose phantoms of NCs were prepared in Eppendorfs where a series of concentrations of NCs were vortexed and sonicated in agarose water solutions before the gel formed. The volume was kept at 1 mL with 0.63 wt% of agarose (Conda, Madrid, Spain). The corresponding iron doses (mmol/L) were calculated according to the wt% of SPIONs in each sample. T2 maps of the phantoms were acquired at 7 T in a 70/30 Bruker USR Biospec system (Bruker GmbH, Ettlingen, Germany), as follows: multi-slice multi-echo (MSME) sequence with echo time (TE) = 13 ms, repetition time (TR) = 4000 ms, field of view (FOV) = 5.5 × 11 mm, and three slices of 1 mm thickness. The quantitative T2 values were obtained from hand-drawn ROIs by using curve fitting in the Image Sequence Analysis (ISA) software along with the instrument.

2.6. In Vitro Toxicity Evaluation of the NCs

Two parallel methods assessed the toxicity of the NCs on human brain endothelial cells (hCMEC/D3): a viability assay based on WST-8 tetrazolium salt reduction (cell counting Kit-8, Dojindo) and direct cell counting. First, 10^4 viable cells per well were seeded on a 24-well plate pre-treated with collagen (rat tail type I, Corning) in 400 µL of endothelial growth medium (EGM2 from Lonza with 2% fetal bovine serum and half the amount of the growth factors that were included in the kit). After incubation for 72 h at 37 °C with 5% of CO_2, the cells were at 80–90% confluence and medium was changed to endothelial basal medium (EBM2, Lonza) containing NCs at 25, 50, 100, 500, and 1000 µg/mL. After 48 h, the cells were washed and incubated with 10% WST-8 solution for two hours. Culture supernatants were centrifuged at 20,000 rpm for 5 min. to remove NCs detritus that could interfere with the dye absorption before determining the absorbance at 450 nm. Cells were trypsinized and resuspended in growth medium and diluted 1:1 in Trypan Blue in order to perform cell counting in a Neubauer chamber. Cell viability and count are expressed as the percentage of absorbance or number of cells as compared with the control (vehicle without NCs). ANOVA test and Dunnett's multiple comparisons post-hoc test was performed vs. the control.

2.7. In Vitro Observation of NCs Cellular Uptake

The hCMEC/D3 endothelial cells were seeded in cover-slips that were pre-treated with collagen (2×10^4 cells/well in 24 well plates) and 24 h later were exposed to 50 µg/mL of empty fluorescent NCs. After an additional 24 h of culture, the wells were washed with PBS, fixated with 4% paraformaldehyde, and mounted with Vectashield antifade mounting medium (Vector Laboratories) with propidium iodide for nucleic acid counterstaining. Additionally, some of the cells were stained with PKH26 lipophilic fluorescent dye for cell membrane labeling according to the manufacturer's protocol. Images at 63× were obtained on a fluorescent confocal microscope (LSM 980 with Airyscan 2 detector, Zeiss, Oberkochen, Germany).

2.8. BSA Loading in NCs and Release Kinetics

The albumin content of the NC was directly determined while using the CBQCA protein assay kit (Invitrogen™ ref. C6667), which determines the protein concentration based on the production of fluorescent products measurable at $\lambda_{ex}/\lambda_{em}$ = 450 nm/550 nm via non-covalent interaction between CBQCA and primary aliphatic amines of proteins. This highly sensitive fluorescence-based method showed compatibility with DMSO, SPIONs, detergents, and other substances that interfere with other commonly used protein determination methods. Lyophilized NCs encapsulating albumin as well as empty NCs as control were fully dissolved in DMSO at 100 mg/mL. The protein contents in the NCs lysates were measured and calculated based on the difference in fluorescence with the control and a calibration curve drawn with standard albumin solutions, the protein contents in the BSA solutions used for encapsulation were also measured. As listed in Table 1 for the two types of NCs, at least two replicate NCs batches of each were measured for the BSA loading and encapsulation efficiency (EE%) calculation. All of the measurements were performed in duplicate for each NCs batch. The experimental BSA loading in the NCs is expressed as µg of BSA per mg of NCs (µg/mg) or the wt% of the NCs, and the BSA EE% is calculated, as follows:

$$\text{EE\% BSA} = \frac{\text{Experimental BSA loading}}{\text{Nominal BSA loading}} \times 100\%$$

For the release studies, lyophilized NCs were resuspended in phosphate buffered saline (PBS) (pH 7.4, Sigma ref. D1408) at 10 mg/mL in low protein binding microcentrifuge tubes (Thermo Scientific© ref. 90410). NCs solutions were incubated at 37 °C in a vertical rotator for different time measures to simulate the in vivo environment: right after the resuspension (time 0), and after three hours, six h, one day, and seven days of incubation. In all cases, an aliquot of 200 µL was frozen

at −80 °C until protein determination. Before the CBQCA assay, the aliquots were centrifuged at 15,000× *g* rcf to separate supernatant and pellet. The amount of protein release was directly calculated as total released protein and indirectly from the remaining protein in the pellet as indirect measure. For this purpose, the pellets were fully dissolved in DMSO and then compared with the intact NCs fully dissolved in DMSO (100 mg/mL) used as the 100% release set up. Four BSA-loaded NCs batches and one of H_2O-NCs batch as control were used and measures done in duplicate. The release profiles were expressed in terms of cumulative release and plotted vs. time.

3. Results and Discussion

3.1. Photoluminescent PLGA-BPLP Copolymer

BPLPs are degradable oligomers synthesized from biocompatible monomers, including citric acid, aliphatic diols, and various amino acids via a convenient and cost-effective polycondensation reaction. BPLPs present some advantages over the traditional fluorescent organic dyes and quantum dots due to their cytocompatibility, minimal chronic inflammatory responses, controlled degradability, and excellent fluorescence properties [16]. Here, L-cysteine was selected and introduced into the polyester structure that was made of biocompatible monomers of citric acid and aliphatic 1,8-octanediol, since previously reported BPLP from this starting amino acid exhibited the highest quantum yield (62.3%) [16]. The fluorophore structure of BPLP was verified as a fused ring structure ((5-oxo-3,5-dihydro-thiazolopyridine-3,7-dicarboxylic acid, TPA) [21]. ATR-FTIR was also used to confirm the chemical structure of the as-synthesized BPLP (Figure 2A). Strong absorptions from the molecular backbone of the polyester were observed i.e., peaks at 1044 cm^{-1}, 1176 cm^{-1}, and 1716 cm^{-1} are attributed to the C=O stretch, C–O asymmetrical, and symmetrical stretches of the ester bond, respectively, the peaks at 2930 cm^{-1} and 2856 cm^{-1} are attributed to the C-H stretches of alkane from 1,8-octanediol and the band near 3467 cm^{-1} is from the −OH. NH bending of the secondary amide at 1527 cm^{-1} and −SH at 2575 cm^{-1} confirm that L-cysteine is chemically bound to the poly(diol citrate) chain. The shoulder band near 1635 cm^{-1} is attributed to the C=O stretching of the tertiary amide from the TPA ring. The average molecular weight (M_w) of BPLP measured by matrix-assisted laser desorption/ionization time of flight mass spectroscopy (MALDI-TOF-MS) was 1044 g/mol (Figure S2). The BPLP oligomer served as a macroinitiator to react with L-lactide and glycolide via a ring-opening polymerization to produce PLGA-BPLP [17]. The as-synthesized PLGA-BPLP (75:25):1 with molar ratios equal to 75:25 for L-lactide to glycolide and equal to 1:100 for BPLP to total L-lactide and glycolide was reported to have desirable glass transition temperature (Tg, 32.5 °C), mechanical properties, fluorescence properties, and degradation rate of the resulting product [17]. Moreover, we have proved here that the 75:25 formulations are more suitable for the fabrication of NCs by a double mini-emulsion method than the PLGA-BPLP (50:50):1 one, as shown in the following section.

The obtained PLGA-BPLP copolymer (Figure 2B inset) exhibits the inherent photoluminescence from the BPLP. The similarities of bands and shapes of the IR spectra of the as-synthesized PLGA-BPLP and commercial PLGA (Figure 2B), for instance, bands at 1084 cm^{-1}, 1165cm^{-1}, and 1747 cm^{-1} from the ester bonds in PLGA indicate their similar chemical structure, given the fact that BPLP is a very small portion of the PLGA-BPLP copolymer.

The fluorescence of the as-synthesized BPLP and PLGA-BPLP was evaluated and Figure 3A,B depict the excitation and emission spectra. The similar spectra further confirm the inherent photoluminescence of PLGA-BPLP from BPLP. Importantly, the fluorescence intensity of PLGA-BPLP only slightly decreased (10%) after 10 min. of continuous illumination under confocal microscope at 10% of laser power (0.40 ± 0.01 μW) (Figure 3C). When considering the laser power applied to observe stained cells is generally less than 10%, our photoluminescent polymer would exhibit good photostability at in vitro conditions. The calculated high quantum yields of BPLP (64%) and PLGA-BPLP (33%) from Figure 3D are consistent with the previously reported values [16,17]. The remarkable fluorescence properties that

are shown here endow the PLGA-BPLP copolymer with high potential for the fabrication of functional photoluminescent NCs.

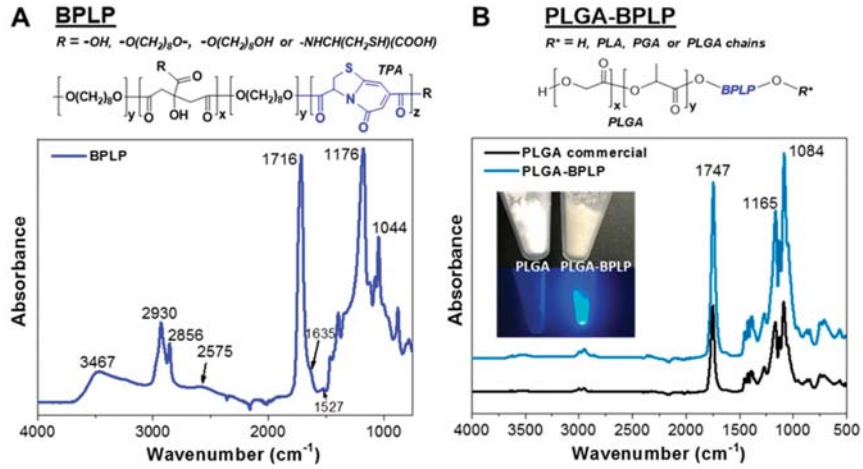

Figure 2. Attenuated total reflectance-Fourier transform infrared (ATR-FTIR) spectra of the as-synthesized biocompatible photoluminescent polymer (BPLP) and PLGA-BPLP copolymer confirming their chemical structures and the successful synthesis. (**A**) BPLP; (**B**) PLGA-BPLP and commercial PLGA as reference. Inset: fluorescence of the PLGA-BPLP under a UV lamp.

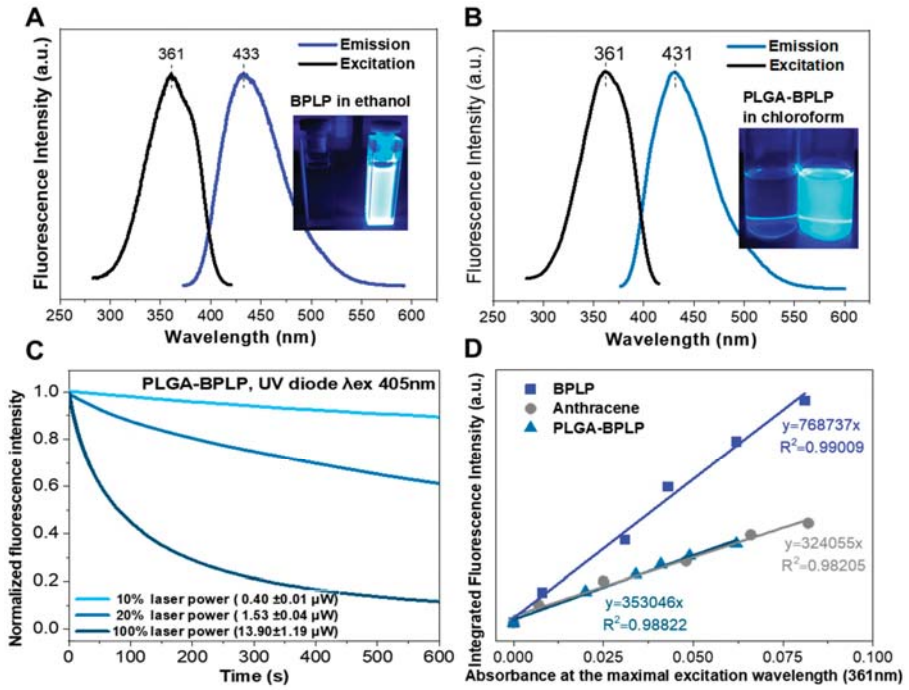

Figure 3. (**A**,**B**) excitation and emission spectra of the as-synthesized BPLP and PLGA-BPLP. Insets: fluorescence of BPLP and PLGA-BPLP dispersed in solutions under a UV lamp; (**C**) photostability evaluation of PLGA-BPLP powder under confocal microscope at different laser power, fluorescence intensity expressed as the percentage vs. the value at the initial time; and, (**D**) fluorescence intensity-absorbance curves of BPLP, PLGA-BPLP, and anthracene used as a reference used to calculate quantum yields.

3.2. Fabrication of PLGA-BPLP NCs Combining Other Functional Moieties

PLGA-based NCs with BSA encapsulated were prepared by a double emulsion solvent evaporation method with slight modifications from our previously reported method [22]. Functional moieties, such as PLGA-BPLP for the fluorescence imaging, PLGA-PEG to increase hydrophilicity and sealthness, and SPIONs for magnetic targeting and MRI (Figure 4A,B) can be incorporated to the organic phase during the NCs fabrication process (see Table 1). The first important remark is that NC morphology was not affected, even when using 100 wt% of PLGA-BPLP (75:25):1 (Figure S3A). A formulation with 90 wt% of PLGA-BPLP (75:25):1 was selected to allow for NC PEGylation by the addition of 7 wt% of PLGA-PEG and for the benefit of higher fluorescence intensity (Figure S4). Note that 7 wt% of PLGA-PEG (3 wt% PEG, Figure S3B) (NC2) was found to be the maximum amount that can be mixed in the organic phase during the NCs fabrication process, due to the amphiphilic property of PLGA-PEG. For a larger wt% of PLGA-PEG, the morphology and size of NCs were not maintained. As shown in the SEM image (Figure 4C), non-PEGylated and PEGylated NCs, as listed in Table 1, both contain ~6 wt% of SPIONs and depict homogeneous spherical morphologies and sizes (d.nm ~270) being similar to other reported PLGA systems that are suitable for intravenous administration [23]. The upper inset in Figure 4C shows a representative broken NC, exposing the hollow core where the protein drug is loaded. We have also found that the PLGA-BPLP (50:50):1 polymer from using initial molar ratio of LA:GA = 50:50 and BPLP:(LA + GA) = 1:100 was not as suitable for the fabrication of NCs. NCs with homogeneous morphology and narrow size distribution were attained only up to a maximum of 30 wt% of modified PLGA (Figure S3C) and without the possibility of further adding PLGA-PEG when using PLGA-BPLP (50:50):1 (Figure S3D). These results are in accordance with the higher glass transition temperature and better mechanical properties of PLGA-BPLP (75:25):1 over those of PLGA-BPLP (50:50):1 [17]. As expected, the NCs with a higher fraction of PLGA-BPLP (75:25):1 (90 wt%) show higher fluorescence intensity than the ones that were obtained with PLGA-BPLP (50:50):1 (30 wt%) at the same concentration (Figure S4).

Regarding magnetic loading, up to 6 wt% of SPIONs could be loaded without affecting the NCs morphology and yielding a saturation magnetization (M_S) value of around 4 emu/g NCs (Figure 4D). In addition, the lower blocking temperature (T_B, 33 K) of SPIONs in the NCs (Figure 4D inset) than the SPIONs of dry powder (55 K, Figure 4B inset) further demonstrates that the SPIONs are well dispersed in the polymer matrix. Note that a high magnetic loading is desirable for the magnetic retention of NCs. This is illustrated in the inset images of Figure 4D, where the darker-coloured water suspension of NCs with 6 wt% of SPIONs were adsorbed faster to the tube wall on the magnet side than the NCs with 1 wt% SPIONs loading at the same concentration, promisingly benefiting the magnetically targeted drug delivery as compared to the previously reported results [4,24]. Note that the superparamagnetic behaviour of NCs at room temperature (lack of coercivity, Figure S5) ensures no magnetic interactions among NCs in the absence of an external magnetic field, minimizing the risk of embolization during i.v. administration.

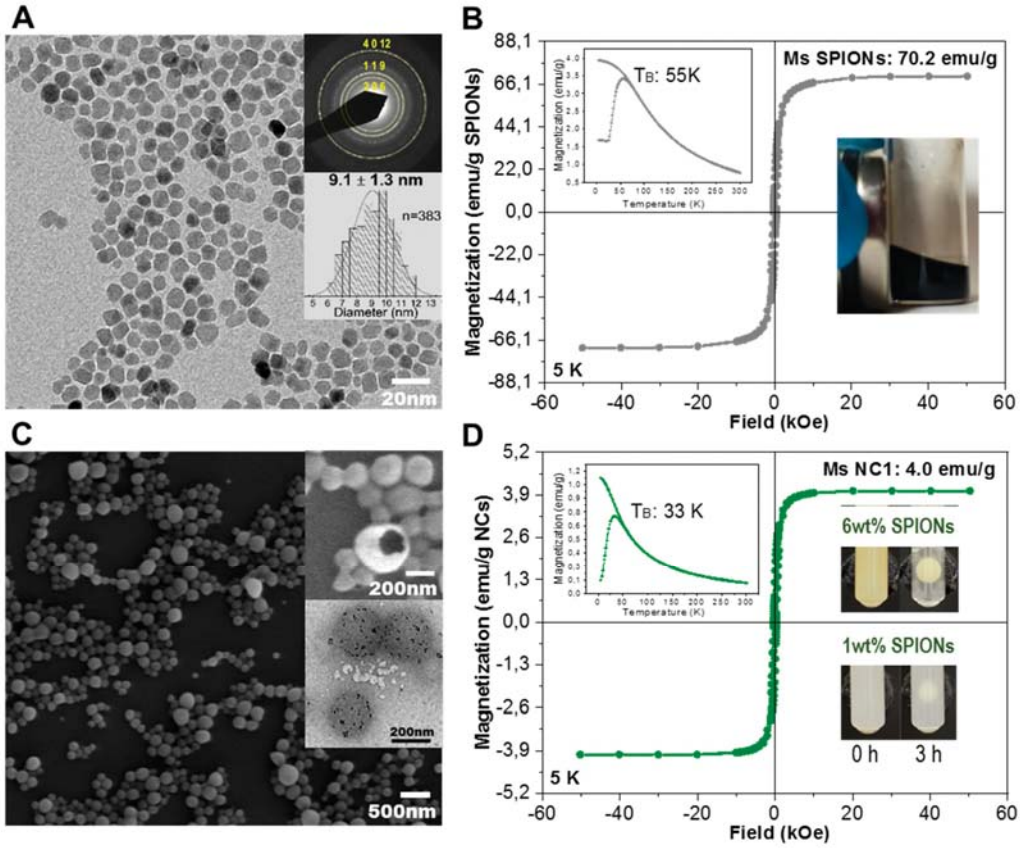

Figure 4. (**A**) Representative transmission electron microscope (TEM) image of the oleic acid (OA) coated SPIONs with the upper inset showing the selected area electron diffraction (SAED) pattern of maghemite and lower inset a size distribution histogram of the particles in the image; (**B**) hysteresis loop (5 K) and ZFC-FC (inset) for the OA-superparamagnetic iron oxide nanoparticles (OA-SPIONs), inserted picture shows the stable OA-SPIONs in dichloromethane attracted by an external magnet; (**C**) representative SEM image of lyophilized NCs with the upper inset showing the hollow core of a nanocapsule and lower inset a TEM image of three NCs with the SPIONs visible as black spots well distributed in the polymer matrix; (**D**) hysteresis loop (5 K) and ZFC-FC (inset) for the lyophilized nanocapsule batch NC1, inserted pictures show the water suspension of these NCs (2 mg/mL) where the 6 wt% loading of SPIONs were adsorbed faster to the tube wall on the magnet (diameter 8mm, surface field ~0.4 T) side than that of 1 wt% loading.

It is well reported that the surface PEGylation of engineered nanoparticles provides them with stealth character increasing blood circulation time since nanoparticles are less visible to the reticulo-endothelial system [6]. We evaluated the flocculation regime of the NCs with a Turbiscan to confirm successful surface modification with PEG, since the long hydrophilic PEG chains (Mn 5000) on the surface of the NCs are expected to increase the stability of the NCs in water suspension and decrease the sedimentation rate. Sedimentation of the NCs suspension was monitored for 24 h. Figure 5A shows that, as NCs sedimentation progresses, the back scattering signal of the bottom part of the suspension increases from an increasingly higher concentration of NCs, while the signal of the top part decreases. The sedimentation rates of non-PEGylated and PEGylated NCs were compared with or without a physiological concentration of BSA (0.5 mM) in Figure 5B, as expected the bottom back scattering signal of the PEGylated NCs media increases at a slower rate than the non-PEGylated ones

both with and without BSA, which demonstrates a better dispersibility of the NCs due to the surface hydrophilic PEG chains. Note that the sedimentation rates of non-PEGylated and PEGylated NCs both slow down with the physiological concentration of BSA probably due to the interaction of NCs with the dense BSA solution. Additionally, in Figure 5A, the back scattering signal of the middle part did not vary with time, which means that the NCs were monodispersed at the physiological concentration of BSA and flocculation or coalescence did not occur during the 24 h period. This is in consistent with the DLS size distribution results that are shown in Figure 5C, both non-PEGylated and PEGylated NCs remained monodisperse at the physiological concentration of BSA, which is of great advantage for the i.v. administration and in vivo blood circulation. Nanosight was also used as an additional technique for the determination of size and the concentration of the NCs (Figure 5D). The results show a similar size distribution as obtained by DLS. From the number concentration of the NCs, we can determine a mean mass of 1.06×10^{-11} mg/NC.

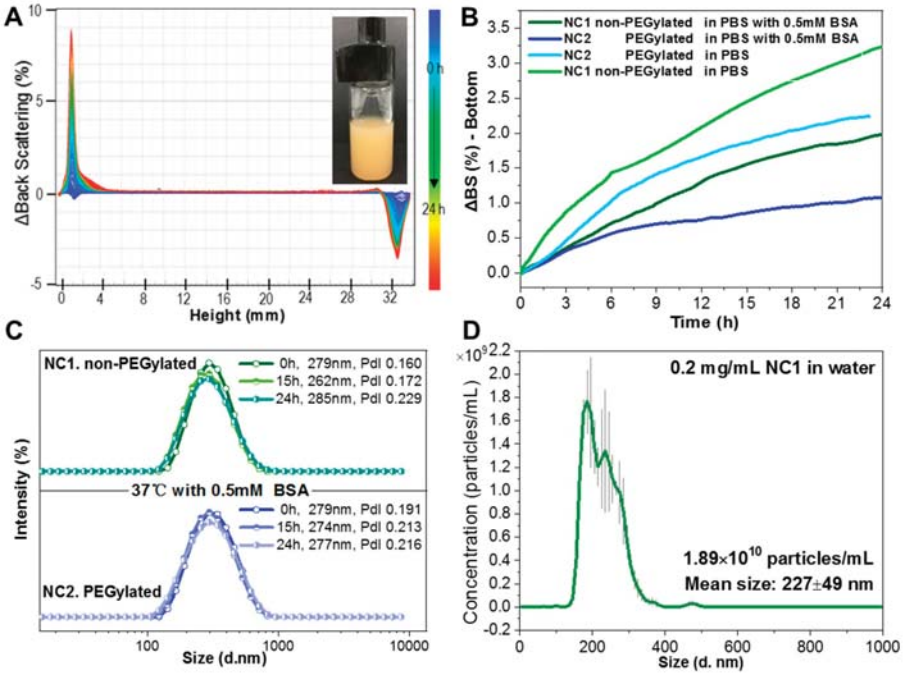

Figure 5. (**A**) Back scattering intensity change of the NC2 PBS suspension (shown inset) containing 0.5 mM of BSA at different height of the vial along 24 h measured by Turbiscan; (**B**) quantified back scattering intensity change of the bottom part of the vial along 24 h for NCs suspension in different media measured by Turbiscan; (**C**) dynamic light scattering (DLS) size distributions of NC1 and NC2 PBS suspensions with 0.5 mM of BSA along 24 h; (**D**) quantitative number concentration and size distribution of the nanocapsules measured by Nanosight (n = 3, mean ± SD with error bar).

3.3. Imaging Performance of the Magnetic Photoluminescent NCs

The fluorescence of the NCs was evaluated, and Figure 6A depicts the excitation and emission spectra. The spectra are similar to those of the PLGA-BPLP polymer shown in Figure 3B. Importantly, the incorporation of SPIONs in the polymer matrix does not quench the fluorescence of NCs. Note that a small displacement of the emission peak wavelength was observed for aqueous dispersed fluorescent NCs when compared to the emission peak of the polymer in a chloroform solution (Figure 3B), which we ascribe to the different interaction of the fluorescent probe with the two solvents. The fluorescence intensities of NCs show a linear dependency on the NCs concentration within a range of 0.1 to 1.0 mg/mL; at higher concentrations the fluorescence shows a trend towards saturation (Figure 6B).

NCs can be clearly imaged with a fluorescence confocal microscope and they show a very good photostability while using 10% of laser power, which is ideal for the observation of in vitro cellular uptake (Figure 6C). The strategy used here confers intrinsic photoluminescence to the PLGA NCs without introducing any cytotoxic quantum dots or photo-bleaching organic dyes when compared to other more conventional approaches that physically blend imaging probes within the carrier that can lead to misinterpretations on the tracing of the carrier [12,13], which may greatly expand the applications of this drug carrier.

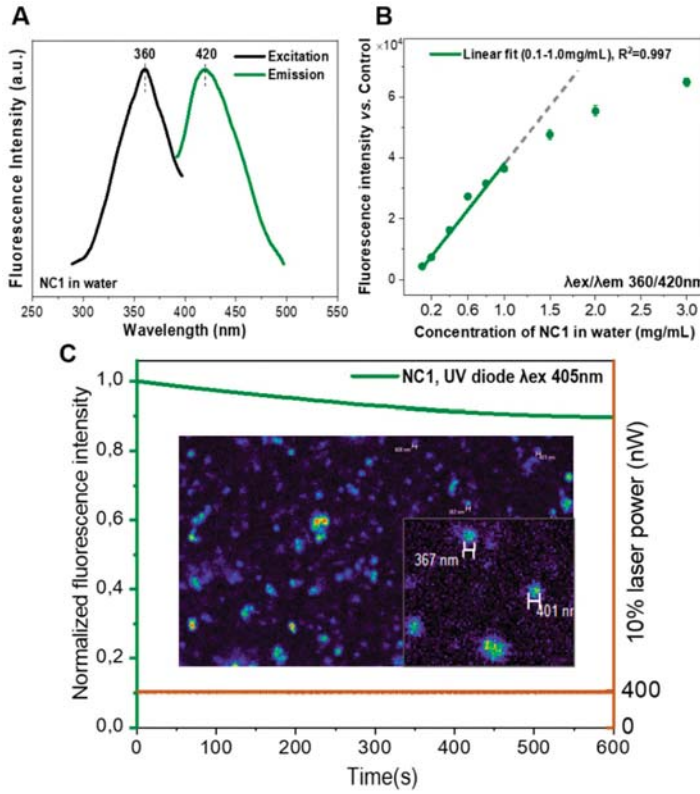

Figure 6. (**A**) Excitation and emission spectra of the nanocapsules (NCs) water suspension; (**B**) fluorescence intensity of different concentrations of NCs measured by microplate reader (n = 2, values represent mean ± sd and subtract values of control non-fluorescence NCs); and, (**C**) photostability evaluation of NCs under confocal microscope at 10% laser power, fluorescence intensity expressed as the percentage vs. the value at the initial time, inset: NC1 water suspension observed at 60× lens.

Phantom studies were conducted to confirm the MRI performance of the capsules. Phantoms of NCs that were dispersed in agarose gel at various concentrations were prepared (Figure 7A). Spin-spin relaxation time (T2) maps clearly exhibit signal decay in a concentration dependent manner. The calculated transverse relaxivity (r_2) values at 7 Tesla of both non-PEGylated NC1 (263 $mM^{-1}s^{-1}$) and PEGylated NC2 (237 $mM^{-1}s^{-1}$) are similar as those seen in Figure 7B, as expected, further demonstrating the similar loading and distribution of SPIONs in the polymer shell matrix for both systems. When compared with other clinically used SPIONs systems, such as Feridex (98 $mM^{-1}s^{-1}$) and Resovist (151 $mM^{-1}s^{-1}$) [25], the much higher r_2 value of our NCs formula is expected to be useful for in vivo MRI tracking of the NCs.

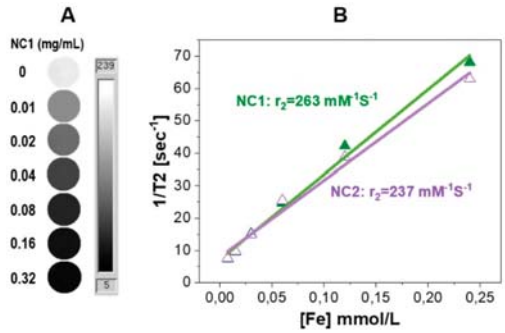

Figure 7. (**A**) T2 maps of a series of concentrations of NC1 in agarose phantoms; (**B**) r_2 relaxivity evaluation for the NCs.

3.4. Cell Viability after NCs Uptake

Photoluminescent NCs were incorporated by brain endothelial cells after several hours in culture, as seen in Figure 8A, with cytoplasmic localization of the NCs in perinuclear structures compatible with Golgi bodies and endosomes. This subcellular localization was confirmed by Z-stack images (Figure 8B). Importantly, this cellular uptake was biocompatible for endothelial cells, as the main exposed cells during NCs circulation in blood vessels, since viability tests did not show signs of cell toxicity at a wide range of NCs concentrations up to 500 μg/mL (Figure 8C,D) and 48 h exposure. Only extremely high doses (1000 μg/mL) with noticeable occupying space difficulties for cell culturing showed a significant reduction in cell viability and number.

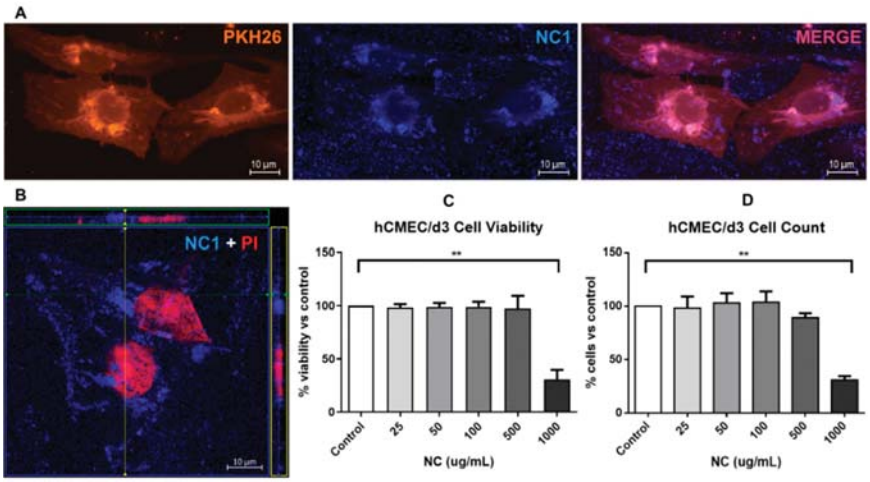

Figure 8. NCs uptake and cytotoxicity in human brain endothelial cells. (**A**) Representative images of hCEMC/d3 cells stained with membrane dye PHK26 and exposed to 50 μg/mL of NC1 for 24 h (63× magnification); (**B**) Orthogonal view of a Z-stack of Propidium Iodide (PI) stained cells (showing the cell nuclei) and the fluorescent NCs; (**C**,**D**) hCEMC/d3 cells were treated for 48 h with different concentrations of NC1 and cell viability was determined with WST-8 reduction assay or tripsinized and counted in a Neubauer chamber, (n = 3–4, values represent mean ± SEM, ** $p < 0.01$).

3.5. Protein Loading and In Vitro Release

Protein loading and encapsulation efficiency were determined by lysing NCs with DMSO and measuring total protein content. The BSA loading content was determined as ~10 μg BSA/mg NCs (1 wt%) with an EE% of around 40% for both NC2.PEGylated and NC1.non-PEGylated systems, as

listed in Table 1, which indicated that the incorporation of PEG does not affect the protein encapsulation process. Note that a protein loading of 1 wt% is much higher than other reported values (0.03 wt% of vessel endothelial growth factor (VEGF) loaded PLGA NCs) [22] and the EE% of 40% is comparable to the PLGA NCs loaded with neurotrophin-3 or brain-derived neurotrophic factor (47%) [26].

BSA-loaded NCs were able to release protein cargo over time at physiological temperature in PBS media (32% protein release in one week). Figure 9A shows a fast BSA release within the first hours, but not after one day, which could be related to the protein degradation in ex vivo conditions of our assays. The amount of released protein in one week was similar when indirectly measured from the pellet retained protein (Figure 9B,C), although the release profile showed a more sustained pattern over time, which could be associated to the protein that was trapped within the PLGA polymer.

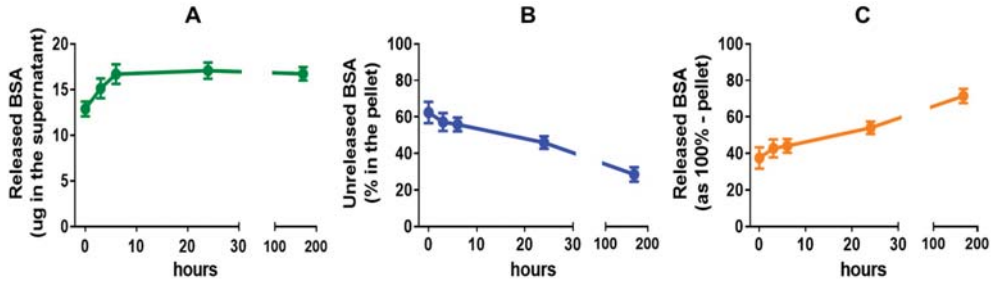

Figure 9. Protein release temporal profile of the NCs. (**A**–**C**) NC1 in PBS (10 mg/mL) were incubated at 37 °C in rotation and the released BSA quantified as total mass of protein released (**A**) together with BSA content in the remaining NCs pellet by DMSO lysis (**B**) and the released BSA calculated indirectly from the pellet values (**C**). The percentage was calculated versus intact unreleased NCs lysated also in DMSO (n = 8, values represent mean ± SEM).

By using the model protein BSA, here we were able to prove the loading capacity and release kinetics of the drug carrier, yet the preservation of protein functionality after the encapsulation process still needs to be investigated. Nevertheless, in a previous work, we have shown that VEGF could be encapsulated following a similar route and VEGF effect on cell proliferation could be determined [22], which implied the preserved protein functionality.

4. Conclusions

We here transform PLGA nanocapsules (NCs) into a highly sensitive, MRI/photoluminescence dual-modal imaging theranostic platform for drug delivery by integrating the biocompatible and photoluminescent polyester BPLP into the PLGA molecular structure, as well as by incorporating superparamagnetic iron oxide nanoparticles (SPIONs). Furthermore, we have shown that PEGylation provides a hydrophilic surface to the NCs slowing down their flocculation rated and without modiying the size, SPIONs content or protein loading capacity of the NCs. In all cases, the functional moieties are embedded in the PLGA shell with minimal interferences between them or with the therapeutic protein. The developed magnetic PLGA-BPLP NCs show biocompatibility in vitro. In this regard, the NCs did not affect the viability of endothelial cells in culture for concentration up to 500 μg/mL and 48 h incubation. Finally, we have shown that the NCs can contain 1 wt% of protein in their core achieved at fabrication level and that one third of the encapsulated protein is released in the first week. Interestingly, the NCs decorated with SPIONs can be exploited for magnetic retention and magnetic guiding.

Supplementary Materials: The following are available online at http://www.mdpi.com/1999-4923/12/1/16/s1. Figure S1: UV-Vis absorbance spectra and fluorescence spectra of the as-synthesized A/B) BPLP, C/D) PLGA-BPLP and E/F) reference anthracene at a series concentrations for fluorescence quantum yield calculation, Figure S2: Matrix-assisted laser desorption/ionization time of flight mass spectroscopy (MALDI-TOF-MS) was used to determine the average molecular weight (Mw) of BPLP. Average Mw calculated from the mass spectrum of BPLP

is 1044 g/mol. For the analysis, the sample was spotted in a MALDI plate with 1,8,9-Antracenotriol (Ditranol) and analyzed using a mass spectrometer (Bruker Daltonics Ultraflex TOF/TOF) in reflectron mode, Figure S3: SEM images and DLS size distributions of NCs fabricated by different types of PLGA-BPLP, Figure S4: Fluorescence intensity of different concentrations of NCs measured by microplate reader at the maximal emission wavelengths (values have subtracted values of control non-fluorescence NCs), Figure S5: Hysteresis loop (300 K) and ZFC-FC (inset) measurements of the lyophilized nanocapsule batch NC2.

Author Contributions: Conceptualization, Y.Z. and A.R. (Anna Roig); Data curation, Y.Z. and M.G.-G.; Formal analysis, all authors; Investigation, Y.Z. and M.G.-G.; Methodology, Y.Z. and M.G.-G.; Resources, A.R. (Anna Rosell) and A.R. (Anna Roig); Supervision, A.R. (Anna Rosell) and A.R. (Anna Roig); Writing—original draft, Y.Z.; Writing—review & editing all authors. All authors have read and agreed to the published version of the manuscript.

Funding: This work was partially supported by the Spanish Ministry of Science, Innovation and Universities through the grants PCIN-2017-090, RTI2018-096273-B-I00, CTQ2017-87637-R, SAF2017-87670-R, SEV-2015-0496 and MDM-2017-0720 and by the Generalitat de Catalunya grants (2017SGR765 & 2017SGR1427). Yajie Zhang was supported by the China Scholarship Council (CSC). The Acciones Complementarias program from the Instituto de Salud Carlos III, Spain, co-financed by the European Regional Development Fund (AC17/00004 grant) as part of the MAGBBRIS project (Euronanomed III 8th joint call), and the RETICS INVICTUS RD16/0019/0021 were acknowledged. Miguel Servet program (CPII15/00003) from Fondo de Investigaciones Sanitarias-Instituto de Salud Carlos III and ERDF, supported A. Roig research contract.

Conflicts of Interest: The authors declare no conflict of interest.

References

1. Kim, D.; Shin, K.; Kwon, S.G.; Hyeon, T. Synthesis and biomedical applications of multifunctional nanoparticles. *Adv. Mater.* **2018**, *30*, 1802309. [CrossRef]
2. Cruz, L.J.; Stammes, M.A.; Que, I.; van Beek, E.R.; Knol-Blankevoort, V.T.; Snoeks, T.J.A.; Chan, A.; Kaijzel, E.L.; Lowik, C. Effect of PLGA NP size on efficiency to target traumatic brain injury. *J. Control. Release* **2016**, *223*, 31–41. [CrossRef]
3. Liu, J.; Xu, H.; Tang, X.; Xu, J.; Jin, Z.; Li, H.; Wang, S.; Gou, J.; Jin, X. Simple and tunable surface coatings via polydopamine for modulating pharmacokinetics, cell uptake and biodistribution of polymeric nanoparticles. *RSC Adv.* **2017**, *7*, 15864–15876. [CrossRef]
4. Cui, Y.; Zhang, M.; Zeng, F.; Jin, H.; Xu, Q.; Huang, Y. Dual-targeting magnetic PLGA nanoparticles for codelivery of paclitaxel and curcumin for brain tumor therapy. *ACS Appl. Mater. Interfaces* **2016**, *8*, 32159–32169. [CrossRef]
5. Danhier, F.; Ansorena, E.; Silva, J.M.; Coco, R.; Le Breton, A.; Préat, V. PLGA-based nanoparticles: An overview of biomedical applications. *J. Control. Release* **2012**, *161*, 505–522. [CrossRef] [PubMed]
6. Swider, E.; Koshkina, O.; Tel, J.; Cruz, L.J.; de Vries, I.J.M.; Srinivas, M. Customizing poly(lactic-co-glycolic acid) particles for biomedical applications. *Acta. Biomater.* **2018**, *73*, 38–51. [CrossRef] [PubMed]
7. Mir, M.; Ahmed, N.; ur Rehman, A. Recent applications of PLGA based nanostructures in drug delivery. *Coll. Surf. B Biointerfaces* **2017**, *159*, 217–231. [CrossRef] [PubMed]
8. Ouyang, Z.; Tan, T.; Liu, C.; Duan, J.; Wang, W.; Guo, X.; Zhang, Q.; Li, Z.; Huang, Q.; Dou, P. Targeted delivery of hesperetin to cartilage attenuates osteoarthritis by bimodal imaging with Gd2 (CO3) 3@ PDA nanoparticles via TLR-2/NF-κB/Akt signaling. *Biomaterials* **2019**, *205*, 50–63. [CrossRef] [PubMed]
9. Yang, R.; Xu, J.; Xu, L.; Sun, X.; Chen, Q.; Zhao, Y.; Peng, R.; Liu, Z. Cancer cell membrane-coated adjuvant nanoparticles with mannose modification for effective anticancer vaccination. *ACS Nano* **2018**, *12*, 5121–5129. [CrossRef]
10. Medina, D.X.; Householder, K.T.; Ceton, R.; Kovalik, T.; Heffernan, J.M.; Shankar, R.V.; Bowser, R.P.; Wechsler-Reya, R.J.; Sirianni, R.W. Optical barcoding of PLGA for multispectral analysis of nanoparticle fate in vivo. *J. Control. Release* **2017**, *253*, 172–182. [CrossRef]
11. Park, J.K.; Utsumi, T.; Seo, Y.E.; Deng, Y.; Satoh, A.; Saltzman, W.M.; Iwakiri, Y. Cellular distribution of injected PLGA-nanoparticles in the liver. *Nanomedicine* **2016**, *12*, 1365–1374. [CrossRef] [PubMed]
12. Abdel-Mottaleb, M.M.; Beduneau, A.; Pellequer, Y.; Lamprecht, A. Stability of fluorescent labels in PLGA polymeric nanoparticles: Quantum dots versus organic dyes. *Int. J. Pharm.* **2015**, *494*, 471–478. [CrossRef] [PubMed]
13. Cook, R.L.; Householder, K.T.; Chung, E.P.; Prakapenka, A.V.; DiPerna, D.M.; Sirianni, R.W. A critical evaluation of drug delivery from ligand modified nanoparticles: Confounding small molecule distribution and efficacy in the central nervous system. *J. Control. Release* **2015**, *220*, 89–97. [CrossRef] [PubMed]

14. Jaiswal, J.K.; Mattoussi, H.; Mauro, J.M.; Simon, S.M. Long-term multiple color imaging of live cells using quantum dot bioconjugates. *Nat. Biotechnol.* **2003**, *21*, 47. [CrossRef] [PubMed]
15. Jamieson, T.; Bakhshi, R.; Petrova, D.; Pocock, R.; Imani, M.; Seifalian, A.M. Biological applications of quantum dots. *Biomaterials* **2007**, *28*, 4717–4732. [CrossRef] [PubMed]
16. Yang, J.; Zhang, Y.; Gautam, S.; Liu, L.; Dey, J.; Chen, W.; Mason, R.P.; Serrano, C.A.; Schug, K.A.; Tang, L. Development of aliphatic biodegradable photoluminescent polymers. *Proc. Natl. Acad. Sci. USA* **2009**, *106*, 10086–10091. [CrossRef]
17. Hu, J.; Guo, J.; Xie, Z.; Shan, D.; Gerhard, E.; Qian, G.; Yang, J. Fluorescence imaging enabled poly(lactide-co-glycolide). *Acta Biomater.* **2016**, *29*, 307–319. [CrossRef]
18. Tao, W.; Zeng, X.; Wu, J.; Zhu, X.; Yu, X.; Zhang, X.; Zhang, J.; Liu, G.; Mei, L. Polydopamine-based surface modification of novel nanoparticle-aptamer bioconjugates for in vivo breast cancer targeting and enhanced therapeutic effects. *Theranostics* **2016**, *6*, 470. [CrossRef]
19. Kumar, P.; Van Treuren, T.; Ranjan, A.P.; Chaudhary, P.; Vishwanatha, J.K. In vivo imaging and biodistribution of near infrared dye loaded brain-metastatic-breast-cancer-cell-membrane coated polymeric nanoparticles. *Nanotechnology* **2019**, *30*, 265101. [CrossRef]
20. Gonzalez-Moragas, L.; Yu, S.-M.; Murillo-Cremaes, N.; Laromaine, A.; Roig, A. Scale-up synthesis of iron oxide nanoparticles by microwave-assisted thermal decomposition. *Chem. Eng. J.* **2015**, *281*, 87–95. [CrossRef]
21. Kasprzyk, W.; Bednarz, S.; Bogdał, D. Luminescence phenomena of biodegradable photoluminescent poly(diol citrates). *Chem. Commun.* **2013**, *49*, 6445–6447. [CrossRef]
22. Carenza, E.; Jordan, O.; Martinez-San Segundo, P.; Jiřík, R.; Starčuk Jr, Z.; Borchard, G.; Rosell, A.; Roig, A. Encapsulation of VEGF 165 into magnetic PLGA nanocapsules for potential local delivery and bioactivity in human brain endothelial cells. *J. Mater. Chem. B* **2015**, *3*, 2538–2544. [CrossRef]
23. Gref, R.; Lück, M.; Quellec, P.; Marchand, M.; Dellacherie, E.; Harnisch, S.; Blunk, T.; Müller, R. 'Stealth'corona-core nanoparticles surface modified by polyethylene glycol (PEG): Influences of the corona (PEG chain length and surface density) and of the core composition on phagocytic uptake and plasma protein adsorption. *Colloids Surf. B Biointerfaces* **2000**, *18*, 301–313. [CrossRef]
24. Butoescu, N.; Seemayer, C.A.; Palmer, G.; Guerne, P.-A.; Gabay, C.; Doelker, E.; Jordan, O. Magnetically retainable microparticles for drug delivery to the joint: Efficacy studies in an antigen-induced arthritis model in mice. *Arthritis Res. Ther.* **2009**, *11*, R72. [CrossRef] [PubMed]
25. Wang, Y.-X.J. Superparamagnetic iron oxide based MRI contrast agents: Current status of clinical application. *Quant. Imaging Med. Surg.* **2011**, *1*, 35. [PubMed]
26. Pakulska, M.M.; Donaghue, I.E.; Obermeyer, J.M.; Tuladhar, A.; McLaughlin, C.K.; Shendruk, T.N.; Shoichet, M.S. Encapsulation-free controlled release: Electrostatic adsorption eliminates the need for protein encapsulation in PLGA nanoparticles. *Sci. Adv.* **2016**, *2*, e1600519. [CrossRef]